

Developing Highly Tunable Polymer-based Networks for Drug Delivery Applications

By

Laken Leona Williams

Dissertation

Submitted to the Faculty of the
Graduate School of Vanderbilt University
in partial fulfillment of the requirements

for the degree of

DOCTOR OF PHILOSOPHY

in

Chemistry

May 10, 2019

Nashville, Tennessee

Approved:

Eva M. Harth, Ph.D.

John A. McLean, Ph.D.

Steven D. Townsend, Ph.D.

John T. Wilson, Ph.D.

Stacey M. Louie, Ph.D.

To Matthew and Joules

ACKNOWLEDGEMENTS

I would first like to express my gratitude and appreciation to my advisor, Professor Eva Harth, for her mentorship, guidance, and advice throughout my graduate education. Thank you for encouraging me to push beyond the boundaries of my own knowledge and explore past my comfort zone. You have always been a source of energy and excitement to help propel my scientific curiosity, and I am very grateful for your support over the years. To all the members, past and present, of the Harth Group, I am eternally grateful to have met each of you. Thank you all for your support, encouragement, editing, idea-bouncing, and much more. Through it all, your comradery has been invaluable. I am grateful for the life-long friends I have found in you.

I would also like to thank each of the faculty members who have served on my advising committee over the past few years: Professors John McLean, Steve Townsend, John Wilson, and Stacey Louie. Thank you all for being a source of wisdom, critical analysis, encouragement, career advice, and support throughout my education. I truly appreciate each of you as your patience and advice has guided me throughout this experience. I'd also like to express my thanks for the financial support of this research through the National Science Foundation Graduate Research Fellowship Program, the Juvenile Diabetes Foundation, the Vanderbilt Department of Chemistry, the Welch Foundation, and the University of Houston Center of Excellence in Polymer Chemistry.

I am also thankful for a couple people with whom I probably never would have started down this path. To Charles Johnson, my high school chemistry teacher who explained every 'exception to the rule' we came across because I just had to know, thank you for encouraging a curious young woman to pursue a career in science. To Professor Derek Patton, I am forever grateful to you for your support during my undergraduate degree, as well as your continued advice and encouragement during graduate school. To all of the Patton Research Group during my time

there, thank you for showing me what it meant to have passion for your work and always strive to excel. I learned so much from each of you that carried me through my graduate work.

I would like to extend a very special thank you to my amazing support network of family and friends who helped me succeed by their continued love and encouragement throughout the journey. To my parents, Trenia Mann and Donnie Kendrick, thank you both for always believing in, encouraging, and supporting me to pursue whatever dreams I had. To my step-parents, Eric Mann and Doreen Kendrick, thank you for loving, supporting, and encouraging me like one of your own. To my grandparents, Travis and Sherry Camp, and Mamie Kendrick, thank you for being a source of wisdom, support, excitement, and inspiration throughout the years. To all of my wonderful friends who have supported me throughout grad school, thank you for being an ear to talk to, a shoulder to cry on, a corny pun to make me laugh, and so much more.

To Joules, who is aptly named due to her boundless energy, I have been blessed by the cuddles, face licks, and the unconditional love only a dog can give. And last but certainly not least, thank you to my incredible husband, Matthew. You are an endless source of strength, love, encouragement, perseverance, and curiosity. I am constantly inspired by your determination and ambition, and I cannot wait to see what the future holds for you. Thank you for always pushing me to be a better version of myself, for your unfailing faith in me, and for being an amazing partner in this life. Without you, none of this would have been possible.

TABLE OF CONTENTS

	Page
DEDICATION	ii
ACKNOWLEDGEMENTS	iii
LIST OF FIGURES	viii
LIST OF SCHEMES	xii
LIST OF EQUATIONS	xiii
LIST OF TABLES	xiv
Chapter	
I. Introduction.....	1
I.1 Application of Polymer Materials in Drug Delivery	1
I.2 Polymeric Nanoparticles in Drug Delivery	3
I.3 Targeted Delivery Systems for Precise Nanomedicine	6
I.4 Synergistic Combination Therapy Through Polymer-based Prodrug Matrices	8
I.5 Dissertation Overview	10
I.6 References	14
II. Exendin-4 Functionalized Nanosponges for the Targeted Imaging of Beta-Cells Toward Treatment of Diabetes	28
II.1 Introduction	28
II.2 Results and Discussion.....	31
II.2.1 Synthesis of Nanosponges in Precise Size and Crosslinking Density	32
II.2.2 Evaluation and Analysis of Size Relationships	34
II.2.3 Functionalization of Nanosponge Surface with Cys40-Exendin-4 Peptide Followed by Attachment of Fluorescent Imaging Agent	37
II.2.4 In Vivo Imaging and Analysis of Targeted Nanosponges using GLP-1R Expressing Tumor Model.....	40
II.2.5 In Vivo Imaging and Analysis of Targeted Nanosponges using Human Islets Grafted in the Fat Pad.....	42
II.2.6 Optimization of Synthetic Design for Nanosponge	

Functionalization to Improve Aqueous Suspension	44
II.2.7 In Vivo Imaging and Analysis of Targeted Nanosponges using Human Islets Grafted in Quadricep	46
II.2.8 In Vitro Release of Imatinib from Nanosponges	49
II.3 Conclusion.....	50
II.4 Experimental	51
II.5 References	59
III. Development of Collagen-Targeted Theranostic Nanosponges for Delivery of Matrix Metalloproteinase 14 Inhibitor Naphthofluorescein.....	65
III.1 Introduction.....	65
III.2 Results and Discussion	70
III.2.1 Integration of T-Peptide_ACPP, Imaging Dye, and Naphthofluorescein into Targeted Nanosponge Construct.....	70
III.2.2 Synthesis and Characterization of Functionalized Nanosponge with Targeting and Imaging Moieties	70
III.2.3 <i>In Vitro</i> Biocompatibility and Cellular Uptake of Nanosponge Construct	74
III.2.4 <i>In Vivo</i> Blood Clearance and Biodistribution of Nanosponge	77
III.2.5 <i>In Vitro</i> Validation of Lysosomal Escape of Nanosponge Construct.....	79
III.2.6 <i>In Vivo</i> Efficacy of Naphthofluorescein-Loaded Targeted Nanocarriers for Increased Collagen Content	80
III.3 Conclusion	82
III.4 Experimental	82
III.5 References	91
IV. Nanonetworks in Controlled Dimensions via Backbone Ketoxime and Alkoxyamine Crosslinks for Controlled Release.....	97
IV.1 Introduction.....	97
IV.2 Results and Discussion	100
IV.2.1 Synthesis and Characterization of Ketoxime Nanoparticles	100
IV.2.2 Synthesis and Characterization of Alkoxyamine Nanoparticles	104
IV.2.3 Analysis of Nanoparticle Size by Transmission Electron Microscopy, Dynamic Light Scattering, and Gel Permeation Chromatography.....	105
IV.2.4 Investigation of pH-dependent Degradation Behavior for Ketoxime and Alkoxyamine Nanoparticles.....	108
IV.2.5 Evaluating the pH-dependent Drug Release Performance of Ketoxime and Alkoxyamine Nanoparticles.....	110
IV.2.6 Tailoring the Drug Release Profiles through Mixed Composition Nanoparticles	113
IV.3 Conclusion	114
IV.4 Experimental.....	115
IV.5 References.....	121
V. Controlled Release of Formaldehyde from Polyglycidol and	

Polyacrylate Prodrugs for Applications in Synergistic Anti-Cancer Therapies	129
V.1 Introduction.....	129
V.2 Results and Discussion.....	133
V.2.1 Synthesis of Polyglycidol Formaldehyde Prodrugs	133
V.2.2 Evaluation of pH Responsive Formaldehyde Release from Polyglycidol Prodrug.....	137
V.2.3 <i>In Vitro</i> Evaluation of Synergistic Effect for Improved Cytotoxicity of 4T1 Cells using Polyglycidol-based Prodrugs	139
V.2.4 Synthesis of Aminoxy Polyglycidol Formaldehyde Prodrug	140
V.2.5 Evaluation of pH Responsive Formaldehyde Release from Aminoxy-Functionalized Polyglycidol Prodrug	143
V.2.6 Increasing Control over Formaldehyde Loading using Tunable Linear Polyacrylate Prodrug Scaffolds.....	145
V.2.7 Synthesis of Poly(Methoxy PEG Acrylate- <i>co</i> -1) (P(MPEGA- <i>co</i> -1)).....	145
V.2.8 Synthesis of Poly(Methoxy PEG Acrylate- <i>co</i> -Solketal Acrylate) (P(MPEGA- <i>co</i> -SA)	148
V.2.9 Preparation of Polyacrylate-based Formaldehyde Prodrugs	145
V.2.10 Evaluation of pH Responsive Formaldehyde Release from Acrylate Prodrugs.....	151
V.2.11 Preparation of Doxorubicin-Loaded Partially Reduced Ketoxime/Alkoxyamine Nanoparticles	153
V.2.12 <i>In Vitro</i> Release of Doxorubicin from Partially Reduced Ketoxime/Alkoxyamine Nanoparticles	154
V.3 Conclusion	155
V.4 Experimental	156
V.5 References.....	166

Appendix

A. References for Adaptations of Chapters	172
B. Curriculum Vitae	173

LIST OF FIGURES

Figure	Page
I-1. Overview of traditional methods vs proposed tunable networks for drug delivery applications	3
I-2. Polymer structures for PLGA, P(VL-OPD), and P(VL-AVL-EVL)	6
I-3. Formaldehyde-doxorubicin conjugates as small molecule prodrugs	9
I-4. Dual drug delivery matrix for controlled release of formaldehyde and doxorubicin	10
II-1. Nanosponge delivery system for targeting of beta-cells located in the Islet of Langerhans.....	31
II-2. Analysis of molecular weight vs size for nanosponges with varying EVL functionality	35
II-3. Analysis of molecular weight vs size for nanosponges with varying EVL functionality and crosslinker equivalents.....	36
II-4. TEM images of nanosponges.....	37
II-5. NMR characterization of functionalized nanosponges	39
II-6. <i>In vivo</i> imaging of animals after treatment with peptide-functionalized dye and nanosponges validating GLP-1R targeting in tumor model.....	41
II-7. <i>In vivo</i> imaging of animals after treatment with Cys40-Exendin-4 and iFluor® 750 nanosponges loaded with Nile Red confirming localization to fat pad graft.....	44
II-8. NMR characterization of optimized nanosponge synthesis with surface allyl quench by PEG conjugation.....	46
II-9. <i>In vivo</i> imaging of animals treated with Cys40-Exendin-4 and Scrambled-Exendin-4 functionalized nanosponges demonstrating targeting to human islet graft in quadricep muscle.....	48
II-10. Drug release profile of imatinib from nanosponges in PBS, pH 7.4	50

III-1. Illustration of blood flow in normal artery vs artery narrowed by atherosclerosis	66
III-2. Fully functionalized nanosponge with collagen-homing T-peptide with ACPP, Cy3 dye, and loaded with naphthofluorescein.....	69
III-3. Overview of mechanism of action of targeted nanosponge loaded with MMP14 inhibitor to reduce collagen degradation in arterial plaques	70
III-4. Particle size analysis via TEM and DLS for nanosponges.....	73
III-5. NMR characterization of nanosponges and their surface functionalization.....	75
III-6. Cell viability of targeted nanosponge construct with RAW and HT1080 cells	76
III-7. Confocal microscopy of nanosponge cellular uptake in HT1080 cells	77
III-8. <i>In vivo</i> analysis of blood clearance and biodistribution of dye-only functionalized nanosponges	78
III-9. Confocal microscopy of RAW cells to confirm nanosponge location outside of lysosomes	80
III-10. Microscopy of carotid plaque section from mouse indicating increased collagen content in targeted nanosponge treated mouse compared to control.....	81
IV-1. Proposed two- or three-step process for ketoxime and alkoxyamine nanoparticles	100
IV-2. GPC traces of P(VL-OPD).....	102
IV-3. Synthesis scheme and NMR characterization of ketoxime nanoparticles.....	103
IV-4. Synthesis scheme and NMR characterization of alkoxyamine nanoparticles.....	104
IV-5. Particle size analysis by TEM and DLS.....	105
IV-6. Schematic representation of nanoparticle series with tables of synthetic parameters and resulting sizes	106

IV-7. GPC analysis of nanoparticles.....	107
IV-8. Hydrolytic degradation analysis of nanoparticles	109
IV-9. Release of BFA from ketoxime and alkoxyamine nanoparticles	111
IV-10. HPLC analysis of physical mixture of drug and polymer or crosslinker	112
IV-11. Release of BFA from mixed composition nanoparticles.....	114
V-1. Overview of proposed dual drug delivery approach for synergistic combination.....	133
V-2. NMR characterization of polyglycidol prodrug, PG-Acetal.....	136
V-3. HSQC NMR characterization of PG-Acetal.....	137
V-4. Cumulative release of formaldehyde from PG-Acetal	138
V-5. Cell viability of 4T1 cells demonstrating efficacy of combination treatment.....	140
V-6. NMR characterization of aminoxy-functionalized prodrug, P(G ^{AO} -G)-Oxime	142
V-7. Cumulative release of formaldehyde from P(G ^{AO} -G)-Oxime	144
V-8. NMR characterization of P(MPEGA-1)	147
V-9. GPC trace of P(MPEGA-1)	147
V-10. NMR characterization of P(MPEGA-SA).....	149
V-11. GPC trace of P(MPEGA-SA)	149
V-12. HSQC NMR characterization of P(MPEGA-1) and P(MPEGA-SA)	151
V-13. Cumulative release of formaldehyde from P(MPEGA-1) and P(MPEGA-SA).....	153

V-14. Cumulative Release of doxorubicin from ketoxime/alkoxyamine nanoparticles.....155

LIST OF SCHEMES

Scheme	Page
II-1. Nanosponge synthesis through crosslinking of VL-AVL-EVL with diamine PEG	34
II-2. Orthogonal synthesis design for attachment chemistry of Cys40-Exendin-4 targeting peptide and fluorescent imaging dye to nanosponge surface	38
III-1. Synthesis scheme for attachment of T-peptide and Cy3 dye to surface followed by post-loading of naphthofluorescein into nanosponges	72
V-1. Scheme of formaldehyde conjugation to polyglycidol.....	134
V-2. Synthesis and deprotection of P(MPEGA-1).....	146
V-3. Synthesis and deprotection of P(MPEGA-SA).....	148

LIST OF EQUATIONS

Equation	Page
II-1. Calculation for Repeat Monomer Unit (RMU).....	33
II-2. Calculation for ketone concentration in reaction.....	33
II-3. Calculation for difference in allylic protons from NMR integration.....	56
II-4. Calculation for determining efficiency of peptide-conjugation to nanosponge surface.....	56
III-1. Calculation for difference in allylic protons from NMR integration.....	87
III-2. Calculation for determining efficiency of peptide-conjugation to nanosponge surface.....	87

LIST OF TABLES

Table

Table

IV-1. GPC and NMR analysis of P(VL-OPD).....101

CHAPTER I

Introduction

I.1 Application of Polymer Materials in Drug Delivery

Polymers are prevalent materials in tissue engineering,¹⁻⁴ medical devices and surgical sutures,⁵⁻⁷ wound healing,⁸⁻¹⁰ along with many other applications. Polymeric drug delivery systems first gained attention due to their ability to encapsulate poorly soluble drugs, increase bioavailability, and reduce toxicity and off-target side effects, all by achieving either temporal or spatial control over cargo release.¹¹ Further exploration of polymer drug delivery systems has led to an increase in complex design and function for smart, precise, and controlled clinical use.¹²⁻¹⁴ Implementation of polymer-based delivery systems have demonstrated the ability to decrease the amount of drug and dosage frequency required, therefore reducing side effects, while maintaining therapeutic levels at the site of action. Additionally, these systems have provided a method for protection of drugs which are rapidly metabolized *in vivo*.¹⁵

Within the vast field of drug delivery, most approaches are based on two main routes of delivery: systemic and localized injectable systems. Systemic delivery, administered to the circulatory system through pathways such as oral, inhaled, or intravenous injections, are often economical, convenient, and fast-acting. However, for some systemic delivery systems, drawbacks can include low drug absorption and negative side effects. A promising strategy for the improvement of systemic drug delivery is employing attachment of a homing ligand where the

delivery vehicle is directed to the site of interest through a biological action, such as the coupling of an enzyme with its substrate.

In contrast, injectable drug delivery systems usually contain a viscous or gel component which localizes the therapeutic(s) to the injection site. Injectable systems are often advantageous for solid tumor treatment, as the chemotherapeutic agents are localized to the tumor site and healthy cells are not exposed to the cytotoxic effects. Furthermore, bone and wound healing are ideal candidates for injectable delivery systems, as the drugs are needed at the direct site to promote cell reproduction and reduce chance of infection. Injectable systems also provide a great system for dual or multiple drug therapy combinations as they can be comprised of different matrices, such as the dispersion of nanoparticles within a hydrogel.¹⁶⁻¹⁷

Recently, perspectives on the state of nanotechnology-based drug delivery systems presented by Chan *et al.*,¹⁸ as well as the views of Park and coworkers¹⁹⁻²¹ on the current landscape of targeted drug delivery, have exhibited a critical tone of the last decade's developments in drug delivery. While it is necessary to continually reassess our progress and critically analyze state-of-the-art approaches in nanomedicine, it has been demonstrated that the current application of nanotechnology for drug delivery systems utilizing targeting ligands, nanocarriers, and controlled release has led to significant advancements in recent years. In comparison to conventional medicines, nanoformulations in particular provide many physical and biological advantages, such as improved drug solubility, decreased toxicity and off-target side effects, enhanced efficacy.²²⁻²⁵ In 2016, roughly 60% of FDA-approved nanomedicines contained polymer materials in the form of drug conjugates, nanoparticles, micelles, or liposomes.²² Within this work, we present new approaches to address the challenges facing modern drug delivery by implementing orthogonal synthetic strategies for targeting ligand functionalization of well-characterized nanocarriers for

site-specific drug delivery which demonstrates successful localization through *in vitro* and *in vivo* modeling; developing novel, crosslinked nanoparticle platforms capable of high cargo loading and controlled drug release with simple protocols for altering size, density, and drug release rates; and the development of macromolecular prodrugs for synergistic, controlled, and tunable small molecule release in combination injectable delivery systems (**Figure I-1**).

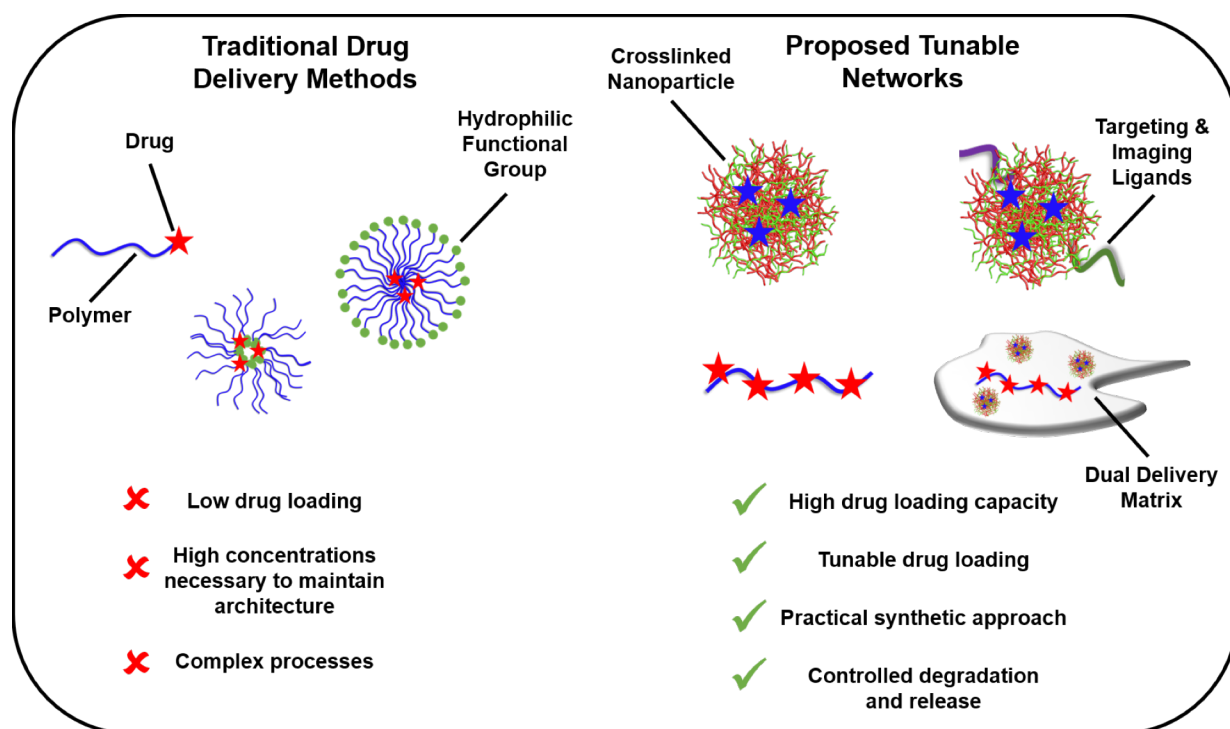


Figure I-1. Overview of polymer-drug conjugate, self-assembled nanoparticle, and micelle drug delivery methods and their limitations compared to proposed work with tunable, degradable polymer networks for enhanced control of drug loading, release, and practicality.

I.2 Polymeric Nanoparticles in Drug Delivery

Nanoparticles for applied drug delivery face many challenges, namely complex manufacturing processes, immune response and endocytosis, and controlling the release of the drug.²⁶⁻³⁰ The techniques used for nanoparticle formation and preparation are vital to controlling

the physiochemical and pharmacokinetic properties of nanomaterials.³¹⁻³³ Traditionally, polymer-based nanoparticles have been prepared through self-assembly or template approaches,³⁴⁻³⁵ where mini- or micro-emulsion, salting out, and solvent evaporation are common techniques.³⁶⁻³⁸ However, precisely governing the properties of these nanomaterials can be difficult and often requires complicated methods, multi-step processes, and expensive equipment,³⁹⁻⁴⁰ leading to the first challenge of nanoparticles in applied drug delivery.

Secondly, special consideration of surface properties is needed to avoid clearance by the immune system during systemic delivery. For example, a major threat to nanocarriers are opsonins, proteins found in the blood which adsorb to the particle surface and act as a bridge between the nanoparticles and phagocytes.⁴¹⁻⁴² These opsonins interact with nanoparticles by intermolecular forces, such as van der Waals, ionic, hydrophobic/hydrophilic, and electrostatic, and the opsonization process occurs to hydrophobic and charged particles much more than that of hydrophilic or non-ionic particles.⁴¹⁻⁴⁴ Methods to develop “stealth” particles which can travel through the body undetected have produced many advancements in nanoparticle technology. For instance, to combat the opsonization process, nanocarriers are traditionally designed with polymer coatings to provide stealth properties which can achieve long residence times in blood circulation.⁴⁵⁻⁴⁶ A common polymer coating, poly(ethylene) glycol or PEG, is widely used as it is easily produced in bulk, cost-effective, and bioinert, and many studies have been undertaken to determine the optimum surface density and molecular weight of PEG coatings.⁴⁷⁻⁴⁹ Moreover, other polymer coatings, including poloxamines,^{41, 43} carbohydrates, and polysorbates, have been widely utilized for different drug delivery applications. As an example, polysorbate coatings have been demonstrated to achieve drug delivery to the central nervous system, a difficult task due to challenges of crossing the blood-brain barrier.⁵⁰⁻⁵²

Lastly, several classes of polymers, including polyurethanes, polystyrenes, polyamides, and polycarbonates, have been extensively utilized as building blocks for nanoparticles which possess a controlled drug release profile. These biodegradable polymer-based nanoparticles are able to encapsulate unstable pharmaceutical agents, improve effectiveness of therapeutics, and provide a modifiable system for delivery.^{33, 36, 53} One of the most widely used polymer classes, polyesters, are popular due to their inert degradation products and ability to break down at physiological pH.⁵³⁻⁵⁵ In particular, poly(lactic-*co*-glycolic) acid (PLGA, **Figure I-2**), has been exhaustively investigated for its application in drug delivery nanostructures,⁵⁶⁻⁵⁷ including particles,⁵⁸⁻⁵⁹ vesicles,⁶⁰ and micelles.⁶¹⁻⁶² However, a limitation to PLGA-based approaches is the inability to chemically crosslink the particles to produce a more stable nanostructure. Moreover, self-assembled nanoparticles often suffer from low drug loading capacity, typically <10 wt %, and faster release profiles.⁶³⁻⁶⁸ An improved strategy was developed in our group through the invention of a polyester nanoparticle which is chemically crosslinked through pendant functional groups of poly(δ -valerolactone-*co*- α -allyl- δ -valerolactone-*co*- α -epoxide- δ -valerolactone) (P(VL-AVL, **Figure I-2**).⁶⁹ Deemed “nanosponge” due to their 3D structure and ability to encapsulate hydrophobic small molecules and subsequently release them at a controlled rate, these nanocarriers provide a unique approach to the development of nanoparticle drug delivery vehicles. Various studies have demonstrated their high drug loading capacity and utility in controlled release of therapeutics, such as paclitaxel, quercetin, and camptothecin.^{17, 70-73}

To further address the challenges faced by polymer nanoparticles in drug delivery, we envision a modified approach to the production of polymer nanoparticles which uses even more practical synthetic methods and simple protocols for the streamlined fabrication of a nanoparticle

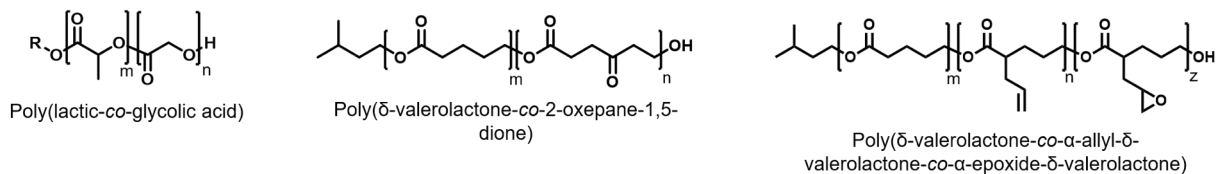


Figure I-2. Polymer structures for PLGA, P(VL-OPD), and P(VL-AVL-EVL) to illustrate the pendant functional groups available for crosslinking in our delivery system compared to traditional PLGA self-assembled nanoparticles.

with tailorable size and density through adjustable synthetic parameters utilizing poly(δ -valerolactone-co-2-oxepane-1,5-dione) (P(VL-OPD, **Figure I-2**). Additionally, an easily modified network chemistry which can be altered to change hydrophilicity, degradation, and drug release kinetics would afford highly tunable drug delivery characteristics. This novel particle platform, synthesized through oxime click chemistry, demonstrates a wide range of tunable properties while maintaining production feasibility.

I.3 Targeted Delivery Systems for Precise Nanomedicine

Continuing to push the boundaries of advanced drug delivery systems, targeted drug delivery approaches have emerged in response to the demand for precision nanomedicine. A major advantage of actively targeted nanocarriers is the ability to target dispersed locations throughout the body, a potentially revolutionary treatment method for hematological conditions, such as leukemia and lymphoma or non-cancer targets where there is no solid tumor for EPR effect to assist localization. Other potential targets characterized by disseminated malignancies which could benefit from actively targeted drug delivery systems are cardiovascular disease, diabetes, Alzheimer's. Approaches to targeting specific biological sites have included chemical

modifications to the drug, surface functionalized of nanocarriers, and prodrugs. Unfortunately, understanding and implementing these targeting strategies is difficult due to the complexity and diversity of each disease, malignant tissue, and biological environment.

Our knowledge and understanding of complex biological processes, such as genetics,⁷⁴⁻⁷⁶ evolution of drug resistance,⁷⁷⁻⁷⁸ and mechanisms of tumor metastases,⁷⁹⁻⁸⁰ are rapidly advancing. Recent merging of precision and nanomedicine have led to a highly integrated approach for targeted drug delivery. Wang et al.⁸¹ reported a precision nanomedicine strategy for the identification of an esophageal squamous cell (ESC) carcinoma molecular target from human patients and utilized this target for precise drug delivery of combination therapy which demonstrated improved efficacy in a mouse model. Other biomarkers, such as those expressed in aggressive forms of cancer,⁸²⁻⁸⁵ can be leveraged for not only prognosis, but targeted treatment as well. Many targeting approaches take advantage of cellular surface receptors, such as the overexpression of human epidermal growth factor receptor 2 (HER2) in breast, ovarian, and gastric cancers as a target for the delivery of anti-tumor drugs as well as imaging agents.⁸⁶

Combined drug delivery and diagnostics, termed theranostics, is another area where targeted approaches can achieve significant results. These platforms allow for the visualization of the tissue and targeting site during treatment, and can provide vital information about the target, such as size, location, and dispersion of cell mass.⁸⁷⁻⁸⁹ In order to conjugate targeting and imaging molecules directly to nanomaterials, the nanoparticle should possess at least two distinct reactive functionalities on the surface. Our previously developed nanosponge affords primary amines and allyls on the surface as functional groups suitable for this purpose.⁹⁰ Through development of orthogonal strategies for conjugation chemistries, theranostic nanocarriers can be designed which possess a targeting moiety, imaging molecule, and entrapped drug cargo.

I.4 Synergistic Combination Therapy Through Polymer-based Prodrug Matrices

As previously mentioned, polymer-drug conjugates are often used in drug delivery through chemical linkage of the drug to polymer chains. Polymer-drug conjugates, or prodrugs, offer similar advantages compared to their small molecule counterparts, such as improved efficacy due to higher bioavailability, prolonged half-life, and increased circulation time.⁹¹⁻⁹² Several polymers have been utilized for prodrugs, including methacrylamides⁹³⁻⁹⁴ and PEG.⁹⁵⁻⁹⁶ A typical method of preparation is by ‘drug-initiated’ polymerization where the drug acts as a polymer initiator, resulting in a 1:1 ratio of polymer:drug.⁹⁷ However, the low ratio of active drug to delivery system requires higher dosing of prodrug to achieve effective treatment. A new approach, through the conjugation of small molecules to many reactive functional groups along a polymer chain, would afford higher concentration of drug within the prodrug formulation. Additionally, this system would afford versatility through the ability to have other reactive handles along the polymer backbone to provide access to additional functionalization, such as imaging or targeting ligands.⁹⁸⁻
99

Synergistic drug combinations, in which the co-administration of therapeutics improves the efficacy of treatment, are an emergent area of research for conditions which prove difficult or unresponsive to current therapeutic approaches. Combining two or more pharmaceutical compounds helps to suppress multi-drug resistance by reaching the desired outcome, e.g. cell death or receptor upregulation, through different mechanisms of action. Most notably, promising strategies include the repurposing and application of previously developed nanotechnologies for new approaches as combination drug delivery systems.¹⁰⁰⁻¹⁰²

Anticancer therapies have greatly benefited from both polymer prodrugs and synergistic drug combinations.^{92, 101, 103} Specifically, recent evaluation of toxic small molecules for synergistic therapies have demonstrated improved efficacy for classic drugs, such as the co-administration of formaldehyde with doxorubicin, an anthracycline class chemotherapeutic.¹⁰⁴⁻¹⁰⁵ A few formaldehyde-doxorubicin conjugates have been developed to take advantage of the synergistic action, however, these prodrugs do not provide a sustained release effect and require frequent dosing (**Figure I-3**).¹⁰⁶⁻¹⁰⁷

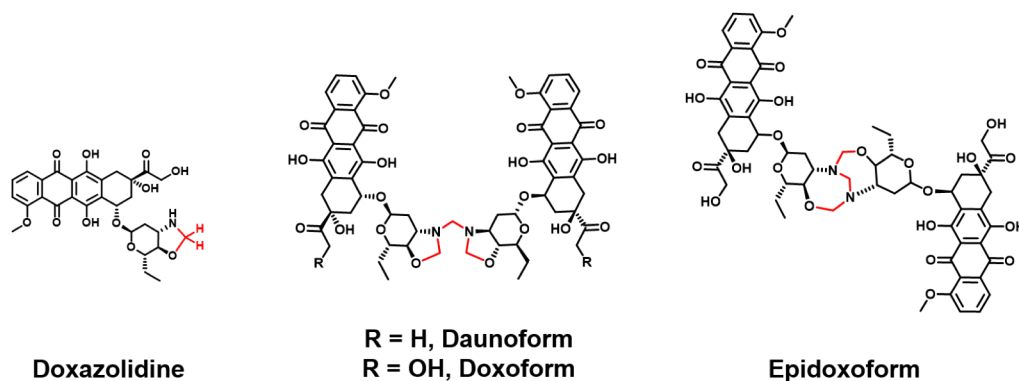


Figure I-3. Formaldehyde-doxorubicin conjugates as small molecule prodrugs.

Polymer prodrugs for the release of carbon monoxide,¹⁰⁸ nitric oxide,¹⁰⁹⁻¹¹¹ and hydrogen sulfide¹¹² have been recently developed, yet, to our knowledge, a polymer-based formaldehyde prodrug capable of sustained release does not exist in the literature. Many synergistic drug combinations would benefit from a dual drug delivery system which provides controlled release of both compounds which can be tailored individually for a customizable drug release profile. For this, we envision two distinct polymer matrices, a formaldehyde-releasing polymer prodrug in the bulk combined with a nanoscale delivery system loaded with doxorubicin (**Figure I-4**). It is the goal of this work to develop a highly functionalized and tunable polymer with reactive

functionality for formaldehyde conjugation with controlled, pH responsive release which could dually serve as a dispersion matrix for the suspension of doxorubicin-loaded nanoparticles.

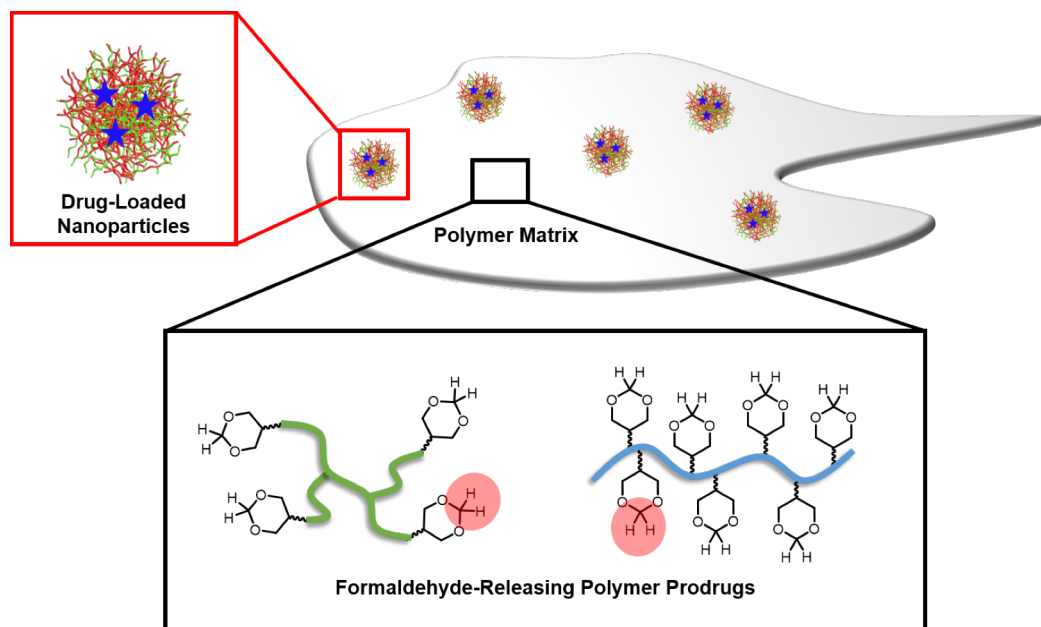


Figure I-4. Dual drug delivery of synergistic combination, doxorubicin and formaldehyde, through drug-loaded nanoparticles entrapped in formaldehyde-releasing polymer prodrug matrix for enhanced anticancer efficacy.

I.5 Dissertation Overview

While the field drug delivery has made great strides in recent years due to expanding nanotechnologies, improved understanding of biological markers for disease, and discovery of synergistic drug combinations, a need still exists for the development of practical approaches to create safe and effective drug delivery solutions for applied use. The aim of this body of work is to develop polymer-based networks which possess high levels of tunability in their molecular architecture, drug loading capacity, and release profiles for application as versatile drug delivery systems. To achieve successful drug delivery, we sought to design polymer networks which are 1) biologically compatible with non-toxic degradation products, 2) capable of encapsulating drugs

often hydrophobic in nature, 3) proficient at suppressing immune response by exhibiting stealth properties, and lastly, 4) exhibit controlled release of payload.

Chapter II details the design of an orthogonal synthesis strategy for the functionalization of a nanocarrier with both a targeting ligand and a dye molecule for the localization and visualization of pancreatic beta-cells. The targeting peptide, Exendin-4, was modified with a cysteine residue for attachment to the nanosponge surface by allylic pendants. For visualization of these targeted nanocarriers *in vivo*, nanosponge primary amines were first transformed to aldehydes through *N*-succinimidyl ester chemistry, followed by conjugation of the hydrazide functionalized imaging dyes to the nanosponge surface. By utilizing thiol-ene and hydrazide-aldehyde click chemistries, we were able to achieve efficient surface functionalization of the nanosponge surface with the targeting and imaging moieties. These particles were evaluated for their targeting ability *in vivo* in three mouse models: first, a tumor expressing GLP-1R; second, a human islet graft located in the fat pad; and lastly, a human islet graft located in the quadriceps muscle. Successful localization of the delivery vehicles demonstrates the potential for this system as a method for visualization and treatment of pancreatic beta-cells.

Chapter III chronicles the implementation of a second targeted drug delivery system which is intended for the treatment of unstable arterial plaques due to cardiovascular disease. These plaques, when degraded by proteins, can rupture and cause myocardial infarction. To prevent the rupture of these plaques, the activity of these proteins can be inhibited by a small molecule drug, naphthofluorescein. The orthogonal strategy presented in Chapter II is again used for the chemical modification of nanosponges to provide surface targeting and imaging molecules. The chosen targeting ligand T-peptide, a novel collagen-homing peptide developed by the Hagemeyer Research Group, was attached to an activatable cell-penetrating peptide (ACPP) designed to cleave

after localization and carry the payload into the cell. The peptide was functionalized with a cysteine residue to enable thiol-ene click chemistry for conjugation to the nanosponge surface. Following attachment of the imaging dye, the nanosponge was post-loaded with the MMP14 inhibitor, naphthofluorescein, to a drug loading of 20 wt%. This targeted nanocarrier demonstrated successful targeting of the degraded collagen present in arterial plaques in both *in vitro* and *in vivo* studies. *In vivo* delivery of naphthofluorescein via the construct demonstrated improved collagen content in the plaques, thereby reducing the chance of heart attack due to plaque rupture. These studies support the potential for this technology to be used for targeted drug delivery to arterial plaques in patients with heart disease.

After successfully applying a targeting strategy to a known platform, we were interested in achieving increased tunability with a simple synthetic approach. Chapter IV reports the development of a novel nanoparticle network derived from a ketone-bearing polyester crosslinked through ketoxime and alkoxyamine linkages with difunctional aminoxy PEG. Oxime-click chemistry as the nanoparticle formation mechanism affords a fast, efficient, and biocompatible network formation. A library of particles was achieved by variation of only two synthetic parameters: percentage of ketone-bearing copolymer functionality and concentration of keto-group. Alteration of these two parameters provided access to a wide range of nanoparticle sizes, from 40 to 210 nm, with three different network densities. Degradation of the polyester particles was analyzed in acidic and neutral conditions to confirm the ketoxime linkage is acid-labile. Additionally, the ketoxime linkages can be reduced to the more stable alkoxyamine which exhibits slower degradation through hydrolysis only. Lastly, Brefeldin A was used as a model drug to evaluate the drug release profiles of the two networks, which demonstrate a controlled release that can be tailored based on network chemistry and environmental pH.

Finally, chapter V explores the application of a novel macromolecular prodrug for release of formaldehyde in conjunction with anthracycline drug, doxorubicin. As the co-administration of formaldehyde with doxorubicin has demonstrated improved anticancer efficacy, we envisioned an injectable combination drug delivery system employing a polymer-based formaldehyde prodrug which can dually serve as a dispersion matrix for doxorubicin-loaded nanoparticles. As our previous work has studied nanoparticle drug delivery systems extensively, we turned our focus toward the development of a macromolecular prodrug for the controlled delivery of formaldehyde. Initially, a semi-branched polyglycidol and its aminoxy functionalized derivative were evaluated for their efficiency as a prodrug. While the aminoxy functionalized polyglycidol had many challenges that led to it not being suitable for this application, we achieved a pH responsive release profile from the polyglycidol-based prodrug as well as improved efficacy when administered in combination with doxorubicin to 4T1 cells. Despite the successful results, the polyglycidol prodrug had limitations of low molecular weight and formaldehyde loading. We envisioned a copolymer which bears pendant diols for formaldehyde conjugation with a tunable copolymer ratio and controlled molecular weight in order to provide a tailorable prodrug. The synthesis of monomers with protected 1,2- and 1,3-diols and the subsequent copolymerization with methoxy PEG acrylate afforded two polymers which possessed tunable handles for formaldehyde conjugation. The release of formaldehyde from the prodrugs exhibited slightly different profiles for each diol in acidic conditions while nearly identical at neutral pH, indicating a pH responsive release as well for the polyacrylate-based prodrugs which is tunable based on the selection of 1,2- or 1,3-diol for formaldehyde conjugation. Additionally, doxorubicin was successfully loaded into ketoxime/alkoxyamine nanoparticles described in Chapter IV and exhibited a pH responsive release profile as well. These prodrugs are poised to be evaluated for their *in vitro* efficacy

alongside doxorubicin-loaded nanoparticles to test the synergistic efficacy of the combination drug delivery system against 4T1 cells.

I.6 References

1. BaoLin, G.; Ma, P. X., Synthetic biodegradable functional polymers for tissue engineering: a brief review. *Sci China Chem* **2014**, *57* (4), 490-500.
2. Iqbal, N.; Khan, A. S.; Asif, A.; Yar, M.; Haycock, J. W.; Rehman, I. U., Recent concepts in biodegradable polymers for tissue engineering paradigms: a critical review. *Int Mater Rev* **2019**, *64* (2), 91-126.
3. Tang, X.; Thankappan, S. K.; Lee, P.; Fard, S. E.; Harmon, M. D.; Tran, K.; Yu, X., Chapter 21 - Polymeric Biomaterials in Tissue Engineering and Regenerative Medicine. In *Natural and Synthetic Biomedical Polymers*, Kumbar, S. G.; Laurencin, C. T.; Deng, M., Eds. Elsevier: Oxford, 2014; pp 351-371.
4. Jafari, M.; Paknejad, Z.; Rad, M. R.; Motamedian, S. R.; Eghbal, M. J.; Najjmi, N.; Khojasteh, A., Polymeric scaffolds in tissue engineering: a literature review. *J Biomed Mater Res B Appl Biomater* **2017**, *105* (2), 431-459.
5. Teo, A. J. T.; Mishra, A.; Park, I.; Kim, Y.-J.; Park, W.-T.; Yoon, Y.-J., Polymeric Biomaterials for Medical Implants and Devices. *ACS Biomater Sci Eng* **2016**, *2* (4), 454-472.
6. Pillai, C. K. S.; Sharma, C. P., Review Paper: Absorbable Polymeric Surgical Sutures: Chemistry, Production, Properties, Biodegradability, and Performance. *J Biomater Appl* **2010**, *25* (4), 291-366.
7. Maitz, M. F., Applications of synthetic polymers in clinical medicine. *Biosurf Biotribol* **2015**, *1* (3), 161-176.

8. Boateng, J. S.; Matthews, K. H.; Stevens, H. N. E.; Eccleston, G. M., Wound healing dressings and drug delivery systems: a review. *J Pharm Sci* **2008**, *97* (8), 2892-2923.
9. Agarwal, A.; McAnulty, J. F.; Schurr, M. J.; Murphy, C. J.; Abbott, N. L. In *Polymeric materials for chronic wound and burn dressings*, Woodhead Publishing Ltd.: 2011; pp 186-208.
10. Kamoun, E. A.; Kenawy, E.-R. S.; Chen, X., A review on polymeric hydrogel membranes for wound dressing applications: PVA-based hydrogel dressings. *J Adv Res* **2017**, *8* (3), 217-233.
11. Liechty, W. B.; Kryscio, D. R.; Slaughter, B. V.; Peppas, N. A., Polymers for drug delivery systems. *Annu Rev Chem Biomol Eng* **2010**, *1*, 149-173.
12. Priya James, H.; John, R.; Alex, A.; Anoop, K. R., Smart polymers for the controlled delivery of drugs – a concise overview. *Acta Pharm Sin B* **2014**, *4* (2), 120-127.
13. Kamaly, N.; Yameen, B.; Wu, J.; Farokhzad, O. C., Degradable Controlled-Release Polymers and Polymeric Nanoparticles: Mechanisms of Controlling Drug Release. *Chem Rev* **2016**, *116* (4), 2602-2663.
14. Talelli, M.; Duro-Castaño, A.; Rodríguez-Escalona, G.; Vicent, M. J., Chapter 11 - Smart polymer nanocarriers for drug delivery. In *Smart Polymers and their Applications*, Aguilar, M. R.; San Román, J., Eds. Woodhead Publishing: 2014; pp 327-358.
15. Tiwari, G.; Tiwari, R.; Sriwastawa, B.; Bhati, L.; Pandey, S.; Pandey, P.; Bannerjee, S. K., Drug delivery systems: An updated review. *Int J Pharma Investig* **2012**, *2* (1), 2-11.
16. Giordano, C.; Albani, D.; Gloria, A.; Tunesi, M.; Rodilossi, S.; Russo, T.; Forloni, G.; Ambrosio, L.; Cigada, A., Nanocomposites for neurodegenerative diseases: hydrogel-nanoparticle combinations for a challenging drug delivery. *Int J Artif Organs* **2011**, *34* (12), 1115-1127.
17. de la Croix Ndong, J.; Stevens, D. M.; Vignaux, G.; Uppuganti, S.; Perrien, D. S.; Yang, X.; Nyman, J. S.; Harth, E.; Elefteriou, F., Combined MEK inhibition and BMP2 treatment

promotes osteoblast differentiation and bone healing in Nf1Osx $-/-$ mice. *J Bone Miner Res* **2015**, *30* (1), 55-63.

18. Wilhelm, S.; Tavares, A. J.; Dai, Q.; Ohta, S.; Audet, J.; Dvorak, H. F.; Chan, W. C. W., Analysis of nanoparticle delivery to tumours. *Nat Rev Mater* **2016**, *1* (16014), 1-12.

19. Park, K., Facing the truth about nanotechnology in drug delivery. *ACS Nano* **2013**, *7* (9), 7442-7447.

20. Bae, Y. H.; Park, K., Targeted drug delivery to tumors: myths, reality and possibility. *J Control Release* **2011**, *153* (3), 198-205.

21. Kwon, I. K.; Lee, S. C.; Han, B.; Park, K., Analysis on the current status of targeted drug delivery to tumors. *J Control Release* **2012**, *164* (2), 108-114.

22. Bobo, D.; Robinson, K. J.; Islam, J.; Thurecht, K. J.; Corrie, S. R., Nanoparticle-Based Medicines: A Review of FDA-Approved Materials and Clinical Trials to Date. *Pharm Res* **2016**, *33* (10), 2373-2387.

23. Caster, J. M.; Patel, A. N.; Zhang, T.; Wang, A., Investigational nanomedicines in 2016: a review of nanotherapeutics currently undergoing clinical trials. *Wiley Interdiscp Rev Nanomed Nanobiotechnol* **2017**, *9* (1), e1416, 1-18.

24. Ventola, C. L., The nanomedicine revolution: part 1: emerging concepts. *P T* **2012**, *37* (9), 512-525.

25. Havel, H.; Finch, G.; Strode, P.; Wolfgang, M.; Zale, S.; Bobe, I.; Youssoufian, H.; Peterson, M.; Liu, M., Nanomedicines: From Bench to Bedside and Beyond. *AAPS J* **2016**, *18* (6), 1373-1378.

26. Juliano, R., Challenges to macromolecular drug delivery. *Biochem Soc T* **2007**, *35*, 41-43.

27. Khambhla, E.; Shah, V.; Baviskar, K., Drug Delivery to CNS: Challenges and Opportunities with Emphasis on Biomaterials Based Drug Delivery Strategies. *Curr Pharm Design* **2016**, *22* (19), 2913-2922.
28. Muro, S., Challenges in design and characterization of ligand-targeted drug delivery systems. *J Control Release* **2012**, *164* (2), 125-137.
29. Babu, A.; Templeton, A. K.; Munshi, A.; Ramesh, R., Nanoparticle-Based Drug Delivery for Therapy of Lung Cancer: Progress and Challenges. *J Nanomater* **2013**, *2013* (863951), 1-11.
30. Jiang, W.; Kim, B. Y. S.; Rutka, J. T.; Chan, W. C. W., Advances and challenges of nanotechnology-based drug delivery systems. *Expert Opin Drug Del* **2007**, *4* (6), 621-633.
31. Rao, J. P.; Geckeler, K. E., Polymer nanoparticles: Preparation techniques and size-control parameters. *Prog Polym Sci* **2011**, *36* (7), 887-913.
32. Albanese, A.; Tang, P. S.; Chan, W. C. W., The Effect of Nanoparticle Size, Shape, and Surface Chemistry on Biological Systems. *Annu Rev Biomed Eng* **2012**, *14* (1), 1-16.
33. Soppimath, K. S.; Aminabhavi, T. M.; Kulkarni, A. R.; Rudzinski, W. E., Biodegradable polymeric nanoparticles as drug delivery devices. *J Control Release* **2001**, *70* (1), 1-20.
34. Ahlin Grabnar, P.; Kristl, J., The manufacturing techniques of drug-loaded polymeric nanoparticles from preformed polymers. *J Microencapsul* **2011**, *28* (4), 323-335.
35. Nasir, A.; Kausar, A.; Younus, A., A Review on Preparation, Properties and Applications of Polymeric Nanoparticle-Based Materials. *Polym Plast Technol Eng* **2015**, *54* (4), 325-341.
36. Nagavarma, B.; Yadav, H. K.; Ayaz, A.; Vasudha, L.; Shivakumar, H., Different techniques for preparation of polymeric nanoparticles-a review. *Asian J Pharm Clin Res* **2012**, *5* (3), 16-23.

37. Quintanar-Guerrero, D.; Allémann, E.; Fessi, H.; Doelker, E., Preparation Techniques and Mechanisms of Formation of Biodegradable Nanoparticles from Preformed Polymers. *Drug Dev Ind Pharm* **1998**, *24* (12), 1113-1128.
38. Barnard, A. S., Challenges in modelling nanoparticles for drug delivery. *J Phys Condens Matter* **2016**, *28* (023002), 1-25.
39. Xu, S.; Nie, Z.; Seo, M.; Lewis, P.; Kumacheva, E.; Stone, H. A.; Garstecki, P.; Weibel, D. B.; Gitlin, I.; Whitesides, G. M., Generation of Monodisperse Particles by Using Microfluidics: Control over Size, Shape, and Composition. *Angew Chem* **2005**, *117* (5), 734-738.
40. Haynes, C. L.; McFarland, A. D.; Smith, M. T.; Hulteen, J. C.; Van Duyne, R. P., Angle-Resolved Nanosphere Lithography: Manipulation of Nanoparticle Size, Shape, and Interparticle Spacing. *J Phys Chem B* **2002**, *106* (8), 1898-1902.
41. Müller, R. H.; Wallis, K. H.; Tröster, S. D.; Kreuter, J., In vitro characterization of poly(methyl-methacrylate) nanoparticles and correlation to their in vivo fate. *J Control Release* **1992**, *20* (3), 237-246.
42. Roser, M.; Fischer, D.; Kissel, T., Surface-modified biodegradable albumin nano- and microspheres. II: effect of surface charges on in vitro phagocytosis and biodistribution in rats. *Eur J Pharm Biopharm* **1998**, *46* (3), 255-263.
43. Carrstensen, H.; Müller, R. H.; Müller, B. W., Particle size, surface hydrophobicity and interaction with serum of parenteral fat emulsions and model drug carriers as parameters related to RES uptake. *Clin Nutr* **1992**, *11* (5), 289-297.
44. Norman, M. E.; Williams, P.; Illum, L., Human serum albumin as a probe for surface conditioning (opsonization) of block copolymer-coated microspheres. *Biomaterials* **1992**, *13* (12), 841-849.

45. Stuart, A. E., Phagocytic Engulfment and Cell Adhesiveness as Cellular Surface Phenomena. *J Clin Pathol* **1977**, *30* (6), 592-592.
46. Amoozgar, Z.; Yeo, Y., Recent advances in stealth coating of nanoparticle drug delivery systems. *Wiley Interdiscp Rev Nanomed Nanobiotechnol* **2012**, *4* (2), 219-233.
47. Peracchia, M. T.; Fattal, E.; Desmaële, D.; Besnard, M.; Noël, J. P.; Gomis, J. M.; Appel, M.; d'Angelo, J.; Couvreur, P., Stealth® PEGylated polycyanoacrylate nanoparticles for intravenous administration and splenic targeting. *J Control Release* **1999**, *60* (1), 121-128.
48. Peracchia, M. T.; Gref, R.; Minamitake, Y.; Domb, A.; Lotan, N.; Langer, R., PEG-coated nanospheres from amphiphilic diblock and multiblock copolymers: Investigation of their drug encapsulation and release characteristics. *J Control Release* **1997**, *46* (3), 223-231.
49. Peracchia, M. T.; Vauthier, C.; Puisieux, F.; Couvreur, P., Development of sterically stabilized poly(isobutyl 2-cyanoacrylate) nanoparticles by chemical coupling of poly(ethylene glycol). *J Biomed Mater Res* **1997**, *34* (3), 317-326.
50. Gidwani, M.; Singh, A. V., Nanoparticle Enabled Drug Delivery Across the Blood Brain Barrier: in vivo and in vitro Models, Opportunities and Challenges. *Curr Pharm Biotechnol* **2013**, *14* (14), 1201-1212.
51. Alyautdin, R. N.; Petrov, V. E.; Langer, K.; Berthold, A.; Kharkevich, D. A.; Kreuter, J., Delivery of Loperamide Across the Blood-Brain Barrier with Polysorbate 80-Coated Polybutylcyanoacrylate Nanoparticles. *Pharm Res* **1997**, *14* (3), 325-328.
52. Fornaguera, C.; Dols-Perez, A.; Calderó, G.; García-Celma, M. J.; Camarasa, J.; Solans, C., PLGA nanoparticles prepared by nano-emulsion templating using low-energy methods as efficient nanocarriers for drug delivery across the blood–brain barrier. *J Control Release* **2015**, *211*, 134-143.

53. Panyam, J.; Labhasetwar, V., Biodegradable nanoparticles for drug and gene delivery to cells and tissue. *Adv Drug Deliv Rev* **2003**, *55* (3), 329-347.
54. Locatelli, E.; Comes Franchini, M., Biodegradable PLGA-b-PEG polymeric nanoparticles: synthesis, properties, and nanomedical applications as drug delivery system. *J Nanopart Res* **2012**, *14* (1316), 1-17.
55. Pounder, R. J.; Dove, A. P., Towards poly(ester) nanoparticles: recent advances in the synthesis of functional poly(ester)s by ring-opening polymerization. *Polym Chem* **2010**, *1* (3), 260-271.
56. Mir, M.; Ahmed, N.; Rehman, A. U., Recent applications of PLGA based nanostructures in drug delivery. *Colloids Surf B Biointerfaces* **2017**, *159*, 217-231.
57. Makadia, H. K.; Siegel, S. J., Poly Lactic-co-Glycolic Acid (PLGA) as Biodegradable Controlled Drug Delivery Carrier. *Polymers (Basel)* **2011**, *3* (3), 1377-1397.
58. Bala, I.; Hariharan, S.; Kumar, M. N., PLGA nanoparticles in drug delivery: the state of the art. *Crit Rev Ther Drug Carrier Syst* **2004**, *21* (5), 387-422.
59. Sadat Tabatabaei Mirakabad, F.; Nejati-Koshki, K.; Akbarzadeh, A.; Yamchi, M. R.; Milani, M.; Zarghami, N.; Zeighamian, V.; Rahimzadeh, A.; Alimohammadi, S.; Hanifehpour, Y.; Joo, S. W., PLGA-based nanoparticles as cancer drug delivery systems. *Asian Pac J Cancer Prev* **2014**, *15* (2), 517-35.
60. Ye, F.; Barrefelt, A.; Asem, H.; Abedi-Valugerdi, M.; El-Serafi, I.; Saghafian, M.; Abu-Salah, K.; Alrokayan, S.; Muhammed, M.; Hassan, M., Biodegradable polymeric vesicles containing magnetic nanoparticles, quantum dots and anticancer drugs for drug delivery and imaging. *Biomaterials* **2014**, *35* (12), 3885-94.

61. Jeong, B.; Han Bae, Y.; Wan Kim, S., Biodegradable thermosensitive micelles of PEG-PLGA-PEG triblock copolymers. *Colloid Surface B* **1999**, *16* (1), 185-193.
62. Yoo, H. S.; Park, T. G., Biodegradable polymeric micelles composed of doxorubicin conjugated PLGA-PEG block copolymer. *J Control Release* **2001**, *70* (1), 63-70.
63. Li, Y.; Lin, J.; Yang, X.; Li, Y.; Wu, S.; Huang, Y.; Ye, S.; Xie, L.; Dai, L.; Hou, Z., Self-Assembled Nanoparticles Based on Amphiphilic Anticancer Drug-Phospholipid Complex for Targeted Drug Delivery and Intracellular Dual-Controlled Release. *Acs Appl Mater Inter* **2015**, *7* (32), 17573-17581.
64. Hwang, H.-Y.; Kim, I.-S.; Kwon, I. C.; Kim, Y.-H., Tumor targetability and antitumor effect of docetaxel-loaded hydrophobically modified glycol chitosan nanoparticles. *J Control Release* **2008**, *128* (1), 23-31.
65. Liang, H.-F.; Chen, C.-T.; Chen, S.-C.; Kulkarni, A. R.; Chiu, Y.-L.; Chen, M.-C.; Sung, H.-W., Paclitaxel-loaded poly(γ -glutamic acid)-poly(lactide) nanoparticles as a targeted drug delivery system for the treatment of liver cancer. *Biomaterials* **2006**, *27* (9), 2051-2059.
66. Lim, Y. H.; Tiemann, K. M.; Heo, G. S.; Wagers, P. O.; Rezenom, Y. H.; Zhang, S.; Zhang, F.; Youngs, W. J.; Hunstad, D. A.; Wooley, K. L., Preparation and in Vitro Antimicrobial Activity of Silver-Bearing Degradable Polymeric Nanoparticles of Polyphosphoester-block-Poly(l-lactide). *ACS Nano* **2015**, *9* (2), 1995-2008.
67. Jiang, X.; Brinker, C. J., Aerosol-Assisted Self-Assembly of Single-Crystal Core/Nanoporous Shell Particles as Model Controlled Release Capsules. *J Am Chem Soc* **2006**, *128* (14), 4512-4513.
68. Wang, H.; Dong, M.; Khan, S.; Su, L.; Li, R.; Song, Y.; Lin, Y.-N.; Kang, N.; Komatsu, C. H.; Elsbahy, M.; Wooley, K. L., Acid-Triggered Polymer Backbone Degradation and

Disassembly to Achieve Release of Camptothecin from Functional Polyphosphoramidate Nanoparticles. *ACS Macro Lett* **2018**, *7* (7), 783-788.

69. van der Ende, A. E.; Kravitz, E. J.; Harth, E., Approach to Formation of Multifunctional Polyester Particles in Controlled Nanoscopic Dimensions. *J Am Chem Soc* **2008**, *130* (27), 8706–8713.

70. Hariri, G.; Edwards, A. D.; Merrill, T. B.; Greenbaum, J. M.; van der Ende, A. E.; Harth, E., Sequential Targeted Delivery of Paclitaxel and Camptothecin Using a Cross-Linked “Nanosponge” Network for Lung Cancer Chemotherapy. *Mol Pharmaceutics* **2014**, *11* (1), 265-275.

71. Passarella, R. J.; Spratt, D. E.; van der Ende, A. E.; Phillips, J. G.; Wu, H.; Sathiyakumar, V.; Zhou, L.; Hallahan, D. E.; Harth, E.; Diaz, R., Targeted Nanoparticles That Deliver a Sustained, Specific Release of Paclitaxel to Irradiated Tumors. *Cancer Res* **2010**, *70* (11), 4550-4559.

72. Stevens, D. M.; Gilmore, K. A.; Harth, E., An assessment of nanosponges for intravenous and oral drug delivery of BCS class IV drugs: Drug delivery kinetics and solubilization. *Polym Chem* **2014**, *5* (11), 3551-3554.

73. Lockhart, J. N.; Stevens, D. M.; Beezer, D. B.; Kravitz, A.; Harth, E., Dual drug delivery of tamoxifen and quercetin: Regulated metabolism for anticancer treatment with nanosponges. *J Control Release* **2015**, *220*, 751-757.

74. Meyerson, M.; Gabriel, S.; Getz, G., Advances in understanding cancer genomes through second-generation sequencing. *Nat Rev Genet* **2010**, *11* (10), 685-696.

75. Abrahams, B. S.; Geschwind, D. H., Advances in autism genetics: on the threshold of a new neurobiology. *Nat Rev Genet* **2008**, *9* (5), 341-355.

76. Rioux, J. D.; Abbas, A. K., Paths to understanding the genetic basis of autoimmune disease. *Nature* **2005**, *435* (7042), 584.
77. Rosen, B. P.; Mobashery, S., *Resolving the antibiotic paradox: progress in understanding drug resistance and development of new antibiotics*. Springer Science & Business Media: 2012; Vol. 456.
78. Donnenberg, V. S.; Donnenberg, A. D., Multiple drug resistance in cancer revisited: the cancer stem cell hypothesis. *J Clin Pharmacol* **2005**, *45* (8), 872-877.
79. Jayatilaka, H.; Tyle, P.; Chen, J. J.; Kwak, M.; Ju, J.; Kim, H. J.; Lee, J. S. H.; Wu, P.-H.; Gilkes, D. M.; Fan, R.; Wirtz, D., Synergistic IL-6 and IL-8 paracrine signalling pathway infers a strategy to inhibit tumour cell migration. *Nat Commun* **2017**, *8*, 1-12.
80. Steeg, P. S., Targeting metastasis. *Nat Rev Cancer* **2016**, *16*, 201-218.
81. Wang, X.-s.; Ding, X.-z.; Li, X.-c.; He, Y.; Kong, D.-j.; Zhang, L.; Hu, X.-c.; Yang, J.-q.; Zhao, M.-q.; Gao, S.-g.; Lin, T.-y.; Li, Y., A highly integrated precision nanomedicine strategy to target esophageal squamous cell cancer molecularly and physically. *Nanomedicine* **2018**, *14* (7), 2103-2114.
82. Gaudreau, P.-O.; Stagg, J.; Soulières, D.; Saad, F., The Present and Future of Biomarkers in Prostate Cancer: Proteomics, Genomics, and Immunology Advancements. *Biomark Cancer* **2016**, *8* (Suppl 2), 15-33.
83. Prensner, J. R.; Rubin, M. A.; Wei, J. T.; Chinnaiyan, A. M., Beyond PSA: The Next Generation of Prostate Cancer Biomarkers. *Sci Transl Med* **2012**, *4* (127), 127rv3, 1-23.
84. Kleer, C. G.; Cao, Q.; Varambally, S.; Shen, R.; Ota, I.; Tomlins, S. A.; Ghosh, D.; Sewalt, R. G. A. B.; Otte, A. P.; Hayes, D. F.; Sabel, M. S.; Livant, D.; Weiss, S. J.; Rubin, M. A.;

- Chinnaiyan, A. M., EZH2 is a marker of aggressive breast cancer and promotes neoplastic transformation of breast epithelial cells. *Proc Natl Acad Sci USA* **2003**, *100* (20), 11606-11611.
85. Winter, J. M.; Yeo, C. J.; Brody, J. R., Diagnostic, prognostic, and predictive biomarkers in pancreatic cancer. *J Surg Oncol* **2013**, *107* (1), 15-22.
86. Tai, W.; Mahato, R.; Cheng, K., The role of HER2 in cancer therapy and targeted drug delivery. *J Control Release* **2010**, *146* (3), 264-275.
87. Turner, J. H., An introduction to the clinical practice of theranostics in oncology. *Br J Radiol* **2018**, *91* (1091), 1-9.
88. Blau, R.; Krivitsky, A.; Epshtein, Y.; Satchi-Fainaro, R., Are nanotheranostics and nanodiagnosics-guided drug delivery stepping stones towards precision medicine? *Drug Resist Updat* **2016**, *27*, 39-58.
89. Howell, M.; Wang, C.; Mahmoud, A.; Hellermann, G.; Mohapatra, S. S.; Mohapatra, S., Dual-function theranostic nanoparticles for drug delivery and medical imaging contrast: perspectives and challenges for use in lung diseases. *Drug Deliv Transl Res* **2013**, *3* (4), 352-363.
90. van der Ende, A.; Croce, T.; Hamilton, S.; Sathiyakumar, V.; Harth, E., Tailored polyester nanoparticles: post-modification with dendritic transporter and targeting units via reductive amination and thiol-ene chemistry. *Soft Matter* **2009**, *5* (7), 1417-1425.
91. Delplace, V.; Couvreur, P.; Nicolas, J., Recent trends in the design of anticancer polymer prodrug nanocarriers. *Polym Chem* **2014**, *5* (5), 1529-1544.
92. Greco, F.; Vicent, M. J., Combination therapy: Opportunities and challenges for polymer-drug conjugates as anticancer nanomedicines. *Adv Drug Deliv Rev* **2009**, *61* (13), 1203-1213.

93. Zhang, J.; Liu, Y.-F.; Liu, L.-X.; Zhang, Y.-Z.; Qiao, C.-A.; Zhou, Y.-Z., Poly[N-(2-hydroxypropyl)methacrylamide] prodrug for metaxalone via a chloroacetyl chloride linker: Synthesis and controlled release evaluation. *J Appl Polym Sci* **2012**, *125* (2), 1538-1543.
94. Vinciguerra, D.; Denis, S.; Mougin, J.; Jacobs, M.; Guillaneuf, Y.; Mura, S.; Couvreur, P.; Nicolas, J., A facile route to heterotelechelic polymer prodrug nanoparticles for imaging, drug delivery and combination therapy. *J Control Release* **2018**, *286*, 425-438.
95. Banerjee, S. S.; Aher, N.; Patil, R.; Khandare, J., Poly(ethylene glycol)-Prodrug Conjugates: Concept, Design, and Applications. *J Drug Deliv* **2012**, *2012* (103973), 1-17.
96. Choe, Y. H.; Greenwald, R. B.; Conover, C. D.; Zhao, H.; Longley, C. B.; Guan, S.; Zhao, Q.; Xia, J., PEG prodrugs of 6-mercaptopurine for parenteral administration using benzyl elimination of thiols. *Oncol Res* **2004**, *14* (9), 455-68.
97. Guégain, E.; Tran, J.; Deguettes, Q.; Nicolas, J., Degradable polymer prodrugs with adjustable activity from drug-initiated radical ring-opening copolymerization. *Chem Sci* **2018**, *9* (43), 8291-8306.
98. Larson, N.; Ghandehari, H., Polymeric conjugates for drug delivery. *Chem Mater* **2012**, *24* (5), 840-853.
99. Paramjot; Khan, N. M.; Kapahi, H.; Kumar, S.; Bhardwaj, T. R.; Arora, S.; Mishra, N., Role of polymer–drug conjugates in organ-specific delivery systems. *J Drug Target* **2015**, *23* (5), 387-416.
100. Gilmore, K. A.; Lampley, M. W.; Boyer, C.; Harth, E., Matrices for combined delivery of proteins and synthetic molecules. *Adv Drug Deliv Rev* **2016**, *98*, 77-85.
101. Hu, Q.; Sun, W.; Wang, C.; Gu, Z., Recent advances of cocktail chemotherapy by combination drug delivery systems. *Adv Drug Deliv Rev* **2016**, *98*, 19-34.

102. Kemp, J. A.; Shim, M. S.; Heo, C. Y.; Kwon, Y. J., “Combo” nanomedicine: Co-delivery of multi-modal therapeutics for efficient, targeted, and safe cancer therapy. *Adv Drug Deliv Rev* **2016**, *98*, 3-18.
103. Kratz, F.; Warnecke, A., Finding the optimal balance: Challenges of improving conventional cancer chemotherapy using suitable combinations with nano-sized drug delivery systems. *J Control Release* **2012**, *164* (2), 221-235.
104. Barthel, B. L.; Mooz, E. L.; Wiener, L. E.; Koch, G. G.; Koch, T. H., Correlation of in Situ Oxazolidine Formation with Highly Synergistic Cytotoxicity and DNA Cross-Linking in Cancer Cells from Combinations of Doxorubicin and Formaldehyde. *J Med Chem* **2016**, *59* (5), 2205-21.
105. Cutts, S. M.; Swift, L. P.; Pillay, V.; Forrest, R. A.; Nudelman, A.; Rephaeli, A.; Phillips, D. R., Activation of clinically used anthracyclines by the formaldehyde-releasing prodrug pivaloyloxymethyl butyrate. *Mol Cancer Ther* **2007**, *6* (4), 1450-9.
106. Fenick, D. J.; Taatjes, D. J.; Koch, T. H., Doxoform and Daunofom: Anthracycline–Formaldehyde Conjugates Toxic to Resistant Tumor Cells. *J Med Chem* **1997**, *40* (16), 2452-2461.
107. Burke, P. J.; Koch, T. H., Doxorubicin-formaldehyde conjugate, doxoform: induction of apoptosis relative to doxorubicin. *Anticancer Res* **2001**, *21* (4A), 2753-2760.
108. Nguyen, D.; Nguyen, T.-K.; Rice, S. A.; Boyer, C., CO-Releasing Polymers Exert Antimicrobial Activity. *Biomacromolecules* **2015**, *16* (9), 2776-2786.
109. Du, W.; Zhang, K.; Zhang, S.; Wang, R.; Nie, Y.; Tao, H.; Han, Z.; Liang, L.; Wang, D.; Liu, J.; Liu, N.; Han, Z.; Kong, D.; Zhao, Q.; Li, Z., Enhanced proangiogenic potential of mesenchymal stem cell-derived exosomes stimulated by a nitric oxide releasing polymer. *Biomaterials* **2017**, *133*, 70-81.

110. Kang, Y.; Kim, J.; Lee, Y. M.; Im, S.; Park, H.; Kim, W. J., Nitric oxide-releasing polymer incorporated ointment for cutaneous wound healing. *J Control Release* **2015**, *220* (Pt B), 624-630.
111. Mann, M. N.; Neufeld, B. H.; Hawker, M. J.; Pegalajar-Jurado, A.; Paricio, L. N.; Reynolds, M. M.; Fisher, E. R., Plasma-modified nitric oxide-releasing polymer films exhibit time-delayed 8-log reduction in growth of bacteria. *Biointerphases* **2016**, *11* (3), 031005, 1-11.
112. Foster, J. C.; Matson, J. B., Functionalization of Methacrylate Polymers with Thiooximes: A Robust Postpolymerization Modification Reaction and a Method for the Preparation of H₂S-Releasing Polymers. *Macromolecules* **2014**, *47* (15), 5089-5095.

CHAPTER II

Exendin-4 Functionalized Nanosponges for the Targeted Imaging of Beta-Cells Toward Treatment of Diabetes

II.1 Introduction

Diabetes mellitus type 1 and type 2 is characterized by a decreased or depleted function of the pancreatic beta-cells as a result of apoptosis or inflammation leading to a loss of glycemic control resulting in high blood sugar levels in the body.¹⁻⁴ Beta-cells are responsible for insulin secretion and located in the Islets of Langerhans, a discrete group of cells located within the pancreas. These cells make up a very small percentage of the overall pancreatic mass and are well dispersed throughout the tissue, creating a distinct challenge when treating this disease. Current therapies for treatment of diabetes mainly focus on replacement or regulation of insulin, rather than restoring the function of the beta-cells. However, recent emergence of several small molecule compounds, such as harmine⁵ and imatinib,⁶ with promising inhibition of beta-cell death has led to an interest in delivering these drugs directly to the islets.⁷⁻¹⁰ Systemic delivery of these drugs is not practical in a clinical setting due to low percentage of administered dose reaching the target site and high risk of off-target side effects. Therefore, it is apparent that a targeted drug delivery carrier which could entrap the cargo, localize at the surface of beta-cells within the islets, and release the drug would drastically improve the efficacy of these treatments. An attractive targeting site for beta cells is the surface receptor GLP-1R which naturally binds to glucagon-like peptide-1 (GLP-1) as a substrate. Unfortunately, due to its short half-life of 1-2 minutes,¹¹ GLP-1 is not a viable candidate for a targeting moiety, but rather GLP-1 agonists are being investigated for their

potential targeting and treatment ability.¹²⁻¹⁴ Exendin-4 is a well-studied GLP-1 agonist with similar binding activity and a longer half-life than that of GLP-1.¹⁵ Currently marketed as a diabetes type 2 medication that facilitates glucose control in combination with other therapies,¹⁶ Exendin-4 is a promising peptide for targeting beta-cells.

Nanomaterials are becoming increasingly popular for therapeutic delivery systems which suffer from reduced efficacy due to early metabolism or drug hydrophobicity.¹⁷⁻²¹ Due to the rising complexity of disease and treatment options, it is necessary to make advancements in the development of targeted systems for specific applications. A variety of current drug delivery systems achieve improved solubilization of hydrophobic drugs or protection of therapeutics that are otherwise not able to be administered. However, these types of systems do not address the complications and challenges presented by off-target side effects or reduced efficacy at treatment site due to non-localized drug. Nanoparticles are an extremely attractive delivery platform for small molecules. Precisely tuning the size and crosslinking density of nanoparticles based on intermolecular crosslinking is of great importance to influence and guide the drug release profile of these nanosystems.²² Designing nanosponge tunability, *i.e.*, preparing particles of different network densities, is reliant upon the pendant functionality of the precursor polymer and the equivalents of the hydrophilic crosslinker incorporated. In our previous work, it is evident that the concentration of the precursor and crosslinker in the solvent is critical to form nanoparticles of a discrete size rather than a bulk gel.

Recent work in nanoparticle drug delivery has focused on the use of poly(lactic-*co*-glycolic acid) (PLGA) self-assembled nanoparticles.²³⁻²⁷ PLGA has degradable ester linkages which make it suitable for drug delivery applications and is often combined with poly(ethylene glycol) (PEG) due to its stealth properties.²⁸ However, due to the self-assembled nature of PLGA particle

formation, the particles cannot be solubilized in organics for further functionalization. In contrast to PLGA nanoparticles, our nanosponge system provides covalent crosslinking forming a nanoparticle with defined sizes and morphology, which are stable in organics and degrade in aqueous solutions.²²

Moreover, the surface functionalities present on the nanosponge provide chemical handles for labeling methods such as thiol-ene, maleimide, or NHS-ester click chemistries.²⁹ Additionally, the stability of the crosslinked system in organic solvents can be used for the post-loading of the nanocarrier with small molecule drugs.^{22,30} The hydrophobicity of the polyester backbone together with the hydrophilic short crosslinker gives these particles an amorphous character at body temperature. Furthermore, after drug loading, the particle can form fine suspensions in aqueous media to be readily injected *in vivo*.³⁰⁻³¹ Therefore, it is our goal in this work to construct a nanosponge platform, capable of entrapping hydrophobic drug therapeutics, which bears Exendin-4 as a targeting moiety for localization at the beta cell surface and a fluorescent dye in order to visualize the targeting efficacy (**Figure II-1**). Preliminary data for *in vitro* evaluation of peptide targeting were extremely promising³² and we sought to translate this work to *in vivo* animal studies using first a GLP-1R expressing tumor model and then human Islets of Langerhans cells.

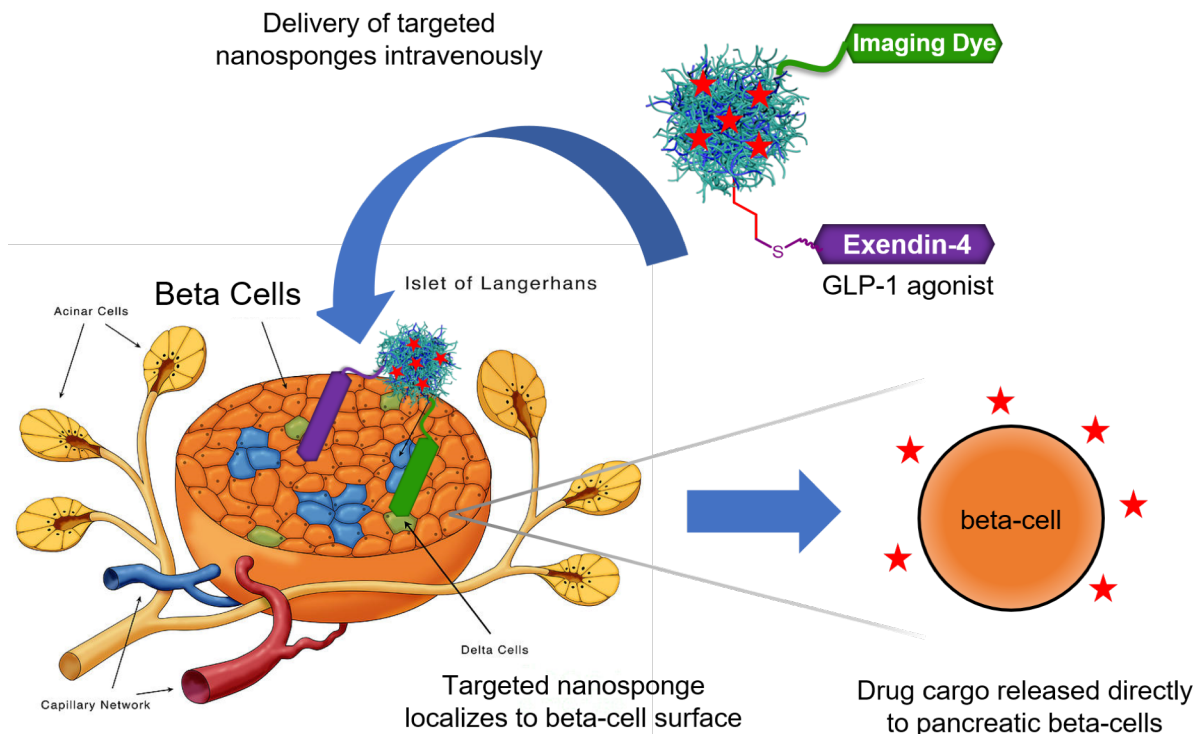


Figure II-1. A nanosponge system labeled with GLP-1R targeting peptide Exendin-4 and a fluorescent imaging tag capable of encapsulating and subsequently delivering hydrophobic small molecule drug cargo directly to pancreatic beta-cells.

II.2 Results and Discussion

Polyester nanosponges of precise dimensions were prepared by epoxide-amine crosslinking followed by surface functionalization with the targeting agent, Cys40-Exendin-4, and a fluorescent imaging dye. An orthogonal synthetic strategy was designed in order to avoid undesirable side reactions or off-target labeling. The fully conjugated construct was evaluated first by *in vivo* analysis with human islets cell grafts located in the fat pad followed by further experiments utilizing a more beneficial subcutaneous quadriceps graft location. Both animal models indicate successful targeting with promising potential for use as targeted drug delivery

vehicles, however, further work to optimize the biological variables and animal models is needed to see the full potential of these materials.

II.2.1 Synthesis of Nanosponges in Precise Size and Crosslinking Density

Polyester nanosponges were prepared by intramolecular crosslinking chemistry between epoxide functionalized polymers and diamine polyethylene glycol (PEG) crosslinkers as previously described.³³ However, obtaining reproducible nanosponge sizes is vital in drug delivery applications and needs further exploration of the technique used to determine reproducibility and precision in fabricating predictable and controlled nanoparticle diameters. Multiple parameters in precursor polymerization and nanosponge synthesis affect the size and crosslink density of the resulting particle. Three important parameters were identified in our analysis: polymer molecular weight, epoxide pendant functionality, and crosslinker equivalents. To produce a range of molecular weights and epoxide functionalities for analysis, poly(δ -valerolactone-*co*- α -allyl- δ -valerolactone- α -epoxy- δ -valerolactone) (P(VL-AVL-EVL)) with molecular weights of 2500-3200 g mol⁻¹ and epoxide functionality of 6-10 mol % were synthesized. It is important to note that the epoxide functionality can be controlled via stoichiometry of the post-polymerization modification reaction in which the pendant allyls are oxidized to epoxides. The ratio of allyl to epoxide can be determined by varying the amount of oxidizing agent. When all allyls are epoxidized, a distinct disadvantage is there are no pendant allyls on the surface of the nanosponge for further functionalization. However, for certain applications, the allyl functionality is not necessary and reduces hydrophilicity, so transforming all allyls to epoxides may be preferred.

For nanosponge fabrication, previous work determined an optimal concentration of 5.4 mM repeat monomer unit (RMU) for desired nanosponge size ranges of ~100 nm.³³ This concentration is calculated based on the repeat unit value for the epoxide functionality in the polymer. The repeat unit is the weight of polymer per one reactive unit, which is used to calculate the moles of reactive units in one polymer. For example, as shown below, if a polymer with a molecular weight of 2,000 g mol⁻¹ contains 10 RMUs bearing pendant functionality, determined by quantitative NMR, the reactive unit of the polymer is 200 g mol⁻¹ RMU. Using this value, the moles of reactive units can be calculated from the polymer weight in order to determine crosslinker equivalencies for nanosponge synthesis.

Equation II-1. Calculation for the Repeat Monomer Unit (RMU) based on molecular weight and epoxide functionality.

$$\frac{2000 \frac{g}{mol}}{10 \text{ RMU}} = 200 \frac{g}{mol \text{ RMU}}$$

Equation II-2. Calculation of RMU per polymer mass for precise concentration of reactive functionality in reaction solution.

$$\frac{2.0 \text{ g polymer}}{200 \frac{g}{mol \text{ RMU}}} = 1.0 \times 10^{-2} \text{ mol RMU}$$

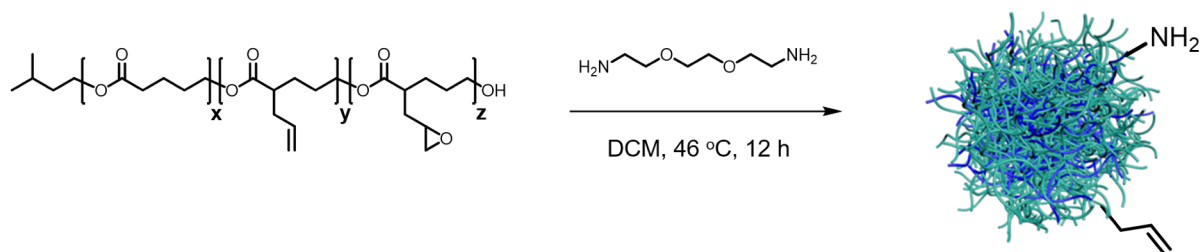
As a general trend, increasing both the polymer molecular weight and epoxide functionality contributed to an increased nanosponge size independently. A narrow polydispersity achieved by use of tin triflate catalyst³⁴ leads to a narrow nanosponge size distribution (~ 10% standard deviation) and improves reproducibility of nanosponge synthesis. The crosslinking reagent

equivalent is calculated based on the amine per epoxide ratio, and an increase in crosslinker equivalent is shown to increase the nanosponge size.

II.2.2 Evaluation and Analysis of Size Relationships

To elucidate greater understanding of the relationship between the synthesis parameters of the nanosponge and its resultant size, we focused our exploration on three parameters: equivalents of crosslinking reagent, polymer molecular weight, and polymer pendant functionality. **Scheme II-1** details the synthetic scheme of nanosponge fabrication by intramolecular crosslinking the polymer containing allylic and epoxide functionality with the diamine polyethylene glycol linker. The concentration of epoxides in the solution was previously determined experimentally and is known to be critical to the formation of discrete particles.

Scheme II-1. Nanosponge synthesis through intramolecular crosslinking of P(VL-AVL-EVL) with diamine PEG crosslinker to produce nanoparticles with primary amine and allylic surface functionality.



Once nanosponges were synthesized, transmission electron microscopy (TEM) was used to characterize the precise dimensions of particles. In **Figure II-2**, a collection of nanosponge diameters were analyzed by evaluating the relationship between polymer precursor molecular

weight and pendant functionality to determine to what extent, if any, these parameters controlled resultant nanosponge size. A trend was observed through graphing the sizes against the molecular weights of each nanosponge where an increase in molecular weight correlates to an increase in size for a given pendant functionality of 6 or 8% epoxide, while maintaining the ratio of 2:1 amines:epoxide for crosslinking reagent.

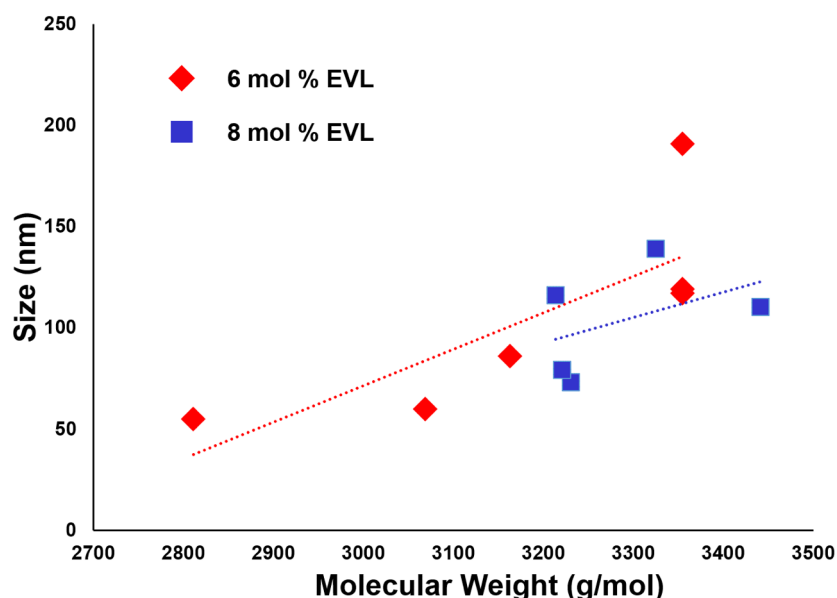


Figure II-2. Analysis of molecular weight vs size for nanosponges prepared with 6 (red diamond) and 8 mol % (blue square) epoxide-containing polymers in a range of molecular weights with their respective trendlines to exhibit trend in increasing size with increasing molecular weight.

Furthermore, we hypothesized that increasing the pendant functionality of a given polymer within the same narrow molecular weight range would increase the size of the particle due to the higher crosslinking density and incorporation of crosslinker. As expected, **Figure II-3A** demonstrates that increasing the epoxide functionality while maintaining similar MW does increase the nanosponge size range. Additionally, the same correlation can be made for an increase in crosslinker equivalents while the MW and epoxide functionality are held constant (**Figure II-**

3B). Understanding these parameters and their effects on the resultant nanosponge, we can begin to use this as a tool to control the synthesis of precise dimensions for these nanoparticles has only small deviations among particle size.

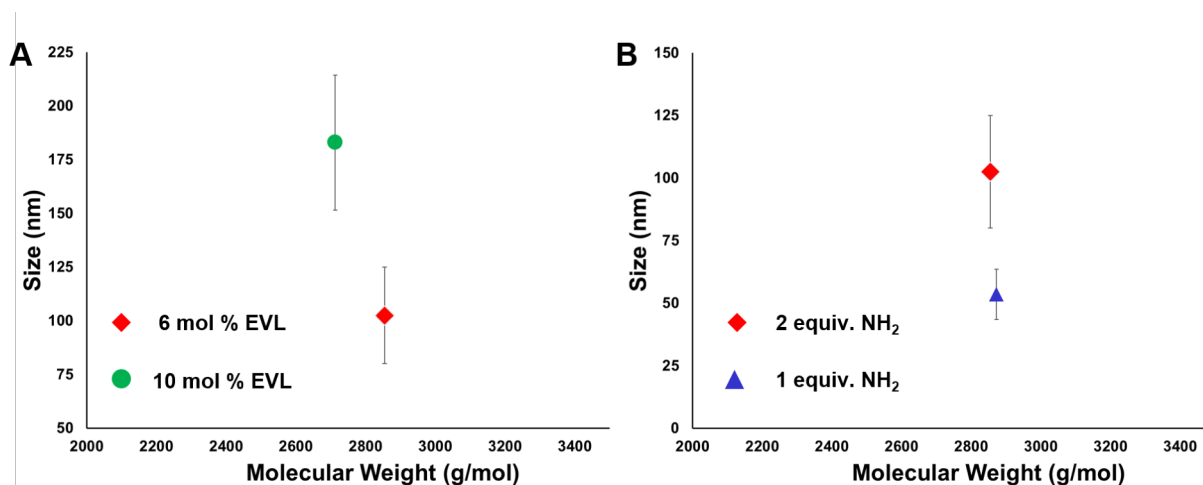


Figure II-3. A) Analysis of molecular weight vs size for nanosponges prepared with 6 (red diamond) and 10 mol % (green circle) epoxide-containing polymers at similar molecular weights to exhibit an increase in size with increased crosslinker equivalents. B) Analysis of molecular weight vs size for nanosponges prepared with 6 mol % EVL and 2 equiv. (red diamond) or 1 equiv. (blue triangle) amine per epoxide crosslinking reagent. An increase in size is observed from increase in crosslinking reagent equivalents while molecular weight and epoxide functionality are held constant. (n=2)

Compared to conventional methods for nanoparticle preparation, the advantages in this approach are the multiple parameters by which precise size and density control can be achieved, the ability to further functionalize the surface of the nanosponge, and the solubility in the organics for hydrophobic drug encapsulation. The versatility of these materials is greatly suited for use in drug delivery applications and we sought to explore their potential with targeted drug delivery approaches.

II.2.3 Functionalization of Nanosponge Surface with Cys40-Exendin-4 Peptide Followed by Attachment of Fluorescent Imaging Agent

Studies indicate that physical characteristics including nanoparticle size influence biological interactions, such as cell trafficking and accumulation.³⁵⁻³⁶ It is crucial that the size of these particles be well-defined with narrow distributions in order to be viable candidates for drug delivery applications.³⁷ For solid tissue targeting, particles should be 200 nm or smaller with narrow distribution to take advantage of the enhanced permeation and retention (EPR) effect³⁸ as well to avoid rapid clearance from the bloodstream and accumulation in the liver and spleen.³⁹ For this reason, we targeted the size range of 70-80 nm by employing the techniques previously described for a precise nanoparticle fabrication, and we achieved polyester nanospheres of ~70 nm in diameter (**Figure II-4**). For attachment of the peptide targeting unit and the imaging dye, we leveraged the free primary amines and allyl functionalities on the nanosponge surface to design a synthetic strategy which utilizes orthogonal attachment chemistries (**Scheme II-2**). Two

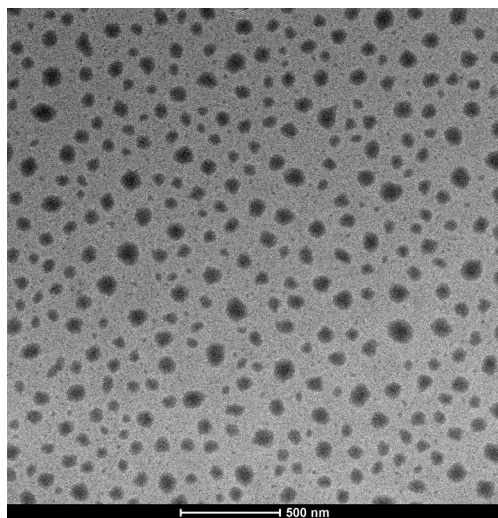
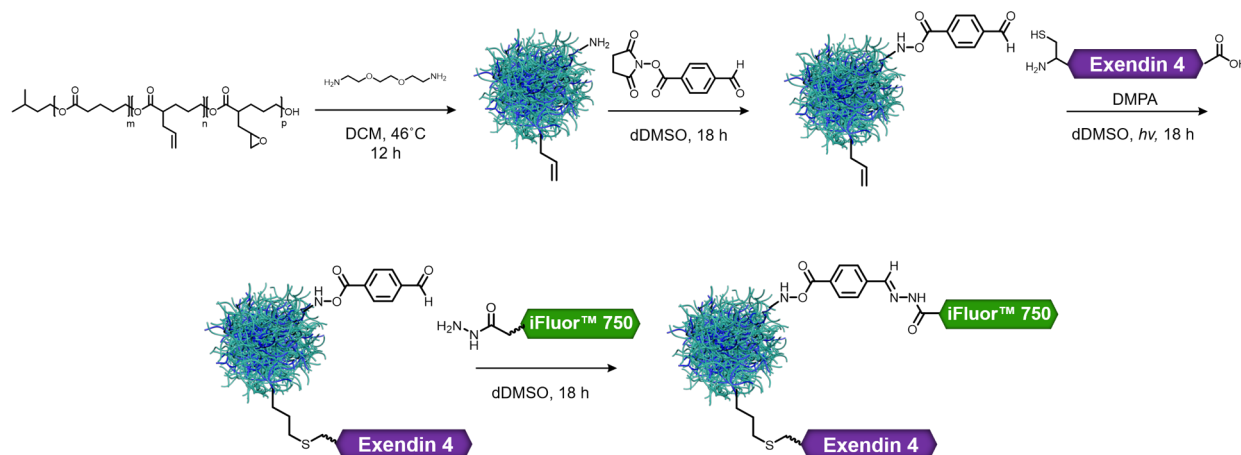


Figure II-4. TEM images of nanospheres prepared by described intramolecular crosslinking technique with allylic and primary amine surface functionality with measured dimensions of 70 nm \pm 14.

Scheme II-2. Orthogonal chemistry design for Cys40-Exendin-4 attachment to nanosponge surface via thiol-ene click chemistry followed by conjugation of iFluor™ 750 hydrazide-functionalized imaging dye through the reaction with aldehyde installed by NHS ester coupling with nanosponge surface primary amines prior to peptide attachment.



orthogonal click chemistries were employed due to their ease of reaction, high efficiency, and lack of toxic or unwanted byproducts. The targeting peptide of interest, Exedin-4 modified with a cysteine residue at the 40 position to install a free thiol as a reactive handle, was procured from Chem-Impex International at high purity. Photo-initiated thiol-ene click chemistry was employed for peptide attachment and was monitored by reduction of the vinylic proton resonance in ¹H NMR spectroscopy. Quantification of the attachment was determined by comparison of this resonance signal integration prior to and immediately after conjugation. For example, in the NMR spectra shown in **Figure II-5B**, Cys40-Exendin-4 peptide attachment was determined to be approximately 11.5 peptides per particle. A synthetic design utilizing primary amine functionality of the nanosponge could not be realized due to the presence of amines in the targeting peptide which could result in fluorescent labeling of the peptide and potential loss of biological activity. It was obvious that transforming these surface amines to another functional group with equal or increased

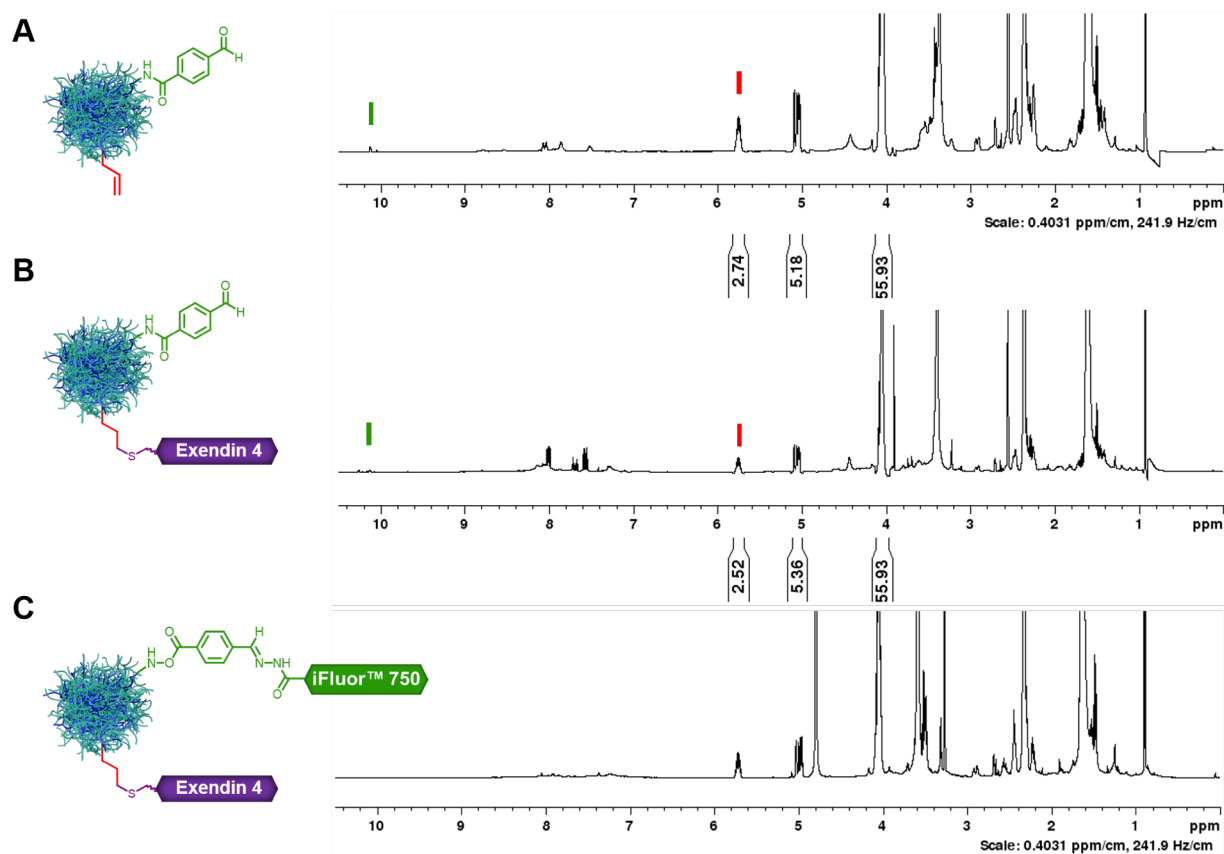


Figure II-5. NMR spectra for A) aldehyde-functionalized nanosponge prior to peptide attachment and B) peptide-conjugated nanosponge which provides quantification for thiol-ene click reaction efficiency and The integration of the vinylic proton resonance prior to peptide attachment is 2.74 and after attachment, the integration for the proton is reduced to 2.52, indicating a reduction in vinylic protons due to the thiol-ene click reaction. C) NMR spectrum after iFluor™ 750 dye attachment, where the disappearance of the aldehyde proton resonance seen in A and B at 10.2 ppm confirms dye conjugation.

reactivity would provide the best route for synthetic design. Prior to peptide functionalization, nanosponges were modified with *N*-succinimidyl-*p*-formylbenzoate to install an aldehyde functionality in place of the primary amines. After peptide attachment, a mono-hydrazide functionalized fluorescent dye, iFluor™ 750, was attached to the nanosponge surface by aldehyde-hydrazide click chemistry (**Scheme II-2**). Dye attachment was confirmed by disappearance of the

aldehyde proton at 10.2 ppm in ^1H NMR seen in **Figure II-5C** and assumed to have achieved 100% efficiency for a total of approximately 13.5 fluorescent molecules per particle.

II.2.4 *In Vivo* Imaging and Analysis of Targeted Nanosponges using GLP-1R-Expressing Tumor Model

Previous work with the Powers Research Group located within the Vanderbilt Diabetes Center confirmed the binding ability of the modified Exendin-4 *in vitro*, and next we were interested in testing this capability *in vivo*. Because human islets come from donors, we first chose to use a model system in place of human Islets for the initial *in vivo* experiments. Instead we utilized a PC9 human lung carcinoma cell line modified to express GLP-1R developed by the Powers laboratory. Unmodified PC9 cells were used as a negative control. Cells were engrafted onto the hind legs of mice and permitted to form a tumor mass over five weeks.

First, to validate the GLP-1R expression of the tumor model, Cys40-Exendin-4 was fluorescently labeled with iFluor™ 750 maleimide-functionalized dye by conjugation via the free thiol of the cysteine residue. The control and experiment animal groups were then injected with the fluorescently tagged peptide (450 μg , 150 μL) and imaged 70 minutes after injection. The accumulation of fluorescence signal was only observed in the PC9:GLP-1R animal (**Figure II-6A**), which validates the expression of GLP-1R and the binding capability of Cys40-Exendin-4 in the PC9:GLP-1R tumor model. Following this, nanosponges labeled with Cys40-Exendin-4 and iFluor™ 750 (2.2 mg, 450 μg peptide per mouse) or iFluor™ 750 (2.2 mg) only, prepared as previously described, were injected into PC9:GLP-1R or PC9 animal groups, respectively. Imaging at 24 h post-injection as seen in **Figure II-6B** indicated a localization of targeted

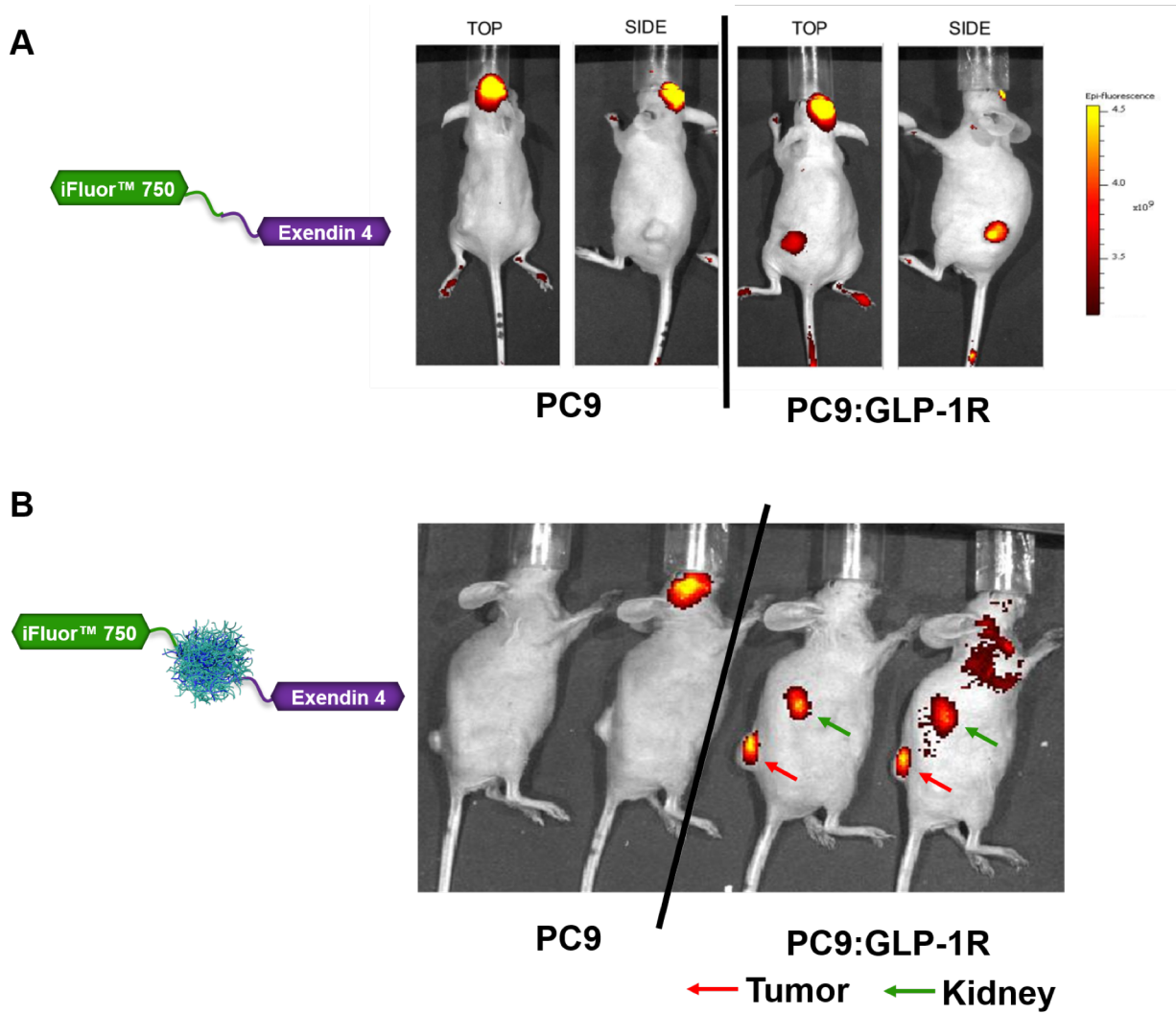


Figure II-6. A) Fluorescence imaging of mice treated with Cys40-Exendin-4 conjugated to maleimide functionalized iFluor™ 750 dye 70 minutes post-injection. Top and side view of control animal with PC9 unmodified tumor, no observed fluorescence in tumor; top and side view of animal with PC9 tumor expressing GLP-1R, with fluorescence signal indicating an accumulation of fluorescent tagged peptide. The accumulation of the dye-labeled peptide in the PC9:GLP-1R tumor demonstrates successful binding of Cys40-Exendin-4 to GLP-1R after conjugation to another molecule. B) Fluorescence imaging of mice treated with targeted nanosponge functionalized with Cys40-Exendin-4 and iFluor™ 750 dye. Imaging was performed 24 h post-injection. Mice in the PC9 group (n=2) exhibit no accumulation of nanosponge construct in tumor. Mice in PC9:GLP-1R group (n=2) exhibit strong fluorescence in the tumor region as indicated by the red arrow. Fluorescence was detected in the kidney (green arrow) due to clearance of the material through polyester degradation. Injections and in vivo imaging were performed by Neil Phillips in the Powers Research Group. *Unpublished data.*

tumor. The lack of localization from dye-only nanosponges within the PC9 tumor confirms that the peptide-labeled construct is responsible for binding to GLP-1R and is not a false positive through enhanced permeability and retention (EPR) effect by which materials in the nanoparticle size regime can accumulate in tumor tissue more readily than normal tissue. Additionally, it is promising that no accumulation of nanosponges was detected in the liver of the mice, confirming non-toxicity of the labeled nanosponge. Fluorescence signal observed in the kidney due to clearance of the material was expected due to the degradable nature of the polyester nanosponge platform.

II.2.5 *In Vivo* Imaging and Analysis of Targeted Nanosponges using Human Islets Grafted in the Fat Pad

Once the *in vivo* targeting of the nanosponge was confirmed with the previous tumor model, we sought to confirm the efficacy of this construct to target naturally expressed GLP-1R *in vivo* with human islets. Evaluating these targeting constructs *in vivo* with human islets proved challenging due to the large variability and unpredictability of the islet donor pool. Because islet grafts are acquired from human donors, each group of islets will have varied expression of GLP-1R, as well as varied viability ratios. After the group of islets are grafted in the animal, the vascular network surrounding the graft can greatly affect the success of the experiment due to the reliance of bloodstream circulation for targeting.

Initial studies were conducted using human islets grafts placed in the fat pad of a mouse located in the kidney region. The grafts were allowed to stabilize for 6-7 weeks then mice were then injected with peptide- and dye-labeled nanosponges. Both *in vivo* imaging and *ex vivo*

imaging was performed at 24 h post-injection to visualize the pancreas, kidneys, and fat pad to determine if a localized fluorescence signal could be detected. The first experiments exhibited no fluorescence in the fat pad after 24 h, illustrating that further work toward optimization of the experimental conditions and timescale for targeting *in vivo* were necessary.

It was hypothesized that the fatty composition of the tissue around the islets graft may be contributing to the attenuation of the fluorescence signal, making detection of the nanoparticles much more difficult. In order to combat this, we decided to encapsulate the fluorophore Nile Red into the nanosponge after peptide and fluorescent dye labeling to increase the fluorescence signal. Nile Red was mixed with the labeled nanosponges in minimal organic solvent (DMSO) then precipitated into a composition of water with 1% D- α -Tocopherol PEG 1000 succinate as a surfactant. The surfactant aids in the resuspension of the nanosponges by increasing hydrophilicity of the surface. The post-loading procedure used for the encapsulation of Nile Red serves as a model for potential hydrophobic drug molecules for treatment. Animals treated with the Nile Red-loaded, labeled nanosponges exhibit strong fluorescence signal in the fat pad 24 h post-injection with the 650 nm channel, indicating localization of the targeted construct to the islets graft in the fat pad (**Figure II-7**). Mice injected with this Nile Red-loaded nanoparticle construct show a strong fluorescence signal in the fat pad after 24 hours when imaged using the Nile Red fluorescence channel (650 nm), indicating localization of the targeted nanoparticles to the islets graft. These results were extremely promising, and we sought to continue improvements to our system to achieve a practicable targeted drug delivery nanocarrier.

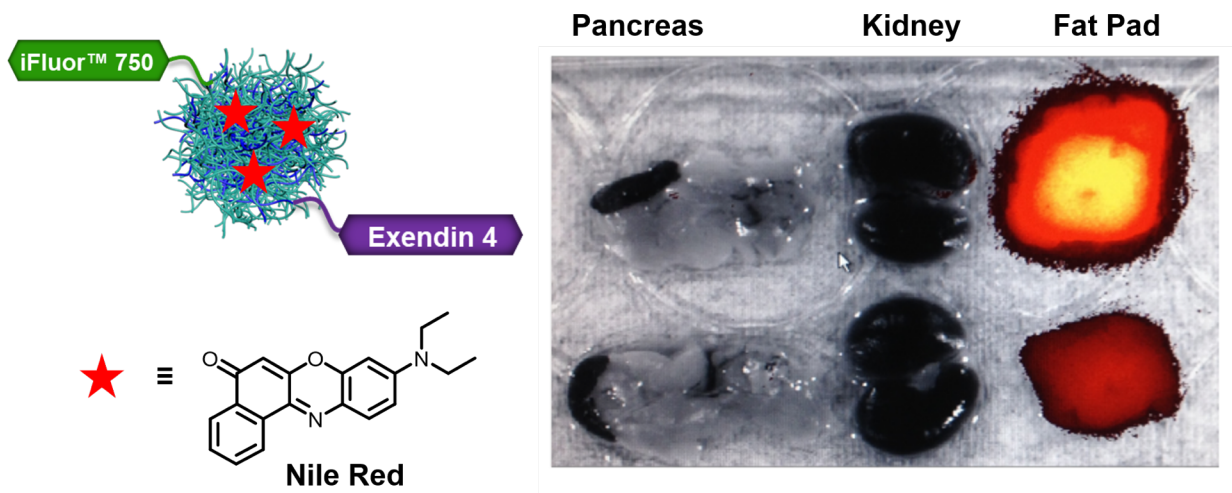


Figure II-7. Fluorescence imaging of mice treated with Cys40-Exendin-4 and iFluor™ 750 conjugated nanosponges loaded with Nile Red. *Ex vivo* imaging of pancreas, kidney, and fat pad. Fat pad exhibits strong fluorescence signal indicating a localization of nanosponge construct to the islet graft, while no signal is detected from pancreas or kidney. Injections and imaging were performed by Neil Phillips in the Powers Research Group. *Unpublished data.*

II.2.6 Optimization of Synthetic Design for Nanosponge Functionalization to Improve Aqueous Suspension

In previous experiments, we observed difficulty achieving a fine, homogenous suspension of the fully functionalized construct in aqueous media. To ensure a homogenous injection of material into each animal, we needed to improve the suspension of our material in buffer. It was our hypothesis that the fluorescent labeling dye, iFluor™ 750, was impeding the suspension of nanosponge into aqueous buffer and it was evident that further optimization of the synthetic strategy and labeling protocol was needed. We transitioned to a fluorescent labeling dye with increased water solubility, SunFluor₇₅₀, and in addition, included a synthetic step in which all remaining allyls on the nanosponge surface were quenched with a short PEG molecule to increase hydrophilicity. We observed a significant improvement in suspension of the nanosponge construct

into aqueous media in preparation for future injections. This improved synthetic strategy was employed for the future *in vivo* imaging of targeted nanosponges using human islets located in the quadriceps of the mouse.

Moreover, when moving forward with the animal studies using human islets grafts in the quadriceps location, a negative control for the *in vivo* studies was also developed and implemented. For these studies, a control within the mouse model itself as used for our tumor model system was not possible, as all human islets grafts will contain GLP-1R. Therefore, it was necessary to establish a nanoparticle control. Rather than use bare nanoparticles as a control, we chose instead to develop a construct that was very similar to the Cys40-Exendin-4 and dye labeled particles. For the control nanoparticles, in place of the Cys40-Exendin-4, we instead attached a peptide having the same 40 amino acids only in a different sequence. As the function of Cys40-Exendin-4 peptide is highly dependent on the order of the amino acids, this “scrambled” version of the peptide should exhibit no binding to GLP-1R. By using this scrambled peptide for our nanosponge control, we ensure that both the experimental group and the control group of material will have similar solubility and circulation kinetics in the mouse model. Additionally, to improve reaction efficiency of the orthogonal click chemistries, a tri-glycine spacer was installed on both peptides, Cys40-Exendin-4 and Scrambled Exendin-4, at the N-terminus prior to the cysteine residue to reduce steric hinderance of the free thiol. Quantification of the PEG molecule was determined to be similar to that of the peptide calculation, by comparison of the vinylic proton resonance integration prior to and after PEG conjugation. In **Figure II-8**, for example, the NMR spectra indicates the attachment of approximately 9.2 PEG molecules per particle.

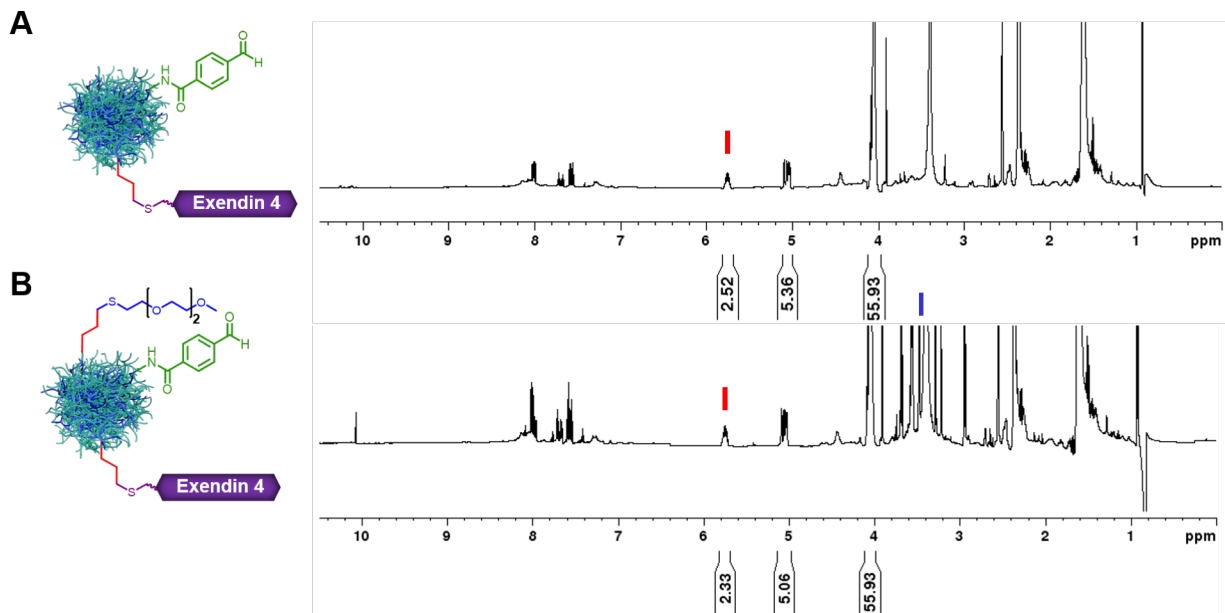


Figure II-8. NMR spectra for A) Cys40-Exendin-4 conjugated nanosponges and B) after quenching all residual surface allyls with PEG to improve hydrophilicity. Reduced integration for vinylic protons indicates successful thiol-ene click reaction for remaining surface functionalities and is used to calculate an average of 9.2 PEG molecules per nanosponge.

II.2.7 *In Vivo* Imaging and Analysis of Targeted Nanosponges using Human Islets Grafted in Quadriceps

Our final *in vivo* experiments utilized a new graft location, the quadriceps of the mouse, which offers a few benefits over the fat pad, mainly a longer viability and ease of imaging *in vivo*. The subcutaneous nature of the graft means there is only a thin layer of skin which the fluorescent signal must pass through to be detected and provides access to recording multiple time points as well. Because of this improved imaging signal using the subcutaneous graft, we omitted the use of Nile Red for these experiments to determine if the signal from the dye was independently strong enough to indicate localization. Human islets were harvested and implanted into the calf muscle of the animal and allowed to stabilize for nine weeks. Peptide- and dye-conjugated nanosponges

containing 618.3 μg Cys40-Exendin-4 peptide and 378 μg SunFluor₇₅₀ imaging dye or 739 μg Scrambled Exendin-4 peptide and 375 μg SunFluor₇₅₀ imaging dye were inserted into the mouse bloodstream through injection via the tail vein. Imaging was conducted at 18 h post-injection and successful localization of nanosponges were observed in the experimental group. We were interested in further experiments to elucidate the timescale of targeting, so we moved forward to animal studies with multiple imaging time points.

With similar concentrations as previous experiments, peptide- and dye-conjugated nanosponges were inserted into the bloodstream via a retro-orbital injection into mice with stabilized quadricep human islets grafts. *In vivo* imaging was performed at 14, 16, 18, and 24 h post-injection. Localization of Cys40-Exendin-4 nanosponges was observed beginning at 14 h in one animal from the experimental group as seen in **Figure II-9**. We attribute this incongruity in localization to the vasculature of the graft in each mouse, hypothesizing that the vascular network of mouse Ex3 did not allow blood circulation to the human islets grafts therefore no targeting of Cys40-Exendin-4 was achieved. As expected, no localization of Scrambled Exendin-4 labeled nanosponges was observed at any time points. The promising results from this study, combined with the previous *in vitro* and *in vivo* experiments, indicate the great potential for this targeted nanosponge system to deliver therapeutics directly to beta-cells within the pancreas for diabetes treatment.

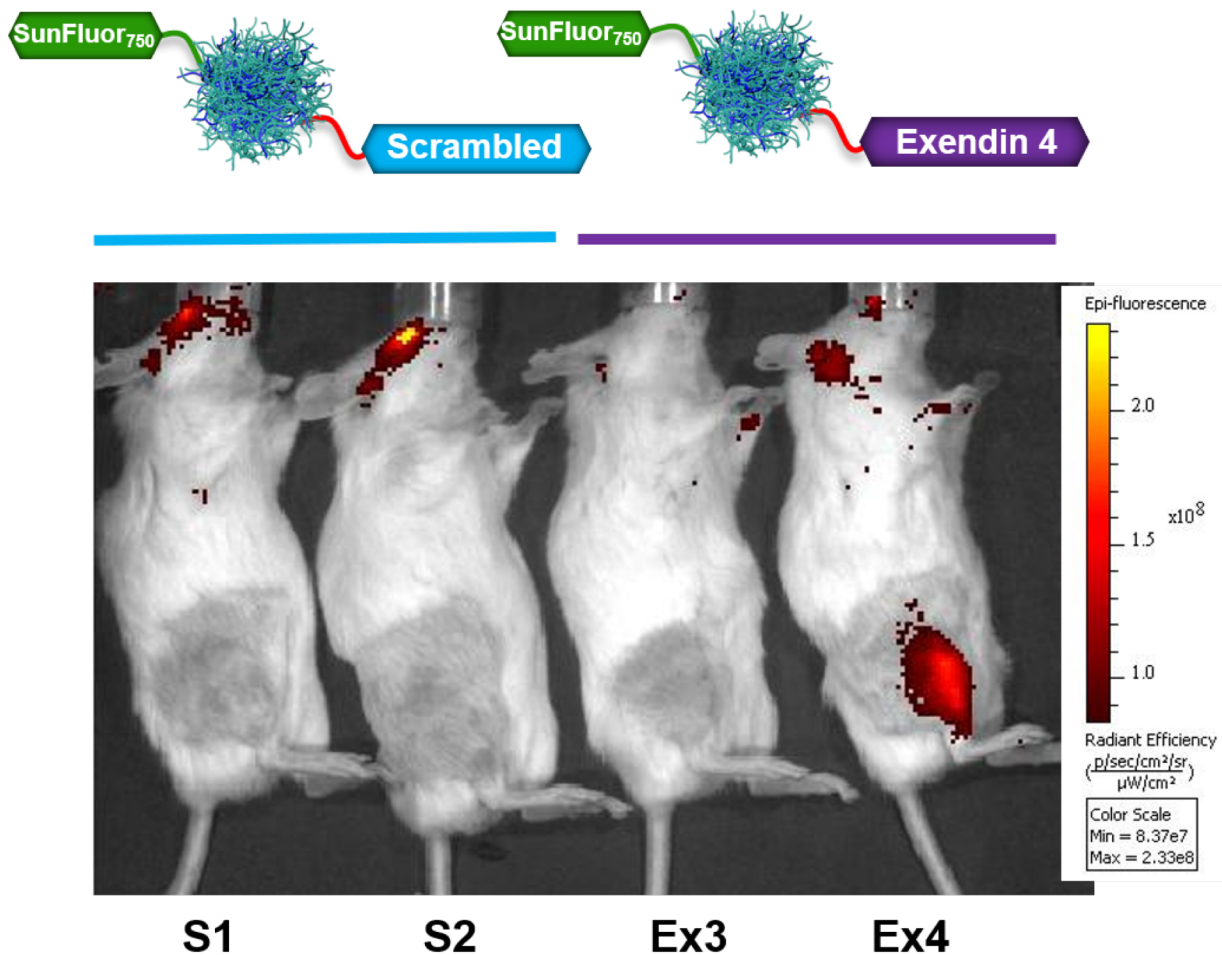


Figure II-9. Fluorescence imaging of mice bearing quadriceps human islet grafts expressing GLP-1R treated with Scrambled-Exendin-4, dye labeled nanosponges (S1, S2) and Cys40-Exendin-4, dye labeled nanosponges (Ex3, Ex4). No signal is detected from the quadriceps grafts of the mice treated with the Scrambled-Exendin-4 peptide as a control as anticipated. Strong signal from Ex4 in the graft location demonstrates the targeting of the Cys40-Exendin-4 nanosponge to the islet graft. The lack of signal from Ex3 is attributed to the potential nature of the vasculature of the quadriceps islet graft to have reduced blood flow to the graft location.

Additional animal studies were conducted to confirm the reproducibility of these results, however during these experiments animal death occurred unexpectedly. Upon *ex vivo* imaging, fluorescence signal was detected in the liver. Unfortunately, it was confirmed by the manufacturer that the SunFluor₇₅₀ fluorescence dye used in the studies contained up to 20% of impurities of di-

functionalized molecules. We determined that these impurities had led to crosslinking between nanoparticles, creating large particle aggregates leading to liver accumulation and death of the animals. Due to the issues encountered with the impure dye, no further animal studies were conducted.

II.2.8 *In Vitro* Release of Imatinib from Nanosponges

As the potential of this nanosponge construct greatly relies on the ability of the nanosponge to release cargo during targeting, we performed an *in vitro* release experiment with nanosponges to evaluate the release profile with a potential diabetes therapeutic, imatinib, as a model. Imatinib, marketed as Gleevec as an anticancer agent, has been investigated as a treatment for diabetes for its role in beta-cell death inhibition.^{6, 40-41} For the release, imatinib was encapsulated into unfunctionalized nanosponges using a nanoprecipitation method³¹ and suspended in PBS (pH 7.4) containing 0.1% v/v Tween-80 surfactant to promote suspension of the drug in the release media and reduce contact loss with drug interactions. At specified time points, the release media was collected after centrifugation of the particles and analyzed by high performance liquid chromatography (HPLC). Unfunctionalized nanosponges were used for this study as the separation technique used to isolate the released imatinib relies on solubility differences of the release media and nanosponges. Due to the peptide and dye molecules greatly improving hydrophilicity of the material, the nanosponges could not be separated from the released drug in this experiment. However, it is not expected that the surface functionalization of the nanosponge with peptide and dye molecules will significantly affect the release kinetics.

For analysis of release kinetics from nanosponges, imatinib-loaded nanosponges were dispersed in PBS (pH 7.4) at 37°C. At specified time points, free drug was separated from encapsulated drug by centrifugation and removed, then replaced with fresh release media. As seen in **Figure II-10**, the release of imatinib from nanosponges exhibited a small burst within the first several hours of approximately 25%, followed by a linear release until reaching 100% released at 16 days. The linear release profile is ideal for drug delivery as there is a constant supply of drug coming from the delivery vehicle during targeting. Methods to reduce the non-encapsulated drug from the loaded nanosponges, such as an additional wash step, can be added to the protocol to minimize free drug on the nanosponge surface which contributes to the observed burst release.

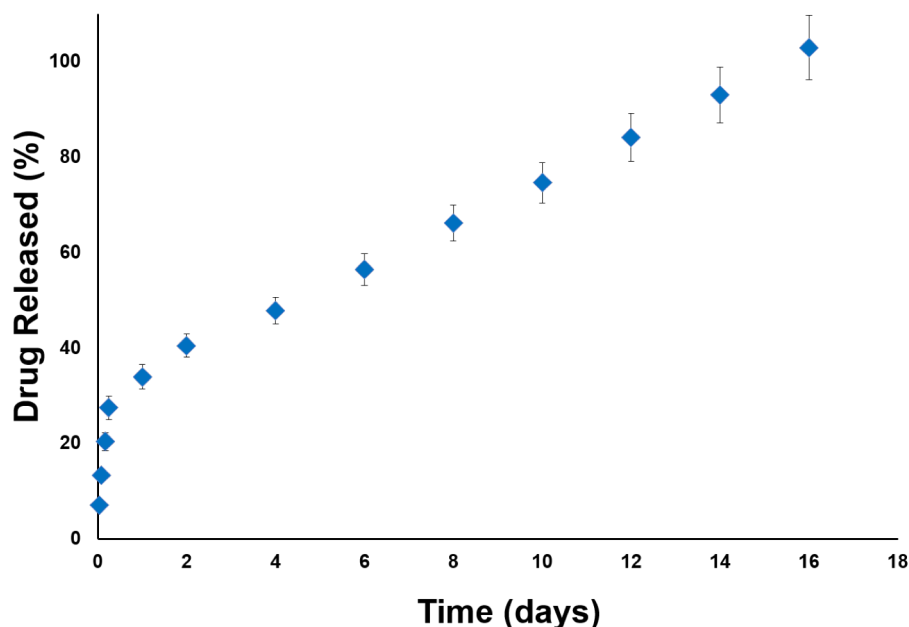


Figure II-10. Drug release profile of imatinib-loaded nanosponges (7 mol % EVL) in PBS (pH 7.4) with 0.1% v/v Tween-80 surfactant. Small burst release was observed in first 6 h up to 25%, with the remaining release rate of drug appearing linear and achieved 100% release at 16 days. Values are the average of measurements in triplicate.

II.3 Conclusion

In summary, we have developed an analysis tool which allows us to precisely predict the size of nanoparticles from the synthetic parameters. We can use this information to prepare particles of desired dimensions with reproducible and reliable homogeneity, and small standard deviations. Furthermore, we can employ orthogonal chemistry to functionalize the nanosponge surface, which contains free amines and allyls, with targeting units, including peptides, and imaging molecules, such as fluorescent dyes. We successfully characterized the attachment of these molecules to the nanosponge and quantified the peptide loading by NMR spectroscopy. Next, we explored the *in vivo* efficacy of the targeting construct in a GLP-1:PC9 tumor model, followed by a human islets model grafted in the fat pad and, finally, the model of a subcutaneous quadriceps graft of the mouse. The promising targeting results from *in vivo* imaging experiments indicate a great potential for this system to translate to clinical applications of targeting pancreatic beta-cells. Additionally, the drug release profile exhibited from imatinib-loaded nanosponges validates the utility of this nanosponge design for targeted drug delivery applications. Further work is needed to optimize the homogeneity of the human islets grafts, evaluate their vasculature prior to targeting experiments, and increase the sample size of animals to validate reproducibility of the construct.

II.4 Experimental

Materials

All peptides and *N*-succinimidyl-*p*-formylbenzoate were custom synthesized by Chem-Impex International (Wood Dale, IL). SunFluor₇₅₀ hydrazide dye was obtained from Nanocs Inc. (New York, NY). SnakeSkin™ 10K MWCO dialysis tubing was purchased from ThermoFisher. Spectra/Por® 1kD MWCO dialysis tubing was purchased from Spectrum Laboratories Inc. SiliaMetS® Cysteine was purchased from Silicycle Inc (. All other reagents were purchased from Sigma-Aldrich or Fisher Scientific and used as received unless otherwise indicated. δ -valerolactone and α -allyl- δ -valerolactone were purified by vacuum distillation immediately prior to use.

Characterization

¹H and ¹³C NMR spectra were obtained on a Bruker AV-400 and AVII-600 MHz spectrometers. An FEI Tecnai Osiris™ transmission electron microscope operating at 200 kV in bright-field mode was used to obtain TEM micrographs of the polymer nanoparticles. For imatinib encapsulation and release analysis, samples were injected (20 μ L injection volume) directly onto a 4.60 x 150 mm, 5- μ m C-8 phase silica column (Phenomenex, Torrance, CA, USA) for HPLC analysis. Imatinib was eluted using an isocratic solvent system of water/methanol/acetonitrile/TFA (70/15/15/0.1). A Waters photodiode array detector (Waters Corporation, Milford, MA, USA)

was used to collect the data. Standard curve and all data were analyzed at 254 nm. Fluorescence imaging was conducted in the Powers Research Group by Neil Phillips.

Synthesis of α -Allyl- δ -Valerolactone (AVL)

Under a dry nitrogen atmosphere performed with Schlenk technique, a 2-neck 500 mL round bottom flask was charged tetrahydrofuran (THF, 156.25 mL). *N,N*-diisopropylethylamine (DIPA, 3.3 mL, 23 mmol) was added at -78 °C and stirred followed by dropwise addition of *n*-butyllithium solution (2.5 M in hexanes, 9.34 mL, 23 mmol) via cannula. The reaction stirred for 15 min and a solution of δ -valerolactone (1.97 mL, 21 mmol) in THF (56 mL) was added dropwise via cannula transfer over 45 min. A mixture of hexamethylphosphoramide (HMPA, 4.43 mL, 25 mmol) and allyl bromide (2.02 mL, 23 mmol) was then added to the reaction dropwise via cannulation and stirred for 15 min. The reaction was allowed to warm to -40 °C and stirred for 2 h. The reaction was then warmed to -10 °C and quenched with sat. ammonium chloride solution (150 mL). The solid salt was removed by filtration and the volatiles removed by evaporation. The concentrated product was extracted with dichloromethane (DCM) and dried with magnesium sulfate (MgSO₄). The product was purified via column chromatography with a gradient of 3-29% ethyl acetate in hexanes over 5 column volumes. (2.07 g, 71%) ¹H NMR (CDCl₃, 400 MHz): δ 5.75 (m, 1H), 5.06 (m, 2H), 4.26 (m, 2H), 2.54 (m, 3H), 2.28 (m, 1H), 2.03 (m, 1H), 1.87 (m, 1H), 1.54 (m, 1H).

General Synthesis of Poly(δ -Valerolactone-co- α -Allyl- δ -Valerolactone-co- α -Epoxy- δ -Valerolactone) (P(VL-AVL-EVL))

A 25 mL round bottom flask equipped with stir bar was flame dried and purged with nitrogen followed by addition of tin trifluoromethanesulfonate ($\text{Sn}(\text{OTf})_2$, 1.3 mg, 3.11 μmol). Isoamyl alcohol (27.24 μL , 0.67 mmol) and DCM (0.96 mL) were added to the flask and stirred for 5 min. α -allyl- δ -valerolactone (AVL, 300 μL , 2.29 mmol) and δ -valerolactone (VL, 1.56 mL, 16.77 mmol) were added sequentially and stirred at room temperature for 18 h. The polymerization was quenched via addition of excess MeOH (~2 mL) then precipitated into cold MeOH to produce a white solid and dried *in vacuo*. (1 g, 50%) ($M_{\text{nNMR}} = 3165.75 \text{ gmol}^{-1}$, VL: 91%, AVL: 9%) ^1H NMR (400 MHz, CDCl_3): δ 0.92 (6H, d, CH_3), 1.61-1.78 (m, CH_2), 2.29-2.42 (m, CH_2 , CH), 3.59-3.75 (m, CH_2), 3.99-4.10 (6H, m, CH_2), 5.04 (2H, m, CH_2) 5.73 (1H, m, CH)

In Step 2: P(VL-AVL) (200 mg, 63.2 mmol, 117.6 mmol allyl) was dissolved in DCM (1.81 mL) in a 6-dram vial with stir bar. Meta-chloroperoxybenzoic acid (mCPBA, 22.3 mg, 129.2 mmol) was dissolved in DCM (1 mL) and transferred to the reaction vial and the cap was sealed with paraffin wax. The reaction stirred at room temperature for 48 h. The organic layer was washed with saturated sodium bicarbonate (NaHCO_3) solution 3x then dried over magnesium sulfate. The polymer was dried *in vacuo* to collect a white waxy solid. (170 mg, 85%) ($M_{\text{nNMR}} = 2972.00 \text{ gmol}^{-1}$, VL = 89%, AVL = 7%, EVL = 4%) ^1H NMR (400 MHz, CDCl_3): δ 0.92 (6H, d, CH_3), 1.61-1.78 (m, CH_2), 2.29-2.42 (m, CH_2 , CH), 2.46 (1H, s, CH_2), 2.75 (1H, s, CH_2), 2.87-2.99 (1H, d, CH), 3.59-3.75 (m, CH_2), 3.99-4.10 (6H, m, CH_2), 5.04 (2H, m, CH_2) 5.73 (1H, m, CH)

General Synthesis of P(VL-AVL-EVL) Nanosponge

Into a 100 mL round bottom flask equipped with a stir bar, poly(VL-AVL-EVL) (200.2 mg, 51.5 μmol , 0.17 mmol epoxide) and DCM (31.43 mL) were added. The reaction flask was heated to

46°C and 2,2-(ethylenedioxy)bis(ethylamine) (49.68 μ L, 0.34 mmol) was added dropwise to the stirring solution. The flask was capped with a water-jacketed condenser and stirred for 12 h. The solvent was removed in vacuo and the nanosponges were transferred to 10K MWCO dialysis tubing and dialyzed against DCM for 48 h then collected and dried in vacuo (134 mg, 67%). ^1H NMR (600 MHz, $\text{DMSO-}d_6$): δ 0.87 (6H, d, CH_3), 1.29-1.68 (m, CH_2 , CH), 2.12-2.36 (m, CH_2 , CH), 2.42 (1H, s, CH_2), 2.70 (1H, s, CH_2), 3.30-3.45 (m, CH_2), 3.45-3.63 (m, CH_2), 3.92-4.10 (6H, m, CH_2), 5.01 (2H, m, CH_2) 5.70 (1H, m, CH)

General Synthesis of Nanosponge Aldehyde-functionalization

Under a nitrogen atmosphere, nanosponges (4.6% AVL, 4.9% EVL, 80.0 mg, 0.53 μ mol) were dissolved in a minimal amount of dimethyl sulfoxide (DMSO, 200 μ L). *N*-succinimidyl-*p*-formylbenzoate (4.0 mg, 16 μ mol) was added to the solution via microsyringe and the reaction was stirred at room temperature for 18 h. The product was purified by dialysis using 10K MWCO dialysis tubing against DCM for 24 hours. The contents of the dialysis tubing were collected and dried in vacuo (56% yield). ^1H NMR (600 MHz, $\text{DMSO-}d_6$): δ 0.87 (6H, d, CH_3), 1.29-1.68 (m, CH_2 , CH), 2.12-2.36 (m, CH_2 , CH), 2.42 (1H, s, CH_2), 2.70 (1H, s, CH_2), 3.30-3.45 (m, CH_2), 3.45-3.63 (m, CH_2), 3.92-4.10 (6H, m, CH_2), 5.01 (2H, m, CH_2) 5.70 (1H, m, CH), 7.90-8.10 (4H, m, CH), 10.20 (1H, s, CHO)

General Synthesis of Cys40-Exendin-4 Conjugation to Nanosponge

Under a nitrogen atmosphere, aldehyde-functionalized nanosponges (50.0 mg, 0.33 μmol) and peptide_ACPP (21.2 mg, 3.33 μmol) were dissolved in minimal DMSO-*d*₆ (200 μL). 2,2-dimethoxy-2-phenylacetophenone (DMPA) (1.12 mg, 4.37 μmol) was added to the reaction mixture via microsyringe. The solution was irradiated at 365 nm and stirred at room temperature for 18 h. Peptide conjugation was quantified via reduction in resonance signal of protons associated with allyl functionality (5.01 and 5.70 ppm) through crude ¹H NMR and calculated to be 7.88 peptides per particle as described below in **Equation S1/S2**. Peptide-conjugated nanosponges were carried forward without further purification. ¹H NMR (600 MHz, DMSO-*d*₆): δ 0.87 (6H, d, CH₃), 1.29-1.68 (m, CH₂, CH), 2.12-2.36 (m, CH₂, CH), 2.42 (1H, s, CH₂), 2.70 (1H, s, CH₂), 3.30-3.45 (m, CH₂), 3.45-3.63 (m, CH₂), 3.92-4.10 (6H, m, CH₂), 5.01 (2H, m, CH₂) 5.70 (1H, m, CH), 7.40-7.50 (m, Ar H), 7.55 (t, Ar H), 7.84-7.93 (m, Ar H), 10.20 (1H, s, CHO)

$$\frac{2.92 \text{ 1H} - 2.72 \text{ 1H}}{2.92 \text{ 1H}} = 0.0685 \text{ 1H}$$

Equation II-3. The integration value from pre-conjugated nanosponge ¹H NMR allyl resonance at 5.01 ppm (2.92) was used to calculate the difference from post-conjugated nanosponge allyl resonance (2.72).

$$\frac{115.18 \text{ allyls}}{\text{nanosponge}} \times 0.068 \text{ 1H} = 7.88$$

Equation II-4. The difference (0.0685) was then multiplied by the average number of allyls per nanosponge to determine the average number of reacted allyls. This value, 7.88, is equal to the average number of peptides conjugated to the nanosponges.

General Synthesis of Fluorescent Hydrazone-Functionalized Dye Conjugation to Nanosponge

Under a nitrogen atmosphere, peptide-functionalized nanosponges (50.0 mg, 0.33 μmol) were dissolved in DMSO-*d*₆ (50 μL). iFluor™ 750 or SunFluor₇₅₀ hydrazone-functionalized imaging dye (1.58 mg, 2.90 μmol [SunFluor₇₅₀]) was added to the reaction vial via syringe. The reaction was stirred in the absence of light at room temperature for 18 h. The resulting mixture was purified by dialysis against a 50:50 v/v mixture acetonitrile:MeOH in 10K MWCO dialysis tubing for 48 hours with 3 solvent changes per day, then diluted in water and lyophilized to collect a powder (80% yield). Successful attachment of the dye at an equivalence of 13.5 dye molecules per nanosponge was verified by the absence of the aldehyde peak at 10.20 ppm. ¹H NMR (600 MHz, DMSO-*d*₆): δ 0.87 (6H, d, CH₃), 1.29-1.68 (m, CH₂, CH), 2.12-2.36 (m, CH₂, CH), 2.42 (1H, s, CH₂), 2.70 (1H, s, CH₂), 3.30-3.45 (m, CH₂), 3.45-3.63 (m, CH₂), 3.92-4.10 (6H, m, CH₂), 5.01 (2H, m, CH₂) 5.70 (1H, m, CH), 6.54-6.77 (m, Ar H), 7.12 (m, Ar H), 7.43 (d, Ar H), 7.73 (t, Ar H), 7.86 (d, Ar H), 8.4 (t, Ar H), 10.20 (1H, s, CHO)

Loading of Nanoparticles with Nile Red

D- α -Tocopherol polyethylene glycol 1000 succinate (0.0256 mg, 2.6 μL), nanoparticles modified with Cys40-Exendin-4 and iFluor750 dye (2.2 mg, 34.4 μL), and Nile Red (0.36 mg, 14.4 μL) were placed in an Eppendorf tube in DMSO and mixed well to obtain a homogenous solution. A 1.0 mL aliquot of cell culture water was then added to the mixture and the contents were again mixed well. The solution was then immediately frozen and lyophilized to obtain Nile Red-loaded nanoparticles.

Evaluating the Targeting of Cys40-Exendin-4 Conjugated, Nile-Red Loaded Nanosponges to Human Islets Grafted in the Fat Pad

Human islets cells were implanted subcutaneously onto the fat pads of mice by collaborators in the Powers lab. Grafts were allowed to stabilize in the mice for several weeks before injections were performed. Mice were then given a retro-orbital injection of 150 μ L of a suspension of nanoparticles conjugated to both the Cys40-Exendin-4 peptide and an iFluor750 dye and loaded with Nile Red (2.2 mg nanoparticles, 720 μ g peptide, 124 μ g imaging dye, and 360 μ g Nile Red per mouse) in a 1% solution of D- α -Tocopherol polyethylene glycol 1000 succinate in PBS. Ex vivo imaging of the pancreas, kidneys, and fat pad was performed 24 hours post-injection.

Evaluating the Targeting of Cys40-Exendin-4 Conjugated, Fluorescently-Labeled Nanosponges to Human Islets Grafted in the Quadricep

Human islets cells were implanted subcutaneously onto the hind limbs of mice by collaborators in the Powers lab. Grafts were allowed to stabilize in the mice for 9 weeks before injections were performed. Mice were then given a retro-orbital injection of 150 μ L PBS containing either 618.3 μ g Exendin-4 peptide and 378 μ g SunFluor₇₅₀ imaging dye or 739 μ g Scrambled Exendin-4 peptide and 375 μ g SunFluor₇₅₀ imaging dye were performed to introduce nanosponge constructs to the bloodstream. *In vivo* imaging was performed at 14, 16, 18, and 24 h post-injection.

Encapsulation of Small Molecule Drug, Imatinib, into Nanosponges

P(VL-AVL-EVL) nanosponges (80.0 mg, 5.3×10^{-4} mmol, 7.0% EVL) were mixed with imatinib (18.1 mg, 3.67×10^{-2} mmol) in DMSO (200 μ L) in a microcentrifuge tube. The sample was subjected to multiple cycles of sonication and mixing until a homogenous solution was achieved. The nanosponge/imatinib mixture was precipitated into the vigorously stirring aqueous solution of 1 wt % D- α -tocopherol polyethylene glycol 1000 succinate in cell culture grade water to encapsulate the drug. The resulting solution was transferred to a centrifuge tube and then centrifuged at 7830 rpm for 20 minutes. The supernatant was decanted and the pellet was washed with 20 mL of cell culture water, then centrifuged again at 7830 rpm for 20 minutes. The supernatant was again decanted and the resulting pellet was resuspended in 5 mL of cell culture water and lyophilized to collect the dried imatinib-loaded nanosponges.

In Vitro Release of Imatinib from Polyester Nanosponges

For *in vitro* release, imatinib-loaded nanosponges (17.0 mg) were placed in a 15 mL centrifuge tube and then 3.0 mL of PBS (pH 7.4, 0.1% v/v Tween-80) was added via syringe and sonicated until the particles formed a fine suspension. The samples were placed in a 37°C bath and at specified time points, the tube was removed from the bath and centrifuged at 7830 rpm for 20 minutes. The supernatant was removed carefully by syringe and replaced with 3.0 mL of fresh release media. Supernatants at each time point were analyzed for imatinib concentration using reverse phase HPLC. Experiments were performed in triplicate.

To determine the efficiency of encapsulation, imatinib-loaded nanosponges (6.70 mg) was dissolved in PBS (0.1% v/v Tween-80) to a concentration of 0.50 mg/mL. HPLC analysis

determined a total of 0.68 mg of imatinib in the 6.70 mg sample, indicating a 10.2% loading capacity of the drug.

II.5 References

1. Classification and Diagnosis of Diabetes Mellitus and Other Categories of Glucose Intolerance. *Diabetes* **1979**, 28 (12), 1039-1057.
2. Butler, A. E.; Janson, J.; Bonner-Weir, S.; Ritzel, R.; Rizza, R. A.; Butler, P. C., β -Cell Deficit and Increased β -Cell Apoptosis in Humans With Type 2 Diabetes. *Diabetes* **2003**, 52 (1), 102-110.
3. Klinke, D. J., II, Extent of Beta Cell Destruction Is Important but Insufficient to Predict the Onset of Type 1 Diabetes Mellitus. *PLoS One* **2008**, 3 (1), e1374, 1-10.
4. Chen, C.; Cohrs, C. M.; Stertmann, J.; Bozsak, R.; Speier, S., Human beta cell mass and function in diabetes: Recent advances in knowledge and technologies to understand disease pathogenesis. *Mol Metab* **2017**, 6 (9), 943-957.
5. Wang, P.; Alvarez-Perez, J.-C.; Felsenfeld, D. P.; Liu, H.; Sivendran, S.; Bender, A.; Kumar, A.; Sanchez, R.; Scott, D. K.; Garcia-Ocaña, A.; Stewart, A. F., A high-throughput chemical screen reveals that harmine-mediated inhibition of DYRK1A increases human pancreatic beta cell replication. *Nat Med* **2015**, 21 (4), 383-388.
6. Lundh, M.; Scully, S. S.; Mandrup-Poulsen, T.; Wagner, B. K., Small-molecule inhibition of inflammatory β -cell death. *Diabetes Obes Metab* **2013**, 15 (0 3), 176-184.
7. Boerner, B. P.; George, N. M.; Mir, S. U. R.; Sarvetnick, N. E., WS6 induces both alpha and beta cell proliferation without affecting differentiation or viability. *Endocr J* **2015**, 62 (4), 379-386.

8. Duan, H.; Arora, D.; Li, Y.; Setiadi, H.; Xu, D.; Lim, H.-Y.; Wang, W., Identification of 1,2,3-triazole derivatives that protect pancreatic β cells against endoplasmic reticulum stress-mediated dysfunction and death through the inhibition of C/EBP-homologous protein expression. *Bioorg Med Chem* **2016**, *24* (12), 2621-2630.
9. Chou, D. H.-C.; Bodycombe, N. E.; Carrinski, H. A.; Lewis, T. A.; Clemons, P. A.; Schreiber, S. L.; Wagner, B. K., Small-Molecule Suppressors of Cytokine-Induced beta-Cell Apoptosis. *ACS Chem Biol* **2010**, *5* (8), 729-734.
10. Lee, J. T. C.; Shanina, I.; Chu, Y. N.; Horwitz, M. S.; Johnson, J. D., Carbamazepine, a beta-cell protecting drug, reduces type 1 diabetes incidence in NOD mice. *Sci Rep* **2018**, *8* (4588), 1-9.
11. Chia, C. W.; Egan, J. M., Biology and therapeutic potential of GLP-1 in the treatment of diabetes. *Drug Discov Today Dis Mech* **2005**, *2* (3), 295-301.
12. Ahrén, B.; Schmitz, O., GLP-1 Receptor Agonists and DPP-4 Inhibitors in the Treatment of Type 2 Diabetes. *Horm Metab Res* **2004**, *36* (11/12), 867-876.
13. Agersø, H.; Jensen, L. B.; Elbrønd, B.; Rolan, P.; Zdravkovic, M., The pharmacokinetics, pharmacodynamics, safety and tolerability of NN2211, a new long-acting GLP-1 derivative, in healthy men. *Diabetologia* **2002**, *45* (2), 195-202.
14. Meier, J. J., GLP-1 receptor agonists for individualized treatment of type 2 diabetes mellitus. *Nat Rev Endocrinol* **2012**, *8* (12), 728-742.
15. Mafong, D. D.; Henry, R. R., Exenatide as a treatment for diabetes and obesity: implications for cardiovascular risk reduction. *Curr Atheroscler Rep* **2008**, *10* (1), 55-60.

16. DeFronzo, R. A.; Ratner, R. E.; Han, J.; Kim, D. D.; Fineman, M. S.; Baron, A. D., Effects of Exenatide (Exendin-4) on Glycemic Control and Weight Over 30 Weeks in Metformin-Treated Patients With Type 2 Diabetes. *Diabetes Care* **2005**, *28* (5), 1092-1100.
17. David, K. I.; Jaidev, L. R.; Sethuraman, S.; Krishnan, U. M., Dual drug loaded chitosan nanoparticles-sugar-coated arsenal against pancreatic cancer. *Colloids Surf B Biointerfaces* **2015**, *135*, 689-698.
18. Kin Man Au, Y. M., Xi Tian, Longzhen Zhang, Virginia Perello, Joseph M. Caster, and Andrew Z. Wang, Improving Cancer Chemoradiotherapy Treatment by Dual Controlled Release of Wortmannin and Docetaxel in Polymeric Nanoparticles. *ACS Nano* **2015**, *9* (9), 8976-8996.
19. Kumar, G. P.; Sanganal, J. S.; Phani, A. R.; Manohara, C.; Tripathi, S. M.; Raghavendra, H. L.; Janardhana, P. B.; Amaresha, S.; Swamy, K. B.; Prasad, R. G., Anti-cancerous efficacy and pharmacokinetics of 6-mercaptopurine loaded chitosan nanoparticles. *Pharmacol Res* **2015**, *100*, 47-57.
20. Liu, Z.; Jiao, Y.; Wang, Y.; Zhou, C.; Zhang, Z., Polysaccharides-based nanoparticles as drug delivery systems. *Adv Drug Deliv Rev* **2008**, *60* (15), 1650-62.
21. Soma, C. E.; Dubernet, C.; Bentolila, D.; Benita, S.; Couvreur, P., Reversion of multidrug resistance by co-encapsulation of doxorubicin and cyclosporin A in polyalkylcyanoacrylate nanoparticles. *Biomaterials* **2000**, *21* (1), 1-7.
22. van der Ende, A. E.; Sathiyakumar, V.; Diaz, R.; Hallahan, D. E.; Harth, E., Linear release nanoparticle devices for advanced targeted cancer therapies with increased efficacy. *Polym Chem* **2010**, *1* (1), 93-96.
23. Sharma, S.; Parmar, A.; Kori, S.; Sandhir, R., PLGA-based nanoparticles: A new paradigm in biomedical applications. *Trends Analyt Chem* **2016**, *80*, 30-40.

24. Cao, L. B.; Zeng, S.; Zhao, W., Highly Stable PEGylated Poly(lactic-co-glycolic acid) (PLGA) Nanoparticles for the Effective Delivery of Docetaxel in Prostate Cancers. *Nanoscale Res Lett* **2016**, *11* (305), 1-9.
25. Chelopo, M. P.; Kalombo, L.; Wesley-Smith, J.; Grobler, A.; Hayeshi, R., The fabrication and characterization of a PLGA nanoparticle–Pheroid® combined drug delivery system. *J Mater Sci* **2016**, *52* (6), 3133-3145.
26. Guan, Q.; Sun, S.; Li, X.; Lv, S.; Xu, T.; Sun, J.; Feng, W.; Zhang, L.; Li, Y., Preparation, in vitro and in vivo evaluation of mPEG-PLGA nanoparticles co-loaded with syringopicroside and hydroxytyrosol. *J Mater Sci Mater Med* **2016**, *27* (2), 24.
27. Cannava, C.; Stancanelli, R.; Marabeti, M. R.; Venuti, V.; Cascio, C.; Guarneri, P.; C. Bongiorno; G. Sortino; D. Majolino; A. Mazzaglia; Tommasinib, S.; Ventura, C. A., Nanospheres based on PLGA/amphiphilic cyclodextrin assemblies as potential enhancers of Methylene Blue neuroprotective effect. *RSC Adv* **2016**, *6* (20), 16720–16729.
28. Locatelli, E.; Comes Franchini, M., Biodegradable PLGA-b-PEG polymeric nanoparticles: synthesis, properties, and nanomedical applications as drug delivery system. *J Nanopart Res* **2012**, *14* (1316), 1-17.
29. van der Ende, A.; Croce, T.; Hamilton, S.; Sathiyakumar, V.; Harth, E., Tailored polyester nanoparticles: post-modification with dendritic transporter and targeting units via reductive amination and thiol-ene chemistry. *Soft Matter* **2009**, *5* (7), 1417-1425.
30. Lockhart, J. N.; Stevens, D. M.; Beezer, D. B.; Kravitz, A.; Harth, E., Dual drug delivery of tamoxifen and quercetin: Regulated metabolism for anticancer treatment with nanosponges. *J Control Release* **2015**, *220*, 751-757.

31. Stevens, D. M.; Gilmore, K. A.; Harth, E., An assessment of nanosponges for intravenous and oral drug delivery of BCS class IV drugs: Drug delivery kinetics and solubilization. *Polym Chem* **2014**, *5* (11), 3551-3554.
32. Gilmore, K. A. Development of Drug Delivery Vehicles for Biomedical Applications. Dissertation, Vanderbilt University, Nashville, TN, 2017.
33. van der Ende, A. E.; Kravitz, E. J.; Harth, E., Approach to Formation of Multifunctional Polyester Particles in Controlled Nanoscopic Dimensions. *J Am Chem Soc* **2008**, *130* (27), 8706–8713.
34. Stevens, D. M., Watson, H.A., LeBlanc, M.A., Wang, R.Y., Chou, J., Bauer, W.S. & Harth, E.M. , Practical polymerization of functionalized lactones and carbonates with Sn(OTf)₂ in metal catalysed ring- opening polymerization methods. *Polym Chem* **2013**, *4* (8), 2470-2474.
35. Wang, A. Z.; Langer, R.; Farokhzad, O. C., Nanoparticle Delivery of Cancer Drugs. *Annu Rev Med* **2012**, *63* (1), 185-198.
36. Shang, L.; Nienhaus, K.; Nienhaus, G. U., Engineered nanoparticles interacting with cells: size matters. *J Nanobiotechnol* **2014**, *12* (5), 1-11.
37. Gaumet, M.; Vargas, A.; Gurny, R.; Delie, F., Nanoparticles for drug delivery: The need for precision in reporting particle size parameters. *Eur J Pharm Biopharm* **2008**, *69* (1), 1-9.
38. Babu, A.; Templeton, A. K.; Munshi, A.; Ramesh, R., Nanoparticle-Based Drug Delivery for Therapy of Lung Cancer: Progress and Challenges. *J Nanomater* **2013**, *2013* (863951), 1-11.
39. Hoshyar, N.; Gray, S.; Han, H.; Bao, G., The effect of nanoparticle size on in vivo pharmacokinetics and cellular interaction. *Nanomedicine (Lond)* **2016**, *11* (6), 673-692.

40. Hägerkvist, R.; Sandler, S.; Mokhtari, D.; Welsh, N., Amelioration of diabetes by imatinib mesylate (Gleevec®): role of β -cell NF- κ B activation and anti-apoptotic preconditioning. *FASEB J* **2007**, *21* (2), 618-628.

41. Hägerkvist, R.; Makeeva, N.; Elliman, S.; Welsh, N., Imatinib mesylate (Gleevec) protects against streptozotocin-induced diabetes and islet cell death in vitro. *Cell Biol Int* **2006**, *30* (12), 1013-1017.

CHAPTER III

Development of Collagen-Targeted Theranostic Nanosponges for Delivery of Matrix Metalloproteinase 14 Inhibitor Naphthofluorescein

III.1 Introduction

Cardiovascular disease is a major health burden and leading cause of mortality and morbidity in developed countries.¹ It is associated with atherosclerosis, or thickening of artery walls as a result of the accumulation of calcium and fatty materials (**Figure III-1**). Unstable plaque rupture in a major coronary artery is responsible for more than two-thirds of fatal myocardial infarctions.² One possibility to develop efficient therapies to stabilize the plaque is to suppress the activity of plaque matrix metalloproteinase (MMP). MMP activity has been associated with reduced collagen content³ of plaques with thin, rupture-prone fibrous caps.⁴ MMP14, a membrane type MMP, has been associated with unstable plaques⁵ and plays a pivotal role in activating

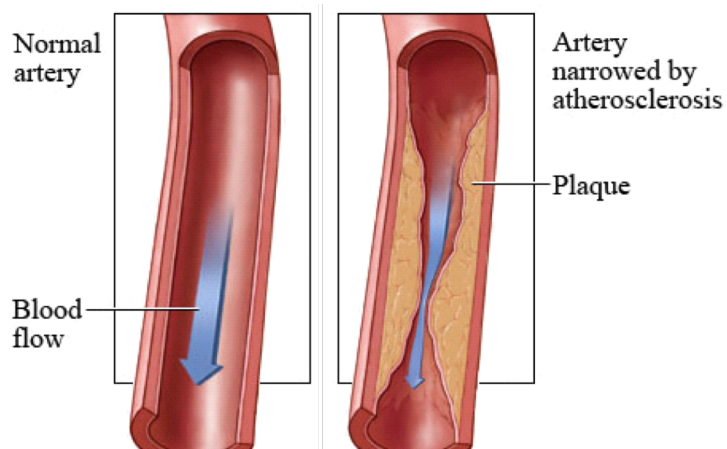


Figure III-1. Illustration of blood flow in normal artery and artery narrowed by atherosclerosis due to the accumulation of plaque.

collagen degradative activity of several other MMPs, such as MMP2⁶ and MMP9⁷. Previous human trials which systemically delivered broad spectrum MMP inhibitors, potentially targeting all 23 groups of MMPs, produced unacceptable side effects from indiscriminate MMP inhibition and off-site effects.⁸⁻⁹ The limitation with broad spectrum inhibition of MMPs in atherosclerotic plaques stems from a current incomplete understanding of the roles of MMPs in plaque stability.¹⁰ MMP14, MMP2 and MMP9 have been studied previously and associated with plaque instability but other MMPs are believed to be potentially beneficial for stable plaque remodelling.¹¹ Consequently there is an urgent need to deliver specific MMP blockers directly into the unstable plaque and tailored nanomedicine in the form of targeted nanoparticles has significant potential for this purpose.

Collagen is a major component of the extracellular matrix of plaques and forms the structural framework for stability.¹² Plaques are formed within the intima layer of the artery¹³ and collagen IV is present in abundance in the basement membrane of intima cells¹⁴ very close to the plaque, making collagen IV an ideal target. Collaborators in the Hagemeyer Research Laboratory located within the Australian Centre for Blood Diseases have developed a novel peptide (T-peptide) capable of specifically targeting and penetrating areas of degraded collagen IV. This peptide is a modified sequence of a peptide developed by Mueller et al¹⁵ known to bind to a cryptic epitope on collagen IV exposed through degradative action of MMP2 and investigate its ability as the homing agent for the delivery system. This approach has the aim to provide specific homing and delivery to areas of the plaque with collagen IV which has been weakened as the result of MMP2 activity. It was necessary to design a peptide that not only targets but also upon successful binding acts as a cell penetrating unit to shuttle the delivery system effectively into the cell to deliver the MMP inhibitor. To this end, the collagen-homing T-peptide (TLTYTWS) was linked

to an activatable cell penetrating peptide (ACPP) that is specifically cleaved by MMP2.¹⁶⁻¹⁸ Briefly, the ACPP comprises a polycationic sequence of 9 D-arginine zippered to a polyanionic sequence of 8 D-glutamic acid held together by a U-shaped peptide linker (5-amino-3-oxapentanoyl flexible hydrophilic linker) that contains an amino acid sequence of PLGC(Me)AG that is preferentially cleaved by MMP2. In this manner, the ACPP is cleaved at its peptide linker unit, releases the polycationic chain of the D-amino arginine sequence to penetrate cell membranes by its net positivity. If any payload, such as drug loaded nanoparticles, are attached to this polycationic arm it is carried along into cells.

Advantages of biodegradable polymeric nanoparticles for drug delivery include the ability to formulate insoluble pharmaceutical agents and improve the bioavailability of therapeutics.¹⁹⁻²¹ Studies indicate that physical characteristics, including nanoparticle size influence biological interactions, such as cell trafficking and accumulation,²²⁻²³ therefore the control over the nanoscopic size range are one of the necessities to develop viable candidates for drug delivery applications.²⁴ For solid tissue targeting, particles 200 nm or smaller with narrow distribution are able to take advantage of the enhanced permeation and retention (EPR) effect.²⁵ Nanoparticles 60-80 nm in size show optimum cell uptake and sustained retention time.²² Therefore, we selected a suitable delivery system of polyester nanonetworks, called nanosponges, which have been designed as cancer targeting delivery systems and show a high targeting ability and efficacy within the size range of ~100 nm.²⁶⁻²⁷ The rationale for the selection of this delivery system is in part due to the ease of the targeting peptide attachment and the post-loading ability of the carrier.²⁸⁻³⁰ The implementation of these nanosponges as a targeted theranostic nanocarrier utilizing peptide homing to deliver a drug with specific MMP inhibition into atherosclerotic plaques is envisioned to have advantages over systemic approaches and to reduce off-target side effects, increase drug

bioavailability at target sites and reduce drug administration frequencies. In this work, we report the synthesis and validation of a peptide-conjugated, dye labeled nanosponge loaded with a specific MMP14 inhibitor drug (**Figure III-2**) for the targeting and delivery to MMP degraded collagen, similar as found in atherosclerotic plaques, which demonstrated the successful uptake into the MMP2 producing HT1080 cell line and increased efficacy of naphthofluorescein treatment for enhanced collagen content *in vivo*.

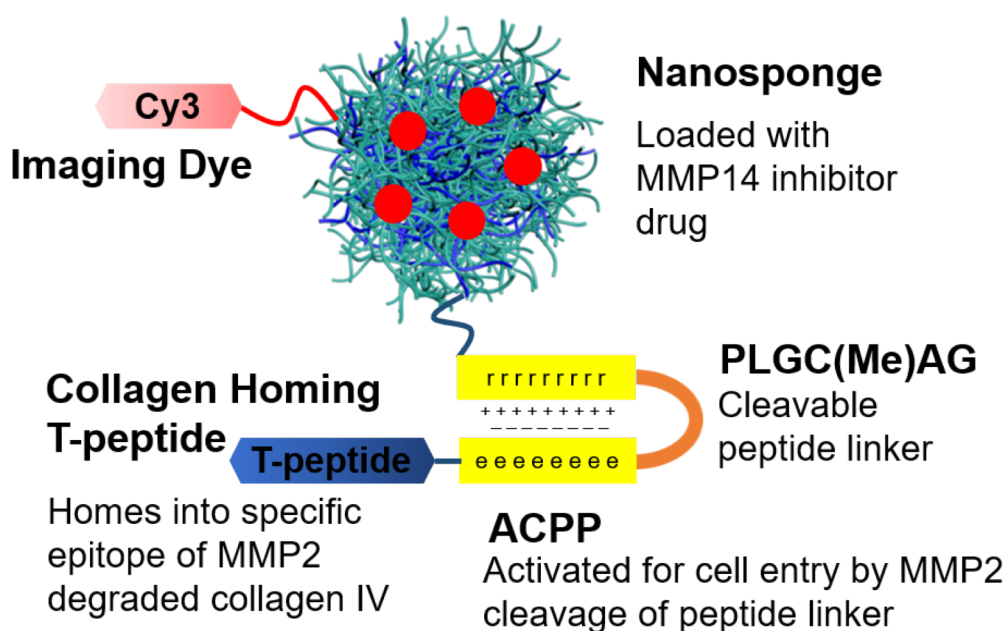


Figure III-2. Fully functionalized nanosponge construct with collagen homing T-peptide, ACPP with cleavable peptide linker by MMP2, Cyanine 3 imaging dye, and loaded with MMP14 inhibitor, naphthofluorescein.

III.2 Results and Discussion

III.2.1 Integration of T-Peptide_ACPP, Imaging Dye, and Naphthofluorescein into Targeted Nanosponge Construct

Unlike other MMPs, MMP14 activation is an intracellular process that requires furin activation. In an attempt to spare unrelated MMPs, we chose naphthofluorescein as the drug payload for the nanocarrier, a hydrophobic small molecule near infrared fluorophore that inhibits furin,³¹ as a drug to specifically stop MMP14 activation. With this, the desired nanocarrier required the integration of three functional components, the targeting peptide, imaging dye and naphthofluorescein MMP14 inhibitor, to achieve plaque-targeting specificity, environment triggered entry of payload into plaque cells, and a controlled delivery of the drug payload (**Figure III-3**).

Conjugating both peptide and imaging dye to the nanosponge surface without compromising the function of either molecule coupled with the complexity and number of functional groups present on the targeting peptide sequence presented synthetic challenges. An orthogonal design was implemented in order to retain the activity of the peptide and dye and perform a sequential conjugation to orthogonal functionalities integrated to the particle backbone. The nanocarrier was synthesized following a reported intermolecular crosslinking technique, to yield nanoparticles in desired sizes of 60-80 nm.²⁷

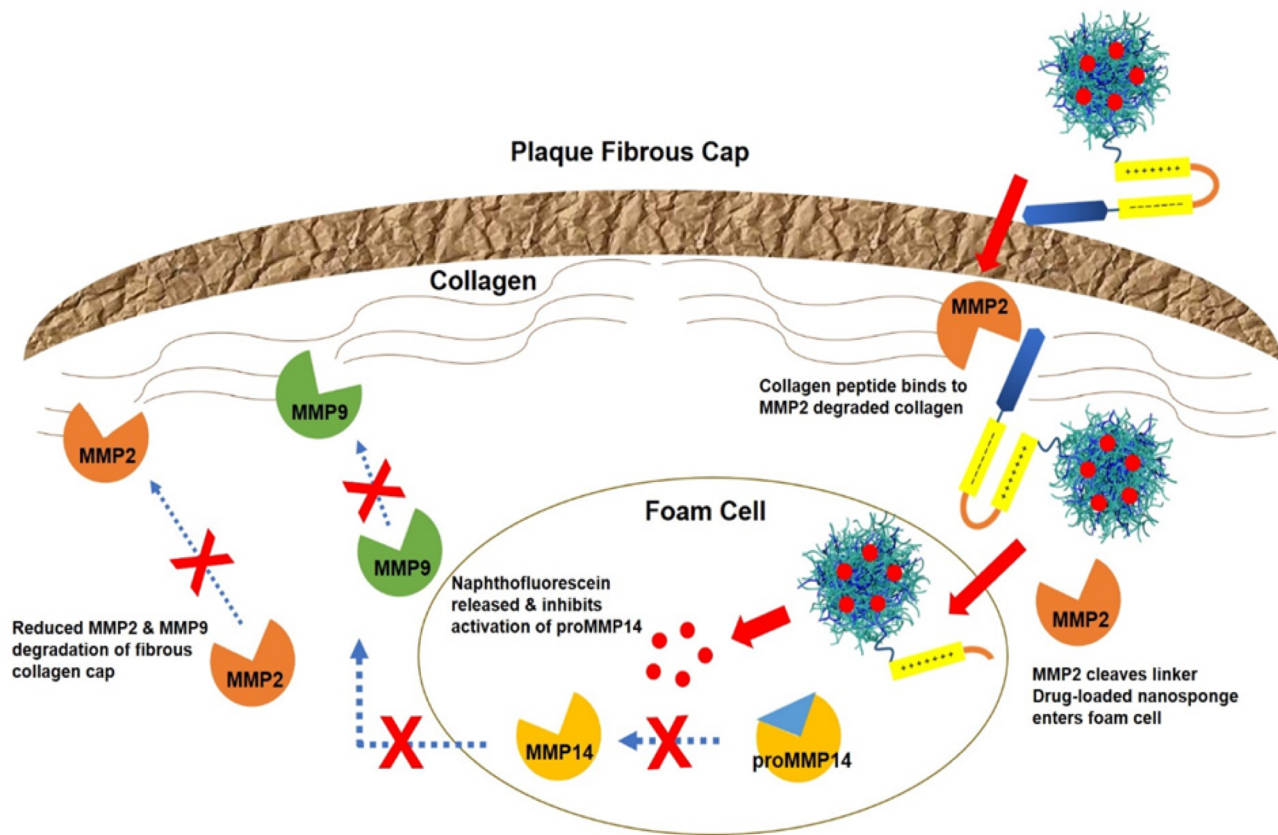
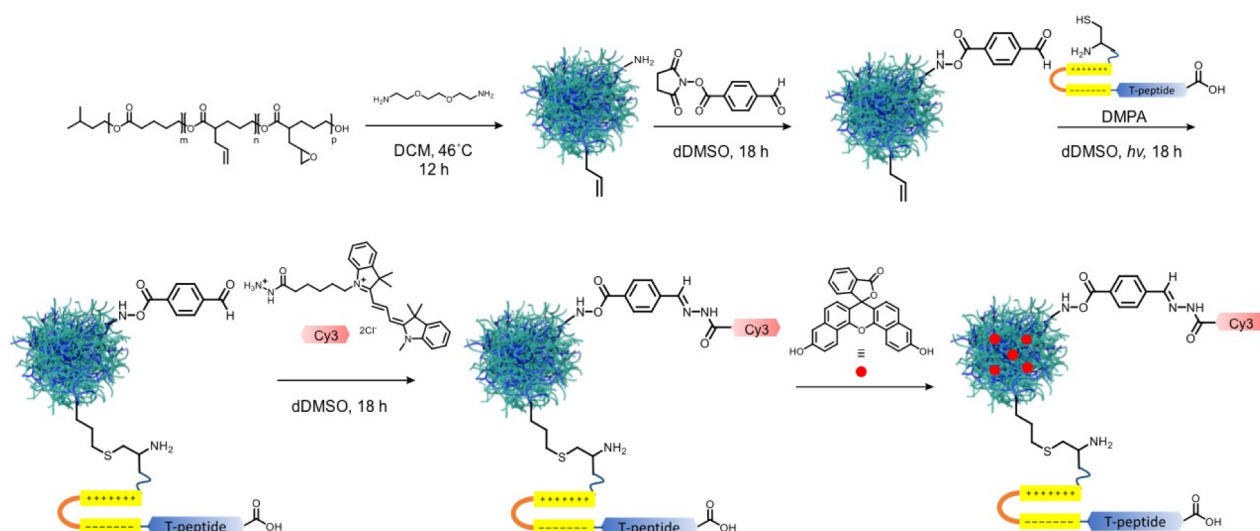


Figure III-3. Overview of mechanism of action of the targeted nanosponge drug delivery system: The collagen-homing peptide binds the MMP2 degraded collagen, followed by the cleavage of the peptide linker by MMP2. The cell penetrating polycationic peptide carries the nanosponge into the foam cells, releases the MMP14 conversion inhibitor naphthofluorescein, thereby inhibiting activation of proMMP14 and reducing the levels of plaque destabilizing MMP2 and MMP9 through preventing their activation.

III.2.2 Synthesis and Characterization of Functionalized Nanosponge with Targeting and Imaging Moieties

To begin, we prepared nanosponges according to previously reported protocols where the crosslinking chemistry involves the reaction of linear polyvalerolactone functionalized with pendant allyl and epoxide groups (**Scheme III-1**) with diamine units.²⁶ The epoxide:amine crosslinking ratio determines the size of the resulting particle and yields a particle with amine and allyl functionalities on the surface as all epoxides have been consumed. This reaction was confirmed by NMR spectroscopy analysis (**Figure III-5A**) and is in agreement with reported results for the synthesis of these nanosponge materials.^{26, 29, 32-34} Transmission electron microscopy (TEM) and dynamic light scattering (DLS) confirmed the synthesized particle for the planned study to be $(70 \pm 14 \text{ nm})$ (**Figure III-4**).

Scheme III-1. Synthesis scheme for the formation of peptide-conjugated, dye-labeled, naphthofluorescein-loaded nanosponges.



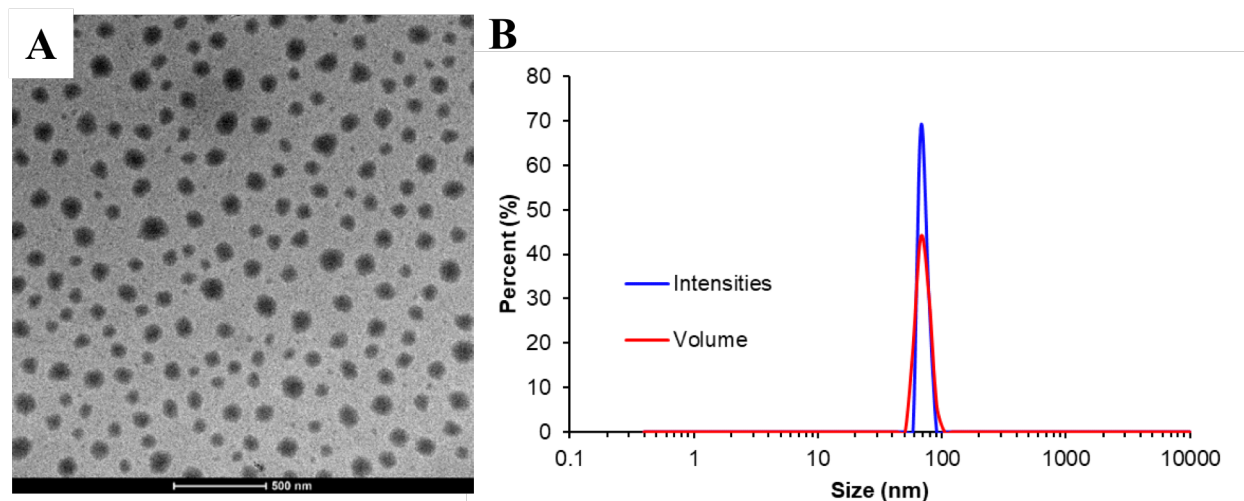


Figure III-4. Particle size analysis via A) TEM images and B) DLS measurements to validate nanospheres size of ~ 70 nm.

The solubility of the particle in organic solvents and the ability to follow conjugations to the polymer backbone by NMR spectroscopy makes the nanoparticle an ideal candidate for the proposed postmodification chemistries shown in **Scheme III-2**. For example, the allyl functionality provided a pathway to conjugate the cysteine functionalized polycationic arm of the T-peptide_ACPP sequence through thiol-ene click chemistry.³⁰ The attachment of imaging dyes is often achieved by conjugation to amine groups through NHS ester chemistries. However, the T-peptide_ACPP sequence contains amine groups and this attachment chemistry would result in labelling the particle and also the targeting peptide. Off-target dye labelling of the peptide could potentially interfere with peptide confirmation and bioactivity, so this was avoided by strategically transforming the amine functionality into an aldehyde to provide an orthogonal surface unit for the attachment of imaging dyes possessing a hydrazide functionality for conjugation (**Figure III-5B**). *N*-succinimidyl-*p*-formylbenzoate was added in an NHS-ester reaction to transform amines to aldehyde entities where the selected cyanine 3 mono hydrazide dye (Cy3) will form a hydrazone bond to exclusively label the surface of the particle (**Scheme III-1**). The synthetic pathway of the

theranostic drug delivery system after nanoparticle formation was performed by first modifying the amine functionality, followed by the attachment of the peptide and then conjugation of the dye to the installed aldehyde functionality as detailed below. In the final step, we loaded the naphthofluorescein in a modified post modification and nanosolubilization method.

In detail, the seven amino acid collagen binding peptide and the ACPD were synthesized by solid phase peptide synthesis and purified using high-performance liquid chromatography (HPLC). Next, the successful attachment of T-peptide_ACPD to the nanosponges was confirmed via ^1H NMR and quantification was determined via reduction in chemical shift at 5.04 and 5.73 ppm (**Figure III-5C**) associated with the allyl protons. The T-peptide_ACPD loading was determined to be 7.88 peptides per particle. For particle tracking *in vitro*, fluorescent cyanine 3 mono hydrazide was conjugated to the nanosponge surface via aldehyde-hydrazide click chemistry using the previously installed aldehyde moiety. The attachment of the dye to the nanosponge surface was confirmed via absence of the aldehyde chemical shift in the ^1H NMR spectra (**Figure III-5D**). In the final step, we loaded the drug of interest, naphthofluorescein, in a modified post modification and nanosolubilization method (see Experimental). Due to the experimental scale we did not precipitate the particle into water but rather washed the particle with excess cell culture water. We determined a drug loading of approximately 23 wt% using this method by HPLC detection. The resulting solution was lyophilized to obtain the full construct of peptide targeted, ACPD functionalized, drug-loaded, Cy3 fluorescent nanosponges.

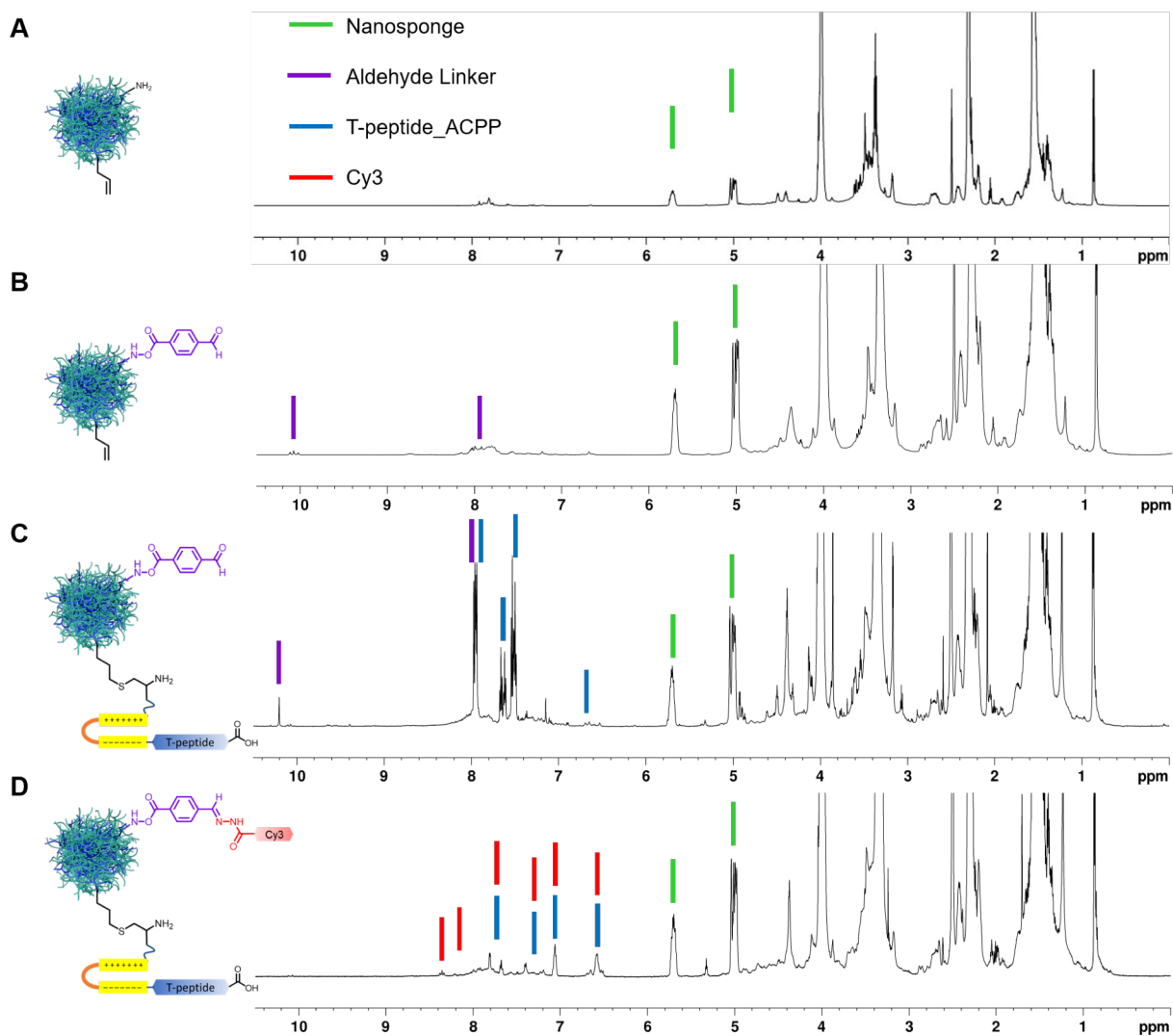


Figure III-5. NMR characterization of nanosponge attachment chemistry sequence after each step: A) nanosponge formation, B) aldehyde attachment, C) T-peptide_ACPP attachment, and D) Cy3 dye attachment.

III.2.3 *In Vitro* Biocompatibility and Cellular Uptake of Nanosponge Construct

First, to ensure biocompatibility of our targeted nanosponge system, peptide labeled empty nanosponges were incubated with RAW and HT1080 cells for 24 h at 37 °C. The results indicated high cell viability for treated cells as shown in **Figure III-6** and confirmed biocompatibility of the system. Next, using the murine fibrosarcoma HT1080 cell line, we investigated cellular uptake of the drug-loaded, peptide and dye conjugated nanosponge construct. HT1080 cells were selected for this analysis as they naturally produce several MMPs, including MMP2.³⁵ Cells were incubated overnight with T-peptide_ACPP-nanosponge construct at 37°C, the cell cytoplasm stained green and examined with confocal live cell microscopy (Nikon A1) in the FITC and TRITC channels. **Figure III-7** clearly shows that the construct had been internalized by the cells as the red signal from the cyanine dye is colocalized with the fluorescence signal from the cytoplasm (green). This internalization of the construct confirms that the conjugation to the nanosponge surface does not

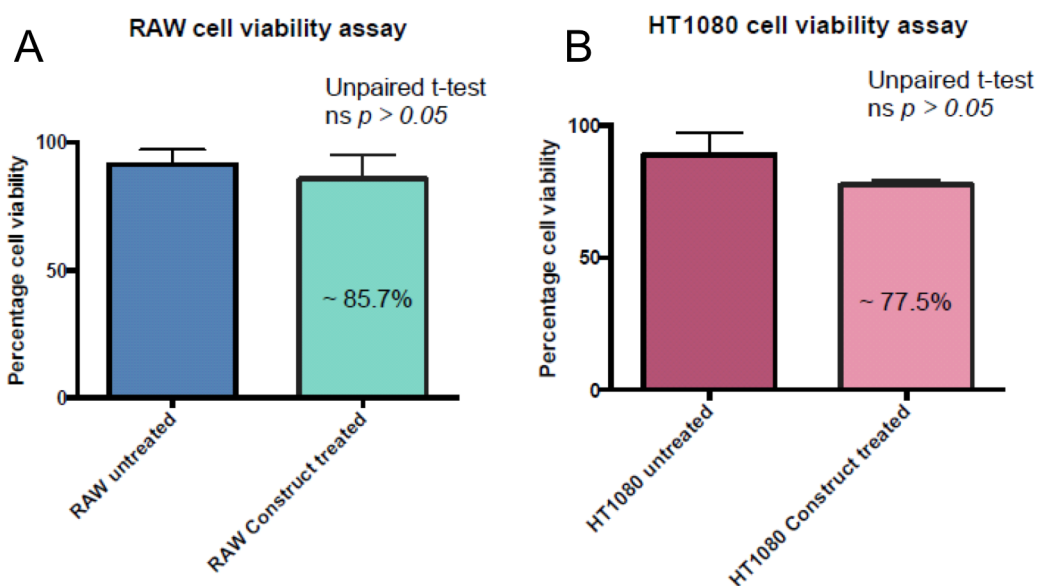


Figure III-6. Cell viability of targeted nanosponge construct in RAW and HT1080 cells to ensure biocompatibility of the nanocarrier confirmed by unpaired t-test as not significant, $p > 0.05$.

interfere with the peptide activity and the particle is successfully taken into cells along with the polycationic arm of the ACPD after cleavage of the linker from MMP2.

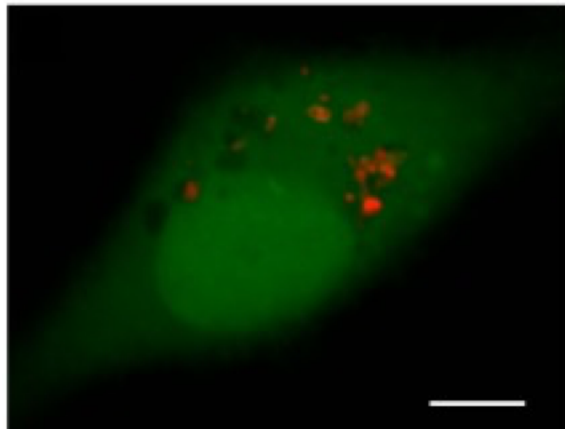


Figure III-7. Confocal microscopy of cellular uptake demonstrated by internal red fluorescence signal from dye-conjugated nanosponge construct. Scale bar = 8 μm .

III.2.4 *In Vivo* Blood Clearance and Biodistribution of Nanosponge

To evaluate the biodistribution of the nanosponge alone *in vivo*, we prepared nanosponges labelled with fluorescent imaging dye only. Animals received 7.2 μg per gram of body weight in a single injection. The blood clearance rate was monitored by amount of nanosponge left in blood stream as a function of time (**Figure III-8A**). The clearance rate of the nanosponges was approximately 10% after 2.5 min. Next, the accumulation of nanosponges was monitored at 1, 4, and 24 h in vital organs of the animals. The images in **Figure III-8C** indicate the largest accumulation of nanosponges are observed in the liver and spleen, however, after 1 h these values are quantified below 10%. At 1 h, nanosponges were distributed approximately 22% in the spleen (**Figure III-8B**). Lung accumulation at 1 h was ca. 8% then decreased to below 3% after 4 h. There is no observed accumulation in the heart and very small trace amounts in the kidney. These

results indicate a low accumulation of non-targeted nanosponges in the cardiovascular tissue which is promising for the avoidance of non-specific targeting activity of the targeted nanosponge.

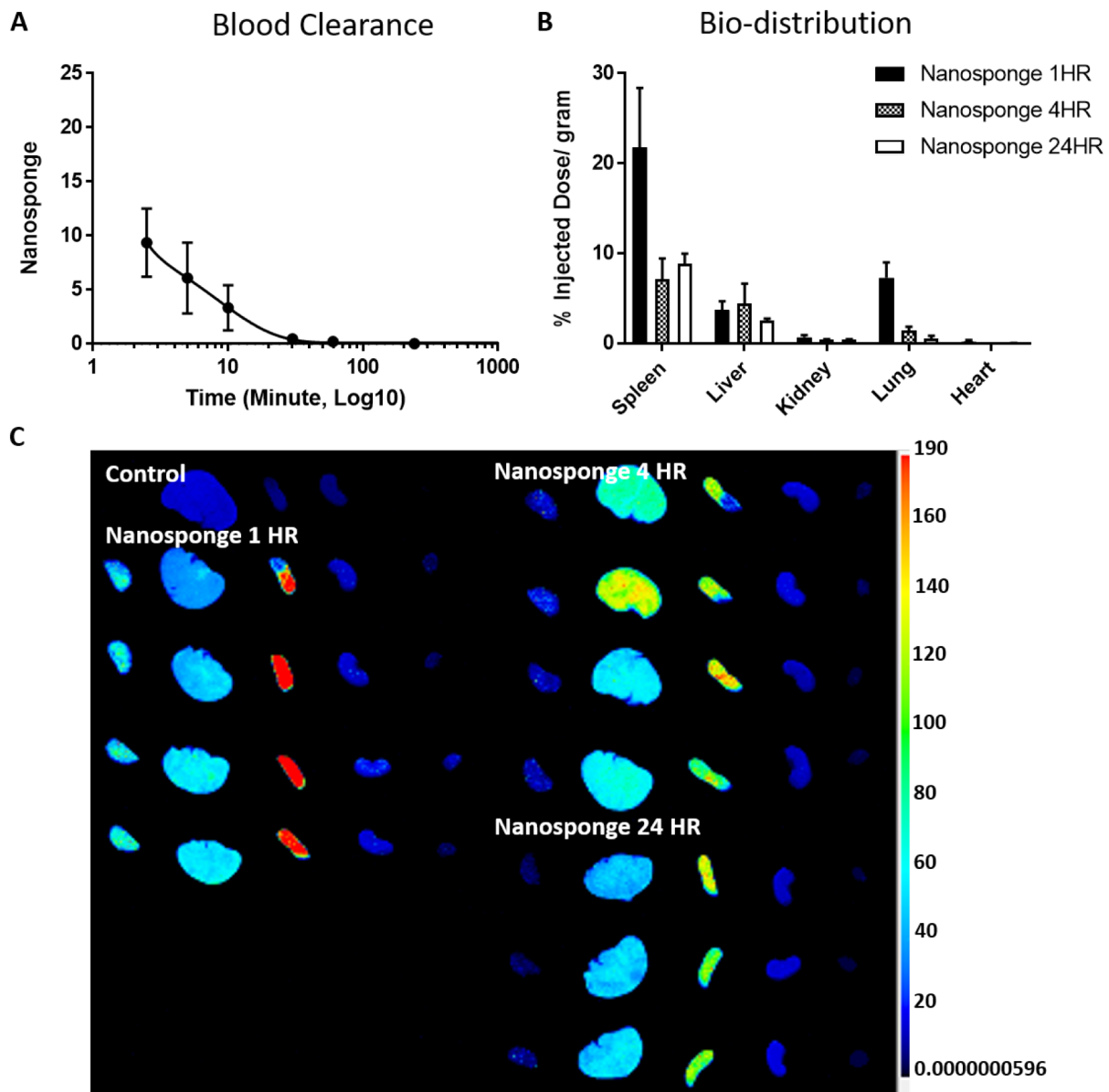


Figure III-8. *In vivo* analysis of blood clearance and biodistribution of dye-labelled empty nanosponges. A) Blood clearance of nanosponges from mice monitored by fluorescence as a function of time. B) Quantified biodistribution data at 1, 4, and 24 h indicating no accumulation of non-targeted nanosponges in cardiovascular tissue. C) Fluorescence imaging of nanosponge biodistribution of control mouse and animals at 1, 4, and 24 h for each organ: (left to right) lung, liver, spleen, kidney, heart.

III.2.5 *In Vitro* Validation of Lysosomal Escape of Nanosponge Construct

Furthermore, we investigated if the nanoparticle construct entered lysosomes when incubated with murine macrophage RAW cells. Murine RAW cells are naturally phagocytic and they also secrete MMPs, including MMP2. By incorporating the ACP that is cleaved by MMP2, we are in fact creating a nanosponge payload that has a net positive charge from the polycationic D-arginine arm attached to it once the peptide linker of the ACP is cleaved. In this manner, it provides a way for 'lysosomal escape' of the drug loaded nanosponge by proton sponge effect,³⁶ allowing the nanosponge to escape back into the cell cytoplasm through the endosomal membrane, avoiding acid degradation of the nanosponge and drug. After an overnight incubation of the Cy3 conjugated nanoparticle construct with RAW cells, the cell cytoplasm was stained with Cell Tracker Green and LysoTracker Blue (Invitrogen). As shown in **Figure III-9**, we observed no colocalization of the red and blue fluorescent signals in the RAW cells, indicating that the nanoparticle constructs have successfully escaped the cell lysosomes. **Figure III-9B** shows 3D image to confirm that the red and blue stain are not colocalized and the nanosponges are completely escaped from the lysosomes.

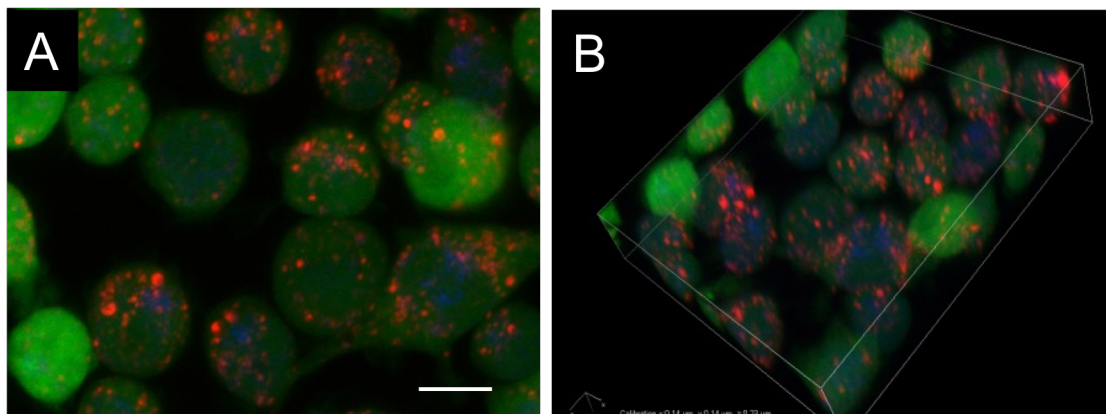


Figure III-9. A) Confocal microscopy of RAW cells to investigate lysosomes location. 2D reconstruction of Z stack confocal images of RAW cells with uptake of Cy3 (red) labeled nanosponge are shown as red dots while the lysosomes are in blue. Scale bar = 8 μ m. (B) 3D snapshot showing that the red and blue dots are spatially apart. Representative images for n=3 are shown.

III.2.6 *In Vivo* Efficacy of Naphthofluorescein-Loaded Targeted Nanocarriers for Increased Collagen Content

Finally, to investigate the effects of naphthofluorescein on the collagen content of unstable plaques, we utilized a novel tandem stenosis mouse model of unstable plaques as previously reported.³⁷ Members of the Hagemeyer group prepared these Apo E knock out mice with sutures in tandem placed at the right carotid artery after 7 weeks of high fat diet to induce formation of unstable plaques. Nanosponges were prepared for the animal study with both peptide and dye-labels with and without drug. Five weeks after the tandem stenosis, the mice received naphthofluorescein-loaded, targeted nanosponge construct with control mice receiving PBS, free naphthofluorescein, or drug-free nanosponges. Each group received a second injection of treatment material after two weeks. Following the treatment, the mice were sacrificed and the right carotid plaques were harvested for collagen quantification using Picrosirius Red stain (**Figure III-10A-D**). In the images of Figure III, the collagen (red) is quantified and the amount compared to the

other groups. The collagen amount, expressed as collagen percentage of the plaque area, revealed marked differences (**Figure III-10E**) between treated (36.88 ± 4.965 , $n=5$) and control mouse groups treated with the free drug (18.87 ± 5.308 , $n=4$), with PBS (14.40 ± 4.522 , $n=4$) and with unloaded empty nanoparticles (16.05 ± 1.994 , $n=4$). An increase in collagen content compared to the control groups can be attributed to the MMP14 inhibition by naphthofluorescein treatment. The reduction of MMP14 activity and therefore collagen degradation leads to an increased stability in the plaque. The collagen content of the targeted, drug-loaded nanocarrier shows an almost 2-fold increase over those treated with free naphthofluorescein. Moreover, there is no significant increase in the collagen content of plaque treated with empty nanospheres or PBS, as expected. These results indicate the efficacy of the naphthofluorescein was significantly improved by encapsulation in the nanosphere and delivery to the site with the targeted nanocarrier system.

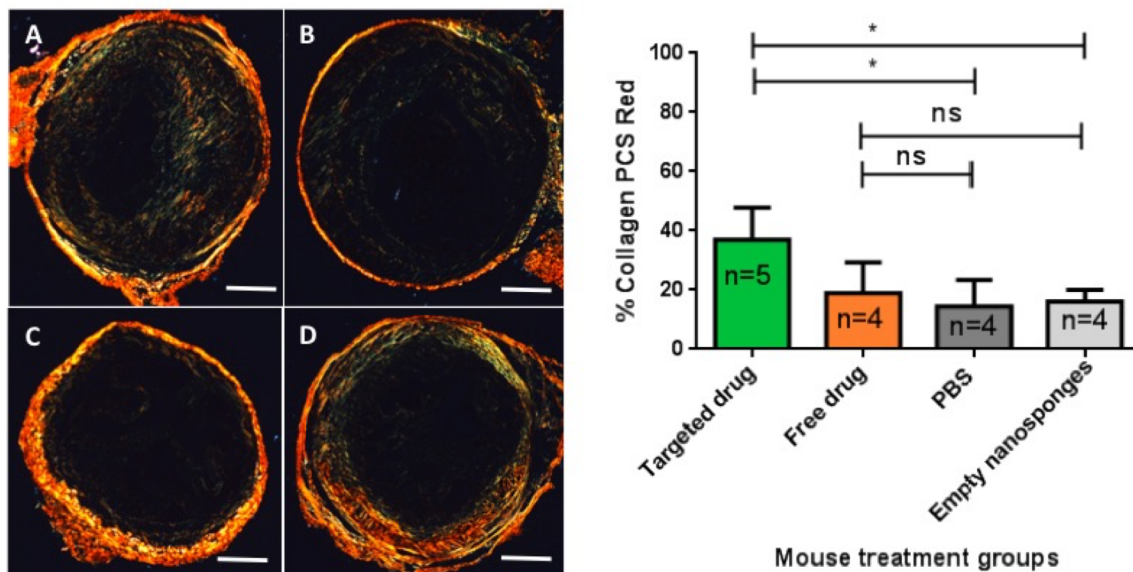


Figure III-10. Polarised light microscopy of carotid plaque section from mouse *in vivo* study (Picosirius Red stained) for (A) mouse treated with targeted drug construct and shows abundant collagen compared to control mice treated with (B) PBS, (C) free drug and (D) empty nanosphere. Scale bars = 100 μm. E) Collagen content as expressed as percentage of the plaque area showing marked differences between mouse treatment groups. Drug treated animals had a significantly higher collagen content of approximately 2-fold compared to control animals.

III.3 Conclusion

In summary, in collaboration with the Hagemeyer Research Laboratory, we have demonstrated successful labeling of a nanosponge with targeting and imaging moieties followed by a post-loading of therapeutic cargo. We have confirmed the activity of the peptide following conjugation to the nanosponge. Naphthofluorescein has been post-loaded in the nanosponge to an encapsulation capacity of 23 wt%. Additionally, we have demonstrated that such peptide-labelled nanocarrier can specifically target MMP2 degraded collagen IV found in unstable plaques and deliver drug cargo to enhance the collagen content of plaques. This study illustrates the translational capability of peptide-directed nanotechnology in biological applications and our designed construct presents great potential for the development of biologic targeted drug delivery therapeutics for the treatment of cardiovascular disease and heart attack prevention.

III.4 Experimental

Materials

All reagents, chemicals, antibodies and solvents were purchased by Bio-Rad (Hercules, CA, USA), EMD Millipore Cooperation (Billerica, MA, USA), Fisher Chemicals (New Jersey, NJ, USA), R&D Systems (Minneapolis, MN, USA), Invitrogen (Carlsbad, CA, USA) Merck (New Jersey, NJ, USA), Pierce (Rockford, IL, USA) and Sigma-Aldrich (St. Louis, MO, USA) and were used per the manufacturer's instructions. Other consumables were from the following commercial sources: Eppendorf (Westbury, NY, USA), BD Bioscience (Bedford, MA, USA), ThermoScientific (Waltham, MA). Buffers and solutions were prepared per standard protocols. δ -valerolactone and α -allyl- δ -valerolactone were purified via vacuum distillation prior to

polymerization. ACPPT-peptide was synthesized by Mei Choy in the Hagemeyer Research Group and used without further purification.

Characterization

^1H and ^{13}C NMR spectra were obtained on a Bruker AV-400 and AVII-600 MHz spectrometers. An FEI Tecnai Osiris™ transmission electron microscope operating at 200 kV in bright-field mode was used to obtain TEM images of the polymer nanoparticles. Dynamic light scattering (DLS) measurements were obtained using a Malvern Panalytical Zetasizer Nano system. High performance liquid chromatography (HPLC) analysis was conducted using a ThermoFisher Ultimate 3000 Instrument equipped with a HPG-3000SD High Pressure Mixing Gradient Pump with DAD-3000 Diode Array Detector and Phenomenex column (Luna 5 μ C18(2) 100Å, 150 x 4.6 mm, 5 μ m). Naphthofluorescein was detected at 254 nm with a 12 min gradient of 0 to 100% Buffer B with a flow rate of 1 mL/min. Buffer A consisted of water with 0.1% trifluoroacetic acid (TFA) and Buffer B was 90% acetonitrile and 10% water with 0.1% TFA. Detection of Cy 3.5 signals of the MMP14 FRET peptide were using a FLUOstar OPTIMA BMG LABTECH 96 microplate fluorescence reader standardised for optic settings of excitation 544 nm and emission 590 nm, temperature settings at 37°C, with readings taken every 10 minutes over a 120-minute duration and double orbital shaking at a width of 4 mm 1 second prior to each cycle. All confocal live cell studies were performed using the Nikon A1r + inverted microscope (Tokyo, Japan) with live cell imaging chamber (designed by Monash Micro Imaging).

Synthesis of α -Allyl- δ -Valerolactone (AVL)

Under a dry nitrogen atmosphere performed with Schlenk technique, a 2-neck 500 mL round bottom flask was charged tetrahydrofuran (THF, 156.25 mL). *N,N*-diisopropylethylamine (DIPA, 3.3 mL, 23 mmol) was added at -78 °C and stirred followed by dropwise addition of *n*-butyllithium solution (2.5 M in hexanes, 9.34 mL, 23 mmol) via cannula. The reaction stirred for 15 min and a solution of δ -valerolactone (1.97 mL, 21 mmol) in THF (56 mL) was added dropwise via cannula over 45 min. A mixture of hexamethylphosphoramide (HMPA, 4.43 mL, 25 mmol) and allyl bromide (2.02 mL, 23 mmol) was then added to the reaction dropwise via cannula and stirred for 15 min. The reaction was allowed to warm to -40 °C and stirred for 2 h. The reaction was then warmed to -10 °C and quenched with sat. ammonium chloride solution (150 mL). The solid salt was removed by filtration and the volatiles removed by evaporation. The concentrated product was extracted with dichloromethane (DCM) and dried with magnesium sulfate (MgSO₄). The product was purified via column chromatography with a gradient of 3-29% ethyl acetate in hexanes over 5 column volumes. (2.07 g, 71%) ¹H NMR (CDCl₃, 400 MHz): δ 5.75 (m, 1H), 5.06 (m, 2H), 4.26 (m, 2H), 2.54 (m, 3H), 2.28 (m, 1H), 2.03 (m, 1H), 1.87 (m, 1H), 1.54 (m, 1H).

General Synthesis of Poly(δ -Valerolactone-co- α -Allyl- δ -Valerolactone-co- α -Epoxide- δ -Valerolactone) (P(VL-AVL-EVL))

A 25 mL round bottom flask equipped with stir bar was flame dried and purged with nitrogen followed by addition of tin trifluoromethanesulfonate (Sn(OTf)₂, 1.3 mg, 3.11 μ mol). Isoamyl alcohol (27.24 μ L, 0.67 mmol) and DCM (0.96 mL) were added to the flask and stirred for 5 min. α -allyl- δ -valerolactone (AVL, 300 μ L, 2.29 mmol) and δ -valerolactone (VL, 1.56 mL, 16.77

mmol) were added sequentially and stirred at room temperature for 18 h. The polymerization was quenched via addition of excess MeOH (~2 mL) then precipitated into cold MeOH to produce a white solid and dried *in vacuo*. (1 g, 50%) ($M_{n,NMR} = 3165.75 \text{ gmol}^{-1}$, VL: 91%, AVL: 9%) ^1H NMR (400 MHz, CDCl_3): δ 0.92 (6H, d, CH_3), 1.61-1.78 (m, CH_2), 2.29-2.42 (m, CH_2 , CH), 3.59-3.75 (m, CH_2), 3.99-4.10 (6H, m, CH_2), 5.04 (2H, m, CH_2) 5.73 (1H, m, CH)

In Step 2: P(VL-AVL) (200 mg, 63.2 mmol, 117.6 mmol allyl) was dissolved in DCM (1.81 mL) in a 6-dram vial with stir bar. Meta-chloroperoxybenzoic acid (mCPBA, 22.3 mg, 129.2 mmol) was dissolved in DCM (1 mL) and transferred to the reaction vial and the cap was sealed with paraffin wax. The reaction stirred at room temperature for 48 h. The organic layer was washed with saturated sodium bicarbonate (NaHCO_3) solution 3x then dried over magnesium sulfate. The polymer was dried *in vacuo* to collect a white waxy solid. (170 mg, 85%) ($M_{n,NMR} = 2972.00 \text{ gmol}^{-1}$, VL = 89%, AVL = 7%, EVL = 4%) ^1H NMR (400 MHz, CDCl_3): δ 0.92 (6H, d, CH_3), 1.61-1.78 (m, CH_2), 2.29-2.42 (m, CH_2 , CH), 2.46 (1H, s, CH_2), 2.75 (1H, s, CH_2), 2.87-2.99 (1H, d, CH), 3.59-3.75 (m, CH_2), 3.99-4.10 (6H, m, CH_2), 5.04 (2H, m, CH_2) 5.73 (1H, m, CH)

General Synthesis of P(VL-AVL-EVL) Nanosponge

Into a 100 mL round bottom flask equipped with a stir bar, poly(VL-AVL-EVL) (200.2 mg, 51.5 μmol , 0.17 mmol epoxide) and DCM (31.43 mL) were added. The reaction flask was heated to 46°C and 2,2-(ethylenedioxy)bis(ethylamine) (49.68 μL , 0.34 mmol) was added dropwise to the stirring solution. The flask was capped with a water-jacketed condenser and stirred for 12 h. The solvent was removed *in vacuo* and the nanosponges were transferred to 10K MWCO dialysis tubing and dialyzed against DCM for 48 h then collected and dried *in vacuo* (134 mg, 67%). ^1H

NMR (600 MHz, DMSO- d_6): δ 0.87 (6H, d, CH₃), 1.29-1.68 (m, CH₂, CH), 2.12-2.36 (m, CH₂, CH), 2.42 (1H, s, CH₂), 2.70 (1H, s, CH₂), 3.30-3.45 (m, CH₂), 3.45-3.63 (m, CH₂), 3.92-4.10 (6H, m, CH₂), 5.01 (2H, m, CH₂) 5.70 (1H, m, CH)

General Synthesis of Nanosponge Aldehyde-Functionalization

Under a nitrogen atmosphere, nanosponges (4.6% AVL, 4.9% EVL, 80.0 mg, 0.53 μ mol) were dissolved in a minimal amount of dimethyl sulfoxide (DMSO, 200 μ L). N-succinimidyl-p-formylbenzoate (4.0 mg, 16 μ mol) was added to the solution via microsyringe and the reaction was stirred at room temperature for 18 h. The product was purified by dialysis using 10K MWCO dialysis tubing against DCM for 24 hours. The contents of the dialysis tubing were collected and dried in vacuo (56% yield). ¹H NMR (600 MHz, DMSO- d_6): δ 0.87 (6H, d, CH₃), 1.29-1.68 (m, CH₂, CH), 2.12-2.36 (m, CH₂, CH), 2.42 (1H, s, CH₂), 2.70 (1H, s, CH₂), 3.30-3.45 (m, CH₂), 3.45-3.63 (m, CH₂), 3.92-4.10 (6H, m, CH₂), 5.01 (2H, m, CH₂) 5.70 (1H, m, CH), 7.90-8.10 (4H, m, CH), 10.20 (1H, s, CHO)

General Synthesis of T-peptide_ACPP Conjugation to Nanosponge

Under a nitrogen atmosphere, aldehyde-functionalized nanosponges (50.0 mg, 0.33 μ mol) and peptide_ACPP (21.2 mg, 3.33 μ mol) were dissolved in minimal d-DMSO (200 μ L). 2,2-dimethoxy-2-phenylacetophenone (DMPA) (1.12 mg, 4.37 μ mol) was added to the reaction mixture via microsyringe. The solution was irradiated at 365 nm and stirred at room temperature for 18 h. Peptide conjugation was quantified via reduction in resonance signal of protons associated with allyl functionality (5.01 and 5.70 ppm) through crude ¹H NMR and calculated to be 7.88

peptides per particle as described below in **Equation III-1/2**. Peptide-conjugated nanosponges were carried forward without further purification. ¹H NMR (600 MHz, DMSO-*d*₆): δ 0.87 (6H, d, CH₃), 1.29-1.68 (m, CH₂, CH), 2.12-2.36 (m, CH₂, CH), 2.42 (1H, s, CH₂), 2.70 (1H, s, CH₂), 3.30-3.45 (m, CH₂), 3.45-3.63 (m, CH₂), 3.92-4.10 (6H, m, CH₂), 5.01 (2H, m, CH₂) 5.70 (1H, m, CH), 7.40-7.50 (m, Ar H), 7.55 (t, Ar H), 7.84-7.93 (m, Ar H), 10.20 (1H, s, CHO)

$$\frac{2.92 \text{ 1H} - 2.72 \text{ 1H}}{2.92 \text{ 1H}} = 0.0685 \text{ 1H}$$

Equation III-1. The integration value from pre-conjugated nanosponge ¹H NMR allyl resonance at 5.01 ppm (2.92) was used to calculate the difference from post-conjugated nanosponge allyl resonance (2.72).

$$\frac{115.18 \text{ allyls}}{\text{nanosponge}} \times 0.068 \text{ 1H} = 7.88$$

Equation III-2. The difference (0.0685) was then multiplied by the average number of allyls per nanosponge to determine the average number of reacted allyls. This value, 7.88, is equal to the average number of peptides conjugated to the nanosponges. Peptide sequence: TLTYTWSGLASPAAPAP-eeeeeeee-(5-amino-3-oxapentanoyl)-PLGC(Me)AG-rrrrrrrrr-GAASPA

General Synthesis of Cyanine 3 Hydrazone Dye Conjugation to Nanosponge

Under a nitrogen atmosphere, peptide-functionalized nanosponges (50.0 mg, 0.33 μmol) were dissolved in dDMSO (50 μL). Cyanine3 mono-hydrazone imaging dye (1.58 mg, 2.90 μmol) was added to the reaction vial via syringe. The reaction was stirred in the absence of light at room

temperature for 18 h. The resulting mixture was purified by dialysis against a 50:50 v/v mixture acetonitrile:MeOH in 10K MWCO dialysis tubing for 48 hours with 3 solvent changes per day, then diluted in water and lyophilized to collect a powder (80% yield). Successful attachment of the dye at an equivalence of 9 dye molecules per nanosponge was verified by the absence of the aldehyde peak at 10.20 ppm. The concentration of the peptide and dye in the fully constructed material were determined to be 243.8 $\mu\text{g mg}^{-1}$ and 281.3 $\mu\text{g mg}^{-1}$ of material, respectively. ^1H NMR (600 MHz, DMSO- d_6): δ 0.87 (6H, d, CH₃), 1.29-1.68 (m, CH₂, CH), 2.12-2.36 (m, CH₂, CH), 2.42 (1H, s, CH₂), 2.70 (1H, s, CH₂), 3.30-3.45 (m, CH₂), 3.45-3.63 (m, CH₂), 3.92-4.10 (6H, m, CH₂), 5.01 (2H, m, CH₂) 5.70 (1H, m, CH), 6.54-6.77 (m, Ar H), 7.12 (m, Ar H), 7.43 (d, Ar H), 7.73 (t, Ar H), 7.86 (d, Ar H), 8.4 (t, Ar H), 10.20 (1H, s, CHO)

General Procedure for Encapsulation of Naphthofluorescein into Nanosponge

In a 1.5 mL conical centrifuge tube, naphthofluorescein (1.6 mg, 3.7 μmol), along with nanosponges (6.4 mg) were dissolved in DMSO (50 μL). The solution was vortexed until a homogeneous solution was achieved. Cell culture water containing 0.1 wt % D- α -tocopherol polyethylene glycol 1000 succinate (1.0 mg, 65.3 μmol) (1.00 mL) was added to the tube and vortexed. The solution was centrifuged at 14000 RPM for 20 min. The supernatant was decanted and cell culture water (1.00 mL) was added to the tube and vortexed again to wash the particles. The mixture was centrifuged again at 14000 RPM for 20 min, the supernatant decanted, and cell culture water (0.5 mL) added to the tube. The resulting solution was lyophilized to obtain drug-loaded nanosponges. To determine drug encapsulation, a calibration curve of naphthofluorescein was determined in 95% ACN:5% DMSO. A known amount of drug-loaded nanosponges were collected after lyophilization (avg. 6.3 mg) and solubilized in minimal DMSO (300 μL) and diluted

in ACN (1:200 and 1:100) for analysis. Naphthofluorescein was detected at 254 nm with a 12 min gradient of 0 to 100% Buffer B with a flow rate of 1 mL/min. Buffer A consisted of water with 0.1% TFA and Buffer B was 90% acetonitrile and 10% water with 0.1% TFA. HPLC analysis indicated an average drug loading of 23.48 wt %.

Confocal Imaging of Live Cells Treated with Targeted Construct

In vitro studies were performed by Mei Choy in the Hagemeyer Research Group. HT1080 murine fibrosarcoma cells and RAW murine macrophage cells were grown on Menzel-Glaser cover slips (No 1.5, 0.17 \pm 0.01 mm) with Dulbecco's Modified Eagle's Medium (DMEM) with 10% fetal calf serum, 1% L-glutamine, 1% non-essential amino acids (NEAA) and 1% penicillin/streptomycin. Cells were incubated with the targeted nanosponge labelled with Cy3 dye and loaded with naphthofluorescein overnight at 37°C with 5% CO₂. The next day, cells were counter-stained with Cell Tracker Green (Invitrogen) for 30 minutes before confocal imaging. The cell coverslip was mounted onto a confocal microscope well containing 500 μ l DMEM for live cell imaging. To locate the presence of lysosomes within the RAW murine macrophage cells, we added LysoTracker Blue (Invitrogen) 5 minutes prior to confocal imaging. To determine the nanoparticle localisation and movement, fluorescent and transmitted light images were collected using a Nikon A1r+ confocal microscope (Tokyo, Japan); equipped with 60x Water Immersion objective (Nikon 60x Plan Apo VC, WI NA 1.2). Images were collected with the 405, 488 and 568 lasers sequentially to minimise bleed through.

Evaluation of T-peptide_ACPP-Nanosponge Associated Cell Toxicity

RAW and HT1080 cells were cultured and cytotoxicity analysis was performed by Mei Choy in the Hagemeyer Research Group. A 6 well plate was seeded with RAW cells and HT1080 cells (120,000 cells each) and topped up with 2 ml complete DMEM media. 50 μ L of T-peptide_ACPP-Cy3 labelled nanosponge (1 mg/ml construct concentration) was added per well and the cells were cultured in a cell incubator at 37 °C for 5 days. Without discarding used media in the wells, adherent cells were scraped gently to dislodge and aspirated into 15 ml Falcon tubes and spun down at 400 rcf for 5 minutes. Then the supernatant was discarded and the cell pellet was resuspended with 1 ml of fresh DMEM. Cell counting was performed using a hemocytometer and 50,000 of each type of cell were put into each well on a 96 well plate. After adding 10 μ L of the alamarBlue® reagent into each well, the microplate was incubated for 2 hours at 37 °C. After that, the 96 well plate was scanned in a colorimetric plate reader (Biorad Benchmark Plus microplate spectrometer) at 570 nm absorbance.

In Vivo Efficacy of Naphthofluorescein-Loaded, Peptide-Labelled Nanocarrier

Animals were prepared for the *in vivo* targeting study by Mei Choy in the Hagemeyer Research Group. Apo E knock out mice received two injections each, two weeks apart of one of four treatment groups: naphthofluorescein-loaded nanosponges containing T-peptide and a Cy3 imaging dye (1.25 mg particles, 14.0 wt% naphthofluorescein), nanoparticles alone (1.06 mg), PBS, and free naphthofluorescein (0.17 mg). Mice were then sacrificed, and their plaques were harvested and subsequently stained for collagen content using both Picrosirius Red and Masons Trichrome staining.

Statistical Analysis

All quantitative data is analyzed by PRISM 6 (GraphPad Software Inc.) and reported as mean \pm one standard deviation. Statistical analysis was performed using ANOVA followed by Tukey's multiple comparison test; with $p < 0.05$ considered statistically significant.

III.5 References

1. Go, A. S.; Mozaffarian, D.; Roger, V. L.; Benjamin, E. J.; Berry, J. D.; Blaha, M. J.; Dai, S.; Ford, E. S.; Fox, C. S.; Franco, S.; Fullerton, H. J.; Gillespie, C.; Hailpern, S. M.; Heit, J. A.; Howard, V. J.; Huffman, M. D.; Judd, S. E.; Kissela, B. M.; Kittner, S. J.; Lackland, D. T.; Lichtman, J. H.; Lisabeth, L. D.; Mackey, R. H.; Magid, D. J.; Marcus, G. M.; Marelli, A.; Matchar, D. B.; McGuire, D. K.; Mohler, E. R.; Moy, C. S.; Mussolino, M. E.; Neumar, R. W.; Nichol, G.; Pandey, D. K.; Paynter, N. P.; Reeves, M. J.; Sorlie, P. D.; Stein, J.; Towfighi, A.; Turan, T. N.; Virani, S. S.; Wong, N. D.; Woo, D.; Turner, M. B., Heart Disease and Stroke Statistics—2014 Update: A Report From the American Heart Association. *Circulation* **2014**, *129* (3), e28-e292.
2. Lafont, A., Basic aspects of plaque vulnerability. *Heart* **2003**, *89* (10), 1262-1267.
3. Schneider, F.; Sukhova, G. K.; Aikawa, M.; Canner, J.; Gerdes, N.; Tang, S.-M. T.; Shi, G.-P.; Apte, S. S.; Libby, P., Matrix Metalloproteinase-14 Deficiency in Bone Marrow-Derived Cells Promotes Collagen Accumulation in Mouse Atherosclerotic Plaques. *Circulation* **2008**, *117* (7), 931-936.
4. Suh, W. M.; Seto, A. H.; Margey, R. J. P.; Cruz-Gonzalez, I.; Jang, I.-K., Intravascular Detection of the Vulnerable Plaque. *Circ: Cardiovasc Imaging* **2011**, *4* (2), 169-178.

5. Johnson, J. L.; Sala-Newby, G. B.; Ismail, Y.; Aguilera, C. M.; Newby, A. C., Low Tissue Inhibitor of Metalloproteinases 3 and High Matrix Metalloproteinase 14 Levels Defines a Subpopulation of Highly Invasive Foam-Cell Macrophages. *Arterioscler, Thromb, Vasc Biol* **2008**, *28* (9), 1647-1653.
6. Sato, H.; Takino, T.; Okada, Y.; Cao, J.; Shinagawa, A.; Yamamoto, E.; Seiki, M., A matrix metalloproteinase expressed on the surface of invasive tumour cells. *Nature* **1994**, *370* (6484), 61-65.
7. Ohuchi, E.; Imai, K.; Fujii, Y.; Sato, H.; Seiki, M.; Okada, Y., Membrane Type 1 Matrix Metalloproteinase Digests Interstitial Collagens and Other Extracellular Matrix Macromolecules. *J Biol Chem* **1997**, *272* (4), 2446-2451.
8. Rosenbaum, E.; Zahurak, M.; Sinibaldi, V.; Carducci, M. A.; Pili, R.; Laufer, M.; DeWeese, T. L.; Eisenberger, M. A., Marimastat in the Treatment of Patients with Biochemically Relapsed Prostate Cancer: A Prospective Randomized, Double-Blind, Phase I/II Trial. *Clin Cancer Res* **2005**, *11* (12), 4437-4443.
9. Coussens, L. M.; Fingleton, B.; Matrisian, L. M., Matrix Metalloproteinase Inhibitors and Cancer—Trials and Tribulations. *Science* **2002**, *295* (5564), 2387-2392.
10. Johnson, J. L.; Fritsche-Danielson, R.; Behrendt, M.; Westin-Eriksson, A.; Wennbo, H.; Herslof, M.; Elebring, M.; George, S. J.; McPheat, W. L.; Jackson, C. L., Effect of broad-spectrum matrix metalloproteinase inhibition on atherosclerotic plaque stability. *Cardiovasc Res* **2006**, *71* (3), 586-595.
11. Johnson, J. L., Matrix metalloproteinases: influence on smooth muscle cells and atherosclerotic plaque stability. *Expert Rev Cardiovasc Ther* **2007**, *5* (2), 265-282.

12. Katsuda, S.; Okada, Y.; Minamoto, T.; Oda, Y.; Matsui, Y.; Nakanishi, I., Collagens in human atherosclerosis. Immunohistochemical analysis using collagen type-specific antibodies. *Arterioscler, Thromb, Vasc Biol* **1992**, *12* (4), 494-502.
13. Libby, P.; Ridker, P. M.; Hansson, G. K., Progress and challenges in translating the biology of atherosclerosis. *Nature* **2011**, *473* (7347), 317-325.
14. LeBleu, V. S.; MacDonald, B.; Kalluri, R., Structure and Function of Basement Membranes. *Exp Biol Med* **2007**, *232* (9), 1121-1129.
15. Mueller, J.; Gaertner, F. C.; Blechert, B.; Janssen, K.-P.; Essler, M., Targeting of Tumor Blood Vessels: A Phage-Displayed Tumor-Homing Peptide Specifically Binds to Matrix Metalloproteinase-2-Processed Collagen IV and Blocks Angiogenesis In vivo. *Mol Cancer Res* **2009**, *7* (7), 1078-1085.
16. Jiang, T.; Olson, E. S.; Nguyen, Q. T.; Roy, M.; Jennings, P. A.; Tsien, R. Y., Tumor imaging by means of proteolytic activation of cell-penetrating peptides. *Proc Natl Acad Sci USA* **2004**, *101* (51), 17867-17872.
17. Olson, E. S.; Jiang, T.; Aguilera, T. A.; Nguyen, Q. T.; Ellies, L. G.; Scadeng, M.; Tsien, R. Y., Activatable cell penetrating peptides linked to nanoparticles as dual probes for in vivo fluorescence and MR imaging of proteases. *Proc Natl Acad Sci USA* **2010**, *107* (9), 4311-4316.
18. Olson, E. S.; Whitney, M. A.; Friedman, B.; Aguilera, T. A.; Crisp, J. L.; Baik, F. M.; Jiang, T.; Baird, S. M.; Tsimikas, S.; Tsien, R. Y.; Nguyen, Q. T., In vivo fluorescence imaging of atherosclerotic plaques with activatable cell-penetrating peptides targeting thrombin activity. *Integr Biol* **2012**, *4* (6), 595-605.

19. Nagavarma, B.; Yadav, H. K.; Ayaz, A.; Vasudha, L.; Shivakumar, H., Different techniques for preparation of polymeric nanoparticles-a review. *Asian J Pharm Clin Res* **2012**, *5* (3), 16-23.
20. Panyam, J.; Labhasetwar, V., Biodegradable nanoparticles for drug and gene delivery to cells and tissue. *Adv Drug Deliv Rev* **2003**, *55* (3), 329-347.
21. Soppimath, K. S.; Aminabhavi, T. M.; Kulkarni, A. R.; Rudzinski, W. E., Biodegradable polymeric nanoparticles as drug delivery devices. *J Control Release* **2001**, *70* (1), 1-20.
22. Wang, A. Z.; Langer, R.; Farokhzad, O. C., Nanoparticle Delivery of Cancer Drugs. *Annu Rev Med* **2012**, *63* (1), 185-198.
23. Shang, L.; Nienhaus, K.; Nienhaus, G. U., Engineered nanoparticles interacting with cells: size matters. *J Nanobiotechnol* **2014**, *12* (5), 1-11.
24. Gaumet, M.; Vargas, A.; Gurny, R.; Delie, F., Nanoparticles for drug delivery: The need for precision in reporting particle size parameters. *Eur J Pharm Biopharm* **2008**, *69* (1), 1-9.
25. Babu, A.; Templeton, A. K.; Munshi, A.; Ramesh, R., Nanoparticle-Based Drug Delivery for Therapy of Lung Cancer: Progress and Challenges. *J Nanomater* **2013**, *2013* (863951), 1-11.
26. Passarella, R. J.; Spratt, D. E.; van der Ende, A. E.; Phillips, J. G.; Wu, H.; Sathiyakumar, V.; Zhou, L.; Hallahan, D. E.; Harth, E.; Diaz, R., Targeted Nanoparticles That Deliver a Sustained, Specific Release of Paclitaxel to Irradiated Tumors. *Cancer Res.* **2010**, *70* (11), 4550-4559.
27. van der Ende, A. E.; Kravitz, E. J.; Harth, E., Approach to Formation of Multifunctional Polyester Particles in Controlled Nanoscopic Dimensions. *J Am Chem Soc* **2008**, *130* (27), 8706–8713.

28. Hariri, G.; Edwards, A. D.; Merrill, T. B.; Greenbaum, J. M.; van der Ende, A. E.; Harth, E., Sequential Targeted Delivery of Paclitaxel and Camptothecin Using a Cross-Linked “Nanosponge” Network for Lung Cancer Chemotherapy. *Mol Pharmaceutics* **2014**, *11* (1), 265-275.
29. van der Ende, A. E.; Sathiyakumar, V.; Diaz, R.; Hallahan, D. E.; Harth, E., Linear release nanoparticle devices for advanced targeted cancer therapies with increased efficacy. *Polym Chem* **2010**, *1* (1), 93-96.
30. van der Ende, A.; Croce, T.; Hamilton, S.; Sathiyakumar, V.; Harth, E., Tailored polyester nanoparticles: post-modification with dendritic transporter and targeting units via reductive amination and thiol-ene chemistry. *Soft Matter* **2009**, *5* (7), 1417-1425.
31. Jiao, G.-S.; Cregar, L.; Wang, J.; Millis, S. Z.; Tang, C.; O'Malley, S.; Johnson, A. T.; Sareth, S.; Larson, J.; Thomas, G., Synthetic small molecule furin inhibitors derived from 2,5-dideoxystreptamine. *Proc Natl Acad Sci USA* **2006**, *103* (52), 19707-19712.
32. Subramanian, S.; Anandam, S.; Kannan, K.; Rajappan, M., Nanosponges: A Novel Class of Drug Delivery System - Review. *J Pharm Pharm Sci* **2012**, *15*, 103-11.
33. Stevens, D. M.; Gilmore, K. A.; Harth, E., An assessment of nanosponges for intravenous and oral drug delivery of BCS class IV drugs: Drug delivery kinetics and solubilization. *Polym Chem* **2014**, *5* (11), 3551-3554.
34. Lockhart, J. N.; Stevens, D. M.; Beezer, D. B.; Kravitz, A.; Harth, E., Dual drug delivery of tamoxifen and quercetin: Regulated metabolism for anticancer treatment with nanosponges. *J Control Release* **2015**, *220*, 751-757.
35. Stanton, H.; Gavrilovic, J.; Atkinson, S. J.; d'Ortho, M. P.; Yamada, K. M.; Zardi, L.; Murphy, G., The activation of ProMMP-2 (gelatinase A) by HT1080 fibrosarcoma cells is

promoted by culture on a fibronectin substrate and is concomitant with an increase in processing of MT1-MMP (MMP-14) to a 45 kDa form. *J Cell Sci* **1998**, *111* (18), 2789-2798.

36. Khalil, I. A.; Kogure, K.; Akita, H.; Harashima, H., Uptake Pathways and Subsequent Intracellular Trafficking in Nonviral Gene Delivery. *Pharmacol Rev* **2006**, *58* (1), 32-45.

37. Chen, Y.-C.; Bui, A. V.; Diesch, J.; Manasseh, R.; Hausding, C.; Rivera, J.; Haviv, I.; Agrotis, A.; Htun, N. M.; Jowett, J.; Hagemeyer, C. E.; Hannan, R. D.; Bobik, A.; Peter, K., A Novel Mouse Model of Atherosclerotic Plaque Instability for Drug Testing and Mechanistic/Therapeutic Discoveries Using Gene and MicroRNA Expression Profiling. *Circ Res* **2013**, *113* (3), 252-265.

CHAPTER IV

Nanonetworks in Controlled Dimensions via Backbone Ketoxime and Alkoxyamine Crosslinks for Controlled Release

IV.1 Introduction

The broader application and implementation of nanoparticle delivery systems in the medical and pharmaceutical field is mostly hindered by the challenges of synthetic approaches to provide robust and practical chemistries without limiting the medical function and efficacy of the final carrier. In the past years, an abundance of delivery strategies have been developed, reaching from core-shell polymersomes,¹⁻³ liposomes,⁴ micellar systems,⁵⁻⁶ star polymers⁷⁻⁹ to polymeric prodrugs,¹¹⁻¹² protein-drug conjugates¹³ and aggregates¹⁴ and self-assembled polymer nanoparticle systems¹⁵. However, it has been shown that one of the most successful delivery systems such as Abraxane®, paclitaxel albumin-bound particles,¹⁶⁻¹⁷ are produced in a facile process while the overall efficacy of the paclitaxel drug is only doubled. This example makes it evident that rapid and inexpensive synthetic procedures are crucial and are chosen over delivery systems in which the synthetic approach is too costly.

Our previous work has focused on a polymeric nanonetwork system, called “nanosponge”, in which a nanonetwork is tailored in its density and size by reacting a linear polyester containing pendant functionalities with a difunctional crosslinking unit.¹⁸ We demonstrate that the percentage of the functional unit in the linear polyester and the amount of the crosslinker in the reaction can

be directly correlated to the produced dimension and the density of the nanonetwork which determines the degradation and drug release profiles of these particles.¹⁹⁻²⁰ In this one-pot method, we could provide degradable network particles in controlled size dimensions reaching from 20-800nm by just varying the concentration parameters of either the pendant functional unit in the linear polymer or by the added amount of the crosslinking entity.^{18, 21} Different crosslinking chemistries were explored, such as amine-epoxy,¹⁸ allyl –thiol,²²⁻²³ thiol-maleimide²⁴ and alkyne-azide²² click chemistries. These reactions relied on the access of pendant functional units in the polyester backbone. Particles generated through the amine-epoxy crosslinking were transformed into drug delivery systems showing a 5 times higher efficacy of paclitaxel.^{21, 25-26} An important feature of these particles is the accessibility of surface functionalization via primary amine groups for the attachment of imaging agents and allyl groups for the conjugation of targeting units by only partially converting allyl groups of the polyester precursor copolymer allyl- δ valerolactone to epoxy groups.

Next, to the ease of the particle preparation and size manipulation,²⁷ the degradation of the particles can be correlated to the network density and influences the drug release profile driven by the hydrolytic degradation of the polyester network. Furthermore, hydrophobic drug molecules can be loaded into the network after its preparation and post-modification, another advantage when choosing these nanosponges.^{18-19, 25, 28} To further expand the availability of nanosponges and working towards an even more facile synthetic process while further enhancing the degradation and drug release possibilities, we sought a crosslinking process that does not depend on pendant functional groups and their modification, but rather engages with functional groups as part of the polymer backbone. Backbone reactivity for crosslinking affords an even more practical synthesis method while simultaneously providing a high variability of particle degradation and drug release.

Oxime click chemistry has been a vital part in the preparation of biocompatible hydrogels²⁹⁻³¹ with self-healing functions,³²⁻³³ lithography materials,³⁴ or is applied in orthogonal conjugation chemistries.³⁵⁻³⁶ The reaction is compatible with aqueous and organic environments and rapidly proceeds at room temperature with high fidelity. The ketoxime bond is a reversible cleavable bond and sensitive towards pH changes and makes these connectivities attractive for controlled disassembly to direct drug release.

Moreover, the ketoxime bond can be converted into a stable non-reversible alkoxyamine bond through reduction, providing the option for tuning and postmodification. Current self-assembled nanoparticle or micelle technologies for pH responsive drug delivery systems undergo rapid release of cargo upon pH change.³⁷⁻³⁸ Our proposed system will provide more complex and tailorable relationships between stimuli-responsive connectivity and drug release while maintaining a practical synthetic design. The integration of ketone functionalities into polymer backbones is primarily conducted by copolymerization of 2-oxepane-1,5-dione (OPD), a 7-membered functionalized lactone. Wooley and coworkers³⁹ investigated the 1,4,8-trioxaspiro[4.6]-9-undecanone (TOSUO) monomer, a protected ketone⁴⁰ to form crosslinked polyester materials, applying reductive amination and amino-oxy chemistries. It was evident that reductive amination chemistries⁴¹ lead to chain scission and degradation products while amino-oxy chemistries formed inter- and intramolecular networks and gels.⁴² So called “particle-like” structures in the pre-gel solutions were observed but not further explored.

In this work, we detail the synthesis of discrete nanoparticles utilizing oxime-click chemistry to produce particles of discrete sizes and crosslinking densities. The ketoxime bond is generated from ketone functional groups integrated in the polyester backbone, to yield either pH-responsive nanonetworks or pH-stable nanoparticles with alkoxyamine bonds after

postmodification reactions. The presented two- or three-step synthetic process (**Figure IV-1**) is ideal to tune the dimension and network densities, degradation and drug release of the particles to prepare a range of delivery systems in a facile manner. The effect of the nanonetwork architecture on drug release was investigated with Brefeldin A, a natural product with a low bioavailability but high DNA fragmentation ability in leukemia and colon carcinoma cell lines.

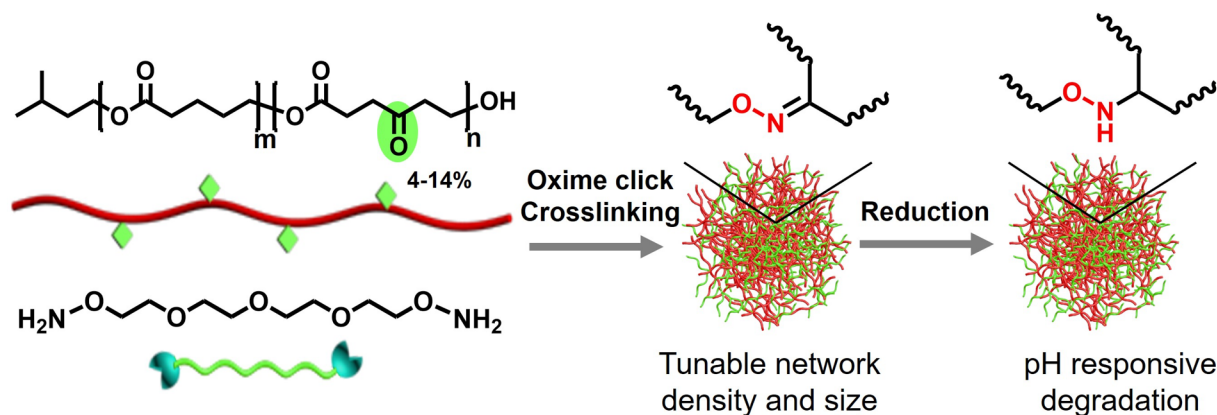


Figure IV-1. Proposed two- or three-step process for fabricating two distinct nanonetworks with controlled density, size, and degradation profiles through crosslinking of difunctionalized aminoxy PEG with linear polyester containing backbone ketone reactivity via oxime-click chemistry.

IV.2 Results and Discussion

IV.2.1 Synthesis and Characterization of Ketoxime Nanoparticles

The particles were prepared by starting with the synthesis of poly(δ -valerolactone-*co*-2-oxepane-1,5-dione) (P(VL-*co*-OPD)) via ring-opening polymerization catalyzed by $\text{Sn}(\text{OTf})_2$. OPD, first reported as a monomer for the copolymerization of polyesters by Jérôme and coworkers,⁴³ was chosen for the ability to directly copolymerize a ketone-bearing unit into the

backbone, affording a one-step polymer precursor preparation. An ideal OPD incorporation of 4-20 mol% was targeted with monomer conversion ranging 47-63% (**Table IV-1**) for all polymers. The monomer feed ratio was varied (6-30 mol%) with a molecular weight target of 4000 gmol⁻¹ to investigate the control provided by increasing the amount of crosslinking functionality throughout the polymer backbone.

Table IV-1. GPC and NMR analysis of P(VL-*co*-OPD).

Monomer Feed Ratio (VL:OPD)	% OPD _{th}	% OPD ^a	OPD conv (%)	Polymer Composition (VL:OPD)	M_n theo (g/mol)	M_n^a (g/mol)	M_n^b (g/mol)	M_w^b (g/mol)	M_w/M_n^b (g/mol)
94:6	6	3.76	63	96:4	4000	4588	3000	4000	1.31
85:15	15	7.52	50	92:8	4000	4420	2800	3900	1.39
70:30	30	14.18	47	86:14	4000	3637	2800	3600	1.31

^a% OPD and M_n determined by 400 MHz ¹H NMR in CDCl₃. ^bMolecular weight and polydispersity measured by GPC at 40 °C in THF and a flow rate of 1 mL/min using using ToSOH EcoSEC HLC-8320GPC system equipped with a refractive index detector, UV-8320 detector, and TSKgel H_{HR} columns (7.8x300mm G5000H_{HR}, G4000H_{HR}, and G3000H_{HR}).

Polymers with 4, 8, and 14 mol % OPD incorporation and molecular weights of around 4 K, 4600, 4420, and 3600 gmol⁻¹, were synthesized as nanoparticle precursors and characterized by ¹H nuclear magnetic resonance (NMR) spectroscopy and gel permeation chromatography (GPC) (**Table IV-1, Figure IV-2**). Not only the percentage of the crosslinking OPD group but also its concentration during the intermolecular crosslinking process is anticipated to have a significant effect on in particle size. To test this hypothesis, two concentrations of 2.7 and 5.4 mM were employed based on the calculated reactive monomer unit (RMU) of precursor polymers. The

higher concentration corresponds to values which were established for the reported synthesis of polyester nanosponges through epoxide-amine crosslinking chemistry, in which the relationship between crosslinker and reactive functionality concentration and particle size was invented and is unique to our polymer nanosystems,¹⁸ and the lower concentration was tested to evaluate the effect on nanoparticle size and control in nanoparticle formation.

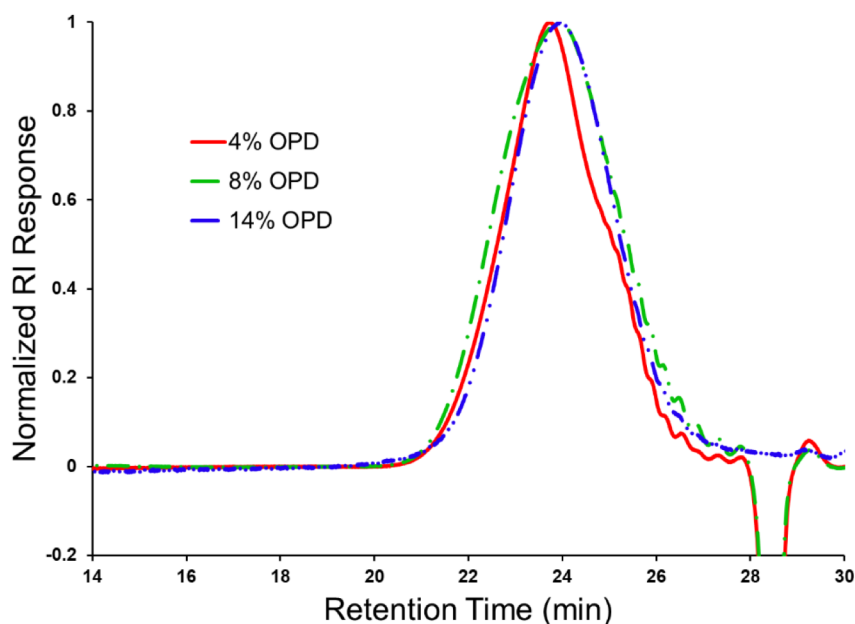


Figure IV-2. GPC traces of P(VL-co-OPD) at varying comonomer ratios, measured in THF at 40 °C with a flow rate of 1 mL/min.

With this approach, we sought to expand the current technology to a new nanoparticle system while increasing practicality and tailorability. The synthesis of the nanoparticle series was started by reacting the three polymer precursors with bis-aminoxy-PEG3 crosslinker at a 2:1 aminoxy:ketone ratio (**Figure IV-3A**). The two concentrations of the keto unit were calculated through the RMU. For example, the polymer containing 14 mol% OPD contains an average of 5 keto-bearing repeat units and has a M_n equal to 3637 g mol^{-1} , therefore the RMU for such a polymer

is 727.4 gmol^{-1} per reactive functional group. To determine the conversion of the crosslinking reactions, aliquots were taken at hourly intervals and no change in ketone conversion was observed after 2 hrs determined by ^1H NMR for the two chosen concentrations. Comparing the resonance at 2.54 ppm, which corresponds to the protons alpha and beta to the ketone unit, to the resonance of the polymer backbone set as an internal standard (**Figure IV-3B**), showed general ketone conversion of ca. 80%. Confirmation of crosslinking was determined by the reduction in intensity of the methylene protons alpha and beta to the ketone at 2.75 ppm and an increase in the resonance of the methylene protons associated with the oxime bond at 2.54 ppm (**Figure IV-3C**).

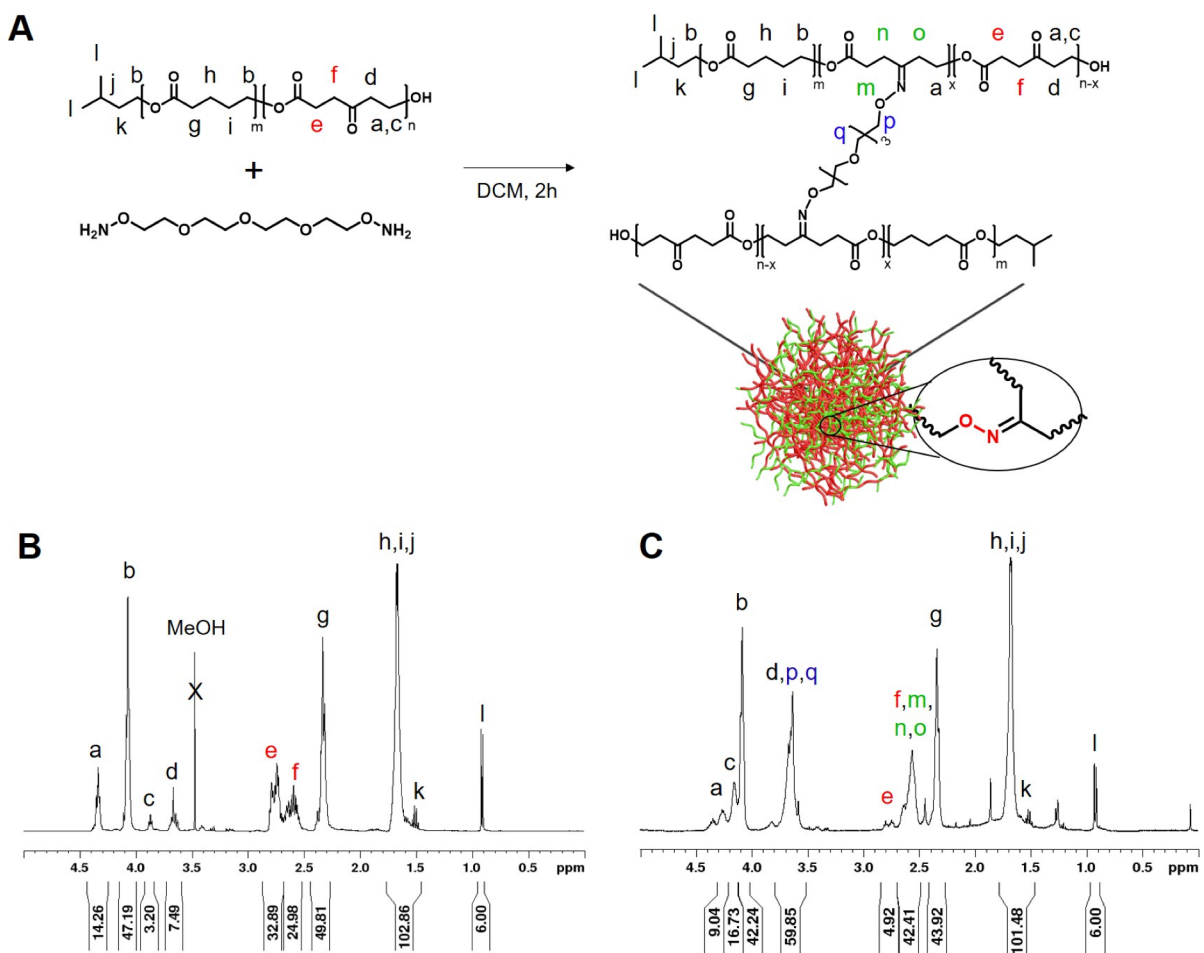


Figure IV-3. A) Synthesis scheme of ketoxime nanoparticles and ^1H NMR characterization of B) P(VL-co-OPD) and C) ketoxime nanoparticles indicating a shift in resonances associated with the ketoxime bond formation.

IV.2.2 Synthesis and Characterization of Alkoxyamine Nanoparticles

The second set of particles, containing the more stable alkoxyamine crosslink, was obtained by reduction of the ketoxime bond with sodium cyanoborohydride directly after nanoparticle formation in a 4h one-pot consecutive procedure (**Figure IV-4A**).⁴⁴⁻⁴⁵ The post-modification was confirmed via ¹H NMR by the reduced intensity at 2.75 ppm and the appearance of the chemical shift at 2.65 ppm (**Figure IV-4C**). The resulting ketoxime and alkoxyamine NPs, NP_{KO} and NP_{AA}, respectively, were purified via dialysis to average yields of 75 wt%. Mass loss

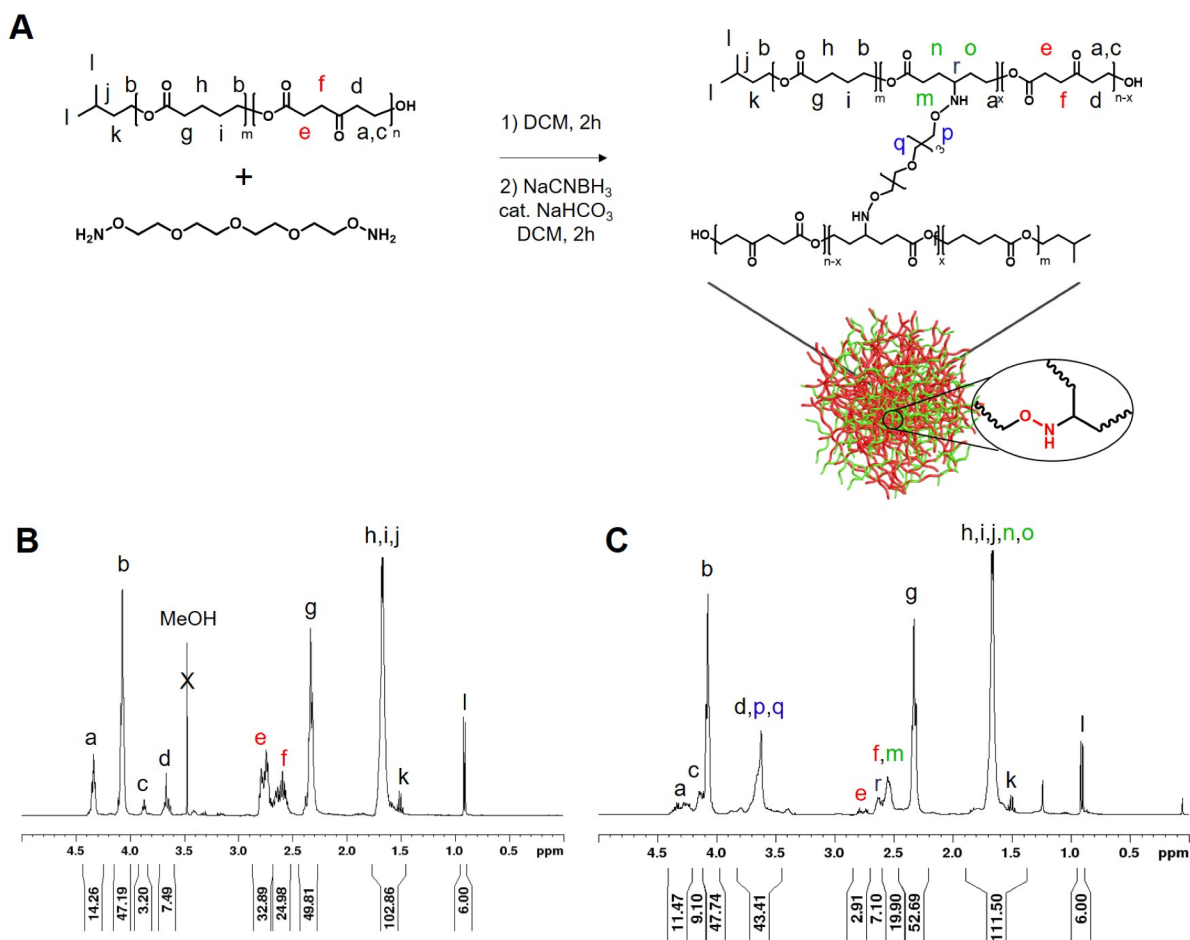


Figure IV-4. A) Synthesis scheme of alkoxyamine nanoparticles and ¹H NMR characterization of B) P(VL-co-OPD) and C) alkoxyamine nanoparticles indicating a shift in resonances associated with the reduction of the ketoxime bond.

was attributed to unreacted polymer and crosslinker removal during purification. Additionally, after purification an increase in the resonance at 3.6 ppm in both **Figure IV-3C** and **IV-4C** is attributed to the methylene protons of the PEG units and further confirms incorporation of the crosslinker.

IV.2.3 Analysis of Nanoparticle Size by Transmission Electron Microscopy, Dynamic Light Scattering, and Gel Permeation Chromatography

Successful formation of discrete nanoparticles was confirmed via transmission electron microscopy (TEM) and dynamic light scattering (DLS) (**Figure IV-5**). NP_{KO} I measured at 39 ± 10 nm in diameter and was synthesized using 4% OPD composition and 2.7 mM ketone concentration. By increasing the polymer concentration calculated for a 5.4 mM for the ketone group by using the RMU calculations, the particle size is yielded a larger diameter of 58 ± 11 nm

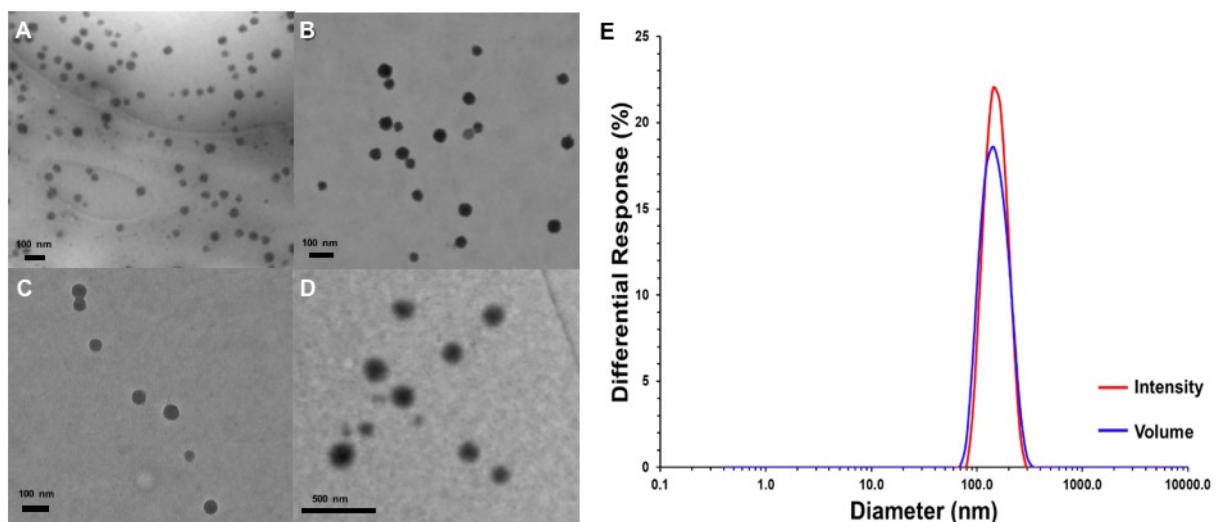


Figure IV-5. TEM images of A) 4% OPD, 2.7 mM NP_{KO} measuring 39 ± 10 nm, B) 4% OPD 5.4 mM NP_{AA} measuring 62 ± 20 nm, C) 8% OPD, 2.7 mM NP_{KO} measuring 81 ± 20 nm, and D) 14% OPD, 2.7 mM NP_{AA} measuring 143 ± 30 nm; E) representative DLS measurement of particle: ~ 165 nm in diameter.

(II). With 8% OPD, a range of ~80-140 nm was observed (III, IV). The largest NP_{KO} VI measured at 173 ± 30 nm in diameter and was synthesized with 14% OPD at a 5.4 mM ketone concentration. Similar diameters were observed in DLS (**Figure IV-6B**), and a small increase in diameter, ~20-27% was attributed to the nature of particles in solution vs. dry states. With this simple two- or three-step procedure, we have achieved a particle library with varied crosslinking density and size distribution (**Figure IV-6A**).

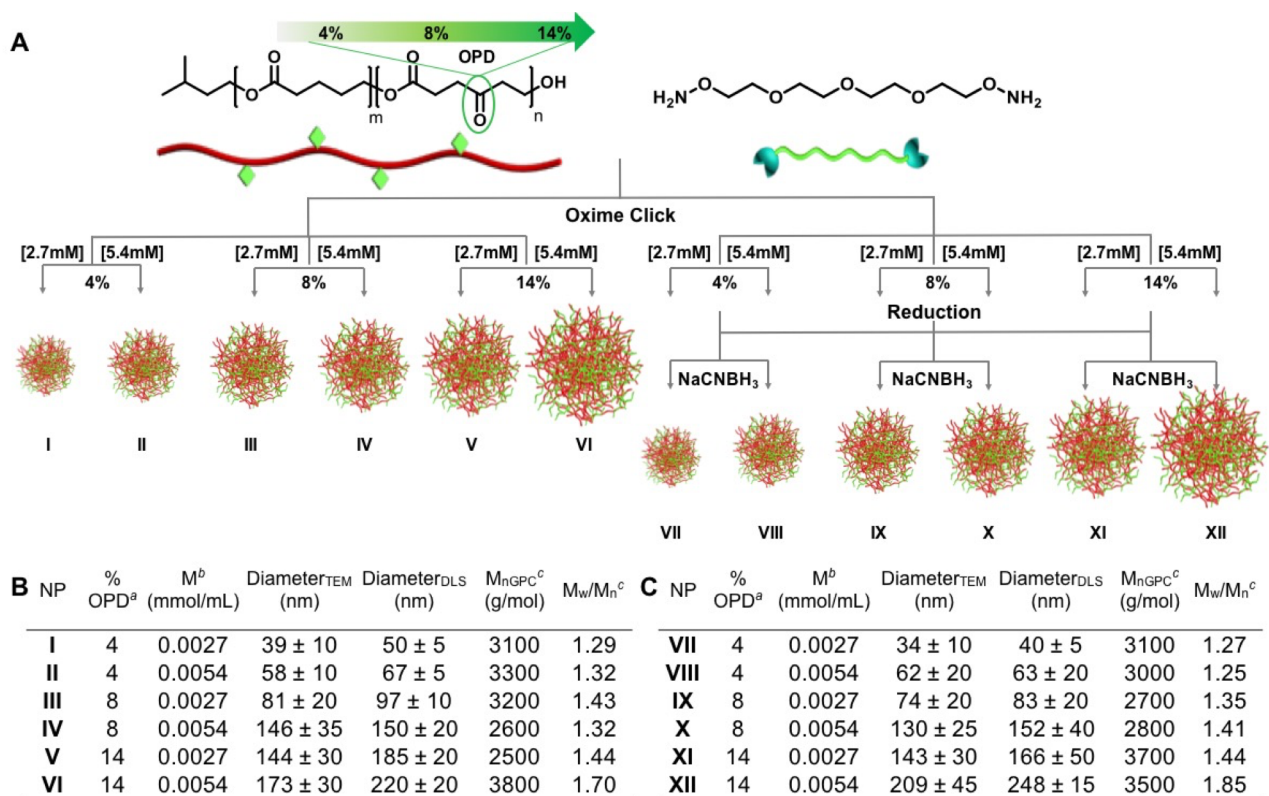


Figure IV-6. A) Schematic representation of the series of NP_{KO} and NP_{AA} with increasing size ranging from 34-209 nm by varying the OPD monomer content and keto-group concentration. Synthetic parameters (ketone concentration and composition of copolymer) of B) six NP_{KO} and C) six NP_{AA} with their resulting diameters as measured by TEM and DLS, molecular weight, and dispersity. ^aPercent functionalization of ketone monomer in the linear polyester precursor as determined by ¹H NMR integration. ^bConcentration of ketone functionality in mmol to mL of dichloromethane. ^cMolecular weight and polydispersity of NPs measured by GPC.

Analysis of NPs via GPC (**Figure IV-7**) was performed to further elucidate the relative size and distribution of these networks. The particles are soluble in organics and can be characterized by SEC methods which is in agreement with previous studies of nanosponge materials through intermolecular crosslinking processes.¹⁸ The aminoxy:ketone crosslinking ratio of 2:1 was the constant parameter throughout the series and the reactive groups per polymer were increased proportionally together with the ketone ratio, leading to the higher crosslinked nanoparticle materials. In general, a narrow Mw/Mn (~1.3-1.85) was observed throughout all particle series, in addition to shifts toward lower retention times correlated to a larger hydrodynamic radius as size and ketone ratio increased and are in agreement with TEM and DLS

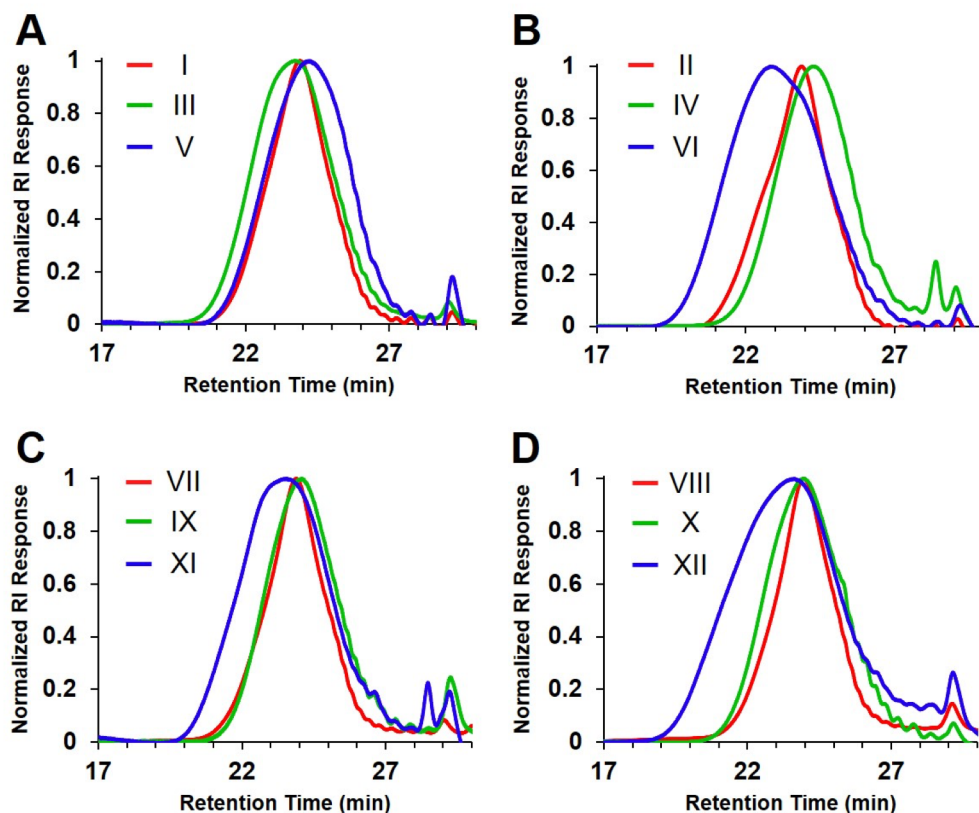


Figure IV-7. GPC analysis of nanoparticles A) I, III, and IV; B) II, IV, and VI; C) VII, IX, and XI; and D) VIII, X, XII. All GPC analysis was performed at 40 °C and a flow rate of 1 mL/min with tetrahydrofuran as eluent.

data for all particles. The symmetry of the GPC traces also indicated an even distribution in particle size across the series and is confirmed by the homogeneity of particles in TEM images (**Figure IV-5**). The particle series prepared with the higher ketone concentration (**Figure IV-7B/D**) showed a broader distribution in comparison to the other series at lower concentration (**Figure IV-7A/C**). It was also observed that particles with a high crosslinking density (VI and XII) and amino-oxy content exhibited broader distributions attributed to the increased degree of aminoxy moieties on the surface of the particle which experience hydrogen bonding between particles as observed in previous work with aminoxy functionalized polymers.⁴⁶ The smallest ketoxime NPs I and II exhibited relatively narrow dispersity ($M_n = 3100 \text{ gmol}^{-1}$, $M_w/M_n = 1.29$ and $M_n = 3300 \text{ gmol}^{-1}$, $M_w/M_n = 1.32$, respectively). The corresponding reduced particles, VII and VIII, resulted in similar narrow dispersity ($M_n = 3100 \text{ gmol}^{-1}$, $M_w/M_n = 1.27$ and $M_n = 3000 \text{ gmol}^{-1}$, $M_w/M_n = 1.25$, respectively). Consistently throughout the two series, the corresponding NP_{KO} and NP_{AA} demonstrate comparable M_n and M_w/M_n . The two largest NPs, VI and XII demonstrated the largest dispersity with $M_w/M_n = 1.70$ and 1.85 .

IV.2.4 Investigation of pH-dependent Degradation Behavior for Ketoxime and Alkoxyamine Nanoparticles

Due to the expected differences pH-responsive characteristics of these two networks, we sought to analyze the degradation patterns of both networks in acidic and neutral environments. NPs were suspended in buffer solution (pH 5.0 and 7.4) at 37°C and monitored at 48 h intervals for 10 days. Analysis of absolute molecular weight via static light scattering (SLS) was performed to determine MW of NPs at each time point and calculated as a percentage of MW remaining from

original MW determined prior to degradation studies (**Figure IV-8**). We selected the largest and the highest crosslinked nanoparticles, VI and XII for the degradation studies. We anticipated a general trend of faster degradation in low pH vs. neutral buffer, with the ketoxime-based NPs degrading at a faster rate than their alkoxyamine counterparts in both conditions. As expected,

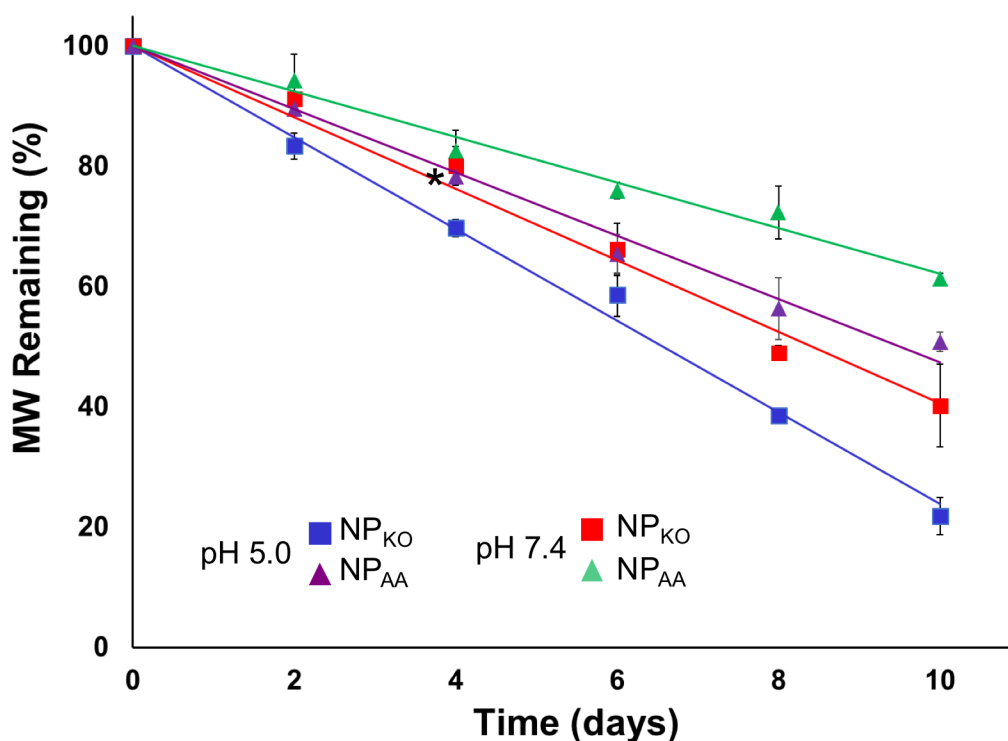


Figure IV-8. Hydrolytic degradation of 14% OPD, 5.4 mM NP_{KO} and NP_{AA} in pH 5.0 (violet and blue line) and pH 7.4 (red and green line) at 37 °C measured by absolute molecular weight via static light scattering, reported as an average of measurements in duplicate. *n=1 due to sample vial breakage prior to analysis.

NP_{KO} exhibited a faster rate of degradation than NP_{AA} in both neutral and acidic conditions due to the acid-labile nature of the oxime bond. Prior to degradation, NP_{KO} MW was determined to be 198 kDa. After 10 days of exposure to acidic buffer, MW was reduced to ~43 kDa, indicating a total mass loss of 78.16% and an average 7.82% per day. Comparatively, analysis of NP_{AA} indicated a 260 kDa starting MW, yet was only reduced to 132 kDa after 10 days in an acidic

environment. This particle exhibited a total mass loss of 49.23% and 4.92% average per day. In PBS, NP_{KO} exhibited the final MW of ~70 kDa, an average loss of 5.98% daily while NP_{AA} measurements indicated a final MW of 159.5 kDa, averaging 3.87% daily mass loss. These results indicating a tunable degradation network based on the pH and chemical nature of the crosslinks.

IV.2.5 Evaluating the pH-dependent Drug Release Performance of Ketoxime and Alkoxyamine Nanoparticles

To examine the effect of the nanostructure on the drug release, we chose Brefeldin A (BFA), a natural product that effects the function of the ER-Golgi network and leading to DNA fragmentation, a new target in the apoptosis of human cancer cell lines.⁴⁷ The drug has shown high potency in HL60 and K562 leukemia cells as well as in HT-29 colon carcinoma cells, cell lines which are p53 null.⁴⁸ Furthermore, BFA enhances the efficacy of widely used drugs such as docetaxel as tested on prostate cancer cells.⁴⁹ BFA was incorporated into the NP_{KO} III and NP_{AA} VII synthesized from 8% OPD precursor. The increased amorphous properties of the OPD containing particles required an optimization of our nanoprecipitation method that afforded a postloading of nanosponges with hydrophobic drugs (see Experimental). The drug loading was determined via HPLC analysis to be 19.6 wt% BFA with a drug loading efficiency of 98% for BFA-NP_{KO} and 13.5 wt% BFA with a 68% drug loading efficiency for BFA-NP_{AA}. The release of BFA from BFA-NP_{KO} and BFA-NP_{AA} was surveyed in identical aqueous media used in the previous degradation study with pH 5.0 and 7.4 (**Figure IV-9**).

NP_{AA} in pH 5.0 exhibited the fastest release rate of the series, releasing 50% cargo in 24 h and 100% in 7 days. Both NP_{KO} and NP_{AA} in pH 7.4 showed a medium release with similarly observed rates with NP_{AA} exhibiting a more linear trend. NP_{KO} in pH 7.4 reached 50% in 48 h and 96% in 11 days. NP_{AA} in pH 7.4 released 50% between 3-5 days and 100% between 9-11 days. These data correspond to the trends observed in the hydrolytic degradation of each particle, however, the release of BFA from NP_{KO} exhibited the slowest release of all particle systems which was not anticipated based on the prior degradation analysis. To seek a rational for contrary release kinetics of the NP_{KO} particle, we hypothesized that the particle during the degradation process yields functional groups such as amino-oxy functionalities and keto units that interact with the drug and result in an increased binding of the drug to the degrading particle. After investigating

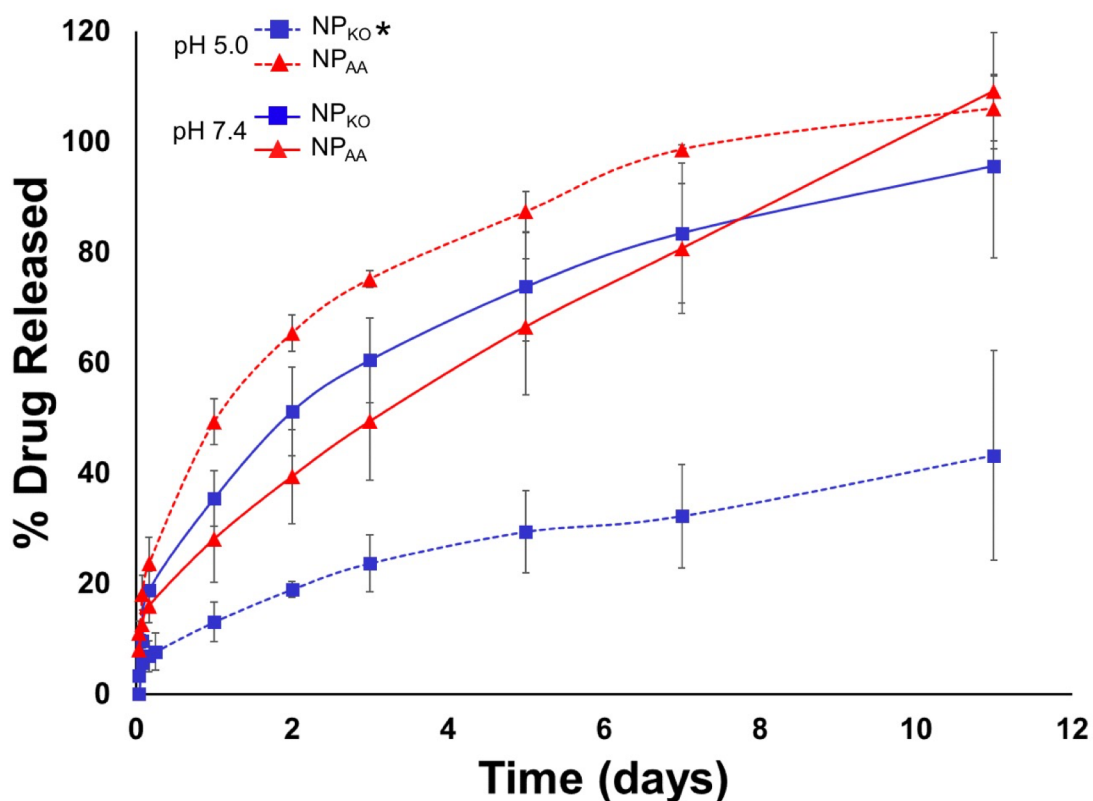


Figure IV-9. Release of BFA from 8% OPD, 2.7 mM NP_{KO}* and NP_{AA} in pH 5.0 and pH 7.4 at 37 °C over 11 days reported as an average of measurements in triplicate. *reported as average of measurements in duplicate.

this hypothesis, no interaction could be detected for drug and aminoxy crosslinker, but a physical mixture of drug and precursor polymer yielded a reduced signal by HPLC after 72 h (**Figure IV-10**) as well as the appearance of large particulates, which indicate an interaction of regenerated keto groups with BFA.

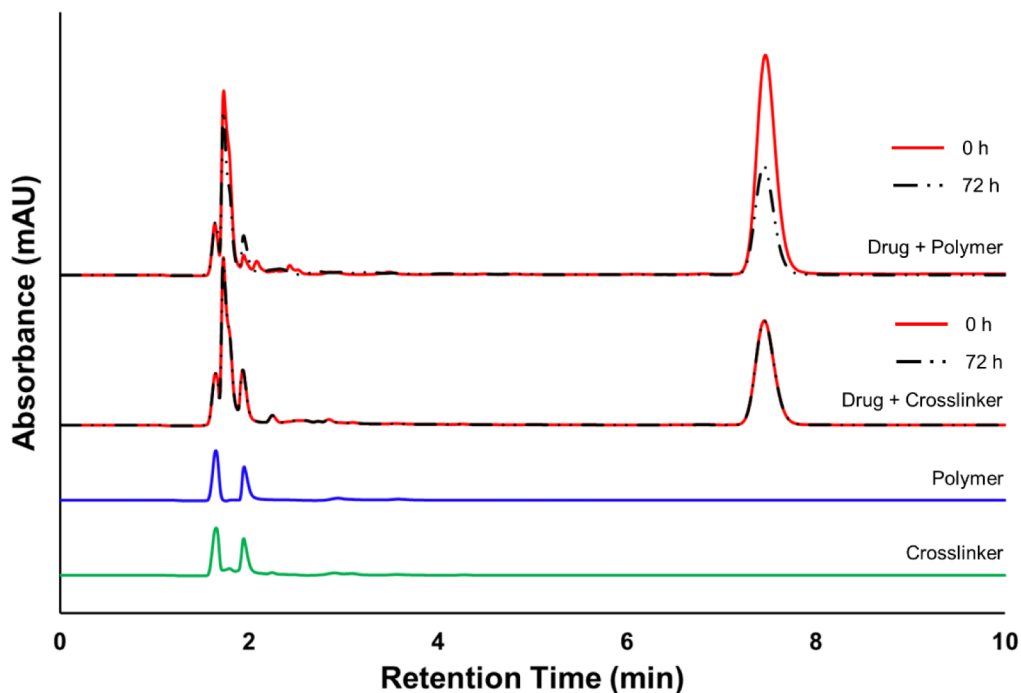


Figure IV-10. HPLC analysis of control experiment with physical mixture of drug (BFA) and polymer (P(VL-*co*-OPD)) or crosslinker (bis(aminoxy) PEG-3) in pH 5.0 at 0 and 72 h post reaction. Reduced absorbance of BFA (ret. time = 7.8 min) of drug + polymer mixture after 72 h indicates presence of hydrophobic or other forces leading to particle-drug interaction.

Moreover, the much slower release rate of the NP_{KO} in acidic conditions could be potentially useful for release of highly potent chemotherapeutics to the extracellular matrix of tumors,⁵⁰⁻⁵² known to exhibit lower pH. Release profiles at neutral pH provide also a tailorable range with medium release profiles. These nanonetworks demonstrate the ability to precisely tune

drug release profiles for fast, medium, or slow rates with continued release through 7-13 days or longer using practical synthetic parameters and fabrication methods.

IV.2.6 Tailoring the Drug Release Profiles through Mixed Composition Nanoparticles

While the distinct drug release profiles we observed demonstrated tunability through network and environmental conditions, we hypothesized that a particle of mixed composition ($\text{NP}_{\text{KO}/\text{AA}}$), that is a combination of both ketoxime and alkoxyamine crosslinks, would provide a third release profile different than its two parent networks. In order to investigate this concept, a third nanoparticle composition was synthesized using the same general procedure for alkoxyamine particles, however, the ratio of reducing agent was decreased to 0.5 equivalents. This would thereby only reduce approximately half of the ketoxime linkages to alkoxyamines, providing both crosslinking chemistries in one particle. After BFA encapsulation, the release of BFA from $\text{NP}_{\text{KO}/\text{AA}}$ was conducted in pH 5.0 and 7.4 buffer solutions (**Figure IV-11**). Interestingly, the release rate of BFA from mixed composition particles under acidic conditions was nearly identical to the release of BFA from NP_{KO} in pH 7.4. This result indicates the same release profile can be achieved at two different pH ranges, thereby offering increased versatility of these nanosystems where a release profile can be tailored to a particular rate under different conditions by synthetic design of the particle. Additionally, the rate of drug release from $\text{NP}_{\text{KO}/\text{AA}}$ under neutral conditions demonstrated that the combination of two networks can yield a distinct release profile with a drug release rate between those observed from NP_{AA} at pH 7.4 and NP_{KO} at 5.0.

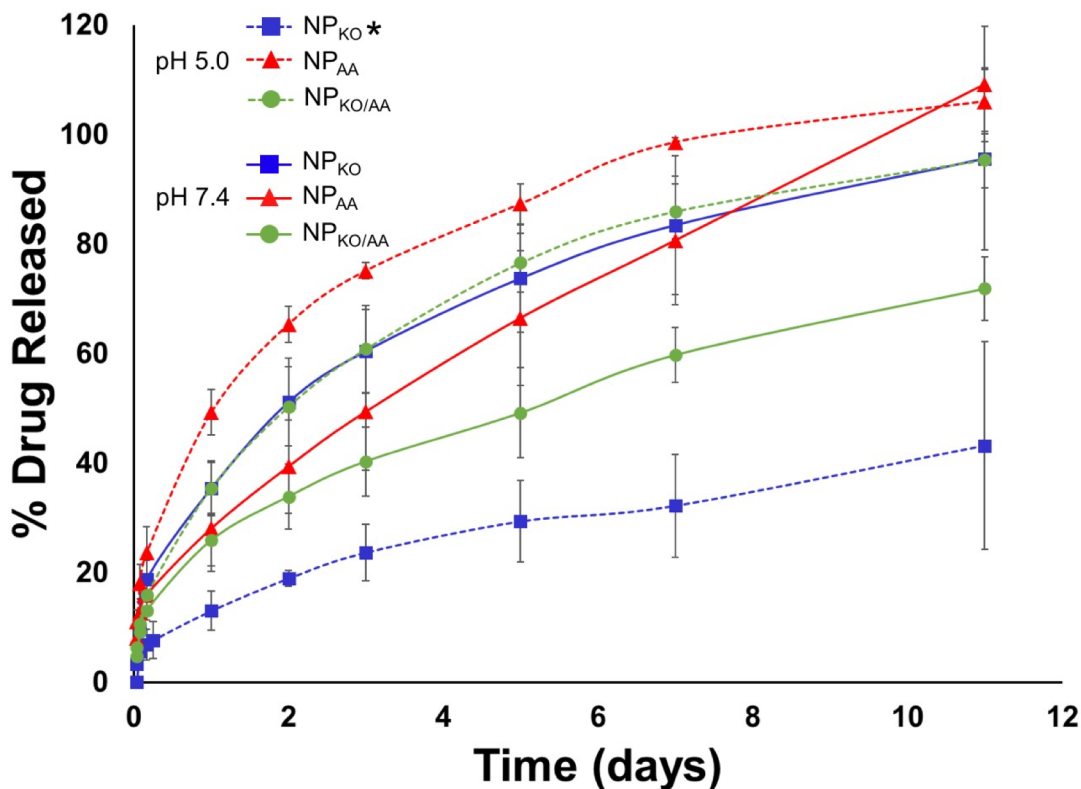


Figure IV-11. Release of BFA from 8% OPD, 2.7 mM NP_{KO/AA} compared to release of NP_{KO}* and NP_{AA} as shown in **Figure IV-9** in pH 5.0 and pH 7.4 at 37 °C over 11 days reported as an average of measurements in triplicate. *reported as average of measurements in duplicate.

IV.3 Conclusion

In this work, we developed a robust nanoparticle formation via protocol for size-controlled, biodegradable, and tunable nanoparticles in the range of 40-200 nm with an adaptable nano-network. Oxime click chemistries have been proven to be ideal to generate not only particles in a two-step procedure from a two-component system through intermolecular chain crosslinking but as well enable a modification of the chemical nature of the particle crosslinks to lead to a tailorable degradation and release to generate a second set of delivery systems in one step. Together with an optimized design, this practical synthesis has demonstrated control over the nanoscopic dimension, crosslinking density, particle degradability, and controlled drug release engaging ketoxime and

alkoxyamine linkage in nanonetworks containing polyesters and PEG units as constitutional elements.

IV.4 Experimental

Materials

SiliaMetS® Cysteine was purchased from Silicycle. Spectra/Por® dialysis tubing (1kD MWCO) was purchased from Spectrum Labs. SnakeSkin™ dialysis tubing (10kD MWCO) was purchased from ThermoFisher Scientific. O,O'-(((oxybis(ethane-2,1-diyl))bis(oxy))bis(ethane-2,1-diyl))bis(hydroxylamine), also referred to as bis(aminoxy)-PEG3, was purchased from Broadpharm. 1,4-cyclohexanedione was purchased from Tokyo Chemical Industry America. All other reagents and solvents were purchased from Sigma-Aldrich and used without further purification unless otherwise noted. δ -Valerolactone was purified via vacuum distillation prior to polymerization.

Characterization

^1H and ^{13}C NMR spectra were recorded on Bruker AV-400, JEOL ECX-400, and JEOL ECA-600 II spectrometers. Chemical shifts were referenced to solvent resonance signals. Gel permeation chromatography (GPC) was conducted on a ToSOH EcoSEC HLC-8320GPC system equipped with a refractive index detector, UV-8320 detector, and TSKgel H_{HR} columns (7.8x300mm G5000 H_{HR} , G4000 H_{HR} , and G3000 H_{HR}) with tetrahydrofuran (THF) as the eluent at a flow rate of 1 mL/min. Transmission Electron Microscopy (TEM) was performed using an JEOL 2000-FX microscope operated at 200kV. Samples for transmission electron microscopy (TEM) were

prepared by dissolving nanoparticles (~0.5 mg) in 0.22 μm filtered acetonitrile (ACN). The samples were then stained with 3 drops of 3% phosphotungstic acid monohydrate and vortexed. Carbon grids were prepared by dipping an Ultrathin Carbon Type-A 400 Mesh Copper Grid in the sample solution three times and allowing to dry at ambient temperature for 12 h. Dynamic light scattering (DLS) was performed on a Malvern Zetasizer Nano system with a fixed angle of 173° at 25°C . All particles were measured in 0.22 μm filtered THF diluted to a concentration that produced the desired count rate with a low signal-to-noise ratio. Static light scattering was performed using the Molecular Weight function of a Malvern Zetasizer Nano system in THF between 0.01-0.1 mg/mL concentrations.

Synthesis of 2-Oxepane-1,5-Dione

Procedure modified from literature.⁴³ Meta-chloroperoxybenzoic acid (11.99 g, 54 mmol) and 1,4-cyclohexanedione (4.0 g, 36 mmol) was dissolved in anhydrous dichloromethane (DCM) (45.5 mL) and refluxed for 3 h. The reaction mixture was cooled to room temperature and a white precipitate was removed by gravity filtration. The precipitate was washed with excess DCM (10 mL) to solubilize any residual product. The organic layer was dried over anhydrous magnesium sulfate and dried in vacuo to collect a white solid. Diethyl ether (10 mL) was added to the flask to wash and collect a white solid via vacuum filtration (80% yield). ^1H NMR (400 MHz, CDCl_3): δ 2.70-2.73 (m, 2H); 2.81-2.85 (m, 4H); 4.42 (t, 2H) ^{13}C NMR (600 MHz, CDCl_3): δ 27.8, 38.5, 44.6, 63.3, 173.5, 205.1

General Synthesis of Poly(δ -Valerolactone-2-Oxepane-1,5-Dione) (P(VL-co-OPD))

Tin(II) trifluoromethanesulfonate (3.93 mg, 9.25×10^{-3} mmol), isoamyl alcohol (81.72 μ L, 7.5×10^{-1} mmol), and DCM (2.61 mL) were added to a flame dried and N₂ purged flask. δ -valerolactone (VL, 2.57 mL, 27 mmol) and 2-oxepane-1,5-dione (OPD, 0.22 g, 1.8 mmol) were added at 0 °C then stirred at room temperature for 18 h. The reaction mixture was quenched with excess methanol (3 mL) and a solid-support metal scavenger (SiliaMetS® Cysteine, 150 mg) was added and stirred for 2 h to capture tin catalyst. The mixture was filtered via gravity filtration and transferred to dialysis tubing (1kD MWCO) and dialyzed against methanol (MeOH)/DCM (1:1) mixture for 24 h, with frequent solvent changes. After dialysis, the solvent was removed under reduced pressure and product dried in vacuo to obtain a light yellow, waxy product. (56% yield) ¹H NMR (400 MHz, CDCl₃): δ 0.90 (d, 6H); 1.6-1.75 (m); 2.23-2.43 (m); 2.25-2.7 (m); 2.7-2.84 (m); 3.4 (t); 3.65 (m); 4.0 (t); 4.3-4.4 (m). ¹³C NMR (600 MHz, CDCl₃): δ 21.25, 27.9, 33.5, 63.8, 173.2, 205.75

General Synthesis of Ketoxime Nanoparticle (NP_{KO})

P(VL-co-OPD) (4% OPD, 50 mg, $4556.20 \text{ g mol}^{-1}$, $2925.14 \text{ g mol}^{-1}$ keto-group, 1.71×10^{-5} mol) was dissolved in dichloromethane (5.70 mL) then added to a 50 mL round bottom flask. O,O'-(((oxybis(ethane-2,1-diyl))bis(oxy))bis(ethane-2,1-diyl))bis(hydroxylamine) (3.83 mg, 1.71×10^{-5} mol, 1 equiv.) was dissolved in dichloromethane (0.63 mL) and added quickly to the polymer solution at a fast vortex. The reaction was stirred for 2 h then immediately transferred to Thermo Scientific™ SnakeSkin™ 10K MWCO Dialysis Tubing. The solution was dialyzed against dichloromethane for 48 h, changing the solvent 3-4 times per day. The solvent was removed via rotary evaporation. The product was dried in vacuo to yield a light tan waxy solid (80% yield).

¹H NMR (400 MHz, CDCl₃): δ 0.90 (d, 6H); 1.6-1.75 (m); 2.23-2.43 (m); 2.25-2.7 (m); 2.7-2.84 (m); 3.4 (t); 3.65 (m); 4.0 (t); 4.3-4.4 (m). ¹³C NMR (600 MHz, CDCl₃): δ 21.32, 25.53, 28.00, 33.62, 63.87, 67.98, 173.30

General Synthesis of Alkoxyamine Nanoparticle (NP_{AA})

To ketoxime nanoparticles (50 mg) formed *in situ*, sodium cyanoborohydride (2.15 mg, 3.42x10⁻⁵ mol, 2 equiv.) and a catalytic amount of saturated sodium bicarbonate solution (100 μL) were added directly to the reaction flask. The reaction stirred for 2 h then was transferred to Thermo Scientific™ SnakeSkin™ 10K MWCO Dialysis Tubing. The solution was dialyzed against a 1:1 mixture of MeOH/DCM for 48 h, with 3-4 solvent changes per day. The solution was filtered with a 0.45 μm filter to remove solid salt particulates and solvent was removed via rotary evaporation. The product was dried *in vacuo* to yield a light tan waxy solid (80% yield). ¹H NMR (400 MHz, CDCl₃): δ 0.90 (d, 6H); 1.6-1.75 (m); 2.23-2.43 (m); 2.25-2.7 (m); 2.7-2.84 (m); 3.4 (t); 3.65 (m); 4.0 (t); 4.3-4.4 (m). ¹³C NMR (600 MHz, CDCl₃): δ 21.32, 25.53, 28.00, 33.62, 63.85, 67.88, 173.26

In Vitro Nanoparticle Degradation Studies

NPs (14% OPD, 5.4 mM, ~170 nm) were suspended in 2 mL of acetate buffer (pH 5.0) or phosphate buffered saline (PBS, pH 7.4) in 1 dram vials with a micro stir bar. The vials were sealed and samples were continuously stirred at 37°C. At 48 h intervals, nanoparticles and degradation products were extracted with dichloromethane (3 x 3 mL). The organic layer was dried over magnesium sulfate and dried *in vacuo*. The degradation of particles was monitored via

static light scattering utilizing the Molecular Weight function of a Malvern Zetasizer Nano instrument.

General Procedure for Encapsulation of Brefeldin A into Nanoparticles

NPs (12.6 mg, 8% OPD, 2.7 mM, ~80 nm) were added to a 1.5 mL centrifuge tube. Brefeldin A (BFA) was solubilized in DMSO and a known concentration of BFA was added to the NPs (3.15 mg, 11.2 mmol). Additional DMSO was added to the mixture up to a total of 50 μ L. Cell culture water containing 0.1% D- α -tocopherol polyethylene glycol 1000 succinate (1 mL) was added to the centrifuge tube and vortexed to induce BFA encapsulation. The mixture was then centrifuged at 14000 RPM for 20 min. The supernatant was decanted, fresh cell culture water (1 mL) was added to wash the particles and vortexed. Centrifugation was repeated at 14000 RPM for 20 min, then the supernatant was decanted to remove any unincorporated drug. Cell culture water (0.5 mL) was added to the mixture, frozen, and lyophilized to produce BFA encapsulated nanoparticles (NP-BFA). HPLC analysis confirmed encapsulation of BFA at an average of 20 wt % with 100% efficiency.

In vitro release of Brefeldin A from Nanoparticles

NP-BFA were weighed into a 1.5 mL centrifuge tube and 1 mL of phosphate buffered saline (PBS, pH 7.4) or acetate buffer (pH 5.0) was added. The mixture was vortexed until the particles were suspended in the media, and then the particles were added to a 1000kD Float-a-Lyzer™ dialysis membrane. The dialysis device was placed in a 50 mL centrifuge tube containing 18 mL of dialysis media and a small stir bar. The centrifuge tube was submerged in a water bath at 37°C and stirred,

and aliquots (150 μ L) were removed from the dialysis media at specified time points and replaced with fresh media. Aliquots were analyzed for BFA concentration via HPLC.

General Synthesis of Partially Reduced Ketoxime/Alkoxyamine Nanoparticle (NP_{KO/AA})

To ketoxime nanoparticles (348 mg) formed *in situ*, sodium cyanoborohydride (6.72 mg, 1.07×10^{-4} mol, 0.5 equiv.) and a catalytic amount of saturated sodium bicarbonate solution (100 μ L) were added directly to the reaction flask. The reaction stirred for 2 h then was transferred to Thermo Scientific™ SnakeSkin™ 10K MWCO Dialysis Tubing. The solution was dialyzed against a 1:1 mixture of MeOH/DCM for 48 h, with 3-4 solvent changes per day. The solution was filtered with a 0.45 μ m filter to remove solid salt particulates and solvent was removed via rotary evaporation. The product was dried *in vacuo* to yield a light tan waxy solid (80% yield). ^1H NMR (400 MHz, CDCl_3): δ 0.90 (d, 6H); 1.6-1.75 (m); 2.23-2.43 (m); 2.25-2.7 (m); 2.7-2.84 (m); 3.4 (t); 3.65 (m); 4.0 (t); 4.3-4.4 (m). ^{13}C NMR (600 MHz, CDCl_3): δ 21.32, 25.53, 28.00, 33.62, 63.85, 67.88, 173.26

General Nanoprecipitation Procedure for Encapsulation of Brefeldin A into NP_{KO/AA}

NPs (134 mg, 8% OPD, 2.7 mM, \sim 80 nm) were added to a 1.5 mL centrifuge tube. Brefeldin A (BFA) was solubilized in dimethyl sulfoxide (DMSO) to a known concentration and then added to the NPs (35.2 mg, 125 μ mol). Additional DMSO was added to the mixture up to a total of 300 μ L. The solution was dispersed equally into seven 1.5 mL centrifuge tubes. Cell culture grade water containing 0.1% D- α -tocopherol polyethylene glycol 1000 succinate (1 mL) was added to each centrifuge tube and vortexed to induce BFA encapsulation. The suspension was then

centrifuged at 14000 RPM for 20 min. The supernatant was decanted, fresh cell culture grade water (1 mL) was added to the particle pellet and vortexed until particles were resuspended. Centrifugation was repeated at 14000 RPM for 20 min, then the supernatant was decanted to remove any unincorporated drug. Cell culture grade water (0.5 mL) was added to the mixture, frozen, and lyophilized to produce BFA encapsulated nanoparticles (BFA-NP). HPLC analysis confirmed encapsulation of BFA at an average of 42 wt % with 210% efficiency.

In vitro release of Brefeldin A from NP_{KO/AA}

BFA-NPs (~5 mg, ~40 wt% BFA) were weighed into a 1.5 mL centrifuge tube and 1 mL 0.1M acetic acid-NaOAc buffer with 0.1% v/v Tween® 80 (pH 5.0) or phosphate buffered saline with 0.1% v/v Tween® 80 (PBS, pH 7.4) was added. The mixture was vortexed until the particles were suspended in the media, and then the particles were transferred to a 1000kD Float-a-Lyzer™ dialysis membrane. The dialysis device was placed in a 50 mL centrifuge tube containing 18 mL of dialysis media and a small stir bar. The centrifuge tube was submerged in a water bath at 37 °C and stirred, and aliquots (150 µL) were removed from the dialysis media at specified time points and replaced with fresh media. BFA concentration in the aliquots was determined via HPLC at 230 nm with isocratic gradient of 57% MeOH : 43% water. Flow rate of 1 mL/min with run time of 10 min yielded a retention time of 7.5 min.

IV.5 References

1. Onaca, O.; Enea, R.; Hughes, D. W.; Meier, W., Stimuli-Responsive Polymersomes as Nanocarriers for Drug and Gene Delivery. *Macromol Biosci* **2009**, *9* (2), 129-139.

2. Scarpa, E.; Bailey, J. L.; Janeczek, A. A.; Stumpf, P. S.; Johnston, A. H.; Oreffo, R. O. C.; Woo, Y. L.; Cheong, Y. C.; Evans, N. D.; Newman, T. A., Quantification of intracellular payload release from polymersome nanoparticles. *Sci Rep* **2016**, *6* (e29460), 1-13.
3. Vlakh, E. G.; Grachova, E. V.; Zhukovsky, D. D.; Hubina, A. V.; Mikhailova, A. S.; Shakirova, J. R.; Sharoyko, V. V.; Tunik, S. P.; Tennikova, T. B., Self-assemble nanoparticles based on polypeptides containing C-terminal luminescent Pt-cysteine complex. *Sci Rep* **2017**, *7* (e41991), 1-10.
4. Danafar, H.; Rostamizadeh, K.; Davaran, S.; Hamidi, M., PLA-PEG-PLA copolymer-based polymersomes as nanocarriers for delivery of hydrophilic and hydrophobic drugs: preparation and evaluation with atorvastatin and lisinopril. *Drug Dev Ind Pharm* **2014**, *40* (10), 1411-1420.
5. Sercombe, L.; Veerati, T.; Moheimani, F.; Wu, S. Y.; Sood, A. K.; Hua, S., Advances and Challenges of Liposome Assisted Drug Delivery. *Front Pharmacol* **2015**, *6* (286), 1-13.
6. Zylberberg, C.; Matosevic, S., Pharmaceutical liposomal drug delivery: a review of new delivery systems and a look at the regulatory landscape. *Drug Deliv* **2016**, *23* (9), 3319-3329.
7. Movassaghian, S.; Merkel, O. M.; Torchilin, V. P., Applications of polymer micelles for imaging and drug delivery. *Wiley Interdiscip Rev Nanomed Nanobiotechnol* **2015**, *7* (5), 691-707.
8. Lu, Y.; Yue, Z. G.; Xie, J. B.; Wang, W.; Zhu, H.; Zhang, E. S.; Cao, Z. Q., Micelles with ultralow critical micelle concentration as carriers for drug delivery. *Nat Biomed Eng* **2018**, *2* (5), 318-325.
9. O'Reilly, R. K.; Hawker, C. J.; Wooley, K. L., Cross-linked block copolymer micelles: functional nanostructures of great potential and versatility. *Chem Soc Rev* **2006**, *35* (11), 1068-1083.

10. Ren, J. M.; McKenzie, T. G.; Fu, Q.; Wong, E. H. H.; Xu, J. T.; An, Z. S.; Shanmugam, S.; Davis, T. P.; Boyer, C.; Qiao, G. G., Star Polymers. *Chem Rev* **2016**, *116* (12), 6743-6836.
11. Delplace, V.; Couvreur, P.; Nicolas, J., Recent trends in the design of anticancer polymer prodrug nanocarriers. *Polym Chem* **2014**, *5* (5), 1529-1544.
12. Nicolas, J., Drug-Initiated Synthesis of Polymer Prodrugs: Combining Simplicity and Efficacy in Drug Delivery. *Chem Mater* **2016**, *28* (6), 1591-1606.
13. Vhora, I.; Patil, S.; Bhatt, P.; Misra, A., Protein- and Peptide-Drug Conjugates: An Emerging Drug Delivery Technology. *Adv Protein Chem Str* **2015**, *98*, 1-55.
14. Gilmore, K. A.; Lampley, M. W.; Boyer, C.; Harth, E., Matrices for combined delivery of proteins and synthetic molecules. *Adv Drug Deliv Rev* **2016**, *98*, 77-85.
15. Su, L.; Li, R. C.; Khan, S.; Clanton, R.; Zhang, F. W.; Lin, Y. N.; Song, Y.; Wang, H.; Fan, J. W.; Hernandez, S.; Butters, A. S.; Akabani, G.; MacLoughlin, R.; Smolen, J.; Wooley, K. L., Chemical Design of Both a Glutathione-Sensitive Dimeric Drug Guest and a Glucose-Derived Nanocarrier Host to Achieve Enhanced Osteosarcoma Lung Metastatic Anticancer Selectivity. *J Am Chem Soc* **2018**, *140* (4), 1438-1446.
16. Green, M. R.; Manikhas, G. M.; Orlov, S.; Afanasyev, B.; Makhson, A. M.; Bhar, P.; Hawkins, M. J., Abraxane((R)), a novel Cremophor((R))-free, albumin-bound particle form of paclitaxel for the treatment of advanced non-small-cell lung cancer. *Ann Oncol* **2006**, *17* (8), 1263-1268.
17. Yuan, D. M.; Lv, Y. L.; Yao, Y. W.; Miao, X. H.; Wang, Q.; Xiao, X. W.; Yin, J.; Shi, Y.; Shi, M. Q.; Zhang, X. W.; Song, Y., Efficacy and safety of Abraxane in treatment of progressive and recurrent non-small cell lung cancer patients: A retrospective clinical study. *Thorac Cancer* **2012**, *3* (4), 341-347.

18. van der Ende, A. E.; Kravitz, E. J.; Harth, E., Approach to Formation of Multifunctional Polyester Particles in Controlled Nanoscopic Dimensions. *J Am Chem Soc* **2008**, *130* (27), 8706–8713.
19. Stevens, D. M.; Gilmore, K. A.; Harth, E., An assessment of nanosponges for intravenous and oral drug delivery of BCS class IV drugs: Drug delivery kinetics and solubilization. *Polym Chem* **2014**, *5* (11), 3551-3554.
20. Passarella, R. J.; Spratt, D. E.; van der Ende, A. E.; Phillips, J. G.; Wu, H.; Sathiyakumar, V.; Zhou, L.; Hallahan, D. E.; Harth, E.; Diaz, R., Targeted Nanoparticles That Deliver a Sustained, Specific Release of Paclitaxel to Irradiated Tumors. *Cancer Res* **2010**, *70* (11), 4550-4559.
21. van der Ende, A. E.; Sathiyakumar, V.; Diaz, R.; Hallahan, D. E.; Harth, E., Linear release nanoparticle devices for advanced targeted cancer therapies with increased efficacy. *Polym Chem* **2010**, *1* (1), 93-96.
22. van der Ende, A. E.; Harrell, J.; Sathiyakumar, V.; Meschievitz, M.; Katz, J.; Adcock, K.; Harth, E., "Click" Reactions: Novel Chemistries for Forming Well-defined Polyester Nanoparticles. *Macromolecules* **2010**, *43* (13), 5665-5671.
23. van der Ende, A.; Croce, T.; Hamilton, S.; Sathiyakumar, V.; Harth, E., Tailored polyester nanoparticles: post-modification with dendritic transporter and targeting units via reductive amination and thiol-ene chemistry. *Soft Matter* **2009**, *5* (7), 1417-1425.
24. Lampley, M. W.; Harth, E., Photocontrolled Growth of Cross-Linked Nanonetworks. *ACS Macro Lett* **2018**, *7* (6), 745-750.

25. Hariri, G.; Edwards, A. D.; Merrill, T. B.; Greenbaum, J. M.; van der Ende, A. E.; Harth, E., Sequential Targeted Delivery of Paclitaxel and Camptothecin Using a Cross-Linked "Nanosponge" Network for Lung Cancer Chemotherapy. *Mol Pharmaceut* **2014**, *11* (1), 265-275.
26. Passarella, R. J.; Spratt, D. E.; van der Ende, A. E.; Phillips, J. G.; Wu, H. M.; Sathiyakumar, V.; Zhou, L.; Hallahan, D. E.; Harth, E.; Diaz, R., Targeted Nanoparticles That Deliver a Sustained, Specific Release of Paclitaxel to Irradiated Tumors. *Cancer Res* **2010**, *70* (11), 4550-4559.
27. Kendrick-Williams, L. L.; Harth, E., Nanosponge Tunability in Size and Crosslinking Density. *J Vis Exp* **2017**, (126), e56073, 1-11.
28. Lockhart, J. N.; Stevens, D. M.; Beezer, D. B.; Kravitz, A.; Harth, E., Dual drug delivery of tamoxifen and quercetin: Regulated metabolism for anticancer treatment with nanosponges. *J Control Release* **2015**, *220*, 751-757.
29. Grover, G. N.; Lam, J.; Nguyen, T. H.; Segura, T.; Maynard, H. D., Biocompatible hydrogels by oxime Click chemistry. *Biomacromolecules* **2012**, *13* (10), 3013-7.
30. Grover, G. N.; Braden, R. L.; Christman, K. L., Oxime Cross-Linked Injectable Hydrogels for Catheter Delivery. *Adv Mater* **2013**, *25* (21), 2937-2942.
31. Collins, J.; Nadgorny, M.; Xiao, Z. Y.; Connal, L. A., Doubly Dynamic Self-Healing Materials Based on Oxime Click Chemistry and Boronic Acids. *Macromol Rapid Comm* **2017**, *38* (6), e1600760 (1-7).
32. Mukherjee, S.; Hill, M. R.; Sumerlin, B. S., Self-healing hydrogels containing reversible oxime crosslinks. *Soft Matter* **2015**, *11* (30), 6152-6161.
33. Nadgorny, M.; Collins, J.; Xiao, Z. Y.; Scales, P. J.; Connal, L. A., 3D-printing of dynamic self-healing cryogels with tuneable properties. *Polym Chem* **2018**, *9* (13), 1684-1692.

34. Lin, F.; Yu, J. Y.; Tang, W.; Zheng, J. K.; Defante, A.; Guo, K.; Wesdemiotis, C.; Becker, M. L., Peptide-Functionalized Oxime Hydrogels with Tunable Mechanical Properties and Gelation Behavior. *Biomacromolecules* **2013**, *14* (10), 3749-3758.
35. Collins, J.; Xiao, Z. Y.; Mullner, M.; Connal, L. A., The emergence of oxime click chemistry and its utility in polymer science. *Polym Chem* **2016**, *7* (23), 3812-3826.
36. Christman, K. L.; Broyer, R. M.; Schopf, E.; Kolodziej, C. M.; Chen, Y.; Maynard, H. D., Protein Nanopatterns by Oxime Bond Formation. *Langmuir* **2011**, *27* (4), 1415-1418.
37. Zhang, X.; Huang, Y.; Ghazwani, M.; Zhang, P.; Li, J.; Thorne, S. H.; Li, S., Tunable pH-Responsive Polymeric Micelle for Cancer Treatment. *ACS Macro Lett* **2015**, *4* (6), 620-623.
38. Du, J.-Z.; Du, X.-J.; Mao, C.-Q.; Wang, J., Tailor-Made Dual pH-Sensitive Polymer–Doxorubicin Nanoparticles for Efficient Anticancer Drug Delivery. *J Am Chem Soc* **2011**, *133* (44), 17560-17563.
39. Iha, R. K.; van Horn, B. A.; Wooley, K. L., Complex, degradable polyester materials via ketoxime ether-based functionalization: Amphiphilic, multifunctional graft copolymers and their resulting solution-state aggregates. *J Polym Sci A* **2010**, *48* (16), 3553-3563.
40. Tian, D.; Dubois, P.; Grandfils, C.; Jerome, R., Ring-opening polymerization of 1,4,8-trioxaspiro[4.6]-9-undecanone: A new route to aliphatic polyesters bearing functional pendent groups. *Macromolecules* **1997**, *30* (3), 406-409.
41. Van Horn, B. A.; Wooley, K. L., Toward cross-linked degradable polyester materials: Investigations into the compatibility and use of reductive amination chemistry for cross-linking. *Macromolecules* **2007**, *40* (5), 1480-1488.
42. Van Horn, B. A.; Wooley, K. L., Cross-linked and functionalized polyester materials constructed using ketoxime ether linkages. *Soft Matter* **2007**, *3* (8), 1032-1040.

43. Latere, J.-P.; Lecomte, P.; Dubois, P.; Jérôme, R., 2-Oxepane-1,5-dione: A Precursor of a Novel Class of Versatile Semicrystalline Biodegradable (Co)polyesters. *Macromolecules* **2002**, *35* (21), 7857-7859.
44. Lane, C. F., Sodium Cyanoborohydride - A Highly Selective Reducing Agent for Organic Functional Groups. *Synthesis* **1975**, *1975* (03), 135-146.
45. Abdel-Magid, A. F.; Carson, K. G.; Harris, B. D.; Maryanoff, C. A.; Shah, R. D., Reductive Amination of Aldehydes and Ketones with Sodium Triacetoxyborohydride. Studies on Direct and Indirect Reductive Amination Procedures1. *J Org Chem* **1996**, *61* (11), 3849-3862.
46. Beezer, D. B.; Harth, E., Post-polymerization modification of branched polyglycidol with N-Hydroxy phthalimide to give ratio-controlled amino-oxy functionalized species. *J Polym Sci A* **2016**, *54* (17), 2820-2825.
47. Wlodkowic, D.; Skommer, J.; McGuinness, D.; Hillier, C.; Darzynkiewicz, Z., ER-Golgi network-A future target for anti-cancer therapy. *Leukemia Res* **2009**, *33* (11), 1440-1447.
48. Shao, R. G.; Shimizu, T.; Pommier, Y., Brefeldin A is a potent inducer of apoptosis in human cancer cells independently of p53. *Exp Cell Res* **1996**, *227* (2), 190-196.
49. Huang, H. R.; Liu, T.; Guo, J. X.; Yu, L.; Wu, X. F.; He, Y.; Li, D. L.; Liu, J. L.; Zhang, K.; Zheng, X.; Goodin, S., Brefeldin A enhances docetaxel-induced growth inhibition and apoptosis in prostate cancer cells in monolayer and 3D cultures. *Bioorganic Med Chem Lett* **2017**, *27* (11), 2286-2291.
50. Ojugo, A. S. E.; McSheehy, P. M. J.; McIntyre, D. J. O.; McCoy, C.; Stubbs, M.; Leach, M. O.; Judson, I. R.; Griffiths, J. R., Measurement of the extracellular pH of solid tumours in mice by magnetic resonance spectroscopy: a comparison of exogenous ¹⁹F and ³¹P probes. *NMR Biomed* **1999**, *12* (8), 495-504.

51. Fukamachi, T.; Chiba, Y.; Wang, X.; Saito, H.; Tagawa, M.; Kobayashi, H., Tumor specific low pH environments enhance the cytotoxicity of lovastatin and cantharidin. *Cancer Lett* **2010**, *297* (2), 182-189.
52. Zhang, X.; Lin, Y.; Gillies, R. J., Tumor pH and its measurement. *J Nucl Med* **2010**, *51* (8), 1167-1170.

CHAPTER V

Controlled Release of Formaldehyde from Polyglycidol and Polyacrylate

Prodrugs for Applications in Synergistic Anti-Cancer Therapies

V.1 Introduction

The implementation of synergistic drug therapies are widely increasing due to enhanced therapeutic selectivity,¹ efficacy and decreased toxicity,² and potential for drug repurposing.³ Discovery of synergistic pharmaceutical combinations has led to improved outcomes for traditionally difficult-to-treat diseases, such as the success of combination antiretroviral therapy for HIV infection⁴⁻⁶ and synergistic immunotherapies for cancer.⁷⁻¹⁰ Increase in drug resistance, immunodeficiency, and other factors that increase difficulty in treatment options have risen in recent decades.¹¹⁻¹³ This changing landscape demands the advancement of complex drug delivery systems with single, dual, and multiple release matrices to provide increased solubilization and protection of pharmaceutical agents, along with combined or sequential release profiles. Recent work in this field has led to the development of a multitude of biocompatible materials which can deliver these toxic small molecules through sustained release. Additionally, the recent emergence of the use of toxic small molecules, such as carbon monoxide, nitric oxide, and formaldehyde, in the application of synergistic therapies has led to increased interest in the role these compounds have and how to best harness their utility. Successful delivery of carbon monoxide to disrupt the function of mitochondria in cancer cells in order to induce apoptosis through utilization of Prussian Blue nanoparticles exhibited a controllable and sustained release mechanism not previously achieved with CO-based delivery complexes.¹⁴ Doxorubicin (DOX), an anthracycline class drug,

has demonstrated enhanced cytotoxicity when co-administered with formaldehyde. Apart from its main mechanism of action in anticancer treatments as a topoisomerase II poison, DOX is also capable of other cellular actions, including the ability to form adducts with DNA. To form the DNA adduct, DOX first reacts with formaldehyde to create an activated Schiff base which is then transformed to a C-glycosidic linkage through the exocyclic amino group of guanine residues.¹⁵ However, for clinical use, formaldehyde, a known carcinogen, cannot be systemically delivered in high dosages and must be formulated in such a way to render it inert until released at the desired treatment location. Leveraging the vicinal amino-alcohol of doxorubicin, Koch formed the formaldehyde 1:1 conjugate doxazolidine and 2:3 conjugate doxoform.¹⁶⁻¹⁸ These conjugates were found to have similar activities against breast cancer cells (MCF-7), with ~100 fold increase in efficacy compared to doxorubicin.¹⁷ This mechanism of action for DNA intercalation provides a novel approach for anticancer treatments through the combined use of doxorubicin and formaldehyde in a single delivery system.

Because of its highly reactive nature, formaldehyde provides both direct access and distinct challenges to the development of a prodrug strategy for its combination therapy with doxorubicin. Polyglycidol, a traditionally hyperbranched polyol, has exhibited great biocompatibility and utility in biomaterials, such as anti-fouling coatings¹⁹ among others.²⁰ While an attractive polymer material for a bulk or gel-based delivery matrix, hyperbranched polyglycidol does not possess a high level of functionality for prodrug conjugation. Our research group has developed a method for synthesis of a semi-branched and functionalized polyglycidol which has increased linearity providing more reactive functional groups, and therefore a higher loading capacity for small molecule conjugations.²¹⁻²² Additionally, our research has previously demonstrated the success of this polymer as a matrix for the suspension of drug-loaded nanoparticles. We hypothesized the

reactive functionality of polyglycidol could be exploited to conjugate formaldehyde to the polymer backbone through acetal linkages to produce the formaldehyde prodrug. As these acetal linkages were expected to be acid-labile, we were interested in investigating the pH-responsive nature of these prodrugs for their application in tumor environments, known to exhibit a low pH.²³⁻²⁵

Furthermore, increasing control over architecture, molecular weight, and functionality is an evolving area in polymer materials. Our interest in controlled radical polymerization (CRP) techniques led us to investigate the preparation of pendant-diol acrylate polymers for increased complexity and design control in the polymer matrix. Recent development of water-soluble CO-releasing polyacrylates prepared by reversible addition fragmentation chain transfer (RAFT) polymerization and its effective antimicrobial activity by Boyer and coworkers²⁶ led to our interest in applying this concept to formaldehyde prodrugs. Through this, we developed a novel polyacrylate bearing pendant diol functionality for the conjugation of formaldehyde. We hypothesize that the kinetic and thermodynamic variations in the ring structure of the acetal formation of both diols will provide tunability in the drug release profile. As such, we synthesized polyacrylates bearing both 1,2- and 1,3-diols to analyze to what extent, if any, this affected the release rate of formaldehyde. Lastly, nanoparticles are a practical and effective choice for doxorubicin encapsulation, as much of our group's research has focused on the development of polyester nanoparticle drug delivery vehicles with controlled and variable sizes, network densities, degradation pathways, and release kinetics.²⁷⁻³³ Recent advancement of our polyester nanosponge system, utilizing oxime-click chemistry for preparing tunable nanoparticles with varied drug release rates was previously described.³⁴ These particles provide an excellent carrier for doxorubicin in anticancer applications, as they can be tailored for pH-responsive or pH-stable networks.

Our proposed approach utilizes conjugation of formaldehyde to a macromolecular prodrug which dually serves as a matrix for the dispersion of DOX-loaded nanoparticles to provide a synergistic, controlled release dual drug delivery system (**Figure V-1**). In this work, we present two distinct methods for the formation of polymer-based formaldehyde prodrugs. First, a low molecular weight, highly viscous polyglycidol with limited formaldehyde loading yet excellent biological compatibility and cytotoxic efficacy in conjunction with DOX. Second, a polyacrylate-based prodrug with customization of kinetics through 1,2- or 1,3-diol selection, controlled molecular weight and copolymer functionality, and reduced viscosity for ease of purification. Each with their unique advantages, the combination or independent use of these materials in conjunction with doxorubicin-loaded nanoparticles has great promise for application in synergistic cancer therapies.

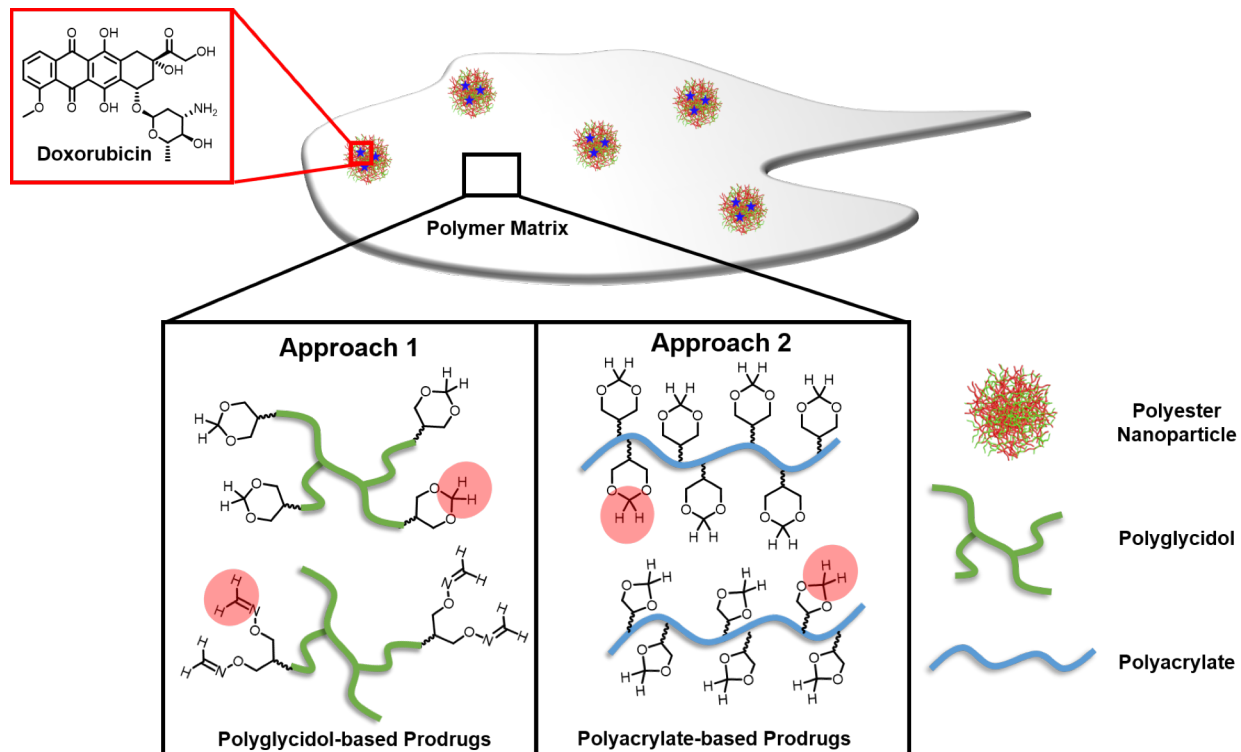


Figure V-1. Overview of the proposed approaches for synergistic combination therapies of formaldehyde and doxorubicin utilizing a macromolecular formaldehyde prodrug of either polyglycidol or polyacrylate backbone with a doxorubicin-loaded crosslinked polyester nanoparticle.

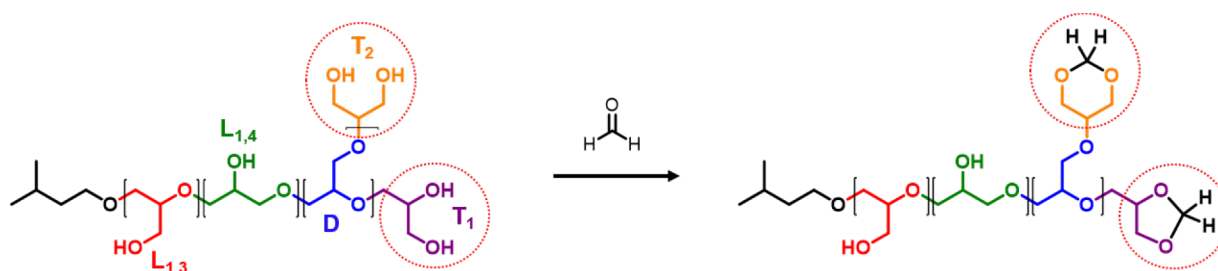
V.2 Results and Discussion

V.2.1 Synthesis of Polyglycidol Formaldehyde Prodrugs

Polyglycidol, a semi-branched polyether bearing primary and secondary hydroxyls, contains terminal units with two primary alcohols in the 1,2- and 1,3-diol arrangement which can be leveraged to form an acid-labile acetal functionality for the conjugation of formaldehyde to the polymer backbone (**Scheme V-1**). Polyglycidol was synthesized, according to previous work in our research group, through cationic ring-opening polymerization catalyzed by tin triflate.^{21, 35-36} We hypothesized that the terminal diol units T_1 and T_2 could serve as conjugation sites for

formaldehyde through an acetal formation. To investigate the formaldehyde conjugation to polyglycidol terminal diol units, formaldehyde solution (37 wt % formaldehyde in water) was mixed with polyglycidol in methanol followed by evaporation of solvent and free formaldehyde to drive the coupling reaction.

Scheme V-1. Scheme for formaldehyde conjugation with polyglycidol and identification of branching units involved.



Formaldehyde is traditionally a difficult molecule to work with, due to its rapid polymerization with itself to form oligomers and adduct formation with methanol and water, common solvents used for the solubilization of polyglycidol. Fortunately, the presence of these byproducts can be differentiated from formaldehyde conjugated to the polymer backbone using NMR spectroscopy techniques, namely ^1H , ^{13}C , and heteronuclear single quantum correlation (HSQC) experiments. After drying, the material was lyophilized to remove any traces of water or formaldehyde, then analyzed by NMR spectroscopy to determine if the acetal had formed. Initially, comparison of the ^1H NMR spectra prior to and after formaldehyde conjugation, three new resonances are obvious: 4.55, 4.65, and 4.74 ppm. The product spectrum exhibited a broad signal at 4.74 ppm which corresponds to the resonance of acetal protons (**Figure V-2**).

Additionally, the resonance at 4.55 and 4.65 ppm were attributed to the methylene protons present in the adduct of formaldehyde with methanol ($\text{CH}_3\text{OCH}_2\text{CH}_2\text{OH}$).³⁷ Next, we performed

inverse gated (IG) ^{13}C experiments to investigate and quantified the appearance of new carbon signals. The prodrug spectrum shows three new carbon signals: 90.56, 91.07, and 91.14 ppm. Resonance at 91.07 and 91.14 ppm are again correlated to the formaldehyde adduct with methanol, which indicates the resonance at 90.56 ppm is the acetal carbon from the formaldehyde conjugate signal. The presence of these adduct signals is indicative of free formaldehyde entrapped in the viscous polymer matrix during drying. 2D heteronuclear experiments, HSQC, were performed to confirm these assignments (**Figure V-3**).

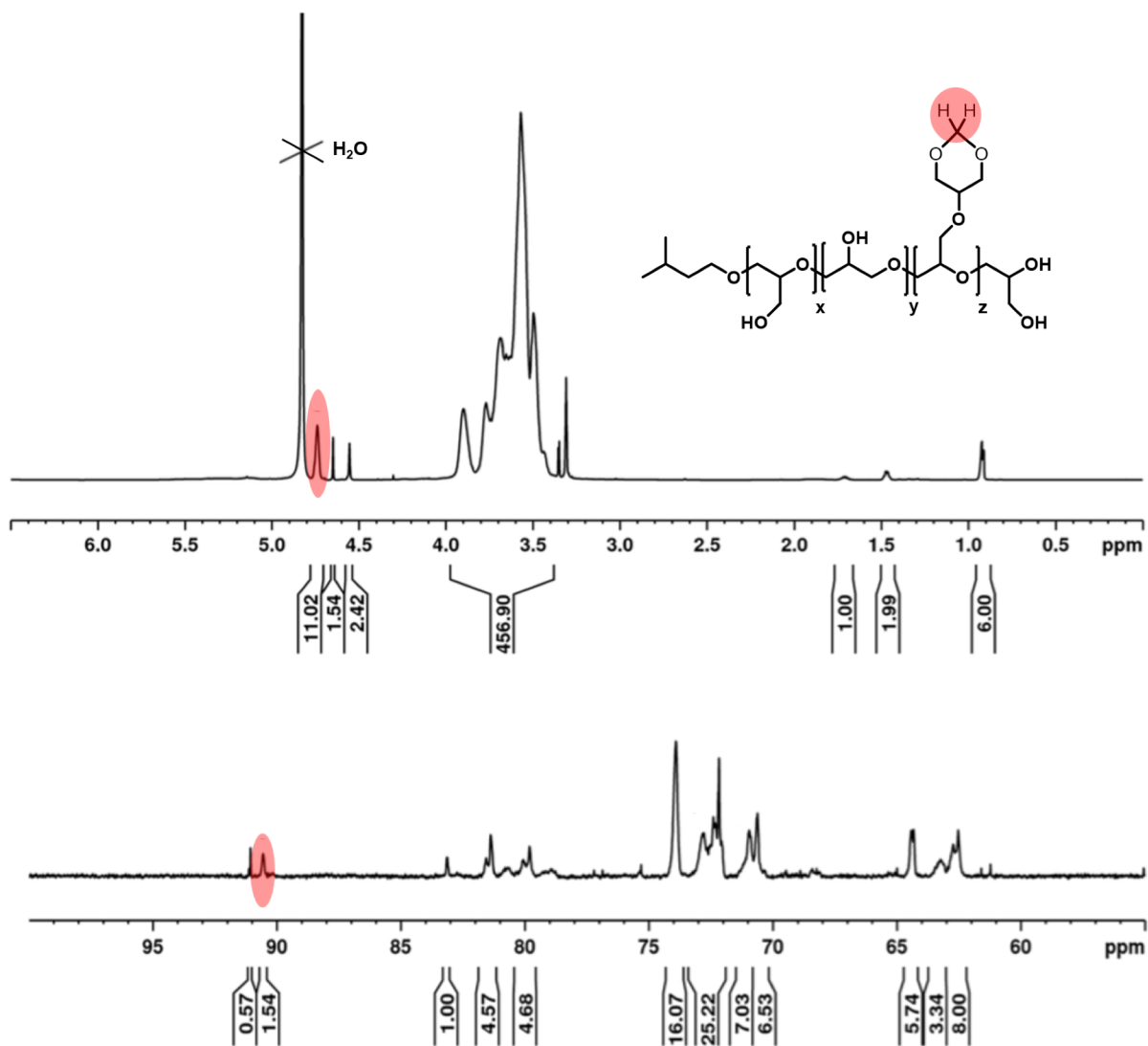


Figure V-2. ^1H NMR (top) and ^{13}C -IG NMR (bottom) spectra for the polyglycidol prodrug, PG-Acetal. In the ^1H NMR, the proton resonance signal at 4.74 ppm associated with the acetal conjugate formation is identified (highlighted in red). The carbon signal at 90.56 ppm corresponding to the acetal carbon has also been identified (highlighted in red).

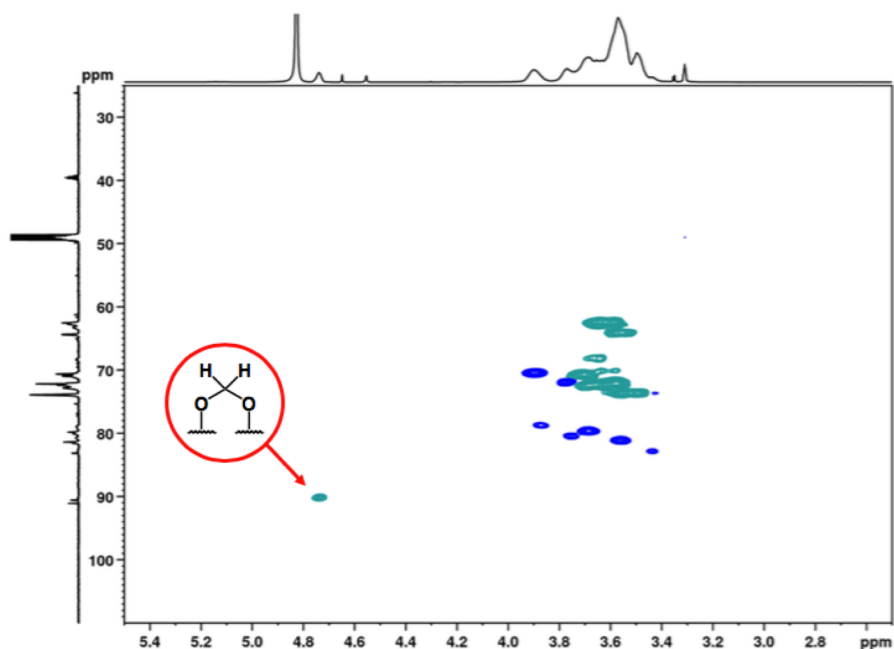


Figure V-3. HSQC NMR spectrum for polyglycidol prodrug to confirm ^1H and ^{13}C assignments.

V.2.2 Evaluation of pH Responsive Formaldehyde Release from Polyglycidol Prodrug

PG-acetal prodrug was suspended in acetic acid-sodium acetate buffer (pH 5.0) or phosphate buffered saline (PBS, pH 7.4) in a Float-a-Lyzer® dialysis device. The dialysis device was submerged in a centrifuge tube containing a known amount of dialysis buffer and continually stirred at 37 °C. Aliquots were removed from the dialysis buffer and analyzed by Purpald® colorimetric assay for formaldehyde concentration. Initial concentration of formaldehyde detected for each release can be attributed to free formaldehyde trapped in the viscous polymer matrix during conjugation but not chemically bound to the polymer. This unbound formaldehyde can be detected by ^1H and ^{13}C NMR analysis, and was calculated to be 1.2 wt %, or approximately 27% of the total formaldehyde in the sample for pH 5 and approximately 48% for pH 7.4. Release of formaldehyde in pH 5.0 exhibited a controlled release over 14 days compared to pH 7.4 in which

very low amounts of formaldehyde release was observed (**Figure V-4**). The burst release exhibited in the first six hours of assay is attributed to the free formaldehyde. The prodrug in pH 5 reached 90% of formaldehyde released in 12 days. These data indicate the acetal linkage is quite stable in neutral conditions, and can be triggered for release upon increase in acidity, which is advantageous for our application as anticancer treatments due to the known acidity of tumor extracellular matrix (pHe).²³⁻²⁵

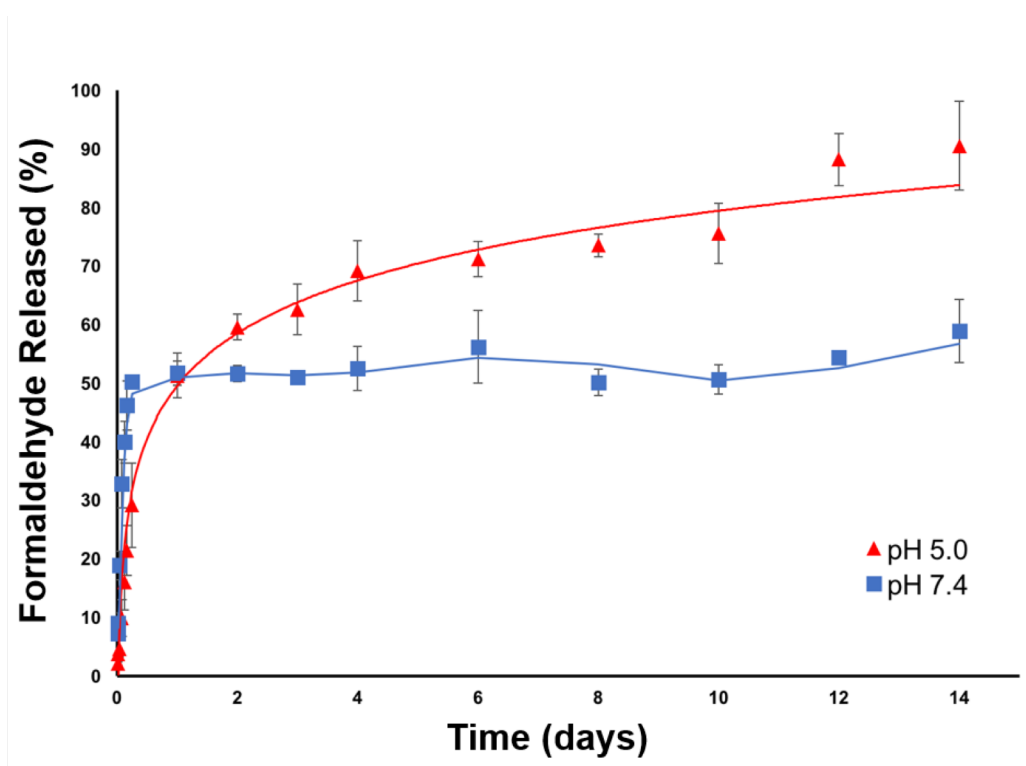


Figure V-4. Cumulative release profile for formaldehyde from polyglycidol prodrug, PG-Acetal, in pH 5 and 7.4 at 37 °C over 14 days demonstrating a pH-responsive release profile for the acetal and little to no release in neutral conditions. Values are averages of measurements in triplicate.

V.2.3 *In Vitro* Evaluation of Synergistic Effect for Improved Cytotoxicity of 4T1 Cells using Polyglycidol-based Prodrugs

As this prodrug is intended for use along with an anthracycline drug for synergistic therapy, we investigated the action of this construct *in vitro*. Preliminary data from our collaboration with the McCullough Research Group (Oregon Health and Science University) provided promising *in vitro* results for the efficacy of the prodrug-doxorubicin combination matrix against MCF-7 breast cancer cells.³⁸ To confirm these results, we performed *in vitro* evaluation of the prodrug material in combination with free doxorubicin using 4T1 mouse breast cancer cells. Free doxorubicin was used as a starting point to test whether an increase in apoptosis of the cancer cells could be observed by the addition of the prodrug. 4T1 cells were seeded into a 96-well plate and then incubated for 24 hours with either free doxorubicin, doxorubicin plus free formaldehyde (formalin solution), or doxorubicin plus the PG-acetal prodrug. The concentration of doxorubicin was 0.1 µg/mL and the concentration of formaldehyde was 0.01 µg/mL for all cases. Treatment was incubated with cells for 24 hours, where then the cytotoxicity was measured against a control (cells without treatment) using a colorimetric cell viability assay. The results of the viability assay shown in **Figure V-5** demonstrate that the combination of doxorubicin with the polyglycidol formaldehyde prodrug is in fact the most efficacious combination for the killing of the cancer cells.

Future steps for *in vitro* evaluation of this prodrug concept will involve the administration of the prodrug containing a suspension of doxorubicin-loaded nanoparticles to closer match the intended delivery method as described previously. Partially reduced ketoxime/alkoxyamine nanoparticles have been successfully loaded with doxorubicin to a loading capacity of 17 wt% and are poised to be tested in conjunction with the PG-acetal prodrug for action against 4T1 cells.

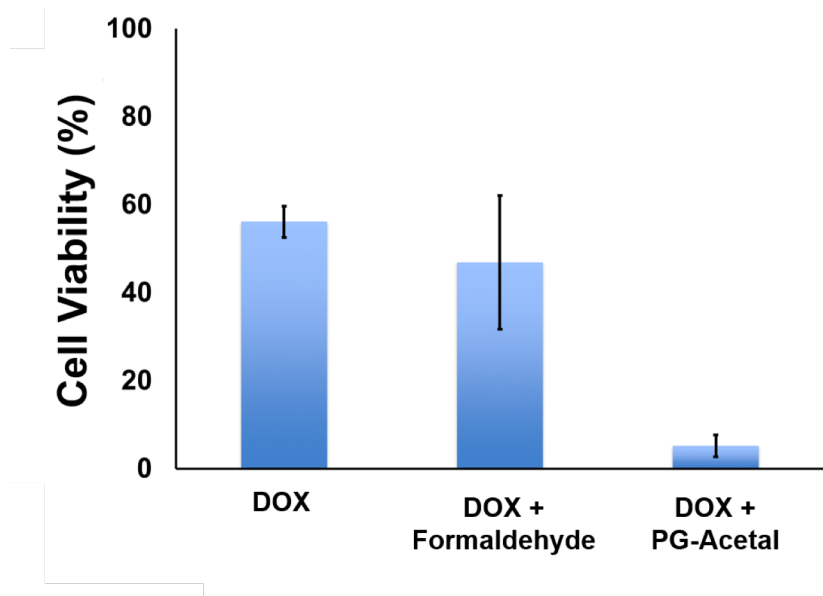


Figure V-5. Cell viability of 4T1 cells to evaluate efficacy of DOX + PG-Acetal combination compared to DOX and DOX + formaldehyde. Analysis determined the cell killing was approximately 11-fold higher with the co-administration of DOX + PG-Acetal than DOX and free formaldehyde. These results indicate the utility of the sustained release prodrug system as a formaldehyde releasing agent for the improved efficacy of doxorubicin against cancer cells. Values are averages of measurements in triplicate.

V.2.4 Synthesis of Aminoxy Polyglycidol Formaldehyde Prodrug

Due to the positive results exhibited by PG-acetal prodrug, we sought to continue our work with polyglycidol-based prodrugs. However, the low molecular weight and limited terminal units of the polyglycidol available for formaldehyde conjugation made it difficult to achieve higher formaldehyde loading necessary for practical clinical use, so we began investigating another potential formaldehyde prodrug using a functionalized polyglycidol that possessed increased reactive functionality. In addition to forming adducts with diol to form acetal, formaldehyde is anticipated to react with aminoxy groups to form an aldoxime bond. Previous work in our lab has led to the development of an aminoxy-functionalized polyglycidol (P(G^{AO}-co-G) which can be prepared with 15-70% aminoxy functionality.²² This functionalized polymer provides

potential versatility for variable loading of formaldehyde. P(G^{AO}-co-G) containing 67% aminoxy was reacted with 37 wt% formaldehyde solution and characterized by NMR as previous with PG-Acetal. **Figure V-6** illustrates the ¹H and ¹³C-IG NMR spectra of P(G^{AO}-co-G)-Oxime. As seen, there are two distinct resonance signals for the oxime protons observed at 6.52 and 7.07 ppm. The ¹³C-IG spectrum exhibits the oxime carbon resonance at 140 ppm, the furthest downfield signal due to its electronegative environment. Similar to the PG-Acetal, the HSQC spectrum confirms the initial assignments.

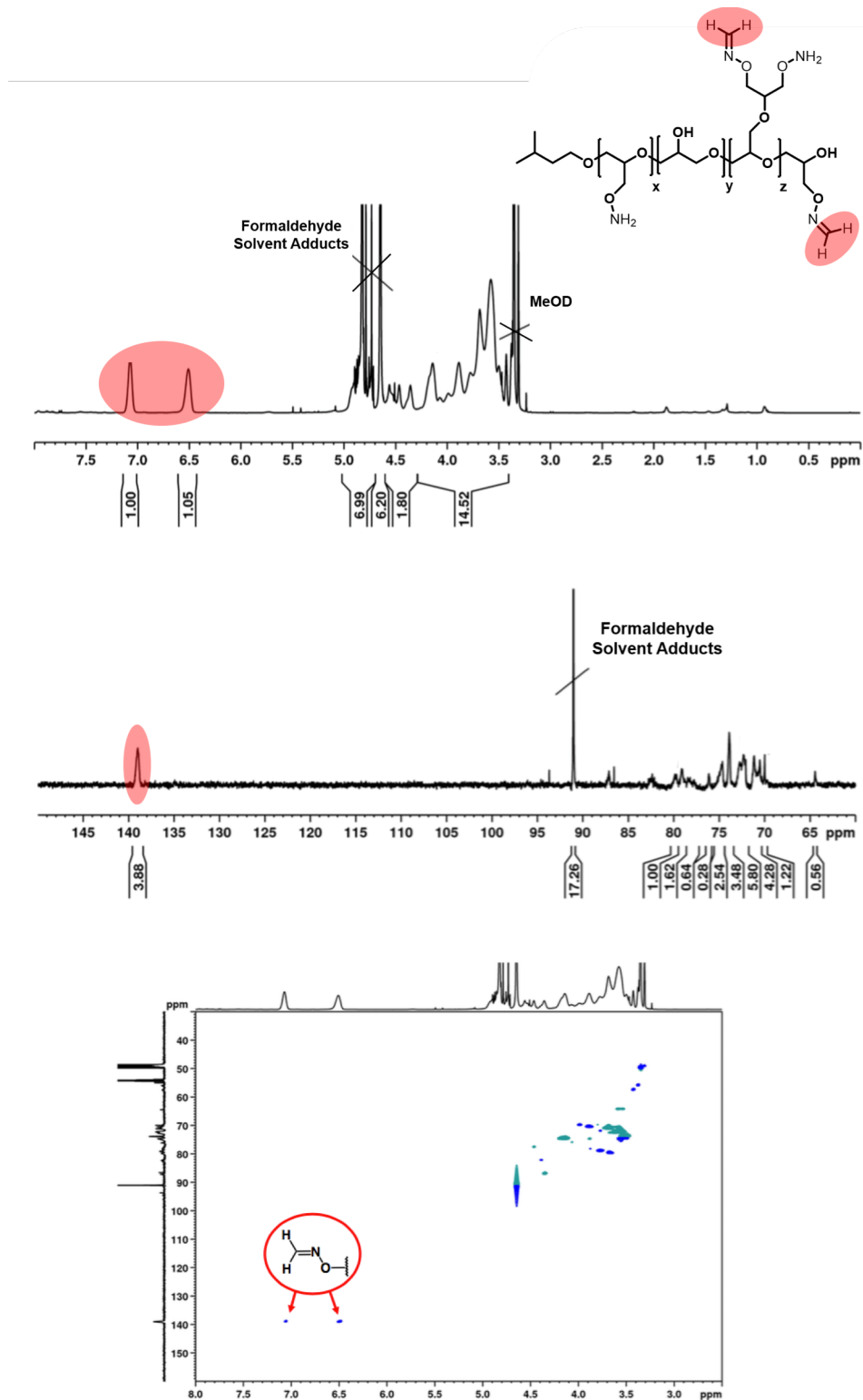


Figure V-6. ¹H (top), ¹³C-IG (middle), and HSQC (bottom) NMR spectra for P(G^{AO}-co-G)-Oxime indicating aldoxime proton resonance signals at 6.52 and 7.07 ppm corresponding to the single carbon resonance at 140 ppm in the ¹³C NMR spectrum (highlighted in red).

V.2.5 Evaluation of pH Responsive Formaldehyde Release from Aminoxy-Functionalized Polyglycidol Prodrug

Analyzing the release of formaldehyde from aminoxy-functionalized polyglycidol prodrug proved to have multiple challenges. Following formaldehyde conjugation and removal of solvent, the material became insoluble in organics or aqueous solvent and could only be solubilized through the addition of strong acid. We hypothesized that the unreacted aminoxy functionalities present on the polymer were contributing to strong intra- and intermolecular hydrogen bonding which formed a gel-like material. Due to the acid-labile nature of the aldoxime bond, the addition of strong acid led to rapid hydrolysis of the formaldehyde from the polymer, reversing the prodrug. Since we attributed this gelation to the hydrogen bonding from unreacted aminoxy functionalities, we increased the equivalents of formaldehyde to aminoxy so that there was a large excess (~50 equiv.) of formaldehyde. However, the disadvantage of this approach was a large amount of free formaldehyde became entrapped in the viscous matrix during the drying procedure. Fortunately, we were able to isolate the free formaldehyde resonance in the ^1H NMR so it is quantifiable, and the release assay can be adjusted for the free formaldehyde.

Following the protocol described above for the PG-Acetal prodrug, P(G^{AO}-co-G)-Oxime prodrug was added to Float-a-Lyzer® dialysis device and suspended in 18 mL of release media, either sodium acetate-acetic acid buffered to pH 5 or PBS buffered to pH 7.4. Aliquots of 100 μL were removed from the release media and replaced with fresh media. The concentration of formaldehyde was analyzed by the Purpald® colorimetric assay. Unfortunately, the analysis of formaldehyde concentration in release solution from both acidic and neutral conditions exhibited almost no release of conjugated formaldehyde from the prodrug (**Figure V-7**). Calculations from the ^{13}C -IG NMR determined this material contains 6.6 wt % formaldehyde bound as an oxime

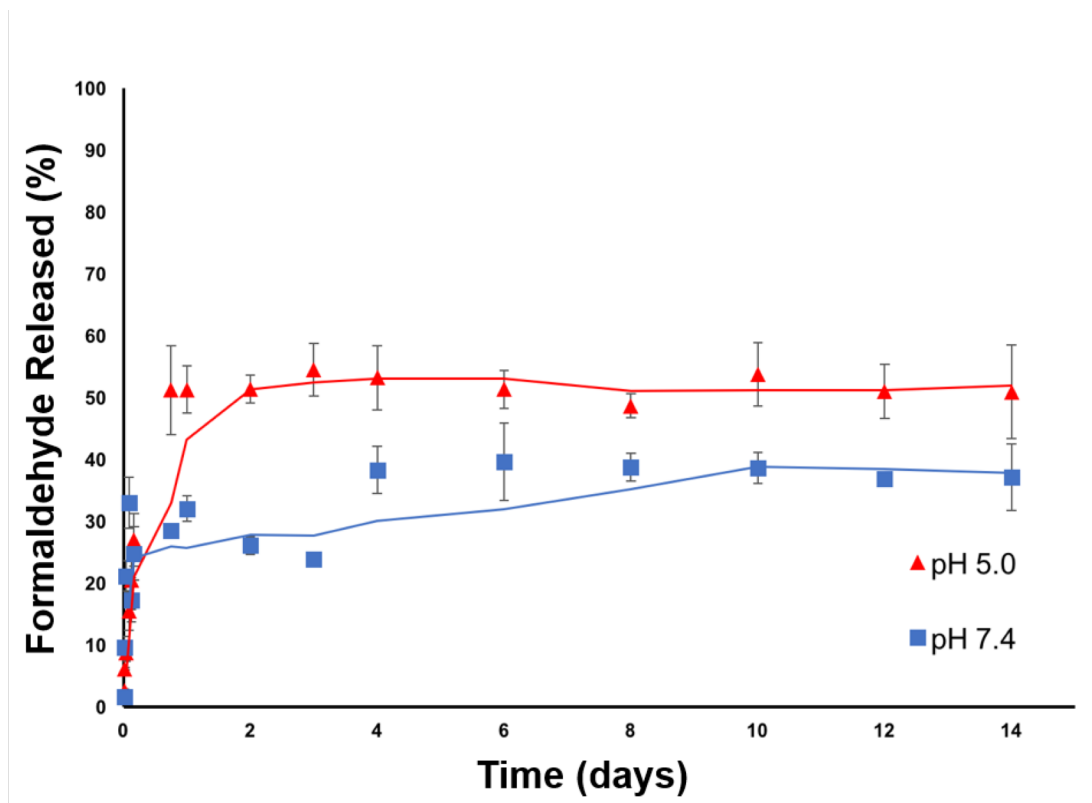


Figure V-7. Cumulative release of formaldehyde from P(G^{AO}-co-G)-Oxime in pH 5 and 7.4 at 37 °C over 14 days. Values are averages of measurements in triplicate.

adduct and 35.7 wt % of the product is the result of formaldehyde adducted to methanol, which as before will be an important practical consideration when analyzing the release profile of the formaldehyde from this prodrug construct. As multiple branching units in this polymer will have amino-oxy functional groups, there is no standard in the ¹³C-IG NMR as there was for the acetal linked prodrug to determine a reaction efficiency. However, the ¹H NMR can provide an estimate by comparing the signal for the backbone protons to that of the oxime protons. Comparison of these integrals demonstrates a 35.2 mol % loading of the formaldehyde onto the backbone. As the precursor was calculated to have a 67 mol % content of amino-oxy group which indicates a reaction efficiency of 52.6%. The free formaldehyde trapped in the prodrug matrix was determined to be

approximately 35.7%. We attributed this lack of release to the strong hydrogen bonding capabilities of the aminoxy functionalities. Through this, we determined the aminoxy-functionalized polyglycidol prodrug was not a suitable approach to the prodrug matrix as we had anticipated.

V.2.6 Increasing Control over Formaldehyde Loading using Tunable Linear Polyacrylate Prodrug Scaffolds

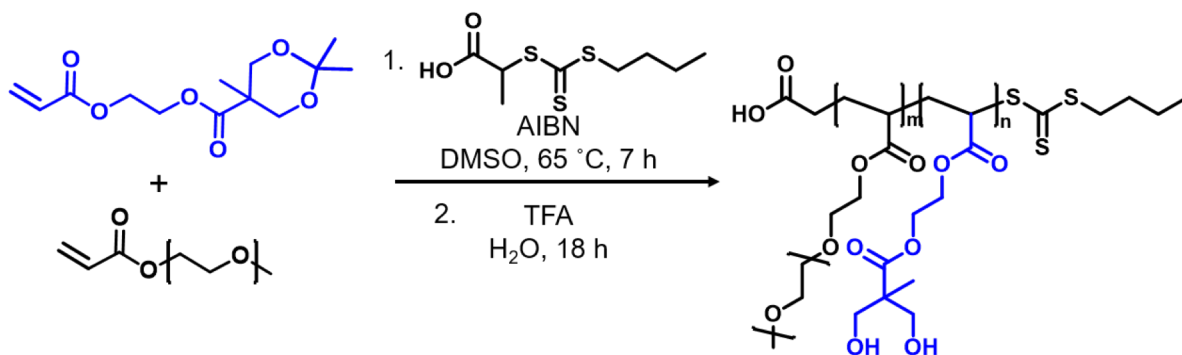
While we have achieved controlled, pH responsive release using the polyglycidol prodrug platform, the low molecular weight coupled with low abundance of terminal units for conjugation significantly limits the formaldehyde loading possible with the polyglycidol matrix. We were encouraged with the increased formaldehyde loading achieved by the development of our P(G^{AO}-*co*-G)-oxime prodrug. However, the difficulty of synthesis and analysis of the aminoxy-functionalized prodrug, due to the strong hydrogen bonding from aminoxy functionalities causing gelation, led us to determine it is not a viable or practical delivery matrix. In an effort to develop a polymer with a variable diol incorporation which could be utilized for tunable formaldehyde loading, linear polyacrylates bearing 1,3- and 1,2-diols were prepared at varying ratios of diol and a range of molecular weights to demonstrate the tailorability of the proposed prodrug matrix.

V.2.7 Synthesis of Poly(Methoxy PEG Acrylate-*co*-1) (P(MPEGA-*co*-1))

First, a protected diol was synthesized by formation of acetonide with a propionic acid and dimethoxypropane catalyzed by *p*-toluenesulfonic acid (PTSA). The acetonide carboxylic acid was then dehydrated to form the anhydride by N,N'-dicyclohexylcarbodiimide (DCC) coupling. The functionalized acrylate was then prepared by esterification of the anhydride with hydroxyethyl

acrylate to afford 1,3-protected diol acrylate (1,3-PDA). Methoxy polyethylene glycol acrylate (MPEGA) was chosen as a comonomer due to its hydrophilicity and viscosity, two properties ideal in the final polymer matrix. Copolymers with molar ratios of 80:20 and 60:40 (MPEGA:1,3-PDA) with a target MW of 10K g mol^{-1} were prepared by thermal initiated reversible addition fragmentation chain transfer (RAFT) polymerization (**Scheme V-2**). The RAFT agent, (2-(*n*-butyltrithiocarbonate)-propionic acid, BTPA) was chosen as the chain transfer agent (CTA) due to its ability to polymerize a wide variety of acrylate monomers.

Scheme V-2. Synthesis scheme of P(MPEGA-*co*-1) and subsequent deprotection to afford the reactive 1,3-diol for formaldehyde conjugation.



In the ¹H NMR spectrum seen in **Figure V-8**, the integration of the methyl protons of the CTA were set to 3.00 as an internal standard against the integrations of the methyl proton resonances for **1** and MPEGA to determine conversion of monomer and molecular weight (19 % **1**, 81 % MPEGA, $M_n = 12,337 \text{ g mol}^{-1}$). Gel permeation chromatography (GPC) was used to further characterize the polymer ($M_n = 11,100 \text{ g mol}^{-1}$, $M_w = 12,400 \text{ g mol}^{-1}$, $D = 1.11$, **Figure V-9**) and confirm the accuracy of the NMR integrations. The narrow dispersity (M_w/M_n) indicates good control over polymerization of the acetonide monomer using BTPA. The polymer was then subjected to trifluoroacetic acid to deprotect the acetonide and afford the reactive 1,3-diol.

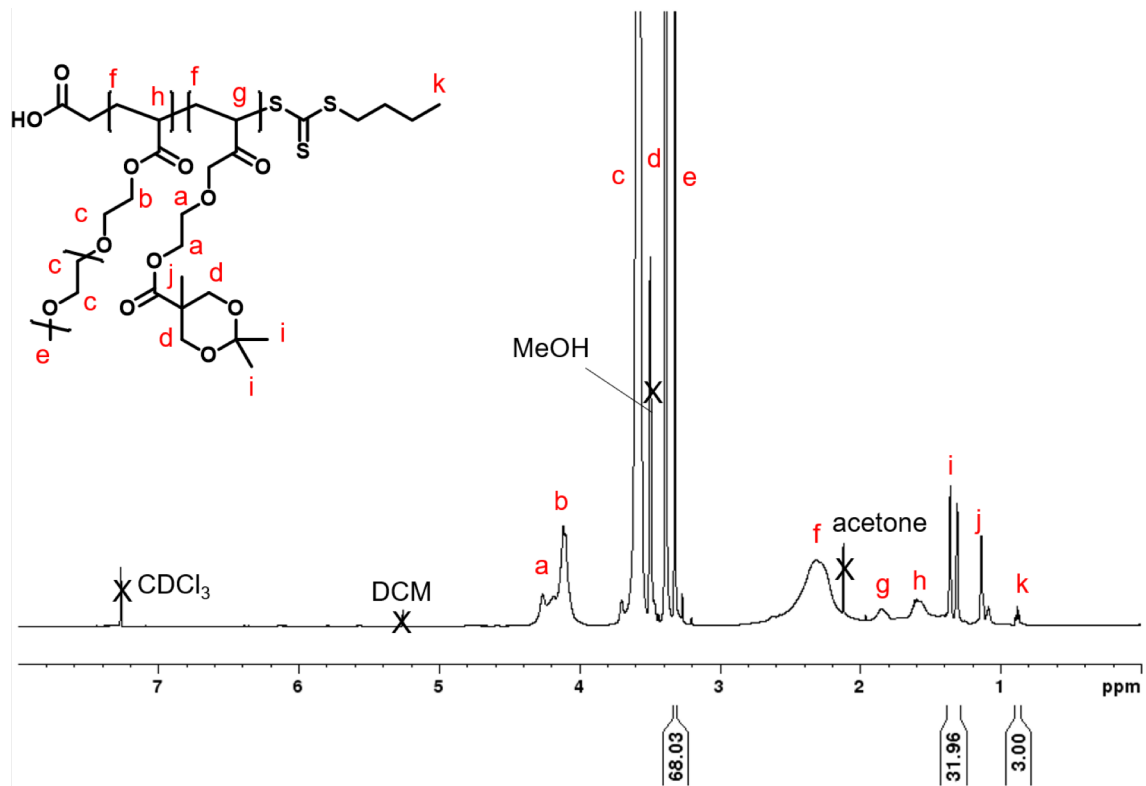


Figure V-8. ¹H NMR (600 MHz) spectrum of P(MPEGA-co-1).

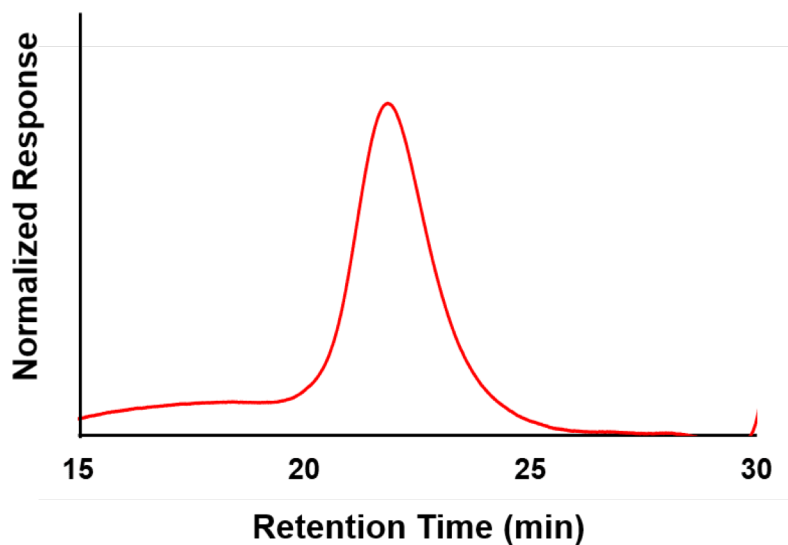
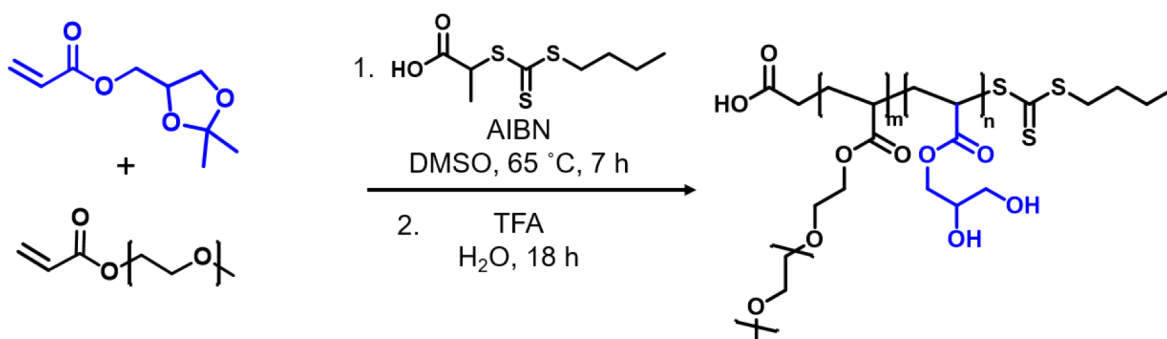


Figure V-9. GPC trace of P(MPEGA-co-1) in DMF with LiBr (0.1% v/v) at 60 °C with 1 mL/min flow rate.

V.2.8 Synthesis of Poly(Methoxy PEG Acrylate-*co*-Solketal Acrylate) (P(MPEGA-*co*-SA))

Additionally, we were interested in exploring the pH responsive behavior of a 5-membered acetal in comparison to the 6-membered structure studied previously. Therefore, in a similar synthetic scheme as for P(MPEGA-*co*-1), we prepared a polymer containing a protected 1,2-diol. First, the protected diol was synthesized by formation of acetonide with a glycerol and acetone catalyzed by *p*-toluenesulfonic acid (PTSA) to form solketal. Solketal was then esterified with acrolyl chloride to afford the 1,2-protected diol acrylate (1,2-PDA). Methoxy polyethylene glycol acrylate (MPEGA) was chosen as a comonomer due to its hydrophilicity and viscosity, two properties ideal in the final polymer matrix. 1,2-PDA was copolymerized with MPEGA in molar ratios of 80:20 and 60:40 (MPEGA:1,2-PDA) with a target MW of 10K g mol^{-1} by RAFT polymerization (**Scheme V-3**). Again, we used the methyl protons of the CTA set to 3.00 as an internal standard for determining the monomer conversion and molecular weight of the polymer (21 % SA, 79 % MPEGA, $M_n = 10,063 \text{ g mol}^{-1}$, **Figure V-10**). Gel permeation chromatography (GPC) was used to further characterize the polymer ($M_n = 10,700 \text{ g mol}^{-1}$, $M_w = 12,500 \text{ g mol}^{-1}$, $D = 1.17$, **Figure V-11**). The polymer was then subjected to trifluoroacetic acid to deprotect the acetonide and afford the reactive 1,2-diol.

Scheme V-3. Synthesis scheme of P(MPEGA-*co*-SA) and subsequent deprotection to afford the reactive 1,2-diol for formaldehyde conjugation.



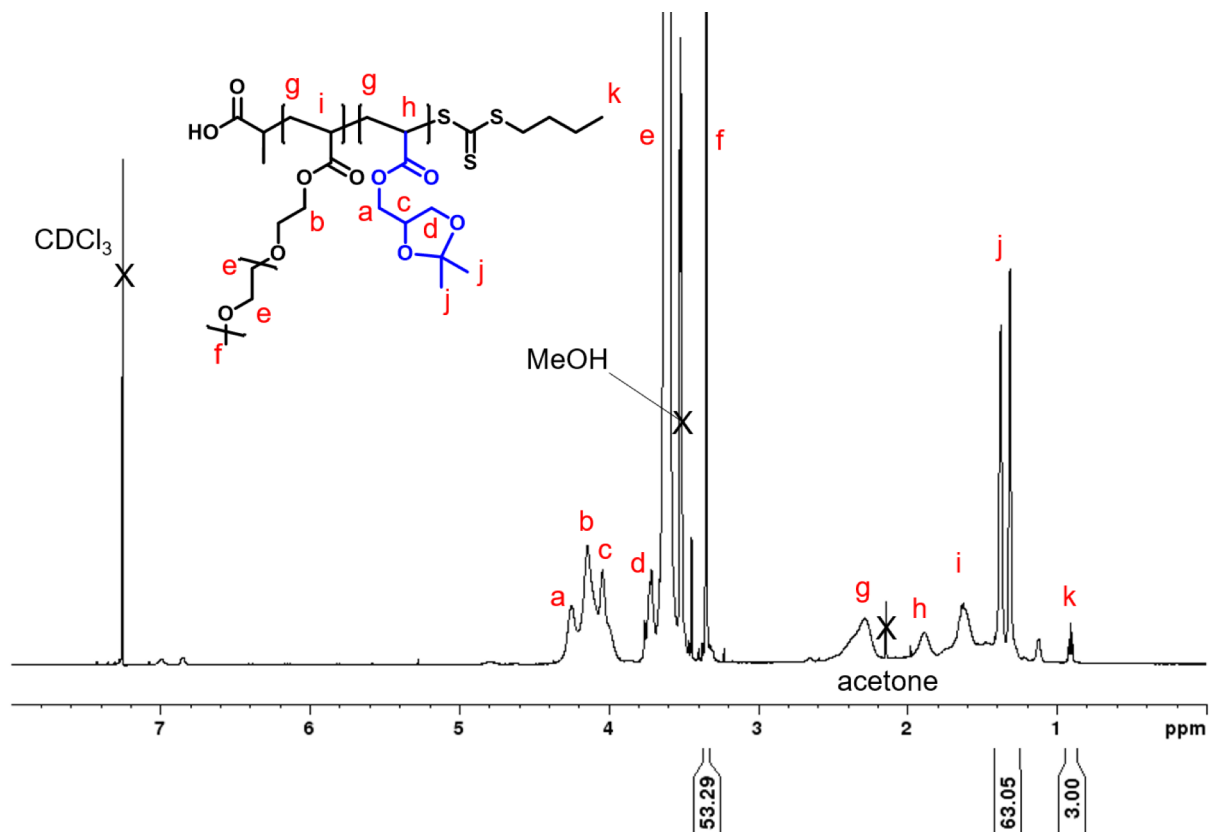


Figure V-10. ^1H NMR (600 MHz) of P(MPEGA-co-SA).

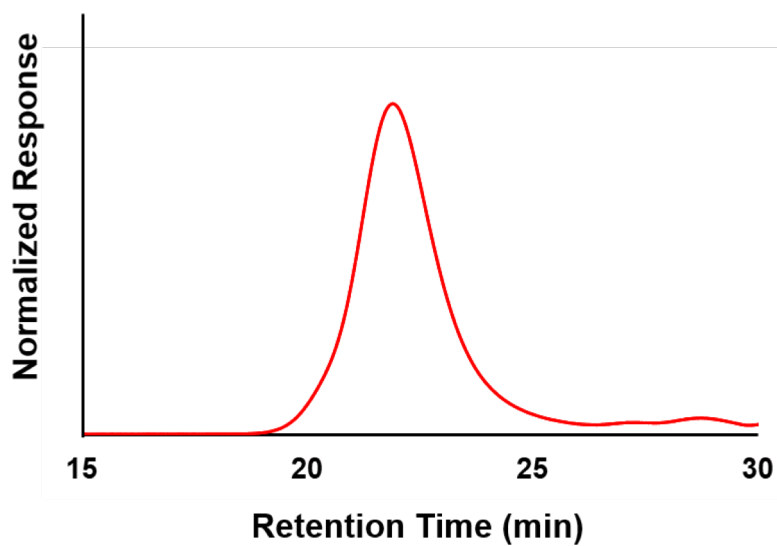


Figure V-11. GPC trace of P(MPEGA-co-SA) in DMF with LiBr (0.1% v/v) at 60 °C with 1 mL/min flow rate.

V.2.9 Preparation of Polyacrylate-based Formaldehyde Prodrugs

To attach formaldehyde to the polymer to form the prodrug, formaldehyde solution was mixed with polymer at a ratio of 50 equiv. formaldehyde:1 equiv. diol. A large excess of formaldehyde was used due to the propensity for formaldehyde to form solvent adducts and oligomerize which precludes it from forming the acetal with the polymer. The formaldehyde-polymer solution was mixed for 2 h at room temperature followed by two cycles of rotary evaporation to remove solvent. The prodrug was then placed under vacuum for 2 h to remove trace amounts of organic solvents. As the acetal protons are in the same ^1H region and shifted slightly upfield from free formaldehyde signals, it can be difficult to distinguish the acetal protons from unreacted formaldehyde remaining in solution. In order to remove the oligomerized formaldehyde remaining after vacuum drying, the mixture was solubilized in cell culture grade water and diluted to approximately 10 mg/mL and transferred to 3K MWCO centrifugal filters and centrifuged at 14K RPM for 40 min to remove excess formaldehyde oligomers. The filtrate was discarded, and the material collected in cell culture grade water and lyophilized. The conjugated material was characterized via ^1H and ^{13}C NMR as well as heteronuclear single quantum correlation (HSQC) spectroscopy. HSQC provides identification of the acetal protons and their corresponding carbon which shifts to ~ 90 ppm after conjugation. As seen in the top of **Figure V-12**, the proton resonance at 4.75 ppm correlates to the carbon resonance at 90.56 ppm for P(MPEGA-*co*-1). The bottom of **Figure V-12** shows the HSQC spectrum for P(MPEGA-*co*-SA) where there is an overlapping proton signal at 4.70 ppm for 89 and 90.56 ppm, as well as two additional proton shifts for 90.56 ppm at 4.63 and 4.53 ppm. This separation in resonances is attributed to the differences in the proton chemical environment exo- and endo- to the oxygens in the ring.

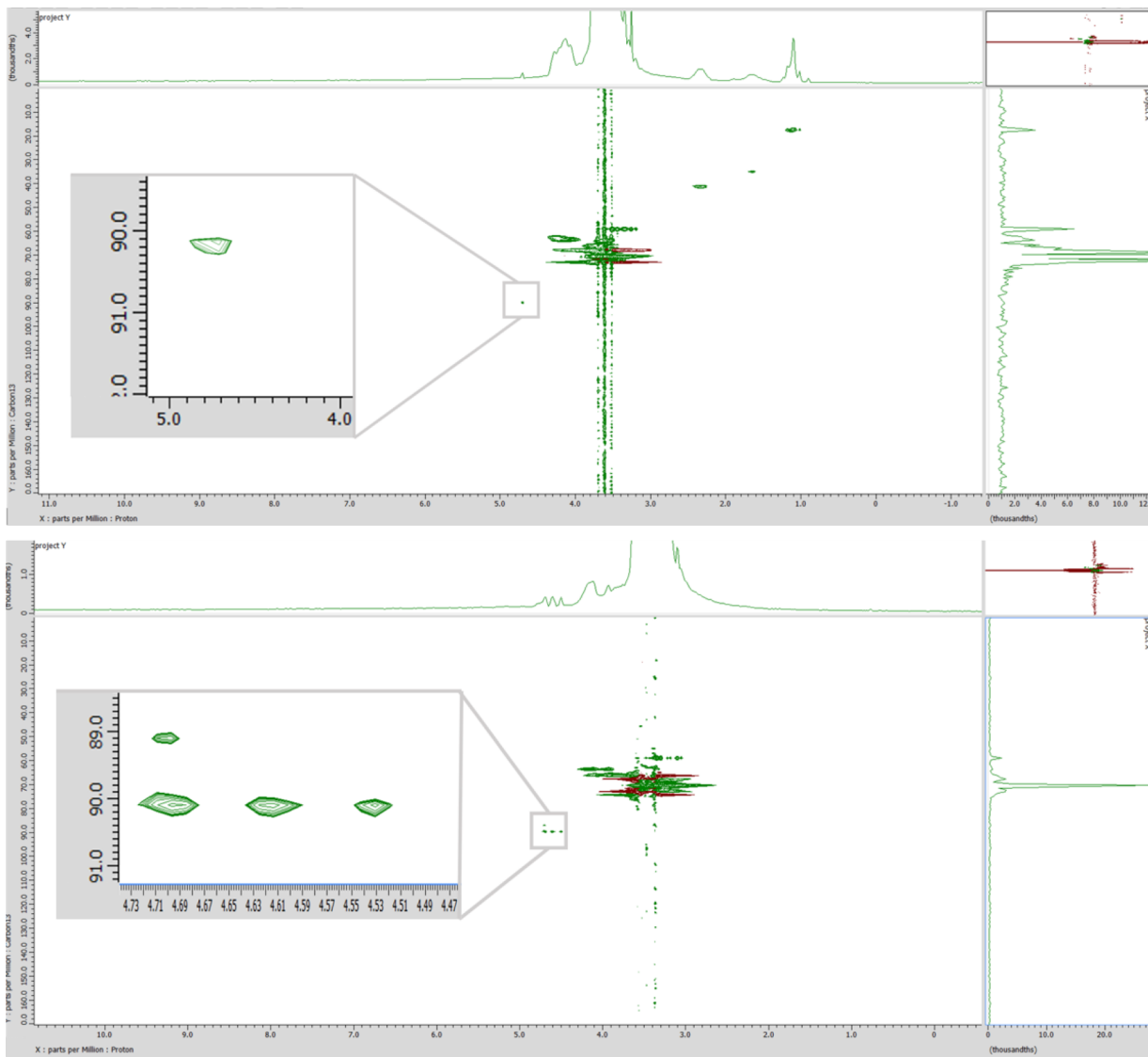


Figure V-12. HSQC spectra of P(MPEGA-*co*-1) (top) with inset of acetal proton signal and P(MPEGA-*co*-SA) (bottom) with inset of acetal signal.

V.2.10 Evaluation of pH Responsive Formaldehyde Release from Acrylate Prodrugs

The prodrugs were suspended in acetic acid-NaOAc buffer (pH 5.0) or phosphate buffered saline (PBS, pH 7.4) in a Float-a-Lyzer® dialysis device. The dialysis device was submerged in a centrifuge tube containing a known amount of dialysis buffer and continually stirred at 37 °C. Aliquots were removed from the dialysis buffer and analyzed by colorimetric assay for

formaldehyde concentration to determine cumulative formaldehyde released over time for each of the prodrugs in acidic and neutral environments (**Figure V-13**). Release of formaldehyde in pH 5.0 exhibited a controlled release over 7 days with a total release of ~75% of formaldehyde compared to pH 7.4 in which a small amount (~14%) of formaldehyde was released for P(MPEGA-*co*-1). Interestingly, the release rate of formaldehyde from the 1,3-diol appears to have a slightly faster rate of release and achieved more total release. In these initial experiments, it is difficult to determine if these differences are significant or attributed to experimental error in detection of formaldehyde in the colorimetric assay. Future work to determine reproducibility of these results in triplicate will be conducted. Nevertheless, these results are promising as they indicate the acetal linkage from the polyacrylate backbone is quite stable in neutral conditions and can be triggered for release upon increase in acidity.

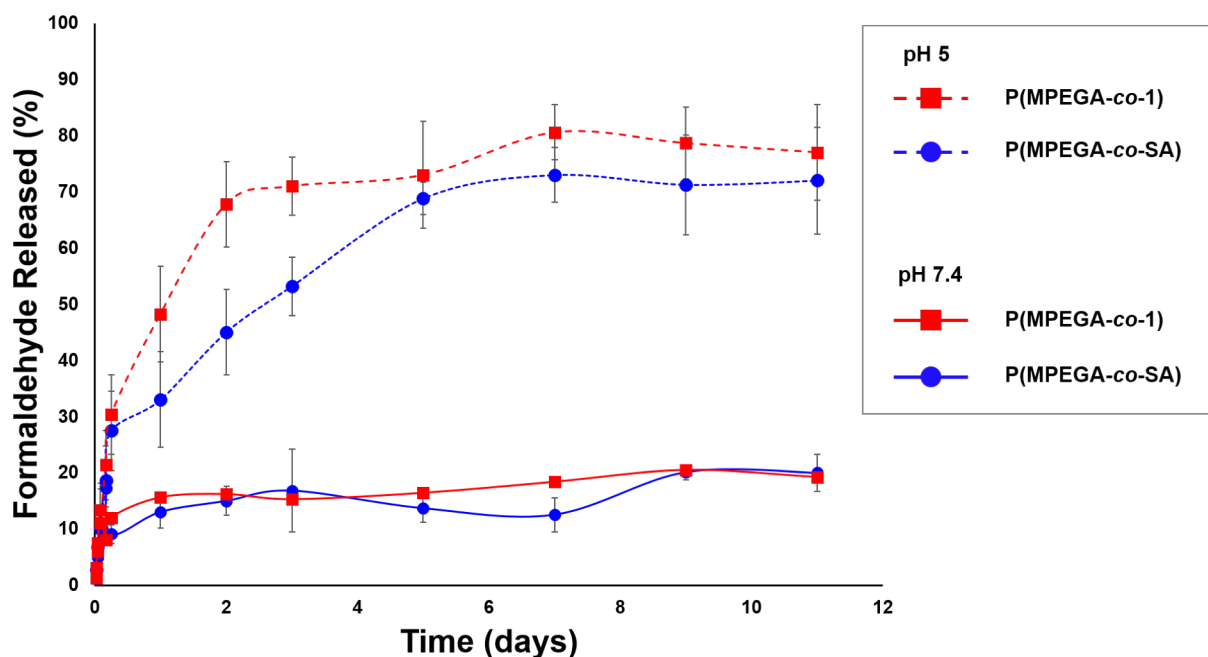


Figure V-13. Cumulative release of formaldehyde from P(MPEGA-*co*-1) (red square) and P(MPEGA-*co*-SA) (blue circle) in pH 5 (dotted line) and 7.4 (solid line) at 37 °C over 11 days. Values are averages of measurements in duplicate.

V.2.11 Preparation of Doxorubicin-Loaded Partially Reduced Ketoxime/Alkoxyamine Nanoparticles

Lastly, we chose to analyze the effect of pH on the release of doxorubicin from crosslinked polyester nanoparticles. We developed these nanoparticles to be highly tunable yet practical drug delivery vehicles for the encapsulation of small molecule hydrophobic drugs. Prepared through oxime click chemistry and partially reduced to a more stable alkoxyamine bond, these particles exhibit a varied degradation and drug release profile.³⁴ Briefly, ketone-bearing copolymer, poly(δ -valerolactone-*co*-2-oxepane-1,5-dione) (P(VL-OPD)), was synthesized to a ketone functionality of 8 mol %. The nanoparticles were synthesized through crosslinking with a bisaminoxy functionalized PEG at a concentration of 2.7 mM ketone to produce nanoparticles with dimensions of ca. 80 nm. After formation of nanoparticles, reducing agent was added to partially reduce the ketoxime crosslinks to alkoxyamine bonds. The partial reduction of the crosslink chemistry provides a tailored degradation and drug release profile.

Doxorubicin was encapsulated into the nanoparticles through a developed nanosolubilization technique. Nanoparticles and doxorubicin were mixed together with minimal organic solvent (DMSO). Water containing 1 wt% D- α -tocopherol polyethylene glycol 1000 succinate was added to the solution quickly and mixed vigorously. The material was centrifuged to collect the particle pellet, then washed with excess water and lyophilized to produce DOX-loaded nanoparticles.

V.2.12 *In Vitro* Release of Doxorubicin from Partially Reduced Ketoxime/Alkoxyamine Nanoparticles

DOX-loaded nanoparticles were suspended in either sodium acetate-acetic acid buffer (pH 5) or PBS (pH 7.4) containing 0.1% v/v Tween-80 as a surfactant. Tween-80 is a common surfactant used for *in vitro* release assays for drugs with poor water solubility, as it promotes suspension of the drug in the release media and increases release profile accuracy when aligned with true physiological conditions.³⁹⁻⁴¹ We again utilized the Float-a-Lyzer® dialysis method, where DOX-loaded nanoparticles were suspended in release buffer and transferred to a 1 mL dialysis pod. The pod was placed in 18 mL of release media inside a large centrifuge tube, and at specified time points, 100 μ L aliquots were removed from the sink and replaced with fresh buffer. The cumulative drug concentration of each aliquot was analyzed by HPLC. **Figure V-14** illustrates the release profile of the DOX-loaded nanoparticles in acidic and neutral conditions.

Interestingly, the cumulative drug released from particles at pH 7.4 is very low, indicating this environment is not favorable for drug release of this system. In contrast, the release of DOX at pH 5 reaches 50% in the first 48 hours and proceeds to level at ~70% drug released after 4 days. It is apparent from these results that some further work is needed to continue optimization of the doxorubicin drug delivery method, however these are promising results for the synergistic release of doxorubicin and formaldehyde in cancer therapies, as the pH-responsive release of DOX-loaded nanoparticles complements the pH-responsive formaldehyde release from the polymer matrix.

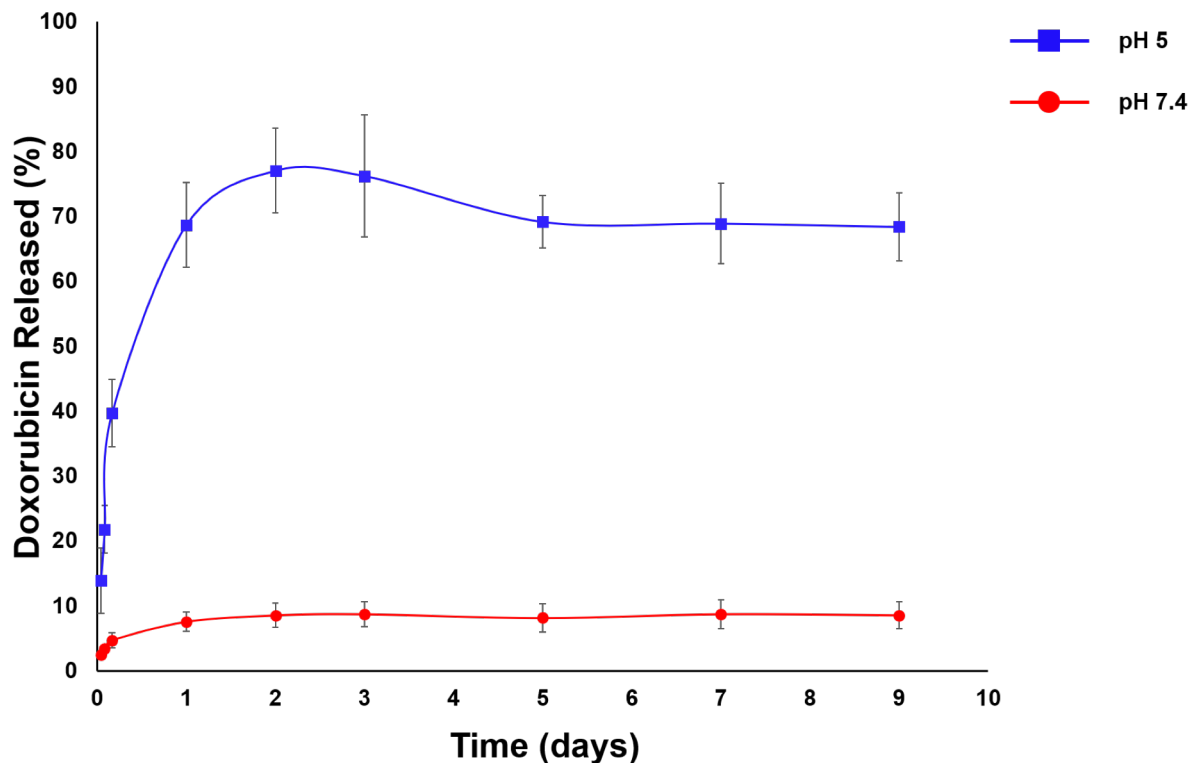


Figure V-14. Cumulative release of doxorubicin from polyester ketoxime/alkoxyamine nanoparticles in pH 5 (blue square) and 7.4 (red circle) at 37 °C over 9 days. Values are averages of measurements in triplicate.

V.3 Conclusion

We have successfully synthesized four distinct polymer materials which can be prepared at a range of molecular weights and functionalization percentages for controlled formaldehyde loading. Polyglycidol and aminoxy polyglycidol were prepared at low molecular weights (~2kD) and formaldehyde was conjugated to form the acetal and oxime prodrugs. These materials were extensively characterized by NMR spectroscopy and evaluated for their *in vitro* release of formaldehyde. A pH-responsive release mechanism was exhibited, and additionally, cell viability experiments with PG-Acetal demonstrated an improved efficacy of doxorubicin cytotoxicity by almost 11-fold against 4T1 cells. Challenges presented by the gelation of the aminoxy

polyglycidol precursor and its prodrug led the development of another polymer backbone which possesses increased practicality and functionality. These polymers proceeded with a practical RAFT polymerization technique and were prepared at precise and controlled molecular weights of approximately 10kD and 20kD. Formaldehyde was successfully conjugated to these polyacrylate-based polymers containing both 1,2- and 1,3-diols and further characterized by NMR spectroscopy. Furthermore, doxorubicin loaded nanoparticles were prepared and evaluated for their *in vitro* release of drug in pH 5 and 7.4 release media. The results indicate an increased release rate of doxorubicin in acidic media, a complementary release profile to that of the prodrugs. Future work will proceed with the evaluation of the polyacrylate formaldehyde prodrugs cell viability alone and in conjunction with doxorubicin-loaded nanoparticles and its efficacy towards 4T1 cells. These materials possess great potential for the synergistic controlled release of formaldehyde and doxorubicin as anticancer treatments.

V.4 Experimental

Materials

All reagents were purchased from MilliporeSigma, Tokyo Chemical Industry America, or Fisher Scientific and used without further purification unless otherwise specified. Methoxy PEG acrylate was passed through column of inhibitor remover prior to polymerization. Spectra/Por® dialysis tubing (MWCO = 1000 Da) and Float-a-Lyzer® (MWCO = 0.1-0.5 kDa) were purchased from Spectrum Laboratories Inc. 2-(*n*-butyltrithiocarbonate)-propionic acid was prepared according to literature.

Characterization

^1H and ^{13}C NMR spectra were recorded on Bruker AV-I 400, Bruker AV-III 600 MHz, JEOL ECX-400, and JEOL ECA-600 II spectrometers. Chemical shifts were referenced to solvent resonance signals. Gel permeation chromatography (GPC) was conducted on a ToSOH EcoSEC HLC-8320GPC system equipped with a refractive index detector, UV-8320 detector, and TSKgel H_{HR} columns (7.8x300mm G5000 H_{HR} , G4000 H_{HR} , and G3000 H_{HR}) with *N*-dimethylformamide (DMF) as the eluent at a flow rate of 1 mL/min. High performance liquid chromatography (HPLC) analysis of drug concentration was conducted using a ThermoFisher Ultimate 3000 HPLC system and Phenomenex column (Luna 5 μ C8(2) 100Å, 150 x 4.6 mm, 5 μ m) with a gradient solvent system of 100% A to 30% A:70% B over 12 min. Solvent A was water with 1% trifluoroacetic acid (TFA), and solvent B was 90% acetonitrile/10% water with 1% TFA. The column was maintained at 35 °C and the absorbance was measured at 475 nm.

Synthesis of Polyglycidol (PG)

Under nitrogen atmosphere, tin(II) trifluoromethanesulfonate (9.1 mg, 21 μ mol) and isoamyl alcohol (90.76 μ L, 0.833 mmol) were added to a 25 mL round bottom flask. Glycidol (4.5 mL, 67 mmol) was added dropwise at 0 °C in portions over 20 min. The reaction was allowed to warm to room temperature and stirred 18 h until reaction mixture viscosity prohibited stirring. MeOH (5 mL) was added and the polymer was precipitated in ethyl acetate (2x) and dried *in vacuo*. (4.6 g, 91%, $M_n = 1.6$ kDa, $M_w = 4.7$ kDa, $D = 2.89$). ^1H NMR (600 MHz, MeOD) δ : 0.92 (6H, d, CH₃), 1.48 (2H, q, CH₂), 1.72 (1H, m, CH), 3.39-3.98 (5H, m, CH₂CHCH₂). ^{13}C -IG NMR (150 MHz, MeOD) δ : 61.3, 61.8, 63.0, 69.3, 69.6, 70.5-71.9, 72.6, 78.6, 80.1, 81.8.

Synthesis of Polyglycidol Formaldehyde Prodrug (PG-Acetal)

PG (500 mg, 480 μmol) was dissolved in MeOH to a concentration of 250 mg/mL and transferred to a 6-dram vial equipped with a stir bar. A 37% formaldehyde solution (214 μL , 2.881 mmol, 6.0 eq) was added to the reaction vial, and the mixture was stirred at room temperature for 1 hour. Methanol was removed via rotary evaporation and water was removed via lyophilization. ^1H NMR (600 MHz, MeOD) δ : 0.92 (6H, d, CH_3), 1.48 (2H, q, CH_2), 1.72 (1H, m, CH), 3.39-3.98 (5H, m, CH_2CHCH_2), 4.74 (2H, s, CH_2). ^{13}C -IG NMR (150 MHz, MeOD) δ : 61.3, 61.8, 63.0, 69.3, 69.6, 70.5-71.9, 72.6, 78.6, 80.1, 81.8, 90.6.

Synthesis of Aminoxy-Functionalized Polyglycidol ($P(\text{G}^{\text{AO}}\text{-co-G})$)

To a 250 mL round bottom flask under argon, a solution of polyglycidol ($M_n = 2067 \text{ gmol}^{-1}$, 4.16 g, 2 mmol) in *N*-dimethylformamide (DMF, 31 mL) was added. *N*-hydroxyphthalimide (5.29 g, 32 mmol) followed by triphenyl phosphine (8.52 g, 32 mmol) was added. Diisopropyl azodicarboxylate (6.32 mL, 32 mmol) was then added dropwise at 0 $^\circ\text{C}$. The mixture was allowed to warm to RT and stirred for 24 h. The reaction was concentrated under reduced pressure and reconstituted in DCM then precipitated twice in ethyl acetate:ether (1:1) to obtain an off-white solid. (5 g, 70%, G = 61%, $\text{G}^{\text{NOP}} = 39\%$). ^1H NMR (400 MHz, d-DMSO) δ : 0.92 (6H, d, CH_3), 1.48 (2H, q, CH_2), 1.72 (1H, m, CH), 3.08-4.29 (5H, m, CH_2CHCH_2), 4.29-5.09 (1H, m, OH), 7.51-7.88 (4H, m, CH)

N-oxyphthalamide-functionalized polyglycidol was solubilized in tetrahydrofuran (THF, 75 mL) and added to a 250 mL round bottom flask equipped with stir bar and argon balloon. MeOH (75 mL) followed by an excess of hydrazine (2.23 mL, 71 mmol) was added and stirred for 18 h. The reaction mixture was filtered through 0.45 μm PTFE filter to remove white solid byproduct and

the filtrate solvent evaporated. The residual solid was resuspended in MeOH and filtered again. The filtrate was transferred to dialysis tubing (MWCO = 1000 Da) and dialyzed against water for 6 h then methanol for 18 h. After dialysis, the product was concentrated and dried *in vacuo*. (1.01 g, 33%, G = 61%, G^{AO} = 39%). ¹H NMR (600 MHz, MeOD) δ : 0.87 (6H, d, CH₃), 1.42 (2H, q, CH₂), 1.66 (1H, m, CH), 3.45-4.28 (5H, m, CH₂CHCH₂). ¹³C-IG NMR (150 MHz, MeOD) δ : 63.8, 69.3, 70.2, 71.7, 73.2, 76.3, 77.5, 78.2, 79.1

Synthesis of Aminoxy-Functionalized Polyglycidol Formaldehyde Prodrug ((P(G^{AO}-co-G)-Oxime)

Aminoxy polyglycidol (150 mg, 51.9 μ mol, 1.0 eq) was dissolved in methanol to a concentration of 37.5 mg/mL and transferred to a 6-dram vial equipped with a stir bar. A 37% formaldehyde solution (269.6 μ L, 3.624 mmol, 7.2 eq/oxime) was added to the reaction vial, and the mixture was stirred at room temperature for 1 hour. Methanol was removed via rotary evaporation and water was removed via lyophilization. ¹H NMR (600 MHz, MeOD) δ : 0.87 (6H, d, CH₃), 1.42 (2H, q, CH₂), 1.66 (1H, m, CH), 3.45-4.28 (5H, m, CH₂CHCH₂), 6.51 (1H, s, CH₂), 7.07 (1H, s, CH₂). ¹³C-IG NMR (150 MHz, MeOD) ¹³C-IG NMR (150 MHz, MeOD) δ : 64.5, 70.0, 70.6, 71.2, 72.5, 73.9, 74.7, 76.1, 77.9, 79.1, 79.8, 139.0

Synthesis of Solketal

Glycerin (15 g, 0.163 mol), PTSA (2.3 mmol), anhydrous acetone (44 mL), and hexanes (44 mL) were added to a reaction flask over 4 Å molecular sieves. The reaction was refluxed for 12 h and sieves were removed by gravity filtration. The product was concentrated, solubilized in ether, and

decanted to purify. (9.7 g, 45%) ^1H NMR (600 MHz, CDCl_3) δ : 1.34 (3H, s, CH_3), 1.41 (3H, s, CH_3), 3.56 (1H, q, CH), 3.73 (2H, m, CH_2), 4.00 (1H, q, CH_2), 4.2 (1H, q, CH_2)

Synthesis of Solketal Acrylate

Under nitrogen atmosphere, solketal (9.2 g, 0.07 mol) and TEA (9.73 mL, 0.07 mol) were added to DCM (140 mL). Acryloyl chloride (5.64 mL, 0.07 mol) was added to the reaction slowly at 0 °C. The reaction proceeded at room temperature for 6 h. The product was washed with sat. sodium bicarbonate solution and DI water. The product was purified by column chromatography with ethyl acetate:hexane mixture (1:2) as eluent. (3.861 g, 30%) ^1H NMR (600 MHz, CDCl_3) δ : 1.37 (3H, s, CH_3), 1.43 (3H, s, CH_3), 3.76 (1H, m, CH), 4.09 (1H, m, CH_2), 4.17 (1H, m, CH_2), 4.2 (1H, m, CH_2), 4.36 (1H, m, CH_2), 5.87 (1H, dd, $\text{HC}=\underline{\text{CH}}_2$), 6.16 (1H, m, $\underline{\text{HC}}=\text{CH}_2$), 6.44 (1H, dd, $\text{C}=\underline{\text{CH}}_2$)

General Procedure for Synthesis of Poly(Methoxy PEG Acrylate-co-Solketal Acrylate) (P(MPEGA-co-SA))

To a sealed 1 dram vial, solketal acrylate (100 mg, 0.595 mmol), methoxy PEG acrylate (1.03 g, 2 mmol), 2-(*n*-butyltrithiocarbonate)-propionic acid (BTPA, 27.6 mg, 0.116 mmol), and azobisisobutyronitrile (AIBN, 1.9 mg, 12 μmol) were dissolved in degassed DMSO in a 1:1 monomer:DMSO ratio, and the mixture was degassed for 20 min. The reaction was heated at 65 °C for 7 h then transferred to dialysis tubing (MWCO = 1000 Da) and dialyzed against 1:1 mixture DCM:MeOH for 24 h. (1.12 g, 98%, M_n = 12 kDa, M_w = 13.9 kDa, \bar{D} = 1.15, MPEGA = 80%, SA = 20%) ^1H NMR (600 MHz, CDCl_3) δ : 0.93 (3H, t, $-\text{S}(\text{CH}_2)_3\underline{\text{CH}}_3$), 1.39 (6H, d, CH_3), 1.63 (s,

CH), 1.90 (s, CH), 2.29 (s, CH), 3.37 (s, -OCH₃), 3.55 (t, -O=COCH₂-), 3.64 (s, -OCH₂CH₂O-), 4.15 (s, -O=COCH₂-), 4.23 (s, -O=COCH₂-), 4.31 (s, -O=COCH₂-)

Synthesis of 2,2,5-Trimethyl-1,3-Dioxane-5-Carboxylic Acid

Under nitrogen atmosphere, 2,2-bis(hydroxymethyl)propionic acid (15 g, 0.111 mol) and 2,2-dimethoxypropane (24.35 mL, 0.198 mol) were dissolved in anhydrous acetone (75 mL). *p*-toluenesulfonic acid monohydrate (PTSA, 1.065 g, 5.6 mmol) was added and stirred for 18 h. Triethylamine (TEA, 0.75 mL, 5.4 mmol) was added and stirred for 5 min. The concentrated product was washed with DI water and extracted with dichloromethane (DCM). The product was dried over magnesium sulfate (MgSO₄) and dried *in vacuo*. (10.52 g, 54%) ¹H NMR (600 MHz, CDCl₃) δ: 1.21 (3H, s, CH₃), 1.37 (3H, s, CH₃), 1.42 (3H, s, CH₃), 3.67 (2H, d, -OCH₂), 4.19 (2H, d, -OCH₂)

Synthesis of 2,2,5-Trimethyl-1,3-Dioxane-5-Carboxylic Anhydride

2,2,5-Trimethyl-1,3-dioxane-5-carboxylic acid (10.52 g, 0.06 mol) was dissolved in DCM (42 mL). *N,N'*-Dicyclohexylcarbodiimide (6.22 g, 0.03 mol) was added to the reaction slowly and stirred for 18 h. The precipitate was removed by filtration and the concentrated product was kept at -20 °C overnight and filtered to remove precipitate then dried *in vacuo*. (8.5 g, 81%) ¹H NMR (600 MHz, CDCl₃) δ: 1.21 (6H, s, CH₃), 1.37 (6H, s, CH₃), 1.42 (6H, s, CH₃), 3.67 (4H, d, -OCH₂), 4.19 (4H, d, -OCH₂)

Synthesis of 2-(Acryloyloxy)Ethyl 2,2,5-Trimethyl-1,3-Dioxane-5-Carboxylate

Under nitrogen atmosphere, 2,2,5-trimethyl-1,3-dioxane-5-carboxylic anhydride (8.5 g, 0.026 mol), 4-(dimethylamino)pyridine (157.16 mg, 0.001 mol), TEA (3.59 mL, 0.026 mol), and DCM (187 mL) were added to a reaction flask. 2-Hydroxyethyl acrylate (2.96 mL, 0.026 mol) was added slowly and stirred for 18 h. The concentrated product was washed with sat. sodium bicarbonate solution (2x) and dried over MgSO₄. Product was kept at 8 °C overnight and precipitate removed by filtration. (8.3 g, 61%) ¹H NMR (600 MHz, CDCl₃) δ: 1.21 (3H, s, CH₃), 1.37 (3H, s, CH₃), 1.42 (3H, s, CH₃), 3.67 (2H, d, -OCH₂), 4.19 (2H, d, -OCH₂), 5.86 (1H, dd, HC=CH₂), 6.16 (1H, m, HC=CH₂), 6.44 (1H, dd, C=CH₂)

General Procedure for Synthesis of Poly(Methoxy PEG Acrylate-co-1) (P(MPEGA-co-1))

To a sealed 1 dram vial, **1** (511.6 mg, 1.2 mmol), methoxy PEG acrylate (1.33 g, 2.7 mmol), BTPA (44.6 mg, 0.18 mmol), and AIBN (3.6 mg, 22 μmol) were dissolved in degassed DMSO in a 1:1 monomer:DMSO ratio, and the mixture was degassed for 20 min. The reaction was heated at 65 °C for 7 h then transferred to dialysis tubing (MWCO = 1000 Da) and dialyzed against 1:1 mixture DCM:MeOH for 24 h. (1.59 g, 85%, Mn = 11.1 kDa, Mw = 12.4 kDa, Đ = 1.12, MPEGA = 73%, **1** = 27%) ¹H NMR (600 MHz, CDCl₃) δ: 0.93 (3H, t, -S(CH₂)₃CH₃), 1.19 (3H, s, CH₃), 1.39 (6H, d, CH₃), 1.63 (s, CH), 1.90 (s, CH), 2.29 (s, CH), 3.37 (s, -OCH₃), 3.55 (t, -O=COCH₂-), 3.64 (s, -OCH₂CH₂O-), 4.15 (s, -O=COCH₂-), 4.23 (s, -O=COCH₂-), 4.31 (s, -O=COCH₂-)

General Procedure for Acetonide Deprotection of P(MPEGA-co-SA) or P(MPEGA-co-1)

To a 1 dram vial with stir bar, polymer (600 mg, 0.388 mmol acetonide) was dissolved in DI water (1.5 mL). Trifluoroacetic acid (11.88 μL, 0.115 mmol) was added and the reaction stirred for 18

h. The solution was transferred to dialysis tubing (MWCO = 1000 Da) and dialyzed against MeOH for 8 h. The polymer was concentrated and dried *in vacuo*. (480 mg, 80%)

General Procedure for Formaldehyde Conjugation to Functionalized Polyacrylate

Polymer (200 mg, 1 equiv.) was weighed into a 1 dram vial with stir bar. Formaldehyde solution (37 wt % in water, 241 μ L, 6 mmol, 50 equiv. per diol or aminoxy) was added to the reaction vial, and the mixture was stirred at room temperature for 2 h. Methanol was removed under evaporation and the mixture was lyophilized. The product was then filtered using ultra centrifugal filters (MWCO = 3 kDa) to remove formaldehyde oligomers and the filtrate discarded. The product was collected and stored at 4 °C until used.

In Vitro Release of Formaldehyde from PG-Acetal and AOPG-Oxime Prodrugs

The in-vitro release of formaldehyde from the prodrugs was determined using Float-A-Lyzer® dialysis tubing (MWCO: 0.1K-0.5K). A sample of PG-acetal prodrug (50.0 mg, 2.54 mg formaldehyde) was suspended in 1.0 mL of either acetate buffer (Sodium acetate/acetic acid, pH 5.0) or PBS (pH 7.4) and transferred to a Float-A-Lyzer® dialysis pod. The pod was then placed in a 50-mL Falcon tube containing 18.0 mL of the corresponding buffer solution. Samples of AOPG-oxime prodrug were prepared in a similar manner with the additional step of adding 75 μ L (pH 5.0) or 20 μ L (pH 7.4) of 12.M HCl to the sample before transferring to the dialysis pod. Falcon tubes were placed in an oil bath at 37 °C and media was stirred constantly using a magnetic stir bar. Samples of 100 μ L were withdrawn from the sink after 15 minutes, 30 minutes, 1, 2, 3, 4, 6, 24, 48, 72, and 96 hours, and then every two days following. An equal amount of fresh media was added to the sink after each withdrawal to maintain sink conditions. The amount of

formaldehyde released at each time point was quantified using a colorimetric assay as described below.

In Vitro Release of Formaldehyde from P(MPEGA-co-SA)-Acetal or P(MPEGA-co-I)-Acetal

Release of formaldehyde from the prodrugs was determined using Float-A-Lyzer® dialysis tubing (MWCO: 0.1K-0.5K). A sample of prodrug (10.0 mg) was suspended in 1.0 mL of either acidic buffer (NaOAc-acetic acid, pH 5.0) or PBS (pH 7.4) and transferred to a Float-A-Lyzer® dialysis pod. The pod was then placed in a 50-mL Falcon tube containing 18.0 mL of the corresponding buffer solution. Falcon tubes were placed in an oil bath at 37 °C and media was stirred constantly using a magnetic stir bar. Samples of 100 µL were withdrawn from the sink at 0.5, 1, 1.5, 2, 4, 6, 24, 48, 72 h and every two days following. An equal amount of fresh media was added to the sink after each withdrawal to maintain sink conditions. The amount of formaldehyde released at each time point was quantified using a colorimetric assay as described below.

Colorimetric Analysis of Formaldehyde Concentration

All reagent solutions were made with cell culture grade water. A 50 µL aliquot of sample was placed in the well of a 96-well plate and 50 µL of 2mM NaIO₄ in 0.2M NaOH was added to the sample. The plate was then incubated for 20 minutes at room temperature in the dark. After 20 minutes, 100 µL of a 34mM solution of 4-amino-3-hydrazino-5-mercapto-1,2,4-triazole (Purpald®) in 2M NaOH was added to the sample and incubated at room temperature for 20 minutes. To develop the color, 100 µL of 33 mM NaIO₄ solution in 0.2M NaOH was added to each well and the absorbance of each well in the plate was read at 550 nm immediately.

Synthesis of Partially Reduced Ketoxime/Alkoxyamine Nanoparticles

P(VL-*co*-OPD) (8% OPD, 50 mg, 4556.20 g mol⁻¹, 1.71×10⁻⁵ mol) was dissolved in dichloromethane (5.70 mL) then added to a 50 mL round bottom flask. O,O'-(((oxybis(ethane-2,1-diyl))bis(oxy))bis(ethane-2,1-diyl))bis(hydroxylamine) (3.83 mg, 1.71×10⁻⁵ mol, 1 equiv.) was dissolved in dichloromethane (0.63 mL) and added quickly to the polymer solution at a fast vortex. After 2 h, sodium cyanoborohydride (6.72 mg, 1.07×10⁻⁴ mol, 0.5 equiv.) and a catalytic amount of saturated sodium bicarbonate solution (100 μL) were added directly to the reaction flask. The reaction stirred for 2 h then was transferred to Thermo Scientific™ SnakeSkin™ 10K MWCO Dialysis Tubing. The solution was dialyzed against a 1:1 mixture of MeOH/DCM for 48 h, with 3-4 solvent changes per day. The solution was filtered with a 0.45 μm filter to remove solid salt particulates and solvent was removed via rotary evaporation. The product was dried in vacuo to yield a light tan waxy solid (80% yield). ¹H NMR (400 MHz, CDCl₃): δ 0.90 (d, 6H); 1.6-1.75 (m); 2.23-2.43 (m); 2.25-2.7 (m); 2.7-2.84 (m); 3.4 (t); 3.65 (m); 4.0 (t); 4.3-4.4 (m). ¹³C NMR (600 MHz, CDCl₃): δ 21.32, 25.53, 28.00, 33.62, 63.85, 67.88, 173.26

Encapsulation of Doxorubicin into Partially Reduced Ketoxime/Alkoxyamine Nanoparticles

NPs (12.6 mg, 8% OPD, 2.7 mM, ~80 nm) were added to a 1.5 mL centrifuge tube. Doxorubicin (DOX) was solubilized in dimethyl sulfoxide (DMSO) to a known concentration and then added to the NPs (3.15 mg, 11.2 μmol). Additional DMSO was added to the mixture up to a total of 50 μL. Cell culture grade water containing 0.1% D-α-tocopherol polyethylene glycol 1000 succinate (1 mL) was added to the centrifuge tube and vortexed to induce DOX encapsulation. D-α-tocopherol polyethylene glycol 1000 succinate is added to coat the particles during encapsulation and aid in resuspension in aqueous media during drug release studies. The mixture was then

centrifuged at 14000 RPM for 20 min. The supernatant was decanted, fresh cell culture grade water (1 mL) was added to the particle pellet and vortexed until particles were resuspended. Centrifugation was repeated at 14000 RPM for 20 min, then the supernatant was decanted to remove any unincorporated drug. Cell culture grade water (0.5 mL) was added to the mixture, frozen, and lyophilized to produce DOX-loaded nanoparticles (DOX-NP). HPLC analysis confirmed encapsulation of DOX at an average of 17.9 wt % with 89.5% efficiency.

V.5 References

1. Lehar, J.; Krueger, A. S.; Avery, W.; Heilbut, A. M.; Johansen, L. M.; Price, E. R.; Rickles, R. J.; Short, G. F., 3rd; Staunton, J. E.; Jin, X.; Lee, M. S.; Zimmermann, G. R.; Borisy, A. A., Synergistic drug combinations tend to improve therapeutically relevant selectivity. *Nat Biotechnol* **2009**, *27* (7), 659-66.
2. Fouquier, J.; Guedj, M., Analysis of drug combinations: current methodological landscape. *Pharmacol Res Perspect* **2015**, *3* (3), e00149, 1-11.
3. Sun, W.; Sanderson, P. E.; Zheng, W., Drug combination therapy increases successful drug repositioning. *Drug Discov Today* **2016**, *21* (7), 1189-1195.
4. Woods, M. L. I.; MacGinley, R.; Eisen, D. P.; Allworth, A. M., HIV combination therapy: partial immune restitution unmasking latent cryptococcal infection. *AIDS* **1998**, *12* (12), 1491-1494.
5. Philippe, B.; Gombert, B.; Ginsburg, C.; Passeron, A.; Stubei, I.; Rigolet, A.; Salmon, D.; Sicard, D., HIV Combination Therapy: Immune Restitution Causing Cryptococcal Lymphadenitis Dramatically Improved by Anti-inflammatory Therapy. *Scand J Infect Dis* **1998**, *30* (6), 615-616.

6. Lennox, J. L.; DeJesus, E.; Lazzarin, A.; Pollard, R. B.; Madruga, J. V. R.; Berger, D. S.; Zhao, J.; Xu, X.; Williams-Diaz, A.; Rodgers, A. J.; Barnard, R. J. O.; Miller, M. D.; DiNubile, M. J.; Nguyen, B.-Y.; Leavitt, R.; Sklar, P., Safety and efficacy of raltegravir-based versus efavirenz-based combination therapy in treatment-naive patients with HIV-1 infection: a multicentre, double-blind randomised controlled trial. *Lancet* **2009**, *374* (9692), 796-806.
7. Vanneman, M.; Dranoff, G., Combining immunotherapy and targeted therapies in cancer treatment. *Nat Rev Cancer* **2012**, *12*, 237-251.
8. Hirooka, Y.; Itoh, A.; Kawashima, H.; Hara, K.; Nonogaki, K.; Kasugai, T.; Ohno, E.; Ishikawa, T.; Matsubara, H.; Ishigami, M.; Katano, Y.; Ohmiya, N.; Niwa, Y.; Yamamoto, K.; Kaneko, T.; Nieda, M.; Yokokawa, K.; Goto, H., A Combination Therapy of Gemcitabine With Immunotherapy for Patients With Inoperable Locally Advanced Pancreatic Cancer. *Pancreas* **2009**, *38* (3), e69-e74.
9. Barati, D.; Shariati, S. R.; Moeinzadeh, S.; Melero-Martin, J. M.; Khademhosseini, A.; Jabbari, E., Spatiotemporal release of BMP-2 and VEGF enhances osteogenic and vasculogenic differentiation of human mesenchymal stem cells and endothelial colony-forming cells co-encapsulated in a patterned hydrogel. *J Control Release* **2016**, *223*, 126-136.
10. Smyth, M. J.; Ngiow, S. F.; Ribas, A.; Teng, M. W. L., Combination cancer immunotherapies tailored to the tumour microenvironment. *Nat Rev Clin Oncol* **2015**, *13* (3), 143-158.
11. Donnenberg, V. S.; Donnenberg, A. D., Multiple Drug Resistance in Cancer Revisited: The Cancer Stem Cell Hypothesis. *The Journal of Clinical Pharmacology* **2005**, *45* (8), 872-877.
12. Holohan, C.; Van Schaeybroeck, S.; Longley, D. B.; Johnston, P. G., Cancer drug resistance: an evolving paradigm. *Nat Rev Cancer* **2013**, *13* (10), 714-26.

13. White, N. J., Antimalarial drug resistance. *J Clin Invest* **2004**, *113* (8), 1084-1092.
14. Li, W. P.; Su, C. H.; Tsao, L. C.; Chang, C. T.; Hsu, Y. P.; Yeh, C. S., Controllable CO Release Following Near-Infrared Light-Induced Cleavage of Iron Carbonyl Derivatized Prussian Blue Nanoparticles for CO-Assisted Synergistic Treatment. *ACS Nano* **2016**, *10* (12), 11027-11036.
15. Cutts, S. M.; Nudelman, A.; Rephaeli, A.; Phillips, D. R., The Power and Potential of Doxorubicin-DNA Adducts. *IUBMB Life* **2005**, *57* (2), 73-81.
16. Burke, P. J.; Koch, T. H., Doxorubicin-formaldehyde conjugate, doxoform: induction of apoptosis relative to doxorubicin. *Anticancer Res* **2001**, *21* (4A), 2753-2760.
17. Fenick, D. J.; Taatjes, D. J.; Koch, T. H., Doxoform and Daunoform: Anthracycline-Formaldehyde Conjugates Toxic to Resistant Tumor Cells. *J Med Chem* **1997**, *40* (16), 2452-2461.
18. Post, G. C.; Barthel, B. L.; Burkhart, D. J.; Hagadorn, J. R.; Koch, T. H., Doxazolidine, a Proposed Active Metabolite of Doxorubicin That Cross-links DNA. *J Med Chem* **2005**, *48* (24), 7648-7657.
19. Lukowiak, M. C.; Wettmarshausen, S.; Hidde, G.; Landsberger, P.; Boenke, V.; Rodenacker, K.; Braun, U.; Friedrich, J. F.; Gorbushina, A. A.; Haag, R., Polyglycerol coated polypropylene surfaces for protein and bacteria resistance. *Polym Chem* **2015**, *6* (8), 1350-1359.
20. Kainthan, R. K.; Janzen, J.; Levin, E.; Devine, D. V.; Brooks, D. E., Biocompatibility testing of branched and linear polyglycidol. *Biomacromolecules* **2006**, *7* (3), 703-709.
21. Spears, B. R.; Waksal, J.; McQuade, C.; Lanier, L.; Harth, E., Controlled branching of polyglycidol and formation of protein-glycidol bioconjugates via a graft-from approach with "PEG-like" arms. *Chem Comm* **2013**, *49* (24), 2394-2396.

22. Beezer, D. B.; Harth, E., Post-polymerization modification of branched polyglycidol with N-Hydroxy phthalimide to give ratio-controlled amino-oxy functionalized species. *J Polym Sci A* **2016**, *54* (17), 2820-2825.
23. Zhang, X.; Lin, Y.; Gillies, R. J., Tumor pH and its measurement. *J Nucl Med* **2010**, *51* (8), 1167-1170.
24. Ojugo, A. S. E.; McSheehy, P. M. J.; McIntyre, D. J. O.; McCoy, C.; Stubbs, M.; Leach, M. O.; Judson, I. R.; Griffiths, J. R., Measurement of the extracellular pH of solid tumours in mice by magnetic resonance spectroscopy: a comparison of exogenous ¹⁹F and ³¹P probes. *NMR Biomed* **1999**, *12* (8), 495-504.
25. Fukamachi, T.; Chiba, Y.; Wang, X.; Saito, H.; Tagawa, M.; Kobayashi, H., Tumor specific low pH environments enhance the cytotoxicity of lovastatin and cantharidin. *Cancer Lett* **2010**, *297* (2), 182-189.
26. Nguyen, D.; Nguyen, T.-K.; Rice, S. A.; Boyer, C., CO-Releasing Polymers Exert Antimicrobial Activity. *Biomacromolecules* **2015**, *16* (9), 2776-2786.
27. Hariri, G.; Edwards, A. D.; Merrill, T. B.; Greenbaum, J. M.; van der Ende, A. E.; Harth, E., Sequential Targeted Delivery of Paclitaxel and Camptothecin Using a Cross-Linked “Nanosponge” Network for Lung Cancer Chemotherapy. *Mol Pharmaceutics* **2014**, *11* (1), 265-275.
28. Passarella, R. J.; Spratt, D. E.; van der Ende, A. E.; Phillips, J. G.; Wu, H. M.; Sathiyakumar, V.; Zhou, L.; Hallahan, D. E.; Harth, E.; Diaz, R., Targeted Nanoparticles That Deliver a Sustained, Specific Release of Paclitaxel to Irradiated Tumors. *Cancer Res* **2010**, *70* (11), 4550-4559.

29. Stevens, D. M.; Gilmore, K. A.; Harth, E., An assessment of nanosponges for intravenous and oral drug delivery of BCS class IV drugs: Drug delivery kinetics and solubilization. *Polym Chem* **2014**, *5* (11), 3551-3554.
30. van der Ende, A.; Croce, T.; Hamilton, S.; Sathiyakumar, V.; Harth, E., Tailored polyester nanoparticles: post-modification with dendritic transporter and targeting units via reductive amination and thiol-ene chemistry. *Soft Matter* **2009**, *5* (7), 1417-1425.
31. van der Ende, A. E.; Harrell, J.; Sathiyakumar, V.; Meschievitz, M.; Katz, J.; Adcock, K.; Harth, E., "Click" Reactions: Novel Chemistries for Forming Well-defined Polyester Nanoparticles. *Macromolecules* **2010**, *43* (13), 5665-5671.
32. van der Ende, A. E.; Kravitz, E. J.; Harth, E., Approach to Formation of Multifunctional Polyester Particles in Controlled Nanoscopic Dimensions. *J Am Chem Soc* **2008**, *130* (27), 8706–8713.
33. van der Ende, A. E.; Sathiyakumar, V.; Diaz, R.; Hallahan, D. E.; Harth, E., Linear release nanoparticle devices for advanced targeted cancer therapies with increased efficacy. *Polym Chem* **2010**, *1* (1), 93-96.
34. Kendrick-Williams, L. L.; Harth, E., Second-Generation Nanosponges: Nanonetworks in Controlled Dimensions via Backbone Ketoxime and Alkoxyamine Cross-Links for Controlled Release. *Macromolecules* **2018**, *51* (24), 10160-10166.
35. de la Croix Ndong, J. D.; Stevens, D. M.; Vignaux, G.; Uppuganti, S.; Perrien, D. S.; Yang, X. L.; Nyman, J. S.; Harth, E.; Elefteriou, F., Combined MEK Inhibition and BMP2 Treatment Promotes Osteoblast Differentiation and Bone Healing in *Nf1(Osx)(-/-)* Mice. *J Bone Miner Res* **2015**, *30* (1), 55-63.

36. Stevens, D. M.; Rahalkar, A.; Spears, B.; Gilmore, K.; Douglas, E.; Muthukumar, M.; Harth, E., Semibranched polyglycidols as “fillers” in polycarbonate hydrogels to tune hydrophobic drug release. *Polym. Chem.* **2015**, *6* (7), 1096-1102.
37. Immanuel Hahnenstein, H. H., Cornelius G. Kreiter, and Gerd Maurer, IH- and ¹³C-NMR Spectroscopic Study of Chemical Equilibria in Solutions of Formaldehyde in Water, Deuterium Oxide, and Methanol. *Ind Eng Chem Res* **1994**, *33*, 1022-1029.
38. McCullough, A.; Gilmore, K. A.; Kendrick-Williams, L. L.; Harth, E., In Vitro Analysis of Polyglycidol Prodrug Efficacy. *Unpublished data* **2015**.
39. Abouelmagd, S. A.; Sun, B.; Chang, A. C.; Ku, Y. J.; Yeo, Y., Release Kinetics Study of Poorly Water-Soluble Drugs from Nanoparticles: Are We Doing It Right? *Mol Pharmaceutics* **2015**, *12* (3), 997-1003.
40. Savjani, K. T.; Gajjar, A. K.; Savjani, J. K., Drug solubility: importance and enhancement techniques. *ISRN Pharm* **2012**, *2012*, 1-10.
41. Nallamolu, S.; Jayanti, V. R.; Chitneni, M.; Kesharwani, P., Solubility Enhancement of Poorly Water-Soluble Drug Aprepitant for Oral Delivery by Self-Micro Emulsifying Drug Delivery System. *Acta Scientific Pharmaceutical Sciences* **2018**, *2* (3), 2-13.

APPENDIX A

References for Adaptations of Chapters

- CHAPTER II. Sections **II.2.1 Synthesis of Nanosponges in Precise Size and Crosslinking Density** and **II.2.2 Evaluation and Analysis of Size Relationships** adapted from Kendrick-Williams, L.L., Harth, E. Nanosponge Tunability in Size and Crosslinking Density. *Journal of Visualized Experiments*. **2017**, (126), e56073.
- CHAPTER III. Kendrick-Williams, L.L., Choy, M.Y., Gilmore, K.A., Carmichael, I., Pearce, H.A., Cody, S.H., Alt, K., Hagemeyer, C.E., Harth, E. “Development of Collagen-Targeted Theranostic Nanosponges for the Treatment of Cardiovascular Disease” *Manuscript Submitted to ACS Chemistry of Materials* **2018**.
- CHAPTER IV. Kendrick-Williams, L.L. and Harth, E. “Second-Generation Nanosponges: Nanonetworks in Controlled Dimensions via Backbone Ketoxime and Alkoxyamine Cross-Links for Controlled Release” *Macromolecules* **2018**, 51 (24), 10160-10166
US Provisional Patent Application #62/755,611
- CHAPTER V. Kendrick-Williams, L.L., Lampley, M.W., Ordonez, E., Harth, E. “Synergistic Dual Drug Delivery with Sustained-release Formaldehyde from Polymer Prodrugs and Doxorubicin Nanoparticles for Improved Antitumor Efficacy” *Manuscript in Preparation*.

APPENDIX B

Curriculum Vitae

Laken L. Williams

(601) 543-3664 || laken.leona.williams@gmail.com || www.linkedin.com/in/lakenwilliams

EXECUTIVE SUMMARY

Vanderbilt PhD, Amgen Scholar, and NSF Fellow with 4 years experience in new platform development of drug delivery systems, seeking technical role in product or process development with cross-functional business responsibilities where my knowledge of polymer chemistry and characterization will add value to your company. Highlights include:

- Knowledgeable innovator with 8 years experience in polymer chemistry and characterization as evidenced by 5 publications in peer-reviewed journals
- Strong leadership skills and experience managing cross-functional collaborations, laboratory resources, and safety standards
- Excellent communication skills in addressing research practices and project results demonstrated by \$138,000.00 fellowship funding and 3 national meeting presentations

EDUCATION

PhD Chemistry 2019
Vanderbilt University, Nashville, TN
Advisor: Eva Harth
Dissertation: Developing Highly Tunable Polymer-based Networks for Drug Delivery Applications

BS Polymer Science (*summa cum laude*), Minor in Chemistry 2015
University of Southern Mississippi, Hattiesburg, MS
Advisor: Derek Patton
Honors thesis: Biomimetic Adhesive Thiol-ene Films for Improved Adhesion

WORK EXPERIENCE

Product Development Scientist II Feb. 2019 (projected start)
The Clorox Company, Pleasanton, CA

- Product development for CloroxPro brand portfolio through formulation and commercialization of new products
- Evaluation of current market trends and existing products

National Science Foundation Graduate Research Fellow
Vanderbilt University, Nashville, TN

2015-2019

- Utilized multiple polymerization techniques to synthesize biodegradable and biocompatible polymers for the development and characterization of novel nanomaterials resulting in 1 publication in a peer-reviewed journal
- Developed post-modification strategies for surface conjugation of targeting and imaging molecules to nanoparticles resulting in submission of a manuscript to a peer-reviewed journal
- Experience in experimental design and analysis of polymer structure-property relationships with a focus in nanomaterials
- Mentored 6 graduate and 2 undergraduate research assistants; managed laboratory inventory, resources, and safety standards
- Instrumentation: NMR, TEM, DLS, MALS, HPLC, GPC, UV-Vis, and IR

Undergraduate Research Assistant
University of Southern Mississippi, Hattiesburg, MS

2011-2015

- Synthesized polymeric thin films and analyzed their structure-property relationships via thermal and mechanical analysis resulting in 2 peer-reviewed publications
- Developed film fabrication methods utilizing spray-deposition, dip-casting, spin-coating, and photopolymerization techniques to prepare superamphiphobic coatings resulting in 1 peer-reviewed publication
- Evaluated thermomechanical properties of polymer substrates via DSC, DMA, and TGA and determined polymer film properties via ellipsometry, optical microscopy, and contact angle
- Developed and analyzed adhesive thin films for improved adhesion via pull-off and cross-hatch adhesion testing

PUBLICATIONS & PATENTS

1. Kendrick-Williams, L.L., Lampley, M.W., Ordonez, E., Harth, E. "Synergistic Dual Drug Delivery with Sustained-Release Formaldehyde from Polymer Prodrugs and Doxorubicin Nanoparticles for Improved Antitumor Efficacy" *Manuscript in Preparation*.
2. Kendrick-Williams, L.L., Choy, M.Y., Gilmore, K.A., Carmichael, I., Pearce, H.A., Cody, S.H., Alt, K., Hagemeyer, C.E., Harth, E. "Development of Collagen-Targeted Theranostic Nanosponges for the Treatment of Cardiovascular Disease" *Manuscript Submitted to ACS Chemistry of Materials*. **2018**.
3. Kendrick-Williams, L.L. and Harth, E. "Second-Generated Nanosponges: Nanonetworks in Controlled Dimensions via Backbone Ketoxime and Alkoxyamine Cross-Links for Controlled Release" *Macromolecules*. **2018**, 51 (24), 10160-10166
4. Harth, E., Kendrick-Williams, L.L. 2018. Second generation nanosponge delivery systems – Nanonetworks through backbone crosslinking. U.S. Patent Application No. 62/755,611, filed Nov. 2018. Patent Pending.
5. Kendrick-Williams, L.L. and Harth, E. "Nanosponge Tunability in Size and Crosslinking Density". *J. Vis. Exp.* **2017**, (126), e56073.

- Xiong, L., Kendrick, L.L., Heusser, H., Webb, J.C., Sparks, B.J., Goetz, J.T., Guo, W., Stafford, C.M., Blanton, M.D., Nazarenko, S., Patton, D. "Spray-Deposition and Photopolymerization of Organic-Inorganic Thiol-ene Resins for Fabrication of Superamphiphobic Surfaces" *ACS Appl. Mater. Interfaces*. **2014**, 6, 10763-10774.
- Baranek, A.D., Kendrick, L.L., Tretbar, C.A., Patton, D.L. "Solvent-free copolymerization of rigid and flexible bis-1,3- benzoxazines: Facile tunability of polybenzoxazine network properties" *Polymer*. **2013**, 54, 5553-5559.
- Baranek, A.D., Kendrick, L.L., Narayanan, J., Tyson, G.E., Wand, S., Patton, D.L. "Flexible aliphatic-bridged bisphenol- based polybenzoxazines" *Polym. Chem*. **2012**, 3, 2892-2900

TECHNICAL SKILLS

Nuclear Magnetic Resonance (NMR) Spectroscopy	Gel Permeation Chromatography (GPC)
Transmission Electron Microscopy (TEM)	Dynamic Mechanical Analysis (DMA)
Differential Scanning Calorimetry (DSC)	UV-Vis Spectroscopy
Thermogravimetric Analysis (TGA)	Ring-Opening Polymerization
RAFT Polymerization	Infrared Spectroscopy (IR)
Thin-film Fabrication	Multi-Angle Light Scattering (MALS)
High Performance Liquid Chromatography (HPLC)	Dynamic Light Scattering (DLS)

SELECTED PRESENTATIONS

- "Development of Collagen-Targeted Theranostic Nanosponges for the Treatment of Cardiovascular Disease," August 2018, 256th American Chemical Society National Meeting – Boston, MA
- "Development of Dual Release Drug Delivery Platforms," August 2016, 252nd American Chemical Society National Meeting – Philadelphia, PA
- "Superamphiphobic Inorganic-Organic Thiol-Ene Surfaces via Spray-Deposition and Photopolymerization," March 2014, 247th American Chemical Society National Meeting – Dallas, TX

SELECTED HONORS, AWARDS, & AFFILIATIONS

- Fellow, National Science Foundation Graduate Research Fellowship Program, 2015-2019
- 1st Place Undergraduate Poster Presentation, Waterborne Symposium, 2015
- Scholar, Amgen Scholars Program, 2014
- Honorable Mention, Barry Goldwater Scholarship and Excellence in Education Foundation, 2014
- Recipient, Benjamin A. Gilman International Scholarship Program, 2013
- American Chemical Society (ACS), Division of Polymer Science & Engineering (PMSE)